U.S. DEPARTMENT OF COMMERCE
National Oceanic and Atmospheric Administration
Environmental Research Laboratories

NOAA Technical Memorandum ERL NSSL-69

PAPERS ON OKLAHOMA THUNDERSTORMS, APRIL 29-30, 1970

Stanley L. Barnes, Editor

Property of
NWC Library
University of Oklahoma

National Severe Storms Laboratory
Norman, Oklahoma
May 1974

PREFACE

During the five years prior to 1970, the National Severe Storms Laboratory developed capability to measure the atmosphere surrounding large, severe thunderstorms. These observations include measurements from forty-four closely-spaced, automatically recording surface stations located in a 1000 square mile area of central Oklahoma, sounding balloons released in and around the surface network, and a system for recording quantized radar information on magnetic tape.

This system was activated in early April 1970, and on April 29th was provided a rare opportunity to observe an eight-hour series of events that ranged from small hailstorms to gigantic, tornado-spawning maelstroms. The data are among the most detailed storm observations acquired to that time. Even the unfortunate damage caused by the tornadoes provided information on the character and structure of these storms.

Although data acquisition techniques had been highly refined by early 1970, techniques to process and assimilate the observations had not been well developed. During the ensuing few months, data were processed to an archive status, and then began a lengthy, often abortive, struggle to analyze the information using computers that were either too small or too remote from the Laboratory to work efficiently for us. Nonetheless, software was developed, observational uncertainties analyzed and results evaluated. In June 1971, NSSL obtained weekend use of a large computer at the NASA Manned Space Center in Houston and our work progressed steadily. Then late in 1972, NSSL procured its first in-house computer facility capable of handling the analysis techniques. With the addition of a drum plotter and software for contouring analyzed fields, the final products became available in mid-1973.

Several papers in this collection are preliminary reports presented at conferences (pages 101, 111, 141). Others have been revised since their first exposure as conference papers (pages 125, 175). Two papers have reached formal publication (pages 195, 215; see Partial List of Other Papers). The rest appear in print for the first time.

Because of the widely-varying backgrounds of these papers, conventions differ, particularly in the use of abbreviations, units and references. However, we have edited each paper for internal consistency, and hope the remaining differences will not be a distraction.

The first two papers provide background details concerning the storms discussed in the remaining eleven papers. Synoptic-scale changes are illustrated in a unique series of regional surface weather maps. The rawinsonde data ensemble depicts the atmosphere's eight-hour trend toward more severe convection. The second paper presents NSSL radar, rawinsonde and surface observations. Some readers may find particularly interesting the sounding profiles shown in relation to radar echoes (pages 25 through 32) and the maps which show relationships among surface measured parameters (pages 53 through 86).

The first thunderstorm to penetrate the network produced small hail and dissipated within the sensor area. Nelson and Barnes find abnormal thunderstorm pressure distribution, marginal thermal instability, shallow moist layer, and unfavorable vertical wind shear as likely causes of this storm's demise. The appendix to this paper, written by Crawford and Brown and later revised by NSSL's Director, Edwin Kessler, gives a capsule view of our early Doppler radar data acquired from Chickasha, Oklahoma, the station over which the storm passed.

Two papers by Henderson concern the second thunderstorm that passed over the network area. A preliminary analysis depicts this storm in vertical cross section and relies heavily upon two in-storm soundings, several ambient soundings, and models of internal structure conceived by other investigators. In his second paper, Henderson compares constant altitude radar maps of precipitation distribution with surface winds, thermal patterns and sounding data. Although the storm possesses many attributes of a supercell storm, Henderson finds a more complex structure. (Typical features of supercell storms are discussed on page 90 and shown in figures 9 and 12, pages 135 and 137.) Apparently this storm's organization is inhibited because of its position in the wake of a large nearby storm. The blocking of upper winds by the upstream storm decreases precipitation removal from the updrafts of the wake storm, thus shortening their life spans.

Surface and upper air data obtained in and near two tornadic supercell storms increase our knowledge of this storm type (pages 125 to 139). Mesocyclone circulation and pressure centers are separated several miles at the surface--probably a result of very high translation speeds. In this case, tornadoes occur behind the center of lowest pressure (mesocyclone scale) near the gust front. Soundings indicate the storm induces vertical stretching in the unsaturated air immediately ahead of the updraft's path. Downdraft impulse on the storm's southwest flank, outside the storm's rainy core, is visualized as initiating gust front acceleration.

The last and largest storm of the night produced twin hook echoes (tornado cyclones) and several tornado funnels. One hook echo was near the main storm updraft and the other was beneath a flanking cell more than 10 miles to the south. Curiously, the circulation of the flanking cell did not influence the surface winds appreciably, even though tornado funnels did reach the ground and cause considerable damage. The paper reports on the evolution of convergence--vorticity couplets in relation to the observed merger of these two cyclones.

Since these storms passed through Oklahoma City during the night, there were few visual observations of the funnels. Damage path details suggest that the most destructive storm (the flanking cell) had a series of small funnels skirting about the larger tornado cyclone's center.

Reed, Easter and Matejka calculate the mass and moisture budgets from five soundings that surround the larger thunderstorm upstream from the storm Henderson studied. They discover elevated maxima in both mass and moisture convergence and relate their findings to parameterization schemes now applied in convective models on a larger scale.

The Greene and Clark paper presents vertically integrated storm reflectivites assumed to measure distribution of liquid water content. Rapid increases in the integral parameter correlate with tornado formation in two instances, but tornado generation is not found in a third storm that also exhibits rapid increase in water content (the same storm Reed et al. study). The reader should note that the storm letter designations applied by Greene and Clark differ from those in the other papers. Their cell C is our Storm F, the first tornadic storm; their D is our E_2; their E and F are our Storm G and its flanking tornado-producing cell.

Infrasound signals measured by Wave Propagation Laboratory scientists, Georges and Greene, apparently do not relate to the tornadic Oklahoma storms, but came from thunderstorms occurring at the same time in Texas. However, the authors do not consider their results conclusive, due to difficulty in data interpretation.

Taylor's paper deals with sferics from the major storm occurrences. Radio frequency burst rates were recorded on several channels: high burst rates at frequencies 1 MHz to 100 MHz were associated only with the very large Storms E, F and G. The last two were known to be tornadic, and there is some indication that Storm E_2 also had an associated circulation. Taylor's work has continued over the intervening years, and he now has modified his equipment to determine azimuth of sferic origin.

Davies reports another radio technique for sensing atmospheric disturbances from large thunderstorms. His system monitors height of the ionospheric F-layer, and has detected both acoustic waves and gravity waves in this layer when thunderstorms penetrate the tropopause. Only an extremely small fraction of a thunderstorm's power goes into producing these waves whose source is unknown.

Although these papers address a variety of storm phenomena, many topics are not discussed. For example, details concerning thunderstorm internal flow are missing because we do not have sufficient data. Since 1970, the Laboratory has concentrated on developing dual-Doppler capability to investigate storm structure, particularly the tornado cyclone's evolution. The first data from this Doppler system has just been acquired at this writing.

Stanley L. Barnes
May 1974

ACKNOWLEDGMENTS

Soon after we realized the comprehensive nature of the 29-30 April 1970 data, NSSL's Director commissioned the study reported in this technical memorandum. The initial target date for publication was January 1972, but for reasons partially explained in the Preface, the major portion of the text was not begun until mid-1973. The encouragement of our colleagues has been greatly appreciated.

The analysts are very much in the debt of NSSL's meteorological and electrical technicians for high quality data sets. NSSL's Computer and Data Processing personnel, headed by Kathryn Gray, helped solve innumerable software problems. Their processing and archiving skills contributed substantially to the project.

Faced with an unusual variety of original illustrations, NSSL's Graphic Arts Section, supervised by Mr. J. T. Lee, gave considerate and quality workmanship. Editorial styling was suggested by Helen Ardrey, NSSL. Overall editorial assistance was provided by Joan Myers, ERL, Boulder. We appreciate their comments and suggestions, and take responsibility for errors which may remain.

Typing and formating the entire volume was the responsibility of Brenda Courtney. The authors thank her for enduring the many drafts, revisions and editings. The extent of her involvement in producing this memorandum is exemplified in the paper on storm damage characteristics which she researched.

Finally, the Laboratory thanks the contributing authors for their willing participation.

TABLE OF CONTENTS

	Page
PREFACE	iii
ACKNOWLEDGMENTS	vi
SYNOPTIC-SCALE ENVIRONMENT OF OKLAHOMA THUNDERSTORMS, APRIL 29-30, 1970 Stanley L. Barnes	1
MESONETWORK OBSERVATIONS AND ANALYSES Stanley L. Barnes	17
STUDY OF A DISSIPATING SEVERE STORM Stephan P. Nelson and Stanley L. Barnes	89
APPENDIX: SUMMARY OF 3-CM DOPPLER RADAR DATA TAKEN ON 29 APRIL 1970 Kenneth C. Crawford and Rodger A. Brown	97
THE INTERNAL STRUCTURE OF A THUNDERSTORM AS REVEALED BY θ_w SURFACES James H. Henderson	101
A DETAILED DESCRIPTION OF THE INTERNAL STRUCTURE OF A THUNDERSTORM James H. Henderson	111
MORPHOLOGY OF TWO TORNADIC STORMS: AN ANALYSIS OF NSSL DATA ON APRIL 30, 1970 Stanley L. Barnes	125
RADAR-OBSERVED MERGER OF TWIN HOOK ECHOES Stanley L. Barnes	141
TORNADO CHARACTERISTICS IMPLIED FROM DAMAGE TRACKS Stanley L. Barnes and Brenda L. Courtney	153
PRELIMINARY RESULTS OF A STUDY OF THE VERTICAL PROFILE OF MEAN DIVERGENCE IN A REGION OF CONVECTIVE UPDRAFTS AND DOWNDRAFTS R. J. Reed, R. C. Easter and T. J. Matejka	167
DEVELOPMENT IN SEVERE STORMS AS REVEALED BY VIL ANALYSIS OF THE APRIL 29-30, 1970, STORM SYSTEM Douglas R. Greene and Robert A. Clark	175
INFRASOUND FROM THE 29-30 APRIL 1970 STORMS Thomas M. Georges and Gary E. Greene	185

Page

RADIO-FREQUENCY ELECTRICAL ACTIVITY ASSOCIATED WITH SEVERE STORMS IN OKLAHOMA DURING APRIL 29-30, 1970 — 195
William L. Taylor

IONOSPHERIC DISTURBANCES DURING THE STORMS OF APRIL 29 AND 30, 1970, AT OKLAHOMA CITY — 215
Kenneth Davies

PARTIAL LIST OF OTHER PAPERS — 233

SYNOPTIC-SCALE ENVIRONMENT OF OKLAHOMA THUNDERSTORMS, APRIL 29-30, 1970

Stanley L. Barnes

National Severe Storms Laboratory
Norman, Oklahoma 73069

Severe thunderstorms developed along a dry line in northwest Texas in advance of a slowly moving long wave trough and moved into central Oklahoma during the evening of April 29-30, 1970. Calculations based on three-hourly weather reports reveal that strong surface moisture convergence characterized the development region throughout the day. National Severe Storms Laboratory rawinsondes, taken over the eight-hour period when storm intensities increased, exhibit deepening low-level moisture, intruding dry air at mid-levels, and increasing winds aloft. Magnitudes of Lifted Index, maximum gust, height of wet-bulb zero and hail size closely agree with the defining studies' results for severe thunderstorms. Trends in these four thermodynamically-based parameters, commonly used to estimate storm intensity, parallel observed changes in storm severity.

1. INTRODUCTION

The Oklahoma storms of April 29-30, 1970, developed in a slowly changing environment. A deep long wave trough moved over the west coast three days earlier and gradually progressed eastward. At the surface, a weak cold front of Pacific origin moved into the Texas-Oklahoma panhandles on the 28th, but became quasi-stationary on the 29th. A dry line developed along the Texas-Oklahoma border (100° W) several days before and remained stationary. During the early part of the week, thunderstorm activity developed along this line in the afternoon, but dissipated as it moved eastward.

Over Oklahoma and eastern Texas, surface dew points climbed into the mid-60's as southerly flow brought moisture from the Gulf of Mexico. However, the moist layer depth was still scant (40 mb) on the morning of the 29th, and a strong inversion (10K potential temperature differential) was present at 900 mb. Winds were strongly sheared below 4 km, but by 0600 CST a 75-kt jet at 500 mb developed over southwestern Oklahoma (fig. 1a). Also locally strong winds (65 kt) at 850 mb, in view of the nearly dry adiabatic lapse rates in the 850-500 mb layer, suggest vertical turbulent momentum exchange above the inversion. At the surface, confluence in the moist southerly and

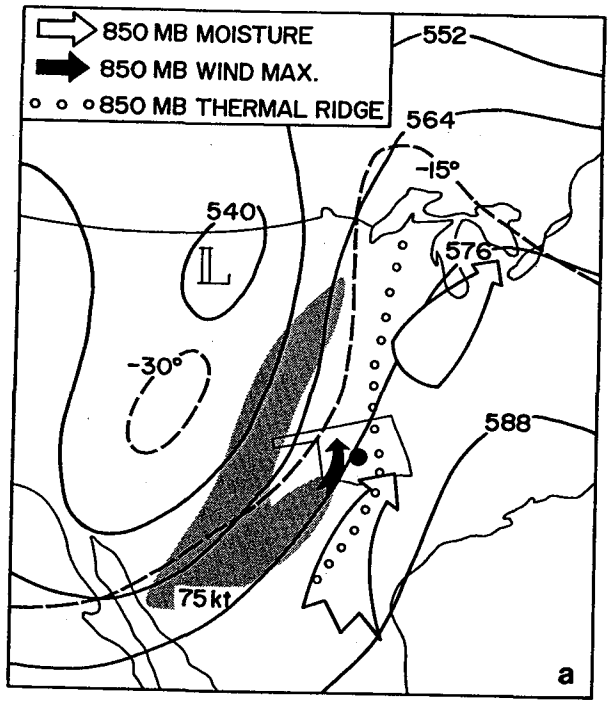

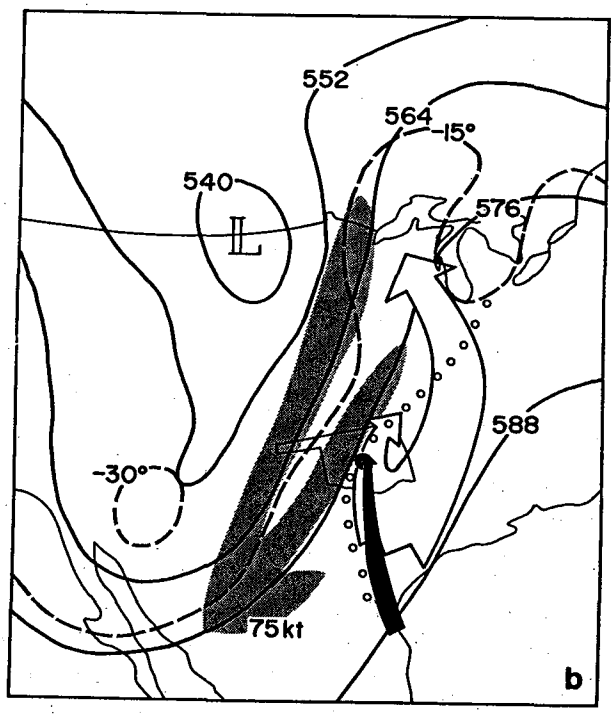

Figure 1. Upper air charts for (a) 0600 CST, and (b) 1800 CST, April 29, 1970. 500 mb contours (solid) and isotherms (dashed) overlay significant 850 mb features identified in (a). 500 mb winds are in excess of 75 kt in shaded area. NSSL mesonetwork is located at black dot in central Oklahoma.

dry southwesterly flow contributed to a local maximum in moisture convergence west of Wichita Falls, Texas (SPS; fig. 2). Beginning at 0800, the NSSL radar detected in this area showers that remained weak and scattered throughout the morning hours. Dry air made some progress into the northwestern part of the state by 0900 (fig. 3), but little organized movement of either the dry line or the front was detected.

A weak, poorly-organized line of showers extended across central Oklahoma at noon and into northern Texas in a general 020-200° direction (fig. 4). Surface flow in the northwestern Texas panhandle had settled from the southwest, but farther south, flow became north to northeasterly. Moisture still converged strongly into the region southwest of SPS.

During the afternoon hours (fig. 5), light to moderate thunderstorms (reflectivity less than 39 dBZ) appeared over much of the state, and more southeasterly flow developed over southern Oklahoma. By 1800 (fig. 6) two lines of moderate to occasionally strong thunderstorms stretched across the state from southwest to northeast. Moisture convergence continued very strong near SPS--the development region for the severe storms to follow.

Aloft, the long wave trough slid eastward (fig. 1b) and the central jet of a three-pronged 500-mb wind maximum extended over western Oklahoma. At 850 mb, a southerly jet brought additional moisture into the central part of the state along with slightly warmer air. The stage was set in Oklahoma and central Texas for a widespread outbreak of severe thunderstorms which would continue into the early morning of the 30th. Five storms would find their way into the NSSL mesonetwork area (black dot in fig. 1). Data obtained during an eight-hour period beginning at 1700 form the basis of other papers in this volume.

We discuss here the environmental changes that contributed to making subsequent storms increasingly severe. Network soundings not in thunderstorms provide information on upper air changes while conventional surface reports give additional insight.

2. MAP ANALYSIS SCHEME

Regional surface maps in figures 2-10 are computer drawn based on reported data interpolated to grid points 13.7 n miles apart. The numerical scheme, an adaptation of that used for mesonetwork analyses (Barnes, 1973), uses only observations taken at one time. Service A teletype weather observations are machine plotted in somewhat conventional manner, except cloud layer information appears above the station model and remarks are placed below. Observations are analyzed over the entire map area, however, only results over the central portion are displayed. Streamlines and contours of moisture convergence[1] are overlayed. In figures 3-8, radar echoes are shaded (NSSL radar was not operating at other map times).

[1]Actually, δ_x (TD·u) + δ_y (TD·v) where TD is dew point, u and v are wind components and δ is the incremental difference between alternate grid point values in the x and y direction.

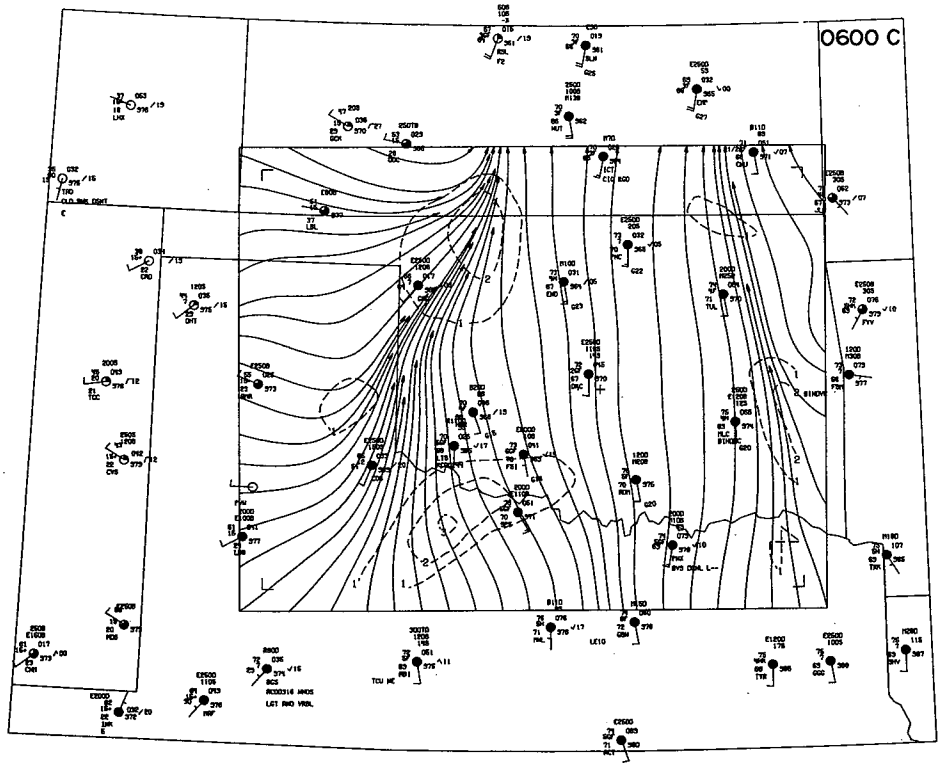

Figure 2. Regional weather map 0600 CST, April 29, 1970. Hourly reports are plotted in conventional manner except ceiling and sky condition appear at top of station circle and remarks appear below. Machine-drawn streamlines (solid) and moisture convergence (dashed) overlay analysis grid area 356 by 288 n miles. NSSL is located by "+". Figures 3 through 10 are similar maps at three-hour intervals. Light and dark shadings indicate regions of weak (< 39 dBZ) and strong (> 39 dBZ) radar echo. Radar patterns are unavailable for 0600 CST on the 29th, 0300 and 0600 CST on the 30th.

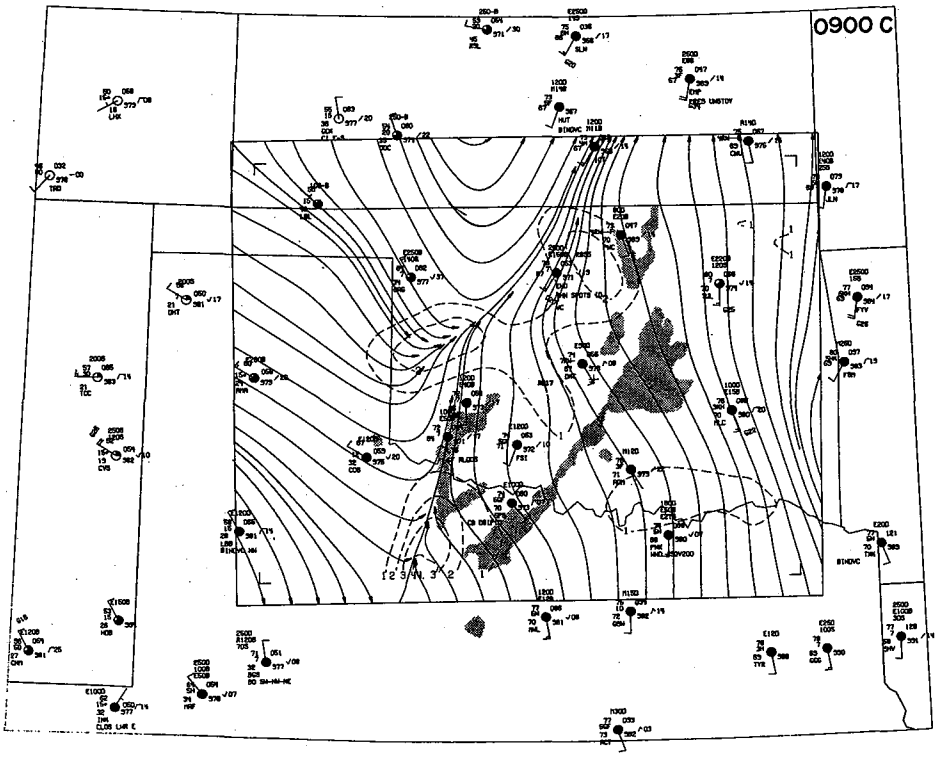

Figure 3. Regional weather map, 0900 CST, April 29, 1970.

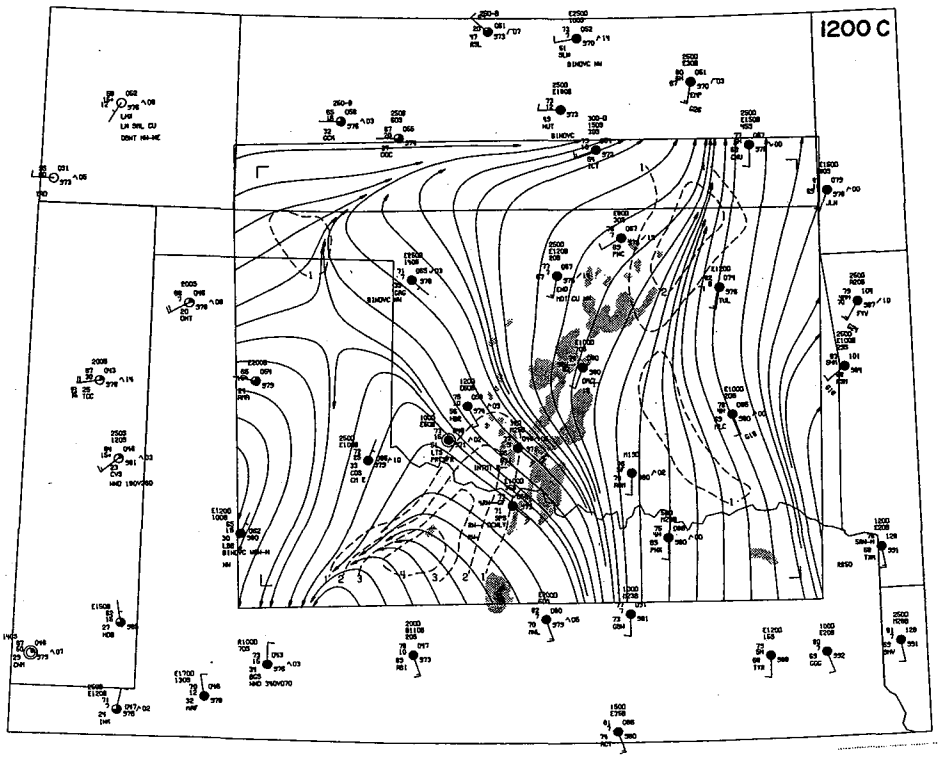

Figure 4. Regional weather map, 1200 CST, April 29, 1970.

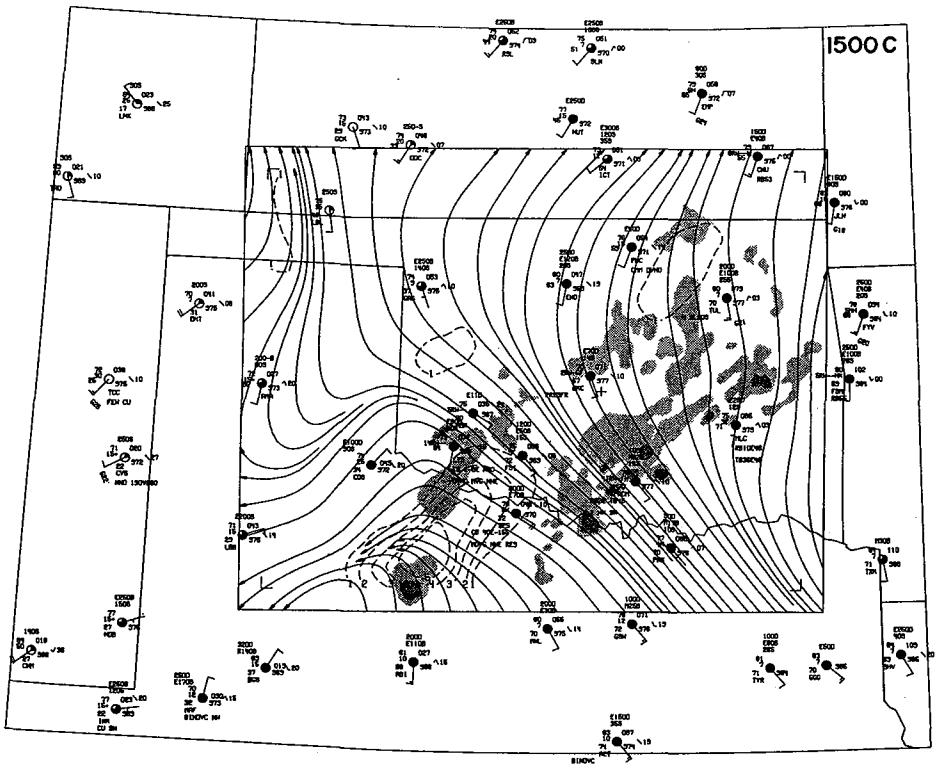

Figure 5. Regional weather map, 1500 CST, April 29, 1970.

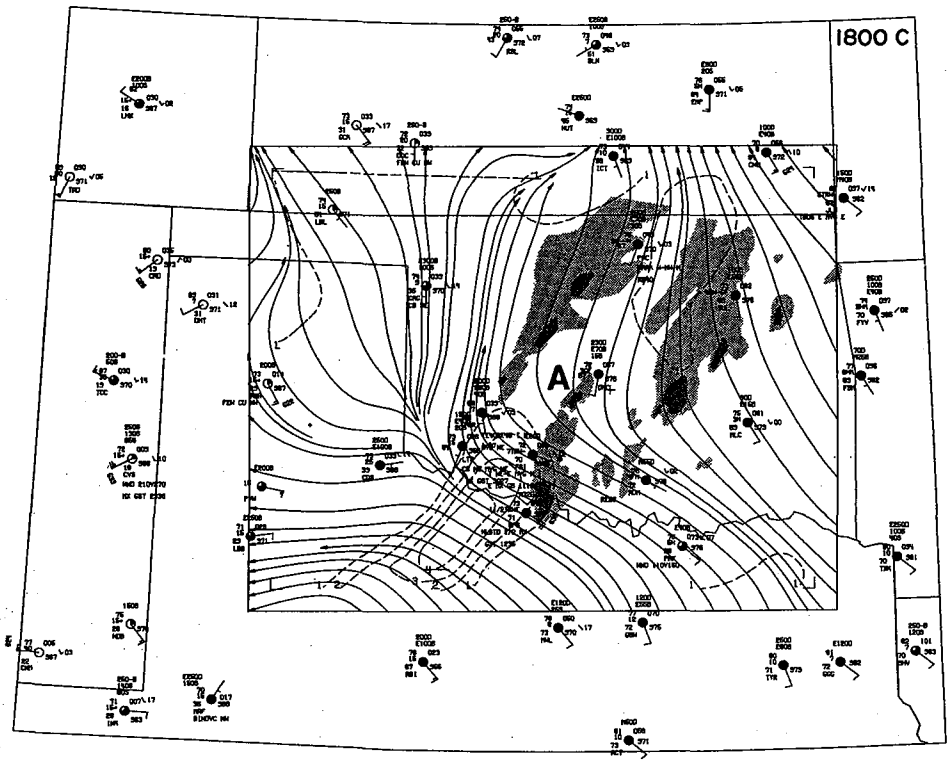

Figure 6. Regional weather map, 1800 CST, April 29, 1970.

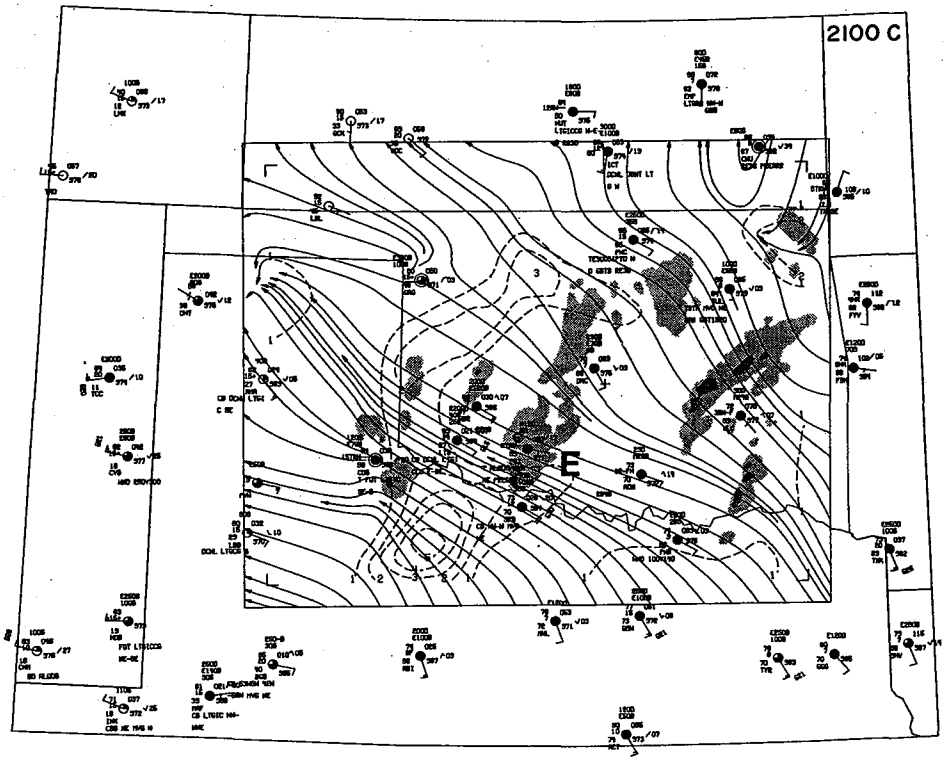

Figure 7. Regional weather map, 2100 CST, April 29, 1970.

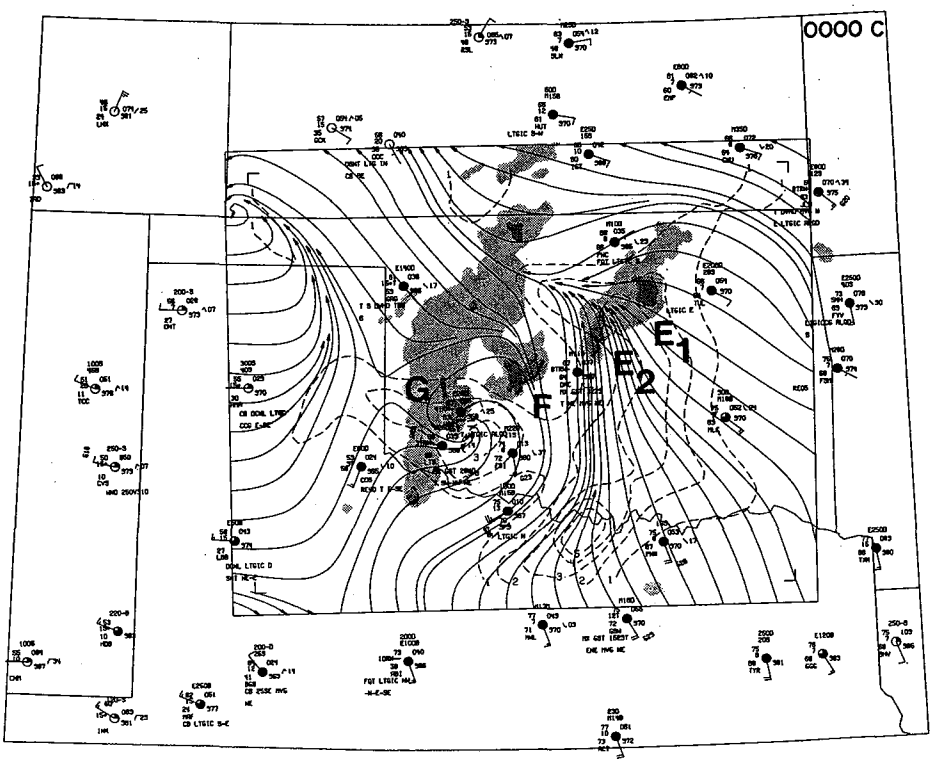

Figure 8. Regional weather map, 0000 CST, April 30, 1970.

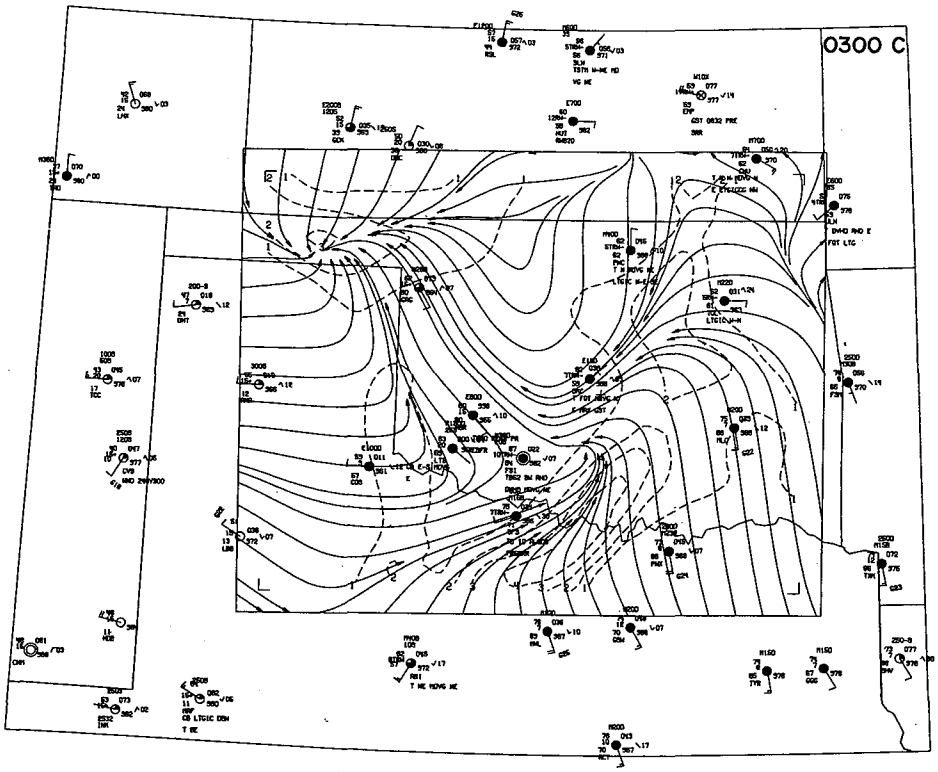

Figure 9. Regional weather map, 0300 CST, April 30, 1970.

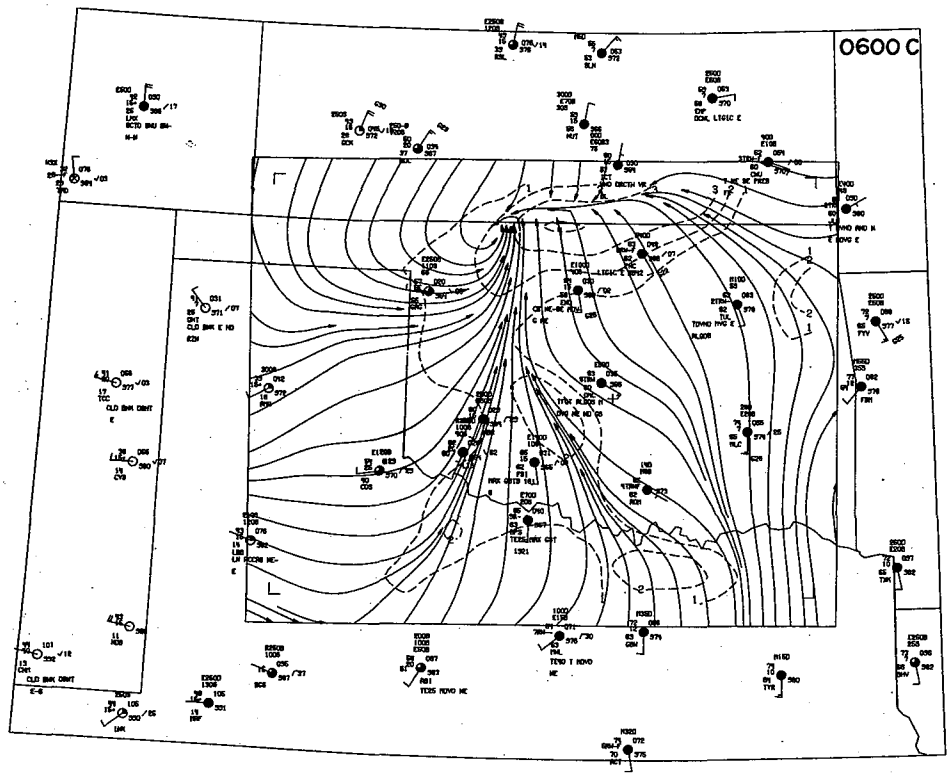

Figure 10. Regional weather map, 0600 CST, April 30, 1970.

When analyzing mesoscale convective systems using only data 50 to 100 n miles apart, there is room for considerable ambiguity and aliasing. For example in figure 2, beyond knowing that strong moisture convergence exists in the triangle Wichita Falls (SPS) to Abiline (ABI) to Childress (CDS), we cannot determine its exact location or configuration. Insofar as observations represent conditions surrounding each station, the analyses adequately represent the meteorological distributions. But where strong small-scale systems (thunderstorms) influence observations singly, analyzed distributions in the surrounding area must be interpreted with caution. Time continuity of mesoscale features and their association with known storm areas increases our confidence in the data's information content and the resultant analyses.[2]

3. REGIONAL WEATHER

In addition to the early morning conditions already discussed, fog and low clouds prevailed in the southerly current over east Texas and Oklahoma. These conditions gave way to middle and high clouds and considerably drier surface air in the Texas panhandle.

At 0600 (fig. 2), moderate moisture convergence results from a confluence zone in the surface streamlines in northwestern Oklahoma. This moisture convergence center drifts eastward across the northern half of the state during the next six hours (fig. 2, 3, and 4) and is associated with weak shower activity. However, the relationship seems coincidental since stronger showers occur where no moisture convergence is indicated. There is a large temperature inversion at low levels which de-couples the surface air from the air above. We feel these early showers were due more to upper air disturbances than boundary layer conditions. The other moisture centers in figure 2 do not persist through the day (fig. 3-6) and are presumed to relate to temporal adjustments in the wind field rather than to travelling disturbances.

Rainstorms appearing on the 1800 map (fig. 6) do not relate to any particular surface features. The large cell near SPS comes from the region of strong moisture convergence (fig. 5) and will diminish as it moves away from that area. In fact, this is generally true of the storms up to 2100; they originate in Texas, drift north-northeastward reaching moderate intensity, and then dissipate. One small hailstorm (Storm A) dies in the network area west of NSSL (fig. 6) and is the subject of another paper (pages 89-100). One other hailstorm is northwest of NSSL at 1710.

By 2100 (fig. 7), changes become evident. Still developing in the SPS-ABI-CDS area, storms maintain their mature stages longer, and begin to reach severe proportions. One large rainstorm develops west of SPS, splits to form the next storms (E_1 and E_2) that cross the Oklahoma City area. Together they deposit more than four inches of rain then move north-northeastward along their major axes. Details of the surface wind field not apparent in these analyses are shown on pages 64 - 75. Meanwhile, near Childress (CDS) the first tornadic storm (Storm F) appears on the west side of the moisture convergence region.

---

[2] Improvements in the mesoscale analysis of hourly surface observations are the subject of continuing research at NSSL.

By 0000 (fig. 8), shower activity over southeastern Oklahoma dissipates and flow now converges toward the two large storms northeast of Oklahoma City. Storm F is west of the city and has a tornado on its southeast flank (near the notch in the echo). Storm G is developing in the vicinity of what appears to be a mesoscale cyclone near the Altus, Fort Sill, Hobart area (LTS, FSI, HBR). The origin of this cyclonic wind system is unknown, and we cannot follow its movement after 0000. We are not able to detect an associated low pressure system. Lowest pressure at 0000 is reported from SPS (1001.0 mb). Three hours later (fig. 9), Hobart (HBR) reports 999.6 mb--the lowest in the area. However, the wind pattern does not relate well to the pressure distribution. As demonstrated by Sasaki (1973), these imbalances between the wind and pressure fields often can be explained in terms of vertical momentum transport mechanism and gravity wave phenomena. Their importance to these storms cannot be determined on the basis of available information.

Primarily due to a wind shift at SPS, the strong moisture convergence center jumps eastward at 0000. Moisture convergence extends northward to the two rainstorms E_1 and E_2, and another center lies near Storm G. Storm F also has strong moisture convergence associated (see pages 78 - 81), but this convergence is not visible in these observations.

A larger cyclonic wind system is observed in the southwest corner of Kansas at 0000. This system moves in the following six hours (fig. 9 and 10) to a position along the Kansas-Oklahoma border, and eventually it will become the main synoptic-scale cyclone. On the morning of the 30th, dry air in west Texas gradually spreads over Oklahoma followed by cooler air from Kansas as the storm system moves northeastward out of the state.

4. CHANGES IN THE AIR ALOFT

Fifty-nine soundings were acquired at nine NSSL mesonetwork stations during an eight-hour period from 1730 to 0130. Thirty to forty rawinsondes sampled the atmosphere outside radar echo boundaries, observing the storms' near environment. To determine change in the synoptic-scale conditions over central Oklahoma, we treat these soundings as though taken from a single geographical location. Trends in wind speed, direction, temperature, and dew point at three levels--850, 700 and 500 mb--are graphically illustrated by regression lines calculated and plotted by machine.

Wind directions (fig. 11) change little during the stormy period: at 700 mb they back slightly, but at 850 and 500 mb they remain essentially constant. Only minor short waves move through the long wave trough during the period. Beginning about 2100 at 850 and 700 mb (fig. 12), wind speeds increase. At 500 mb, speed increases only slightly from 1800 to 2300, then decreases. Net vertical shear from 850 to 500 mb decreases while the shear from the surface to 850 mb increases. This changing vertical wind shear is believed directly related to the observed change in basic storm structure--that is, from multicell to isolated supercell types (Marwitz, 1972a, b).

Temperature lapse rate between 850 and 500 mb (static stability) increases during the early evening, decreases slightly around 2100, and then increases again late in the period (fig. 13). This confirms that the storms did not

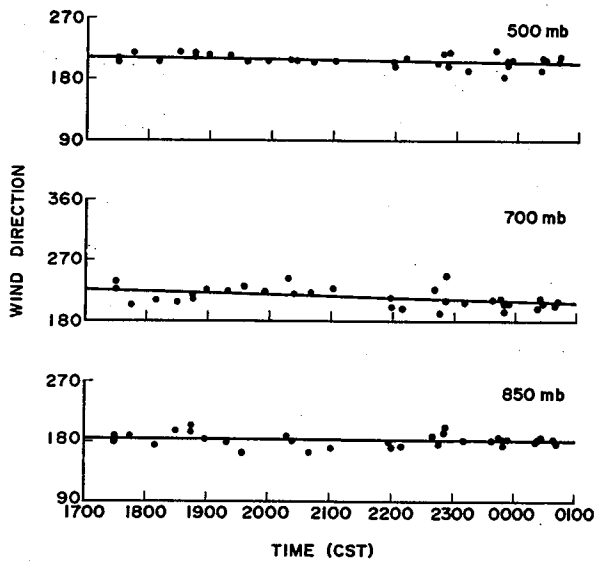

Figure 11. Wind direction trends at 850, 700 and 500 mb levels.

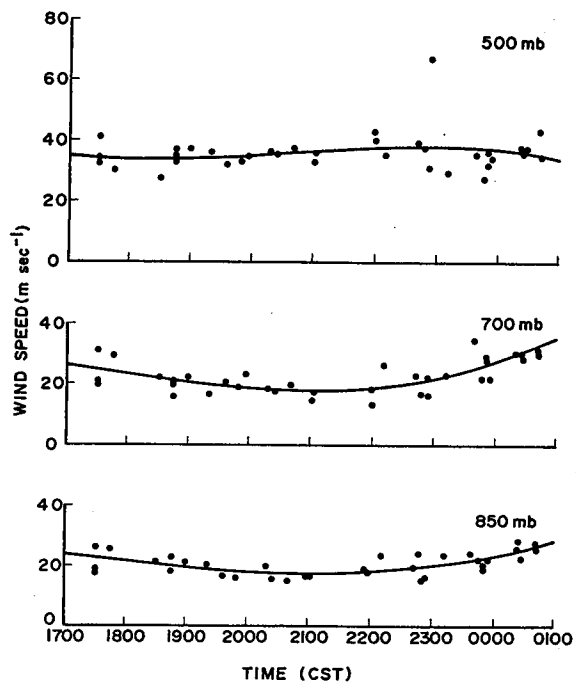

Figure 12. Wind speed trends at 850, 700 and 500 mb levels.

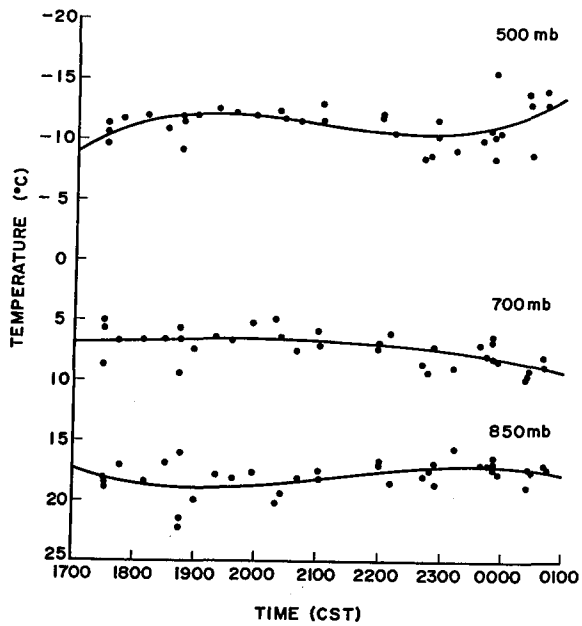

Figure 13. Temperature trends at 850, 700 and 500 mb levels.

develop in response to a short wave of detectable significance. The four 500 mb temperatures near -15C observed just before 0100 are believed due to forced lifting of an inversion by approaching Storm F rather than to cold air advection.

Dew points change dramatically (fig. 14). Moisture at 850 mb increases 10C as the moist surface layer deepens with time. Aloft, dew points diminish rapidly as dry air invades the region from the southwest (Allison et al., 1972).

These changes are summarized in figure 15 which depicts time variation of parameters commonly used to estimate thunderstorm potential and severity prior to occurrence: Lifted Index (Galway, 1956), surface gusts (Foster, 1958), height of wet-bulb zero (Miller, 1967), and hail size (Foster and Bates, 1956).[3]

Lifted Index diminishes from -2 to -7 on the trend line. Extreme variations about the trend line are caused by storm influences on the environment. For example, the two positive values (at 2253 and 2350) were measured close to the west sides of Storms E_1 and E_2 where dry (possibly subsiding) air appears near the surface (pages 30-31). Another sounding, also at 2350, measured the greatest instability (-11), but this too is considered unrepresentative. Apparently the instrument experienced wet-bulb cooling as it rose from a saturated cloud layer into dry air near 500 mb.

[3]Parameters were calculated by electronic computer using software developed by J. H. Henderson, NSSL.

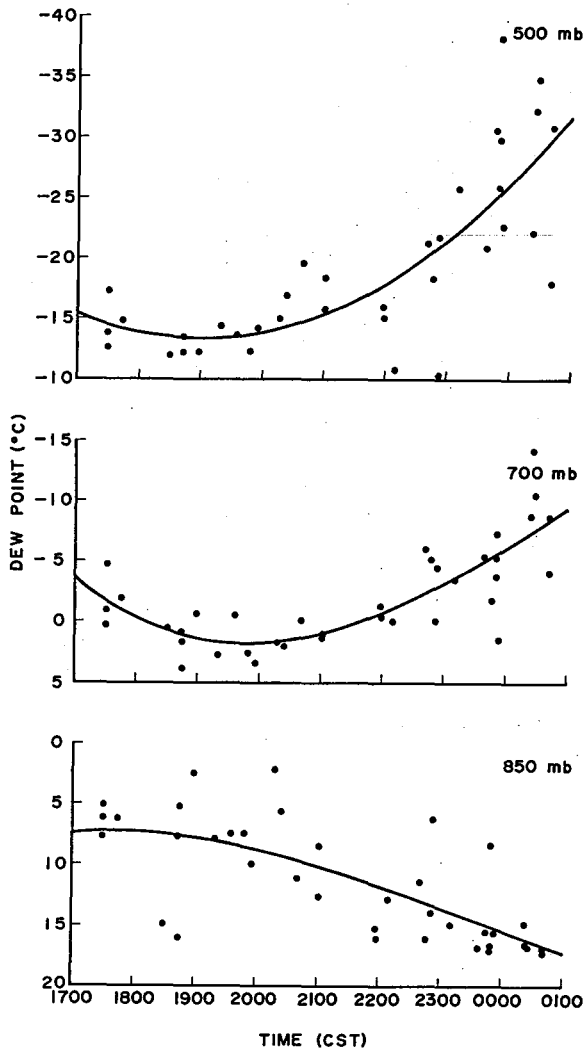

Figure 14. Dew point trends at 850, 700 and 500 mb levels.

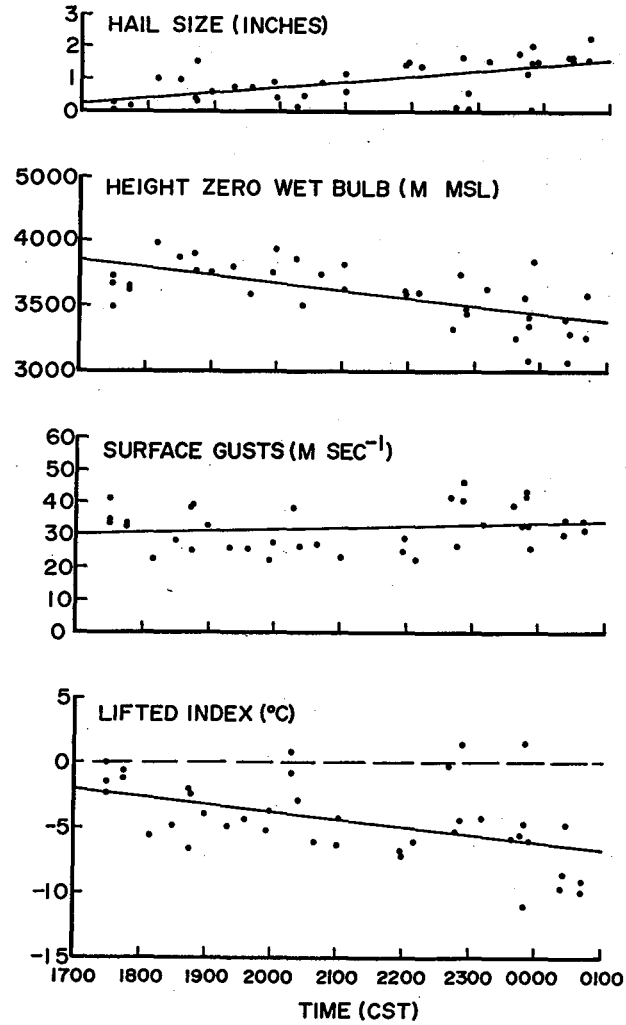

Figure 15. Storm severity parameters calculated from NSSL network rawinsonde data, April 29-30, 1970. All show trend toward increasing severity in agreement with observed storm characteristics.

Estimated surface gusts increase with time. Individual values as high as 47 m sec^{-1} (89 kt) are computed, but on average maximum gusts do not reach 35 m sec^{-1} (68 kt). Observed peak gusts in excess of 25 m sec^{-1} were common over the mesonetwork and several stations reported speeds above 30 m sec^{-1}. Maximum gust in the entire network was 49 m sec^{-1} observed during the passage of a tornado (Storm G). Generally speaking, the maximum gusts estimated from sounding data are somewhat larger than observed. This is in the same sense as Foster's result. On the average, his predicted gusts are 28 percent larger than observed gusts and the average predicted gust from 50 soundings

during this night is 33 percent higher than the average gust observed at 43 stations.[4]

Miller has determined that height of wet-bulb zero (WBZ) relates well to hail and tornado occurrences when the atmosphere's thermal structure yields values from 1524 to 3658 m above ground level (AGL). His data indicates a strong preference for large hail (> 1/2 inch) and fast moving, long path tornadoes (Type I) when WBZ is 2134 to 2743 m AGL. Before the tornadoes developed on the evening of April 29-30, WBZ descended from 3600 to 3100 m (AGL), on the high side of Miller's range but well within the upper limit quoted. In regard to hail, NSSL volunteer observers reported sizes ranging from 1/4 inch early in the evening to 1 1/2 inch with Storm F. These reports correspond nicely with the trend of predicted sizes (fig. 15), but Miller's estimate fails to indicate the largest stones that fell. Storms at Watonga, northwest of Oklahoma City(fig. 6), deposited stones as large as four inches early in the evening (1710). Another report of four inch hail falling at 2230 came from the Martha area (five miles north of Altus). Storm F's precipitation core was over Martha at the time. This report also indicates average hail size only two inches. Apparently, the hail size predictor estimates average stone size rather than maximum size; no sounding indicate the possibility of four inch hail (fig. 15).

In summary, these data confirm the general utility of four severe storm indicators: Lifted Index, surface gusts, height of wet-bulb zero, and hail size. During the eight hours that storms were in or about the NSSL rawinsonde network, the trends consistently paralleled observed changes in storm characteristics--from moderately intense storms that produced mostly small hail and strong, but not severe, surface winds to large tornadic storms that produced giant hail.

However, one finds concern in the data scattered about the trend lines. These soundings were selected because they were not directly influenced by the storms--none were in heavy precipitation and well-behaved ascent rates were common to all. Yet, a large number were indirectly influenced by the ongoing convection. These facts suggest two cautions: (1) when an individual sounding is in a convectively-disturbed atmosphere, its representativeness of synoptic scale environmental conditions is questionable even to the point of being misleading; and (2) any two soundings, say six hours apart, may not reflect the actual trend of atmospheric changes.

5. REFERENCES

Allison, L. J., J. Steranka, G. T. Cherrix and E. Hilsenrath, 1972: Meteorological applications of the Nimbus 4 temperature-humidity infrared radiometer, 6.7 micron channel data. Bull. Amer. Meteor. Soc., 53, 526-535.

Barnes, S. L., 1973: Mesoscale objective map analysis using weighted time-series observations. NOAA Tech. Memo ERL-NSSL-62, 60 pp.

[4]The 49 m sec^{-1} peak gust associated with the tornado was not included in the averaged data.

Foster, D. S., 1958: Thunderstorm gusts compared with computed downdraft speeds. Mon. Wea. Rev., 86, 91-94.

_____, and F. C. Bates, 1956: A hailsize forecasting technique. Bull. Amer. Meteor. Soc., 37, 135-141.

Galway, J. G., 1956: The Lifted Index as a predictor of latent instability. Bull. Amer. Meteor. Soc., 37, 528-529.

Marwitz, J. D., 1972(a): The structure and motion of severe hailstorms. Part I: Supercell storms. J. Appl. Meteor., 11, 166-179.

_____, 1972(b): The structure and motion of severe hailstorms. Part II: Multi-cell storms. J. Appl. Meteor., 11, 180-188.

Miller, R. C., 1967: The wet-bulb zero height. Air Weather Service Tech. Report. No. 200, AWS (MAC), U. S. Air Force, Scott AFB, Ill, Ch. 7.

Sasaki, Y., 1973: Mechanism of squall-line formation as suggested from variational analysis of hourly surface observations. Preprints of Papers, Eighth Conf. on Severe Local Storms, Amer. Meteor. Soc., Boston, Mass, 300-307.

MESONETWORK OBSERVATIONS AND ANALYSES

Stanley L. Barnes

National Severe Storms Laboratory
Norman, Oklahoma 73069

Radar echo photographs at 30-min intervals depict thunderstorm development over Oklahoma on April 29-30, 1970. Fifty-eight soundings acquired over an eight-hour period indicate atmospheric structure on thermodynamic diagrams located relative to significant storm echoes. Five-minute interval surface data graphically illustrate storm events at each of 44 mesonetwork surface stations. Analyses of observed and computed meteorological variables give perspective to surface flow development related to radar echo character. Quasi-steady surface features such as mesocyclones, pseudo fronts, and updraft-downdraft couplets are represented accurately in observations from stations spaced 11 km apart when time-series data are considered relative to the moving storms. Smaller storm details (e.g., tornadoes) only occasionally reveal themselves to station sensors and, therefore, are not resolved in these analyses. Radar reflectivity signatures closely correspond to quasi-steady surface features. In many instances, individual atmospheric soundings support physical interpretations concluded from surface and radar analyses. The relevance of sounding ensembles is less understood, and horizontally mapped meteorological variables must be interpreted with caution.

1. INTRODUCTION

We present processed radar, upper air, and surface observations of storm events from 1700 CST, April 29 to 0200 CST, April 30 in central Oklahoma. Our purpose is to give perspective to the storms' details and to allow the reader to see the data that form the basis of interpretation for singularly important facets elaborated in this volume.

In section 2 a sequence of radar echo photographs provides a general view of the storms as they affected the observational networks. Sounding details in section 3 show the atmosphere's vertical structure in and near storm echoes. Sequence of meteorological events at individual surface stations are graphed in section 4. In section 5 distributions of important meteorological variables are mapped at frequent intervals showing evolutions and structures of storm-influenced surface air flows. For convenience, illustrations are grouped at the end of each section.

Maps detailing the distribution of upper air variables have not been included. Interpretation of these data is difficult because the scale of observations is not uniform (an "aliasing" problem), and their number is not sufficient to determine flow and thermodynamic properties inside the storms. In a few cases, selected soundings yield meaningful details about a storm's near environment, and these results are included elsewhere in this volume. Soundings strongly influenced by storms individually provide interesting glimpses of internal structure (pages 101-123), but generally such soundings should be excluded from analyses based on interpolation techniques (Barnes, 1973).

2. RADAR OBSERVATIONS

The surveillance radar at the National Severe Storms Laboratory is a WSR-57 10-cm radar. Radar specifications and signal processing details are described by Wilk and Kessler (1970). After electronic processing, power received from precipitation is displayed in range-azimuth coordinates on a Plan Position Indicator (PPI). Boundaries between two shades of gray and black (echo cancellation) depict constant reflectivity contours whose values are given in table 1. Tilting the rotating antenna through sequential angles from horizontal provides three-dimensional reflectivity data.

Table 1. WSR-57 Video Contour Levels and Equivalent Reflectivities.

Level	dBm	log Z_e	Shading
1	-98	1.9	Light Grey
2	-92	2.5	Bright
3	-82	3.5	Dark (cancellation)
4	-70	4.7	Light Grey
5	-60	5.7	Bright

Although precipitation had fallen in parts of Oklahoma all day long, storms did not attain strong intensities until late in the afternoon (refer to pages 1 - 15 for a discussion of synoptic-scale events). Eight storms passed through or near the NSSL observation area and are identified alphabetically in order of their passage. The network encompasses an area roughly 40 n miles in diameter (the distance across the first range circle in figs. 1 - 3) and is centered on the northwest edge of the radar ground clutter 18 n miles from NSSL (the dark central spot in each PPI photograph). The radar echoes' precise locations relative to the network are plotted on maps in section 5.

A small hailstorm (A in fig. 1) approaches the network at 1700 CST from a position 40 to 60 n miles southwest of NSSL. Interested readers are referred to the Nelson and Barnes paper for details concerning this storm's last stages (pages 89 - 96). Ninety minutes later (1830), Storm B reaches maturity while passing 40 n miles to the north of the network. At the time, it was thought that some significant detail about inflow to Storm B's updraft might be sensed by the network instruments, but B's passage isn't evident in the recorded measurements. Meanwhile, A dissipates and Storm C nears the southeast corner. It too diminishes rapidly and doesn't influence significantly the network measurements. From 1900 to 2100, small thunderstorms develop along the instrumented area's western edge (Storm D, fig. 1 and fig. 2). However, these storms remain small and weak.

The first storms of major interest develop from a single echo in northwest Texas (determined from longer range display not included here). Having split into two nearly equal parts (E_1 and E_2), the storms lie directly over the network stations at 2230 CST (fig. 2). Henderson (pages 101-123) describes E_1's internal details, and Reed et al. (pages 167-173) compute vertical profiles of divergence and moisture flux from soundings in the vicinity of E_2.

The first tornadic storm of the evening (Storm F, fig. 3) takes on a supercell radar signature (Browning, 1964) at midnight while still some 40 n miles west of NSSL. Moving northeastward, it crosses the mesonetwork's northwest corner. The second tornadic storm (G) rapidly closes distance on Storm F and causes widespread damage that puts several sounding units and the NSSL radar out of operation. These two storms (F and G) are the subjects of several papers in this volume.

Early in the evening (fig. 1) the radar echoes form lines oriented approximately northeast-southwest and spaced on the order of 40 n miles. Individual storms move along these lines while the line themselves gradually drift eastward, suggesting upper air waves that propagate across the direction of flow. However, we are unable to detect such waves in our data.

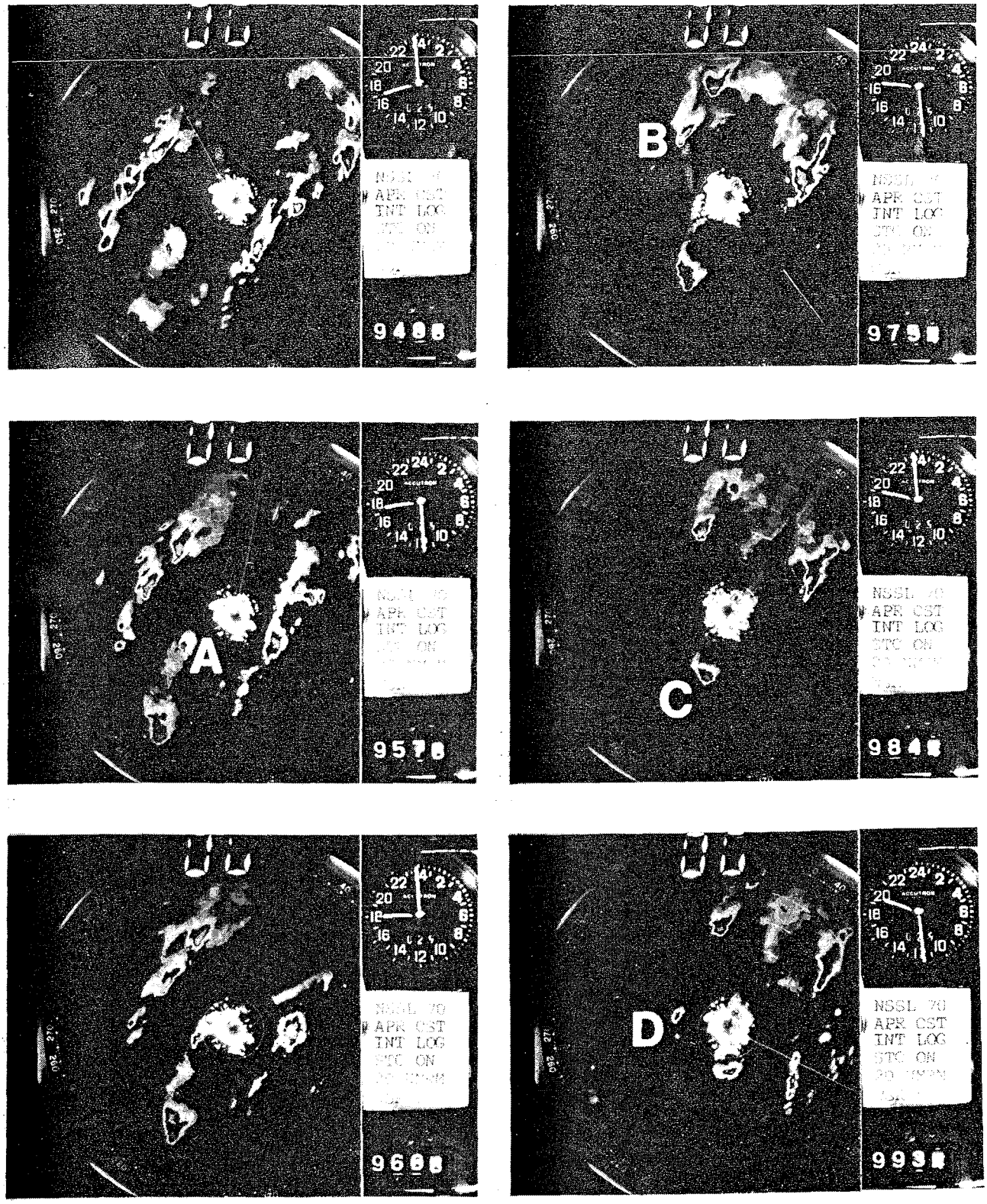

Figure 1. NSSL's WSR-57 integrated video displays at 30-min intervals from 1700 to 1930 CST, April 29, 1970. Range circles are 20 n miles. Storms A, B, C, and D pass near mesonetwork area centered northwest of radar at edge of ground clutter (18 n miles). Network covers area about 40 n miles in diameter.

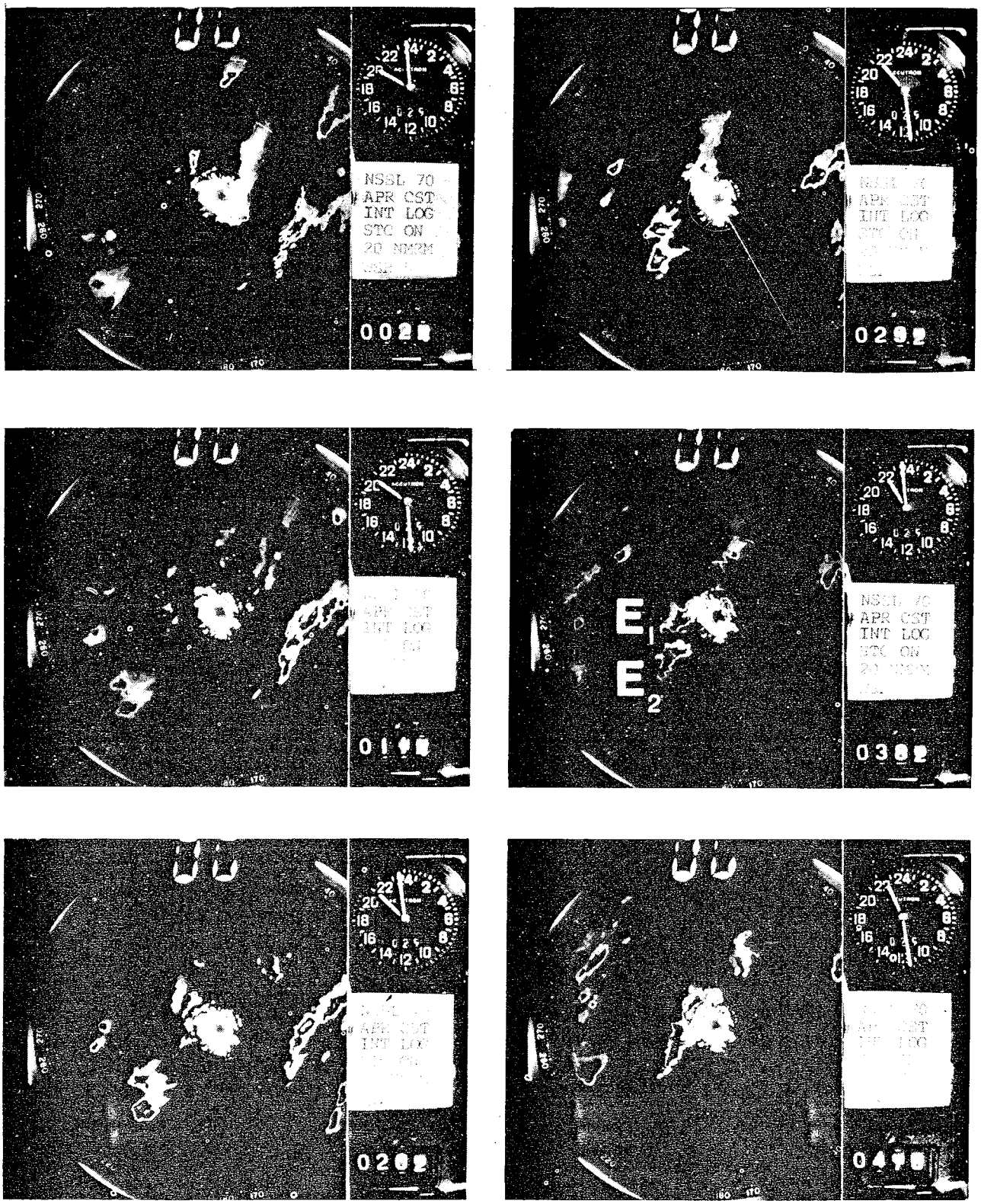

Figure 2. Radar echoes from 2000 to 2230 CST, April 29, 1970. Storms E_1 and E_2 split as they enter viewing area from southwest. By 2230 they lie diagonally across the network.

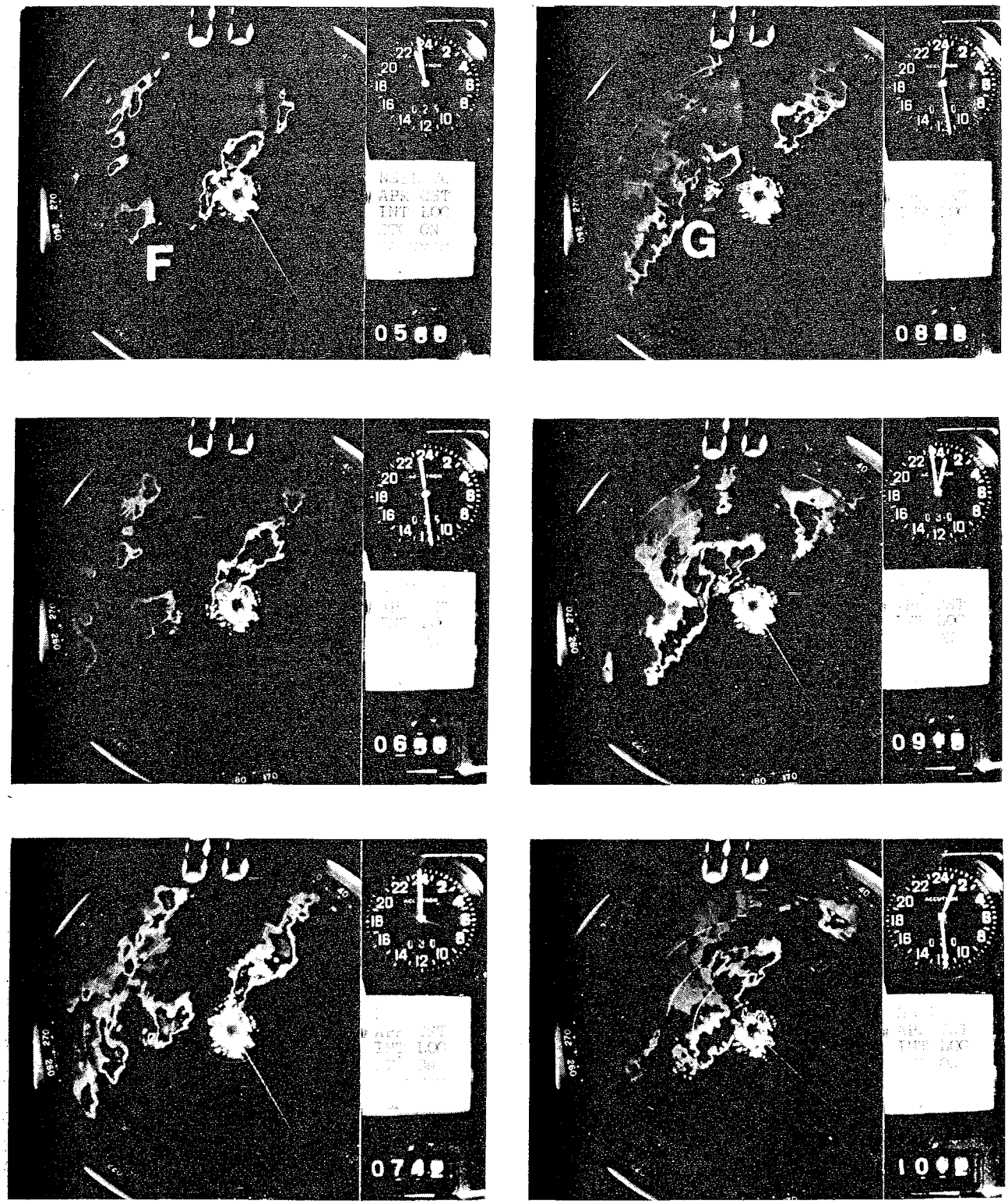

Figure 3. Radar echoes from 2300 to 0130 CST, April 29-30, 1970. Tornadic Storms F and G sweep rapidly across network area.

3. RAWINSONDE OBSERVATIONS

Balloon positions relative to radar echoes appear as dots in figures 4 - 11. Echo photographs depict precipitation in the storms' lowest 1000 m. Balloon positions at 1500 m MSL (about 1200 m above terrain) are adjusted spatially by an amount and in a direction determined by the translation vector for the storm nearest the sounding network (table 2). A balloon's displacement from its true geographic location is a function of the difference between the time the balloon reaches 1500 m and the time the radar PPI is acquired.

Soundings pertinent to each radar photograph time are arrayed on machine-plotted Stüve diagrams. Short line segments extend from the balloon position dots toward the appropriate sounding diagram. On these diagrams, vertical lines are isotherms and horizontal ones are isobars. Sloping dotted lines are mixing ratio labelled at the 500 mb level. The slope of dry adiabats is indicated by the line labelled "280" (K); 10, 20 and 30C moist adiabats curve upward to the left. Winds are drawn along the hydrostatically-calculated height scale at the right. Vectors extend in the direction from which the wind blows (north is the top of the scale); line length indicates wind speed according to the scale line segment labelled "10 mps" (lower right).

Table 2. Storm Vectors Determined from Radar Echo Centroid Fixes.

STORM	TRANSLATION VECTOR Degrees	Knots
A	221	35.0
B	230	36.5
C	225	39.9
D	226	49.8
E_1	227	47.5
E_2	217	35.2
F	233	41.6
G	238	55.5
Mean Wind Vector to 7 km	208	62.1

Balloon ascent is illustrated by a series of circles plotted as height versus time (bottom scale). This scale cycles back to zero for times in excess of 15 and 30 minutes. Changes in the slope of imaginary lines connecting circles indicate changes in balloon ascent rate. Balloons are not filled to ascend at a prescribed rate, so average ascent rate varies from sounding to sounding. However, since individual balloons (300 g) rise at a nearly constant speed through quiet air in the lower atmosphere, changes in ascent rate reflect atmospheric vertical motion. In a few cases, balloons accumulate ice and descend or are caught in downdrafts (fig. 5, 6, 8, 9 and 10). To avoid confusion, winds computed for descending sounding portions are plotted at the time-height circles.

Soundings are identified at lower left by station letter identifier, date, time, and ascent serial number. Launch sites are shown on maps in section 5. Information on sounding acquisition and processing details is contained in NOAA Technical Memorandum ERL-NSSL-53 (Barnes et al., 1971).

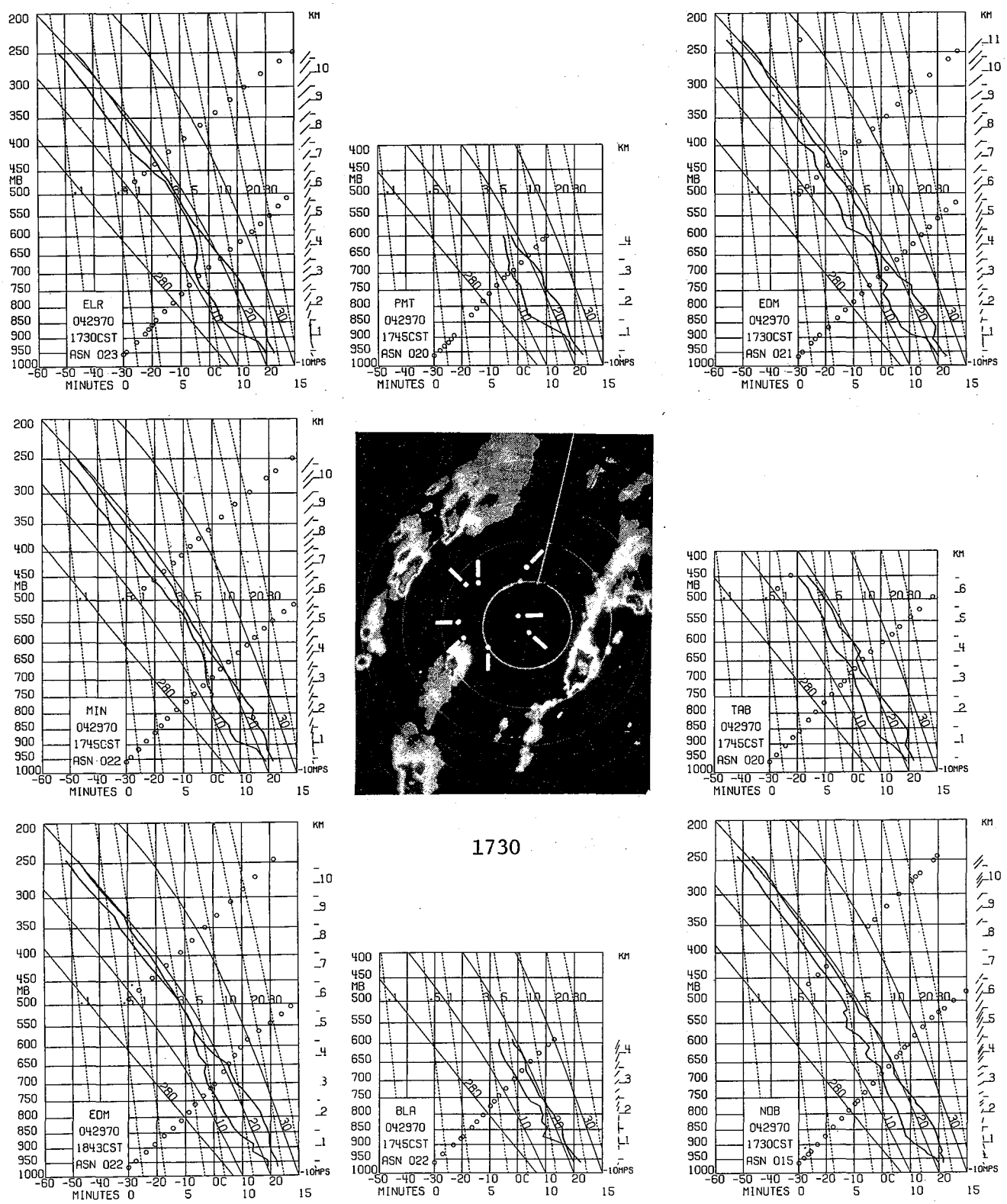

Figure 4. Composite of soundings relative to storms at 1730 CST, April 29, 1970. Balloon positions (dots) at 1500 m altitude (MSL) have been adjusted to account for time differences between soundings and radar display. Short line segments extend from dots toward appropriate soundings. See text for explanation of sounding diagrams.

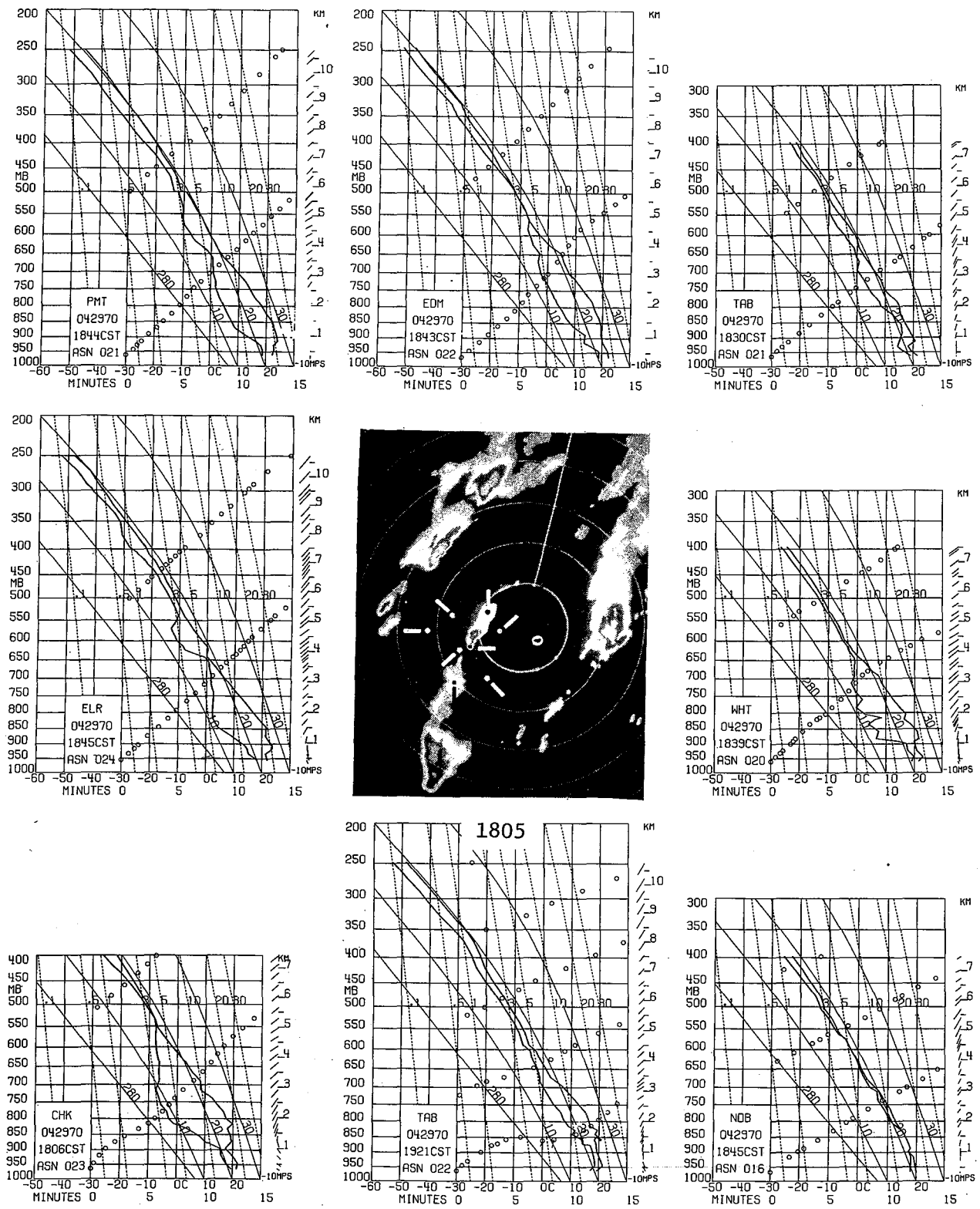

Figure 5. Soundings relative to Storm A 1805 position.

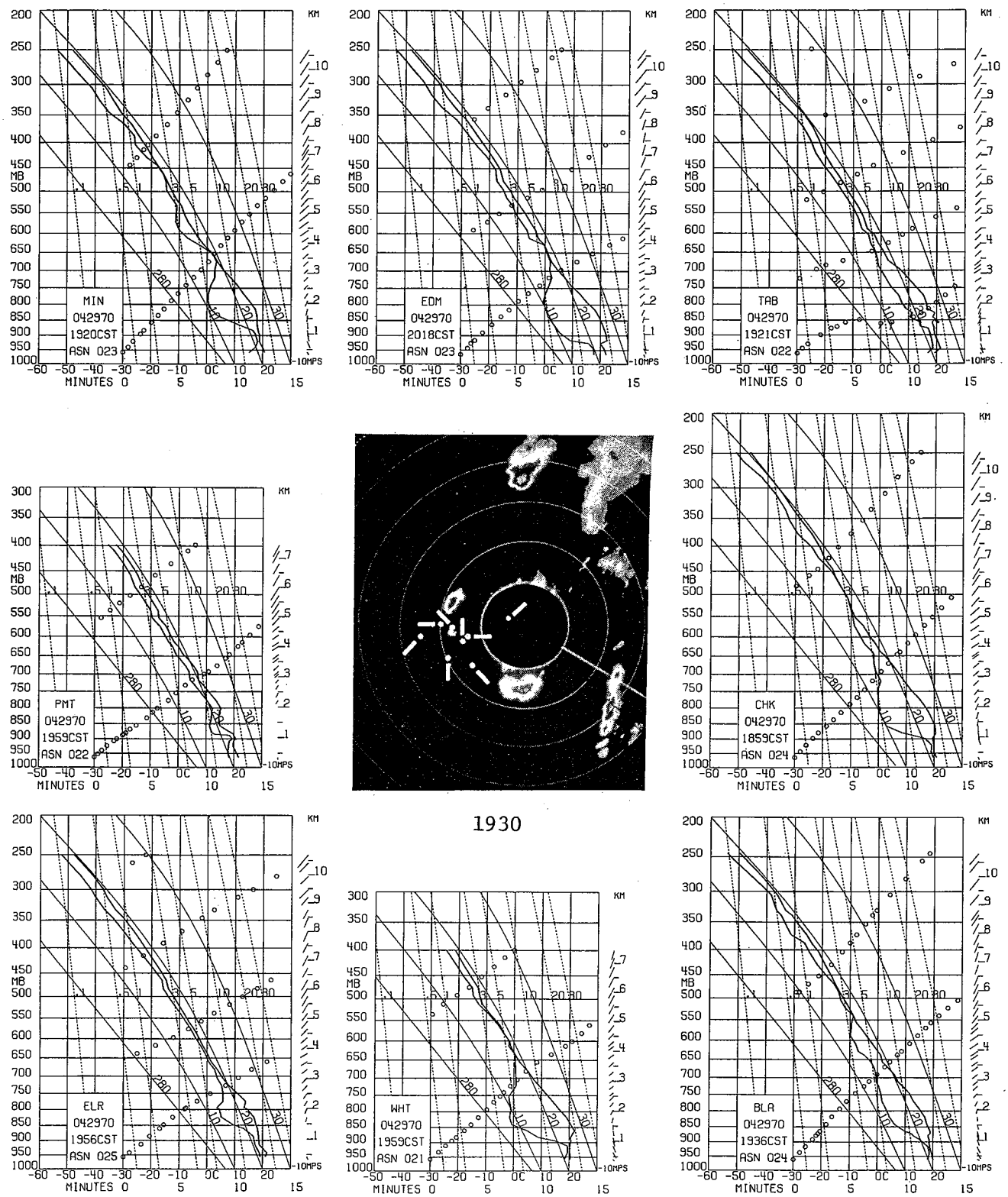

Figure 6. Soundings relative to Storms C and D 1930 positions.

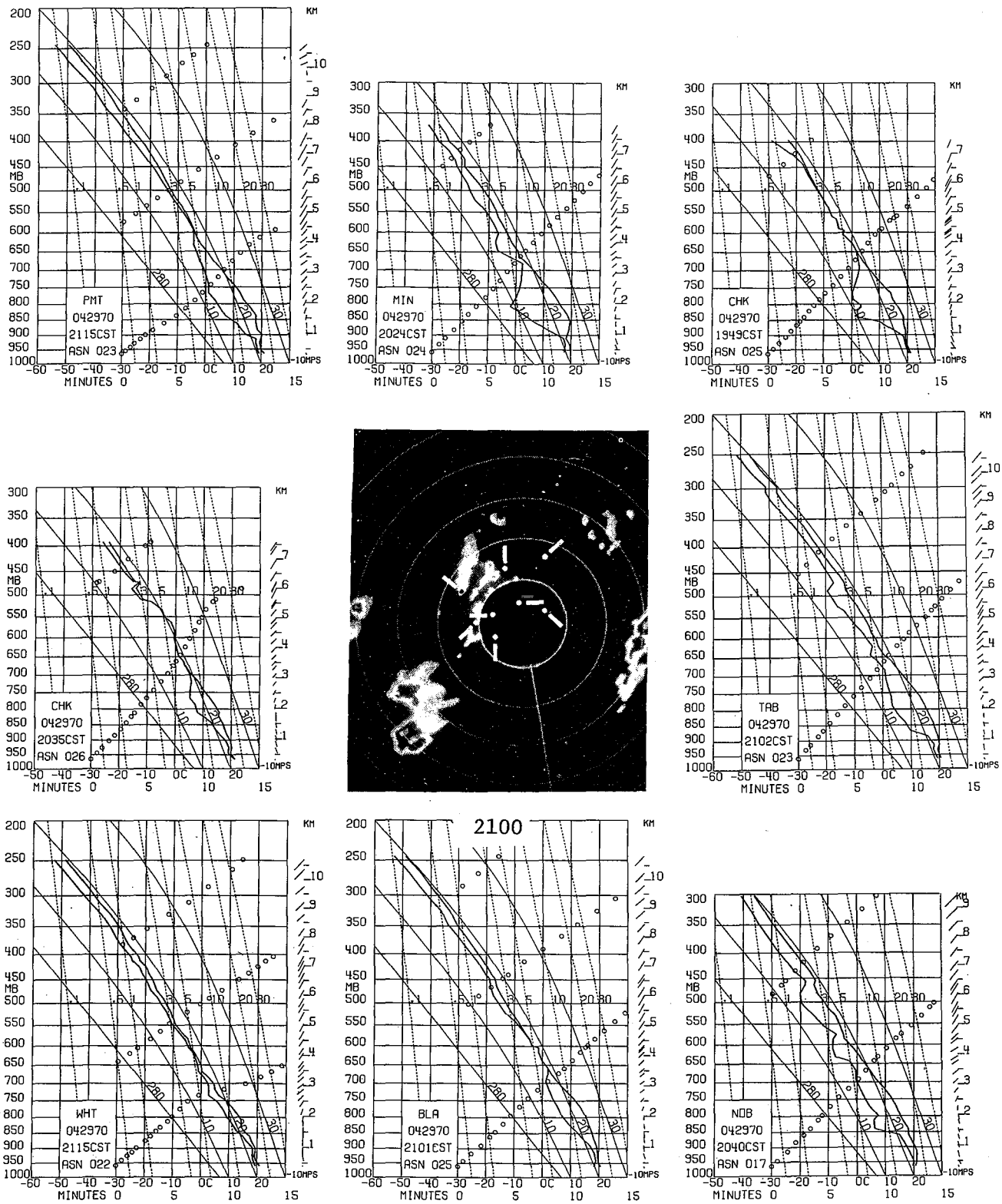

Figure 7. Soundings relative to 2100 storm position.

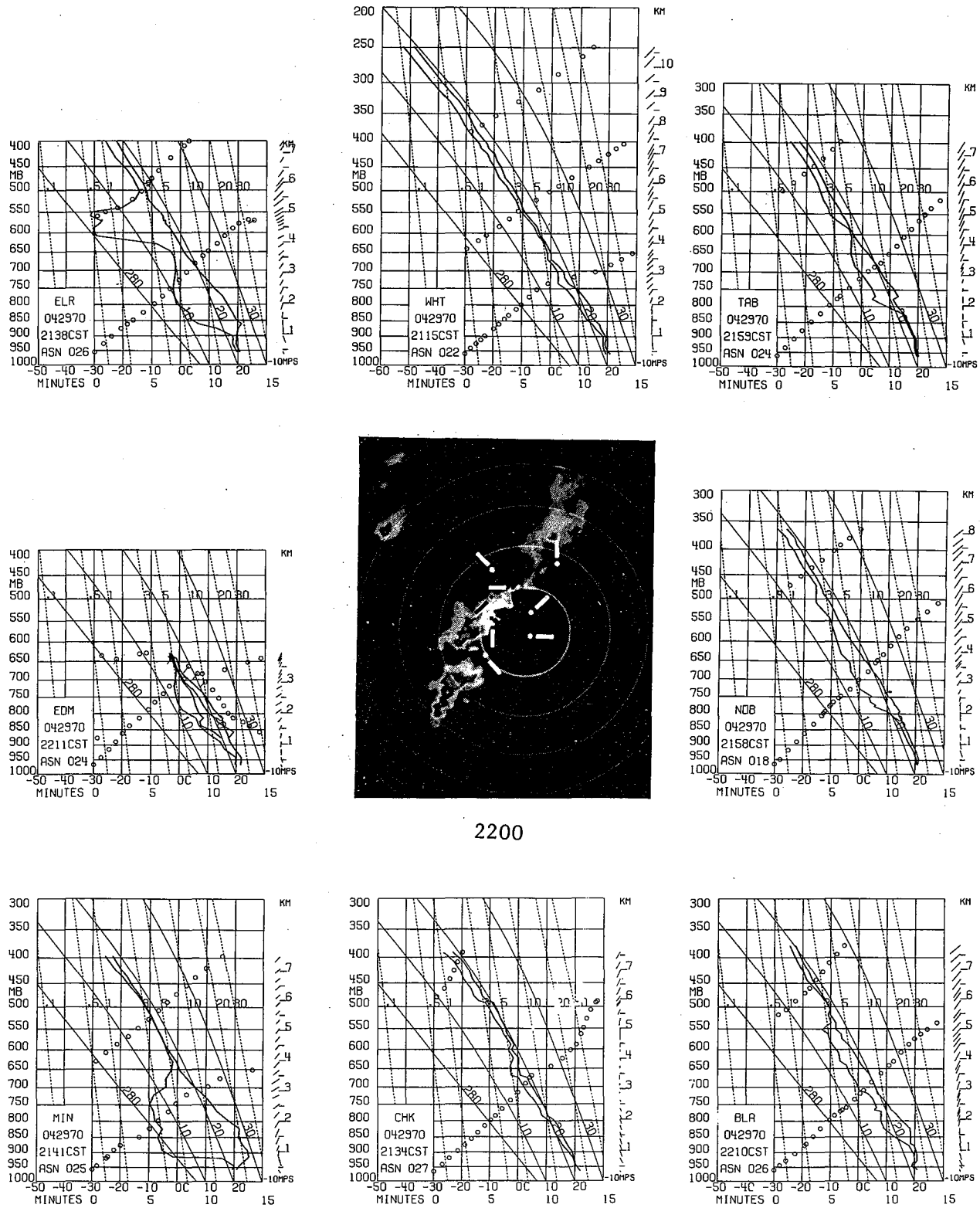

Figure 8. Soundings relative to Storm E_1 2200 position.

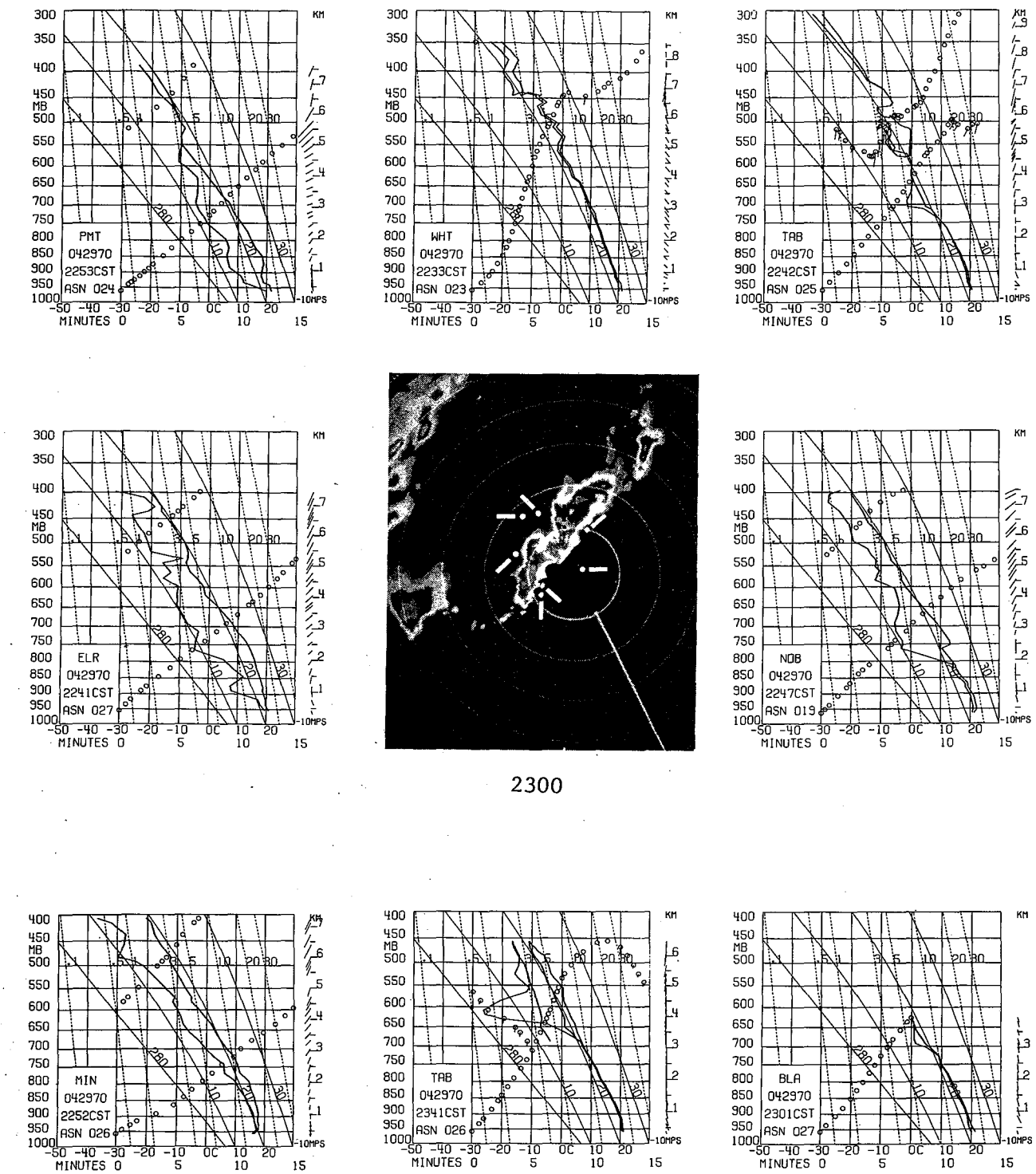

Figure 9. Soundings relative to Storm E_2 2300 position.

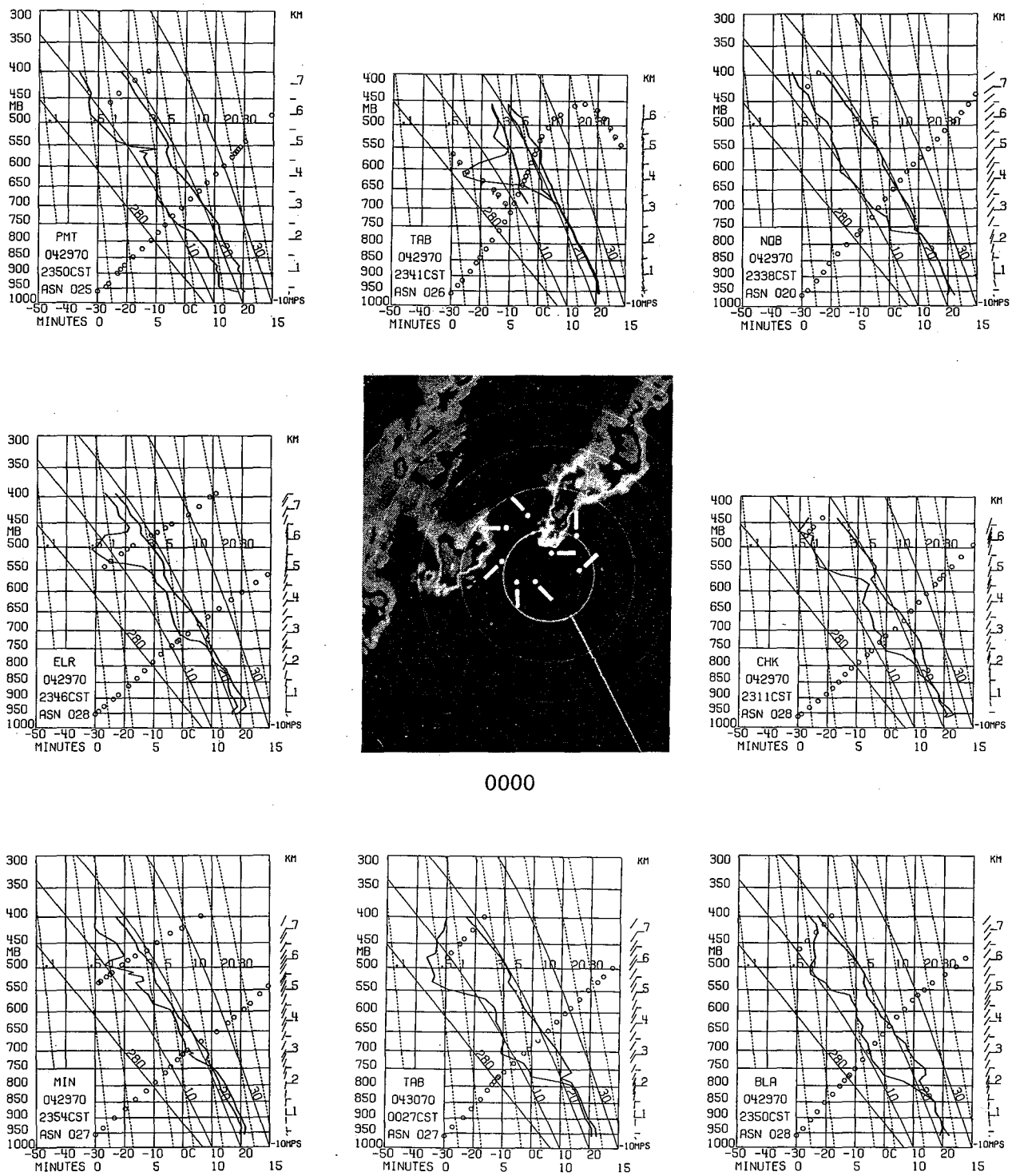

Figure 10. Soundings relative to Storms E_2 and F 0000 positions.

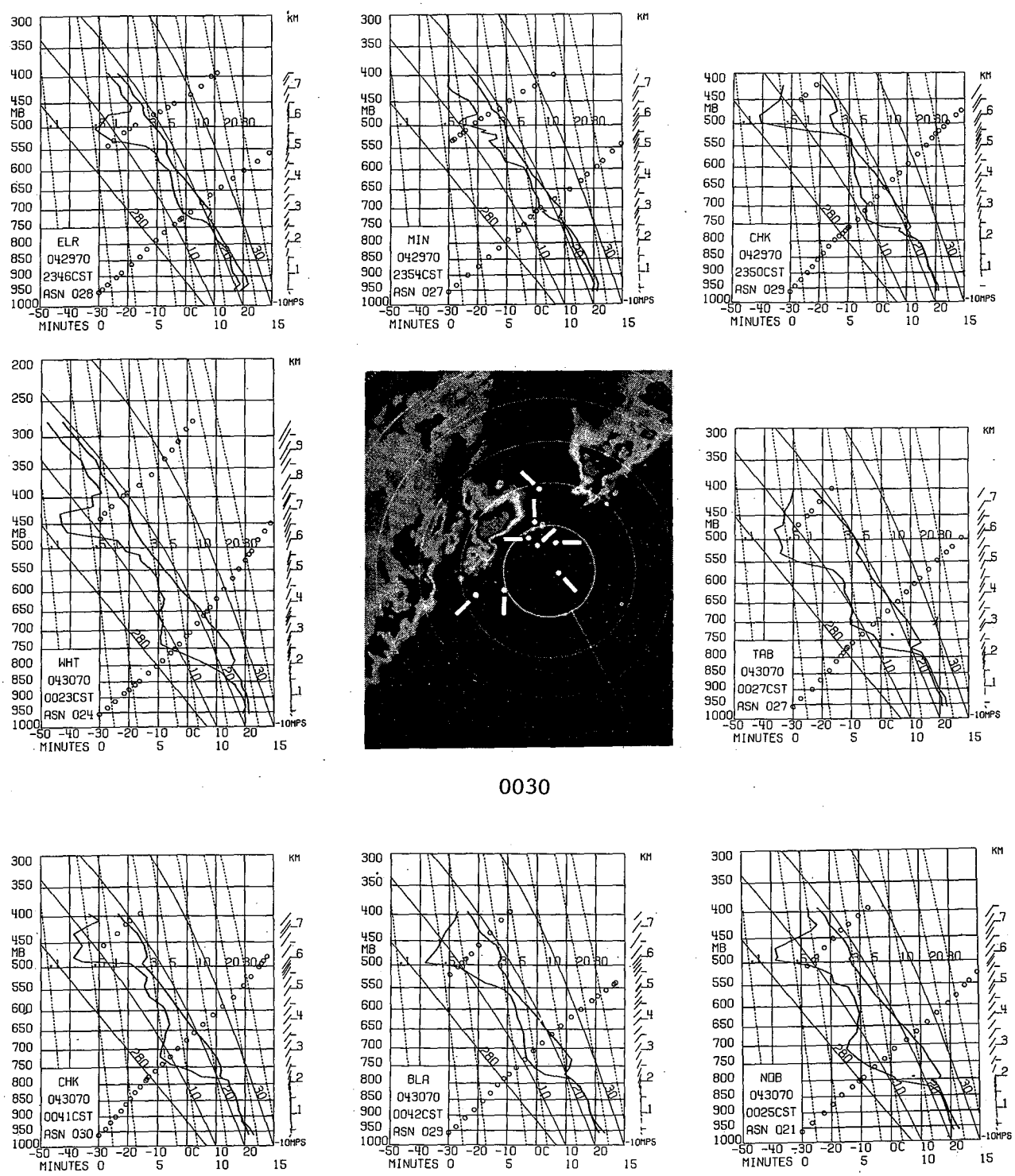

Figure 11. Soundings relative to Storms F and G 0030 positions.

4. SURFACE OBSERVATIONS

Instrumentation and routine records processing for surface mesonetwork stations are described in NOAA Technical Memorandum ERL-NSSL-55 (1971). Here we discuss additional data manipulations manufactured specifically for the April 29-30 storms study.

Analog traces manually digitized at five-minute intervals cover the period from 1700 to 0200 CST. We read instantaneous pressure to $\pm$ 0.005 inches Hg, temperature to $\pm$ 0.5F, relative humidity to $\pm$ 1 percent, and rainfall to $\pm$ 0.01 inches. Winds to $\pm$ 1 kt and 16 compass points ($\pm$ 22.5°) are averaged for the preceding five-minute period. Speed average is estimated visually; direction average is computed from five one-minute readings. Abstracted data, carefully edited by computer, are plotted as graphs and compared to the original traces. Then these data are entered onto a magnetic tape that serves as input for the map analyses in section 5.

Initial results suggest bias errors in these data. Stationary features in wet-bulb potential temperature (θ_W) patterns cannot be explained by storm-related mechanisms. Computation of θ_W is most sensitive to temperature and humidity and to a lesser degree, pressure. The following procedure removes the effect of these bias-type differences in the data ensemble. The 109 abstracted observations define average station temperature. A computer analysis (Barnes, 1973) designed to smooth small irregularities produces areal distribution of average temperatures. Differences between observed averages and smoothed values analyzed at each station's location determines bias corrections. Relative humidities are corrected in the same manner. These corrections, applied individually to each station's observations, range from +2.2 to -1.7F and +7 to -8 percent (table 3). The following station graphs illustrate <u>adjusted</u> temperatures and humidities.

Pressures are adjusted in a slightly different manner. Each station's average pressure during the observation period is summed to yield average pressure for the network area:

$$\overline{P}_{net} = \frac{1}{N} \sum^{N} \overline{P}_i \qquad (1)$$

where N = 44. Similarly, mean altitude computes from

$$\overline{H}_{net} = \frac{1}{N} \sum^{N} H_i . \qquad (2)$$

Pressure differences

$$\delta P_i = \overline{P}_{net} - \overline{P}_i \qquad (3)$$

Table 3. Temperature and Relative Humidity Bias Correction for April 29-30, 1970, Surface Data.

STATION	CELSIUS ΔT CORRECTION	PERCENT ΔRH CORRECTION
1A	0.0	-4.0
WKY	0.0	-4.0
2A	-1.3	0.0
2B	0.0	+1.0
2C	-1.0	+1.0
3A	0.0	+3.0
3B	0.0	0.0
3C	+1.0	+1.0
3D	-0.4	+4.0
4A	-0.5	+2.0
4B	+1.0	+4.0
4C	-0.3	+1.0
WRN	-0.7	-5.0
4D	+1.0	0.0
5A	0.0	0.0
5B	+1.0	+4.0
5C	+0.7	-4.0
5D	-1.0	+6.0
5E	-1.6	-4.0
6A	+1.0	-8.0
6B	0.0	-8.0
6C	-1.0	-4.0
6D	0.0	0.0
7A	0.0	+6.0
7B	-0.7	+7.0
7C	0.0	+1.0
8A	-0.8	-6.0
CHK	+1.0	+3.0
8B	-1.5	+5.0
8C	0.0	-1.0
W1	+2.2	+4.0
W2	0.0	+3.0
W3	+1.0	-3.0
W4	-1.0	-2.0
W5	+1.3	+2.0
W6	-1.0	-3.0
W7	-1.0	-8.0
R1	-0.3	+6.0
R2	+1.4	+1.0
R3	0.0	+6.0
R4	-0.5	+6.0
R5	+1.3	+3.0
R6	+0.4	-2.0
R7	-1.7	-5.0

convert to height increments by the hydrostatic formula

$$\delta h_i = -KT\delta P_i/\overline{P}_i. \tag{4}$$

In (4), K = R/g, the ratio of gas constant for air to acceleration of gravity. Each station's height difference from network mean altitude provides an independent set of height increments:

$$\delta H_i = \overline{H}_{net} - H_i. \tag{5}$$

Correlation between height increments computed from (4) to (5) is 0.97. We conclude that station-to-station mean pressure variations are due almost entirely to altitude difference.

For $\underline{\theta}_w$ computation, observed pressures are adjusted to the network mean pressure, $\overline{P}_{net}$. This adjustment and another technique that yields <u>mesoscale</u> pressure distributions are applied in the next section. The mesoscale technique does not require pressure adjustments to an arbitrary base, therefore, in this section's data, <u>unadjusted</u> pressures are plotted.

Each station's five-minute abstracted data are illustrated in the following 44 graphs. Time increases toward the left giving each graph the appearance of a space section with northeast to the right and southwest to the left. Stations identified in the upper ovals can be located on the radar maps (section 5). Winds are represented in vector form (north at the top); speed scale is shown beneath the word "WIND." Maximum gust (knots) during the preceding five minutes is drawn as a bar graph. Pressure (millibars), temperature (F), relative humidity (percent), accumulated rainfall (inches) and rain rate (inches hr^{-1}) are self-explanatory.

As a convenience to the reader who studies the next section's maps based on these data, station graphs are arranged in the sequence given in table 3.

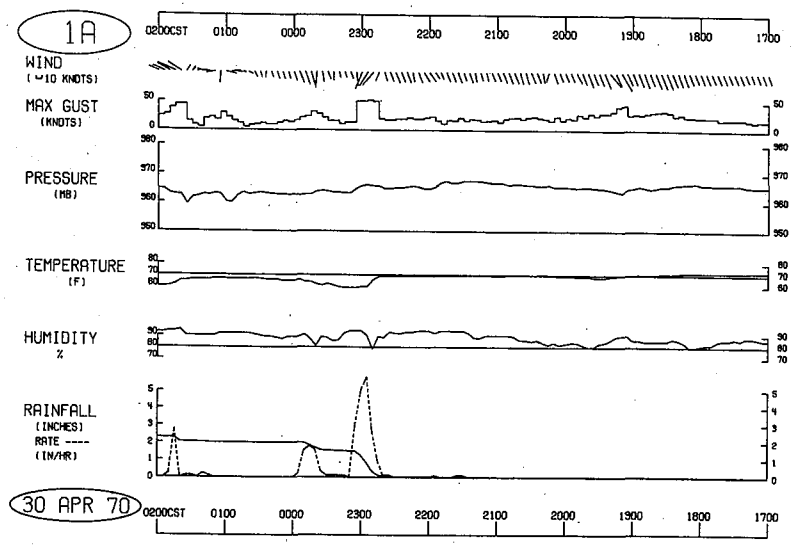
1A
WIND
(~10 KNOTS)
MAX GUST
(KNOTS)
PRESSURE
(MB)
TEMPERATURE
(F)
HUMIDITY
%
RAINFALL
(INCHES)
RATE ----
(IN/HR)
30 APR 70
0200CST 0100 0000 2300 2200 2100 2000 1900 1800 1700

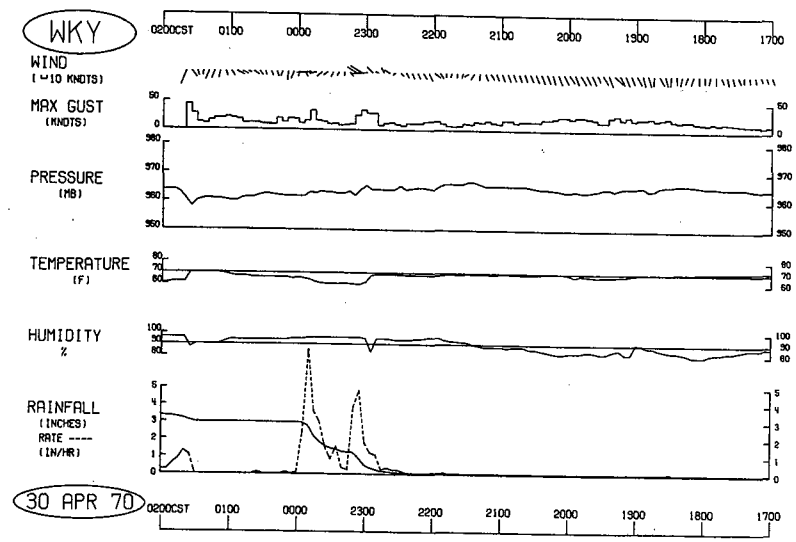
WKY
WIND
(~10 KNOTS)
MAX GUST
(KNOTS)
PRESSURE
(MB)
TEMPERATURE
(F)
HUMIDITY
%
RAINFALL
(INCHES)
RATE ----
(IN/HR)
30 APR 70
0200CST 0100 0000 2300 2200 2100 2000 1900 1800 1700

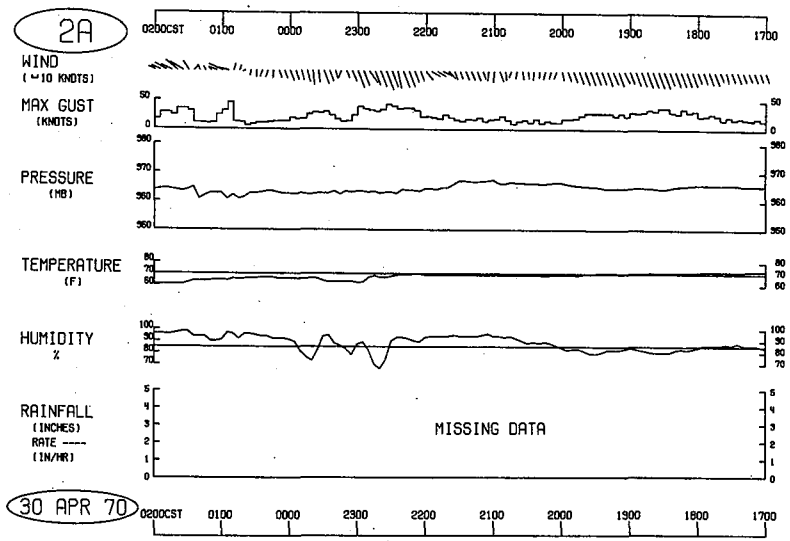
2A
WIND
(~10 KNOTS)
MAX GUST
(KNOTS)
PRESSURE
(MB)
TEMPERATURE
(F)
HUMIDITY
%
RAINFALL
(INCHES)
RATE ----
(IN/HR)
MISSING DATA
30 APR 70
0200CST 0100 0000 2300 2200 2100 2000 1900 1800 1700

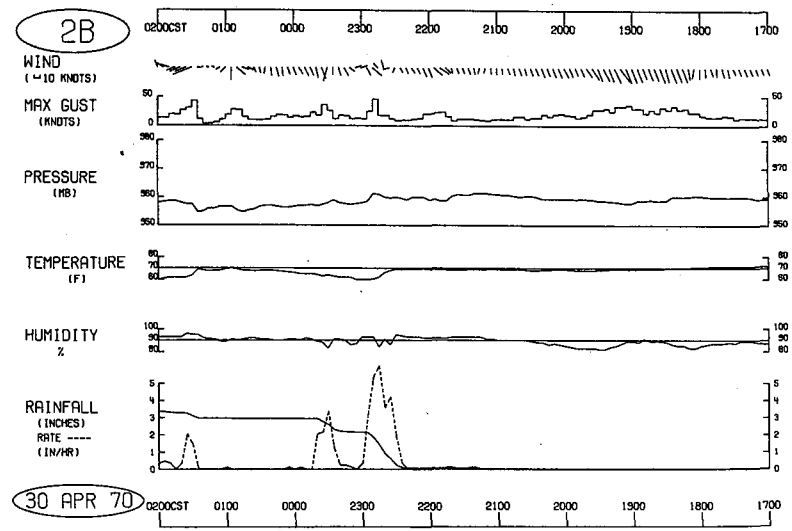
2B
WIND
(~10 KNOTS)
MAX GUST
(KNOTS)
PRESSURE
(MB)
TEMPERATURE
(F)
HUMIDITY
%
RAINFALL
(INCHES)
RATE ----
(IN/HR)
30 APR 70
0200CST 0100 0000 2300 2200 2100 2000 1900 1800 1700

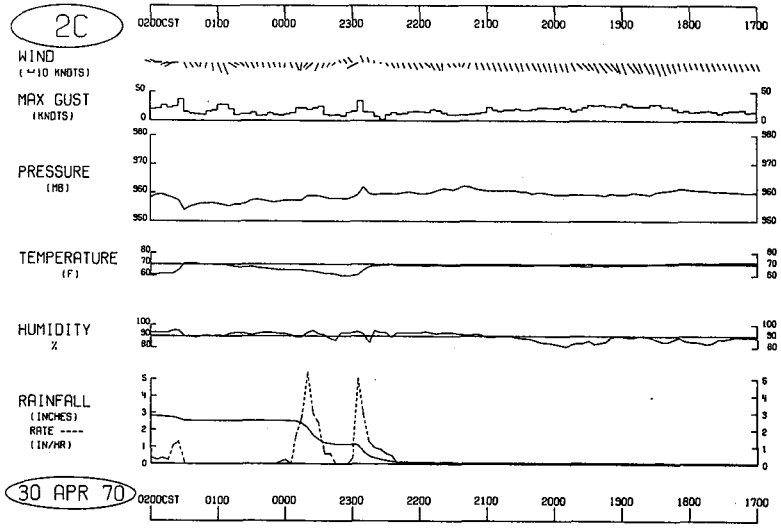
2C
WIND
(10 KNOTS)
MAX GUST
(KNOTS)
PRESSURE
(MB)
TEMPERATURE
(F)
HUMIDITY
%
RAINFALL
(INCHES)
RATE ----
(IN/HR)
30 APR 70
0200CST 0100 0000 2300 2200 2100 2000 1900 1800 1700

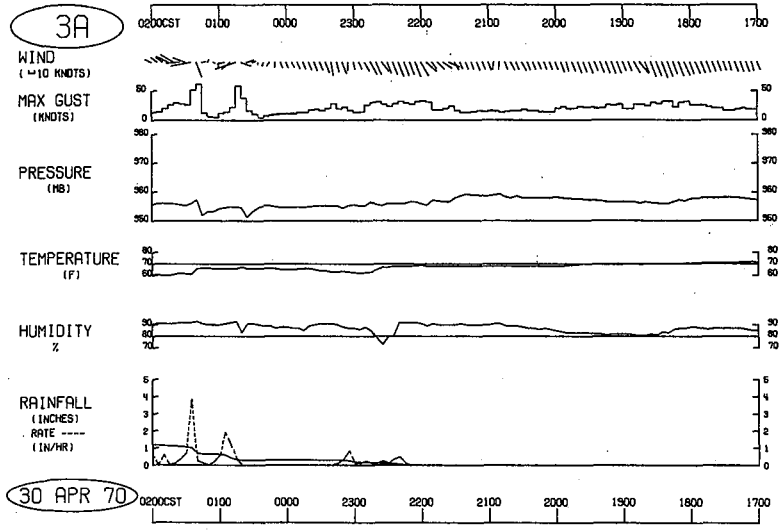
3A
WIND
(10 KNOTS)
MAX GUST
(KNOTS)
PRESSURE
(MB)
TEMPERATURE
(F)
HUMIDITY
%
RAINFALL
(INCHES)
RATE ----
(IN/HR)
30 APR 70
0200CST 0100 0000 2300 2200 2100 2000 1900 1800 1700

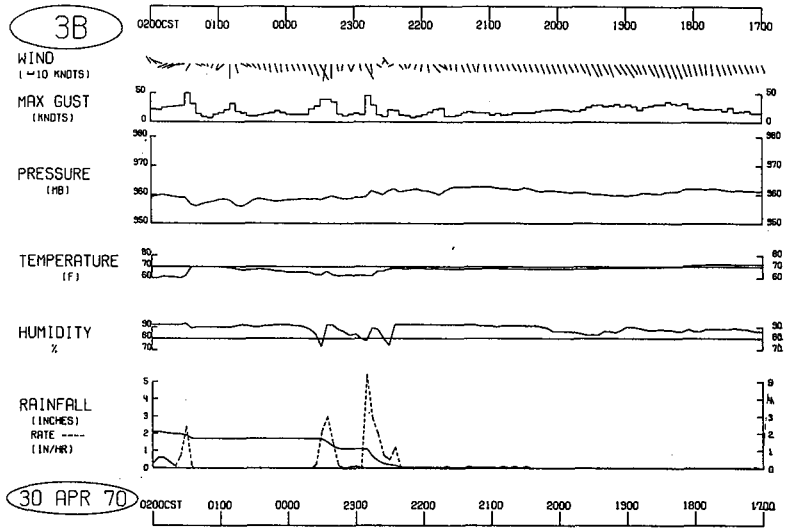
3B
WIND
(10 KNOTS)
MAX GUST
(KNOTS)
PRESSURE
(MB)
TEMPERATURE
(F)
HUMIDITY
%
RAINFALL
(INCHES)
RATE ----
(IN/HR)
30 APR 70
0200CST 0100 0000 2300 2200 2100 2000 1900 1800 1700

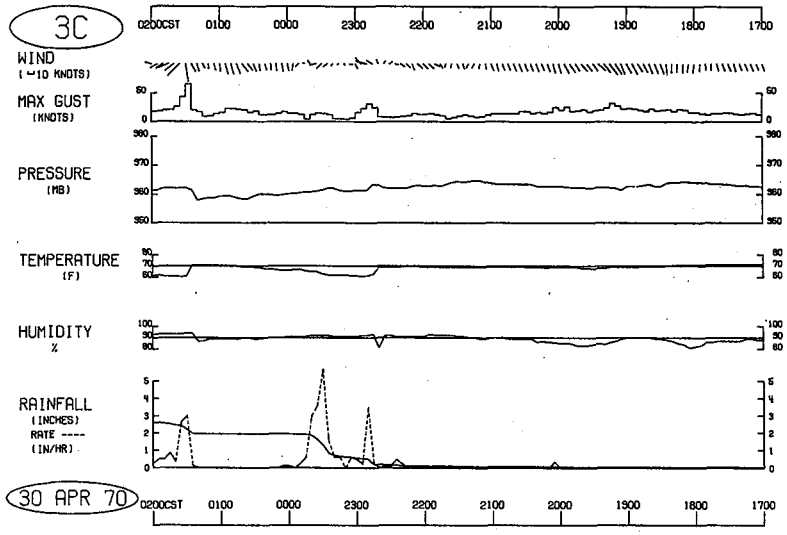
3C
WIND
(10 KNOTS)
MAX GUST
(KNOTS)
PRESSURE
(MB)
TEMPERATURE
(F)
HUMIDITY
%
RAINFALL
(INCHES)
RATE ----
(IN/HR)
30 APR 70
0200CST 0100 0000 2300 2200 2100 2000 1900 1800 1700

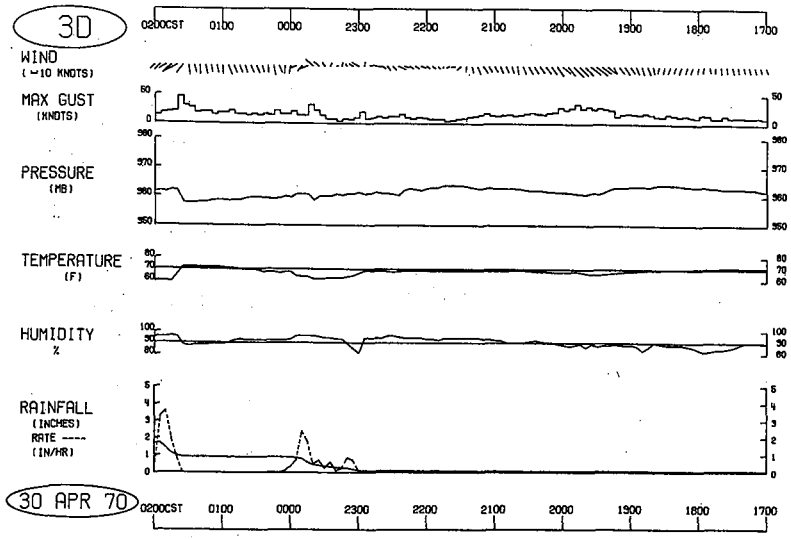
3D
WIND
(~10 KNOTS)
MAX GUST
(KNOTS)
PRESSURE
(MB)
TEMPERATURE
(F)
HUMIDITY
%
RAINFALL
(INCHES)
RATE ----
(IN/HR)
30 APR 70
0200CST 0100 0000 2300 2200 2100 2000 1900 1800 1700

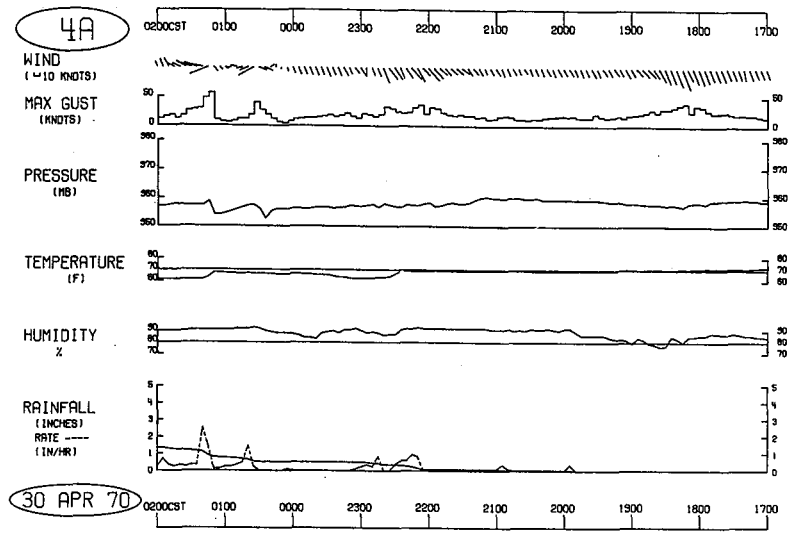
4A
WIND
(~10 KNOTS)
MAX GUST
(KNOTS)
PRESSURE
(MB)
TEMPERATURE
(F)
HUMIDITY
%
RAINFALL
(INCHES)
RATE ----
(IN/HR)
30 APR 70
0200CST 0100 0000 2300 2200 2100 2000 1900 1800 1700

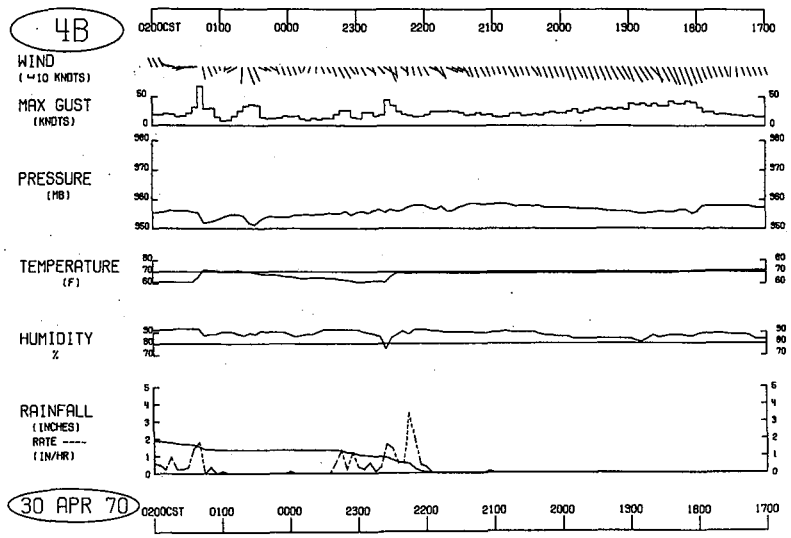
4B
WIND
(~10 KNOTS)
MAX GUST
(KNOTS)
PRESSURE
(MB)
TEMPERATURE
(F)
HUMIDITY
%
RAINFALL
(INCHES)
RATE ----
(IN/HR)
30 APR 70
0200CST 0100 0000 2300 2200 2100 2000 1900 1800 1700

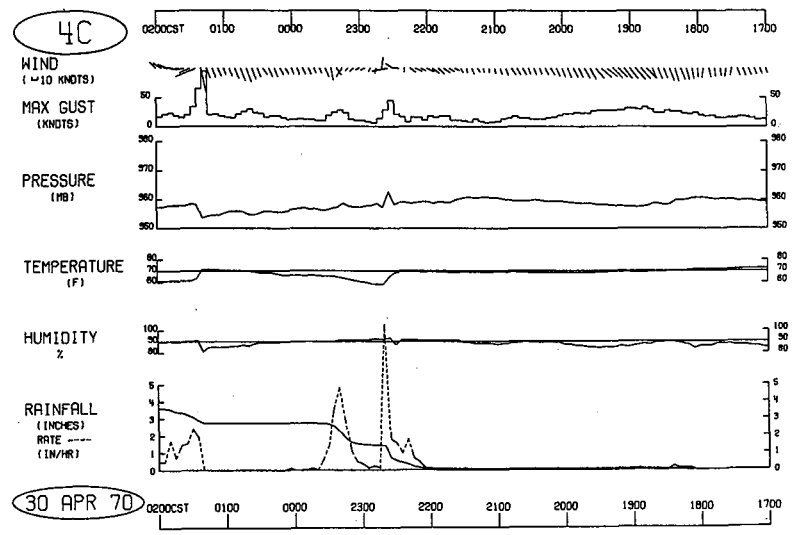
4C
WIND
(~10 KNOTS)
MAX GUST
(KNOTS)
PRESSURE
(MB)
TEMPERATURE
(F)
HUMIDITY
%
RAINFALL
(INCHES)
RATE ----
(IN/HR)
30 APR 70
0200CST 0100 0000 2300 2200 2100 2000 1900 1800 1700

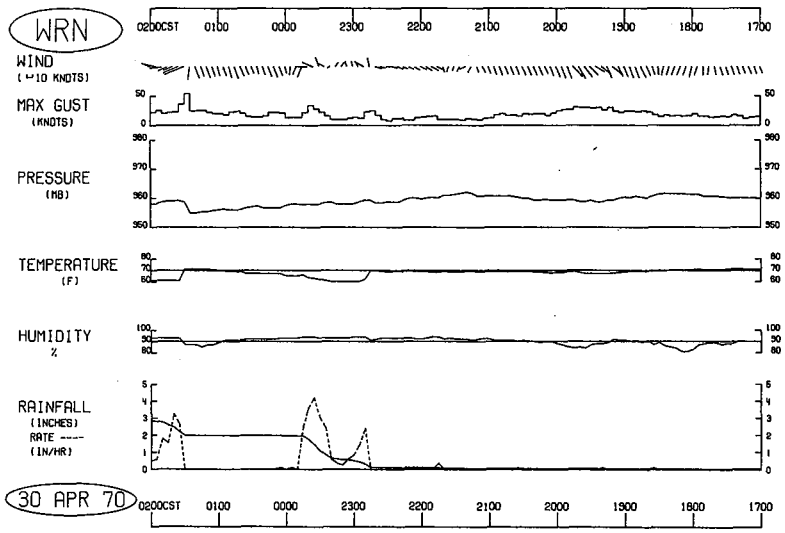
WRN
0200CST 0100 0000 2300 2200 2100 2000 1900 1800 1700
WIND
(~10 KNOTS)
MAX GUST
(KNOTS)
PRESSURE
(MB)
TEMPERATURE
(F)
HUMIDITY
%
RAINFALL
(INCHES)
RATE ----
(IN/HR)
30 APR 70

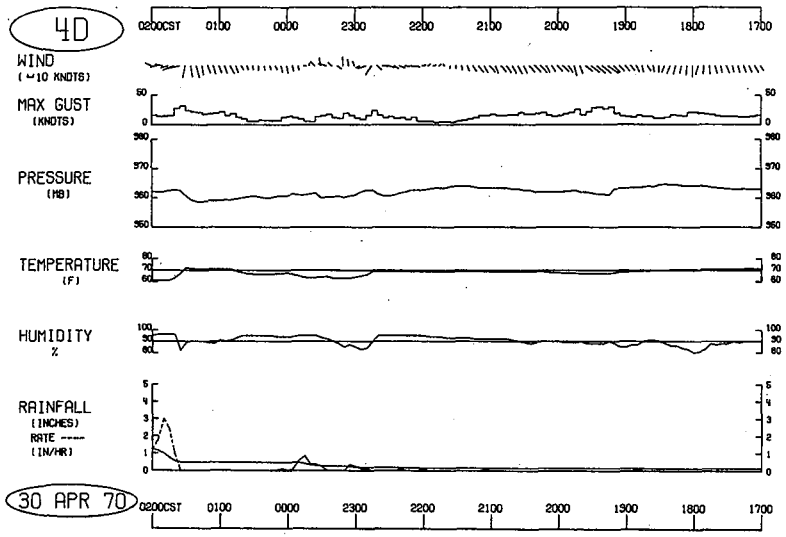
4D
0200CST 0100 0000 2300 2200 2100 2000 1900 1800 1700
WIND
(~10 KNOTS)
MAX GUST
(KNOTS)
PRESSURE
(MB)
TEMPERATURE
(F)
HUMIDITY
%
RAINFALL
(INCHES)
RATE ----
(IN/HR)
30 APR 70

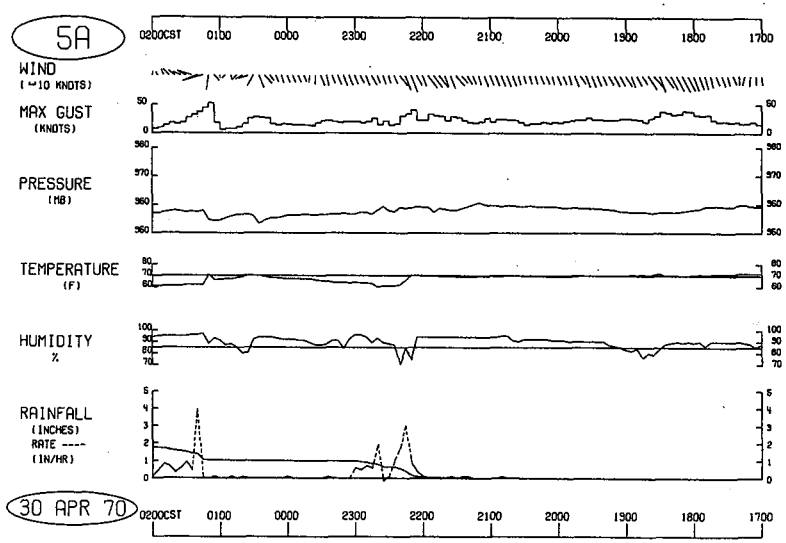
5A
0200CST 0100 0000 2300 2200 2100 2000 1900 1800 1700
WIND
(~10 KNOTS)
MAX GUST
(KNOTS)
PRESSURE
(MB)
TEMPERATURE
(F)
HUMIDITY
%
RAINFALL
(INCHES)
RATE ----
(IN/HR)
30 APR 70

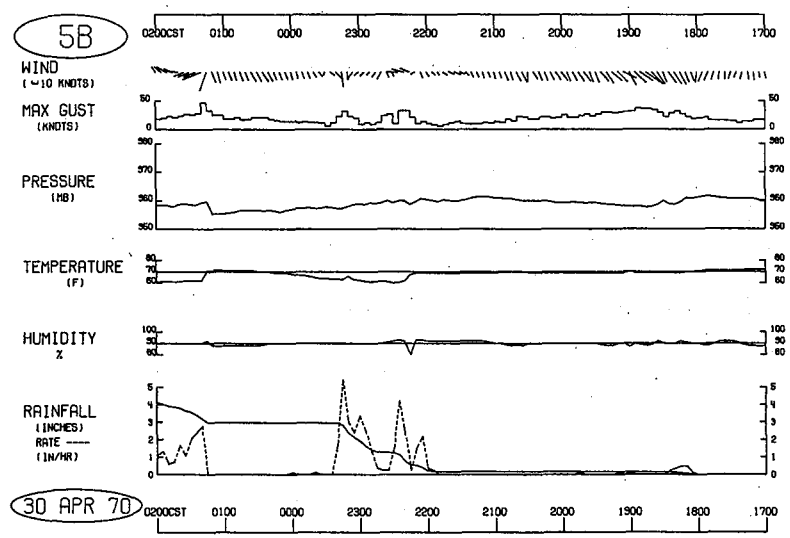
5B
0200CST 0100 0000 2300 2200 2100 2000 1900 1800 1700
WIND
(~10 KNOTS)
MAX GUST
(KNOTS)
PRESSURE
(MB)
TEMPERATURE
(F)
HUMIDITY
%
RAINFALL
(INCHES)
RATE ----
(IN/HR)
30 APR 70

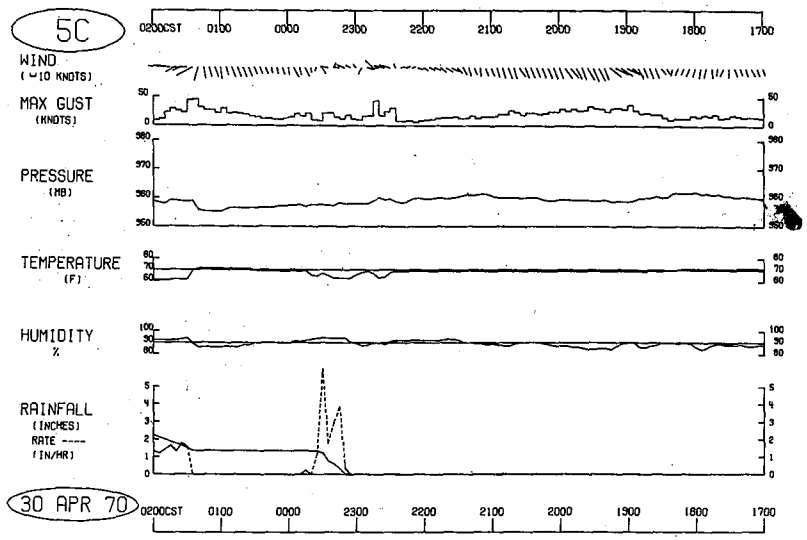
5C
WIND
(10 KNOTS)
MAX GUST
(KNOTS)
PRESSURE
(MB)
TEMPERATURE
(F)
HUMIDITY
%
RAINFALL
(INCHES)
RATE ----
(IN/HR)
30 APR 70
0200CST 0100 0000 2300 2200 2100 2000 1900 1800 1700

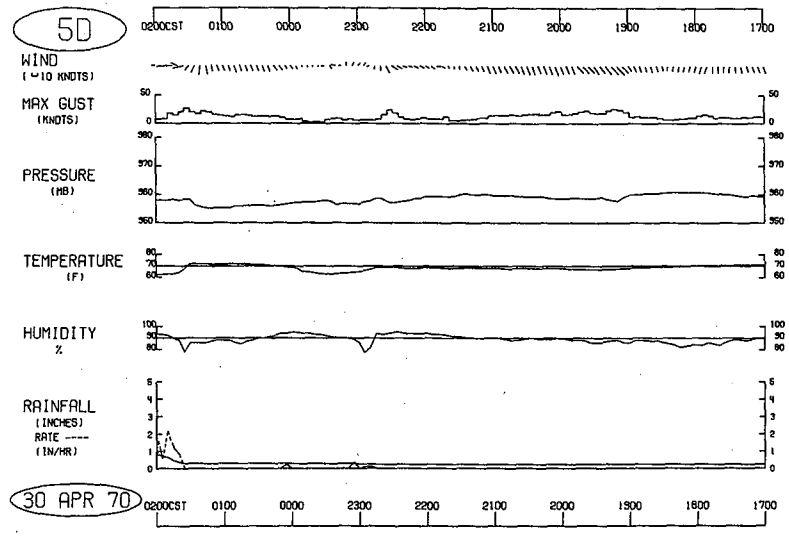
5D
WIND
(10 KNOTS)
MAX GUST
(KNOTS)
PRESSURE
(MB)
TEMPERATURE
(F)
HUMIDITY
%
RAINFALL
(INCHES)
RATE ----
(IN/HR)
30 APR 70
0200CST 0100 0000 2300 2200 2100 2000 1900 1800 1700

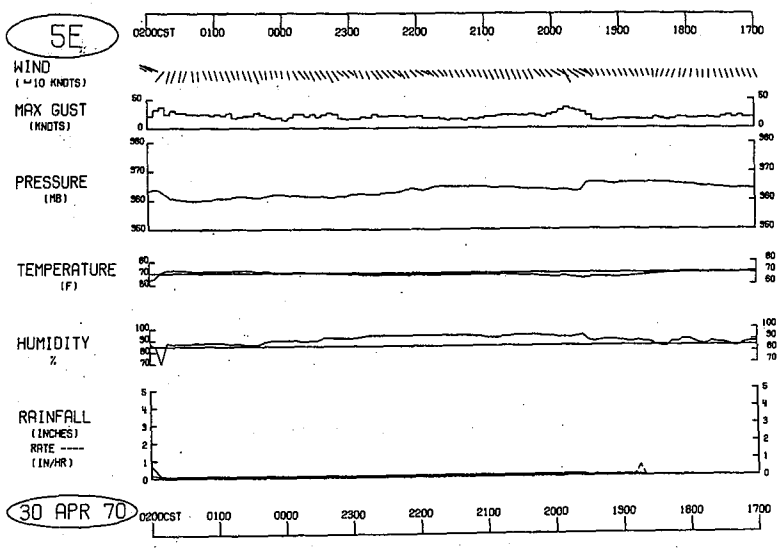
5E
WIND
(10 KNOTS)
MAX GUST
(KNOTS)
PRESSURE
(MB)
TEMPERATURE
(F)
HUMIDITY
%
RAINFALL
(INCHES)
RATE ----
(IN/HR)
30 APR 70
0200CST 0100 0000 2300 2200 2100 2000 1900 1800 1700

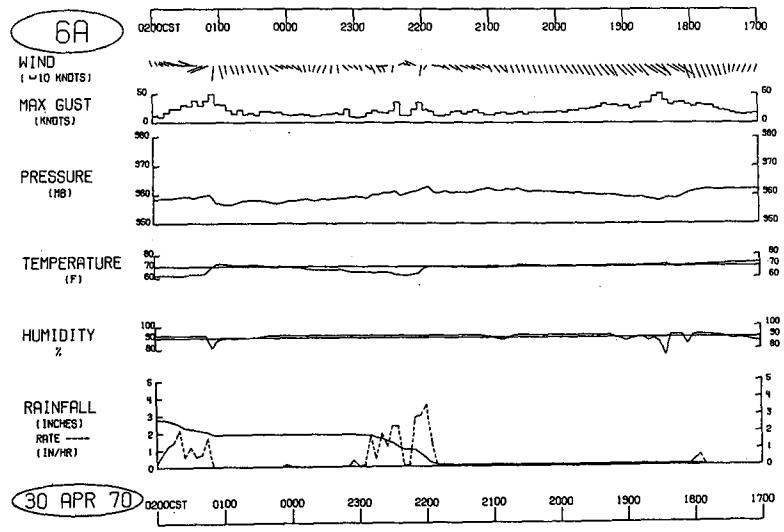
6A
WIND
(10 KNOTS)
MAX GUST
(KNOTS)
PRESSURE
(MB)
TEMPERATURE
(F)
HUMIDITY
%
RAINFALL
(INCHES)
RATE ----
(IN/HR)
30 APR 70
0200CST 0100 0000 2300 2200 2100 2000 1900 1800 1700

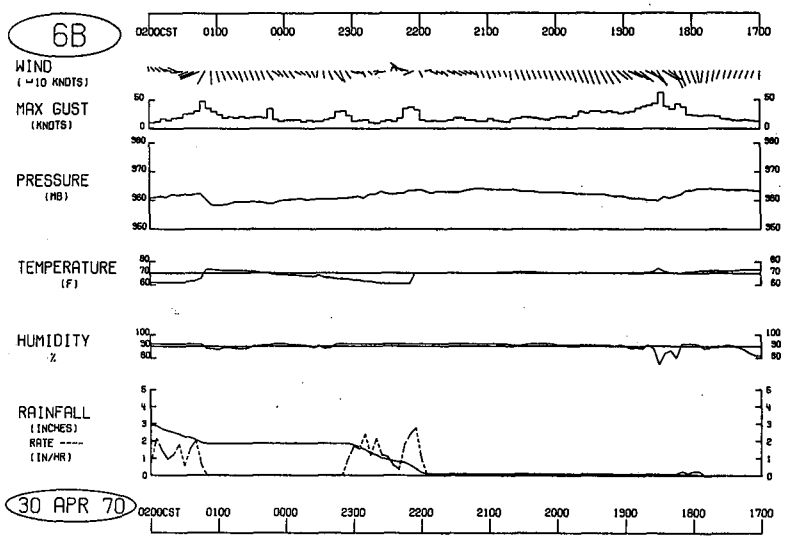
6B
WIND
(10 KNOTS)
MAX GUST
(KNOTS)
PRESSURE
(MB)
TEMPERATURE
(F)
HUMIDITY
%
RAINFALL
(INCHES)
RATE ----
(IN/HR)
30 APR 70
0200CST 0100 0000 2300 2200 2100 2000 1900 1800 1700

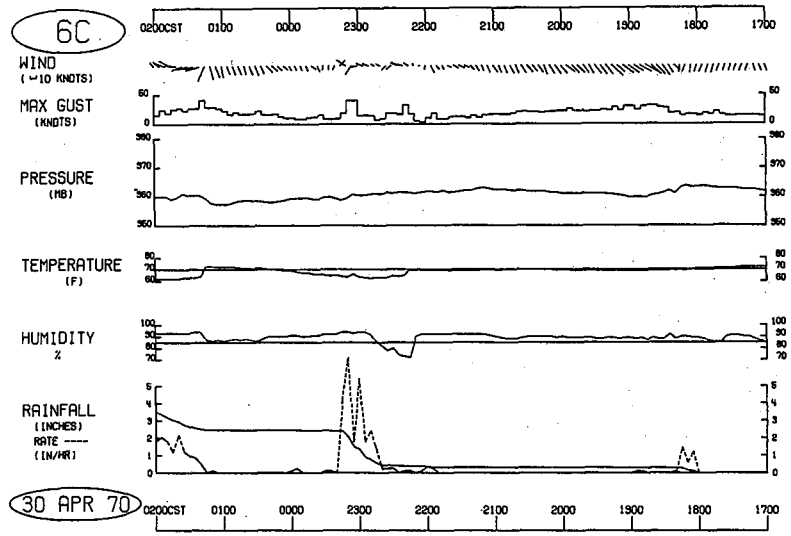
6C
WIND
(10 KNOTS)
MAX GUST
(KNOTS)
PRESSURE
(MB)
TEMPERATURE
(F)
HUMIDITY
%
RAINFALL
(INCHES)
RATE ----
(IN/HR)
30 APR 70
0200CST 0100 0000 2300 2200 2100 2000 1900 1800 1700

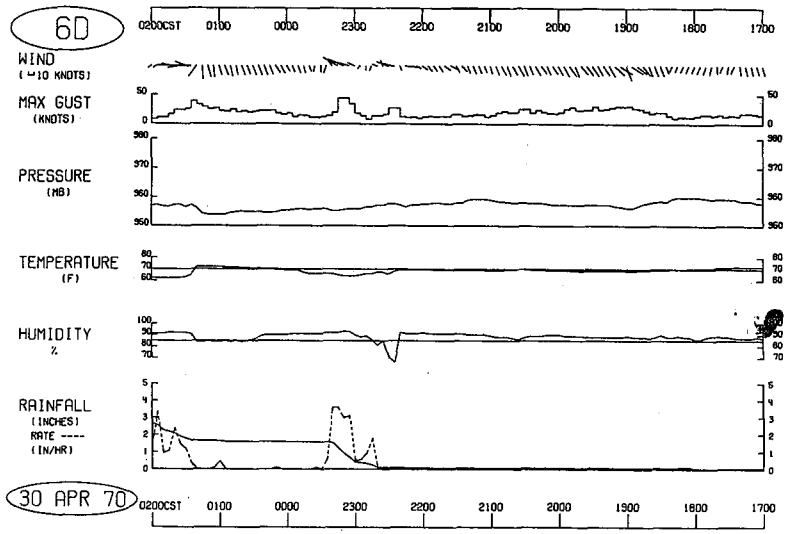
6D
WIND
(10 KNOTS)
MAX GUST
(KNOTS)
PRESSURE
(MB)
TEMPERATURE
(F)
HUMIDITY
%
RAINFALL
(INCHES)
RATE ----
(IN/HR)
30 APR 70
0200CST 0100 0000 2300 2200 2100 2000 1900 1800 1700

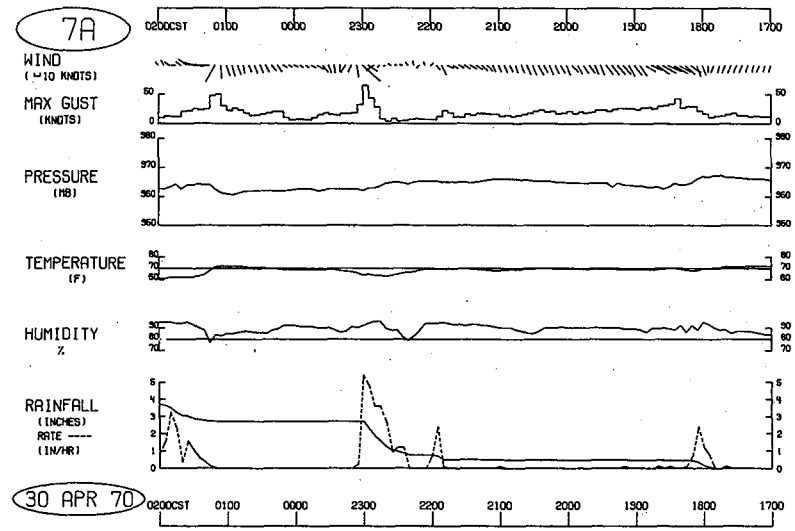
7A
WIND
(10 KNOTS)
MAX GUST
(KNOTS)
PRESSURE
(MB)
TEMPERATURE
(F)
HUMIDITY
%
RAINFALL
(INCHES)
RATE ----
(IN/HR)
30 APR 70
0200CST 0100 0000 2300 2200 2100 2000 1900 1800 1700

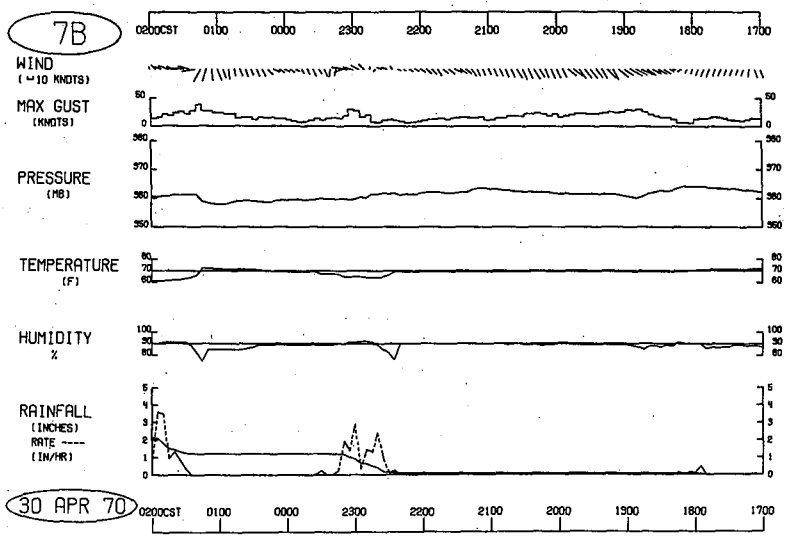
7B
0200CST 0100 0000 2300 2200 2100 2000 1900 1800 1700
WIND
(10 KNOTS)
MAX GUST
(KNOTS)
PRESSURE
(MB)
TEMPERATURE
(F)
HUMIDITY
%
RAINFALL
(INCHES)
RATE ----
(IN/HR)
30 APR 70

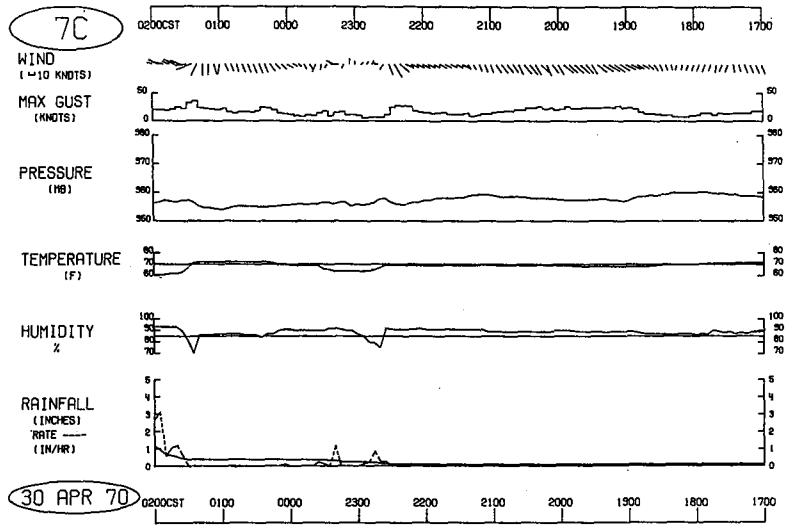
7C
0200CST 0100 0000 2300 2200 2100 2000 1900 1800 1700
WIND
(10 KNOTS)
MAX GUST
(KNOTS)
PRESSURE
(MB)
TEMPERATURE
(F)
HUMIDITY
%
RAINFALL
(INCHES)
RATE ----
(IN/HR)
30 APR 70

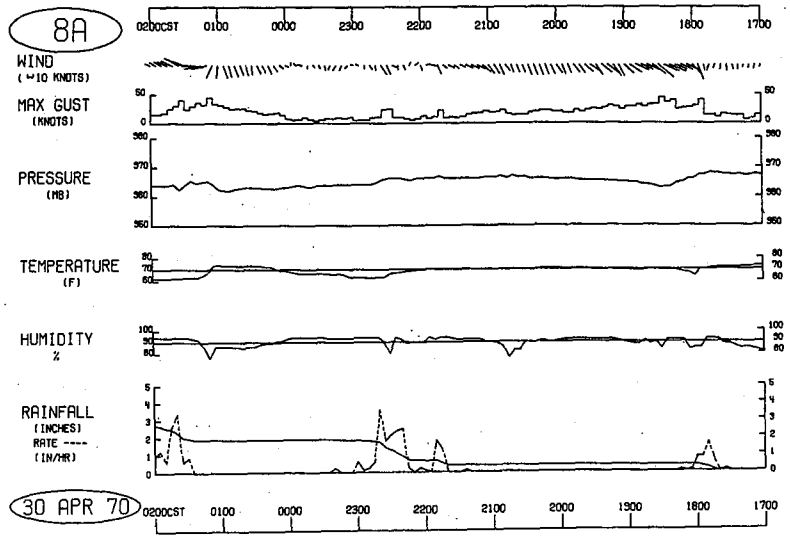
8A
0200CST 0100 0000 2300 2200 2100 2000 1900 1800 1700
WIND
(10 KNOTS)
MAX GUST
(KNOTS)
PRESSURE
(MB)
TEMPERATURE
(F)
HUMIDITY
%
RAINFALL
(INCHES)
RATE ----
(IN/HR)
30 APR 70

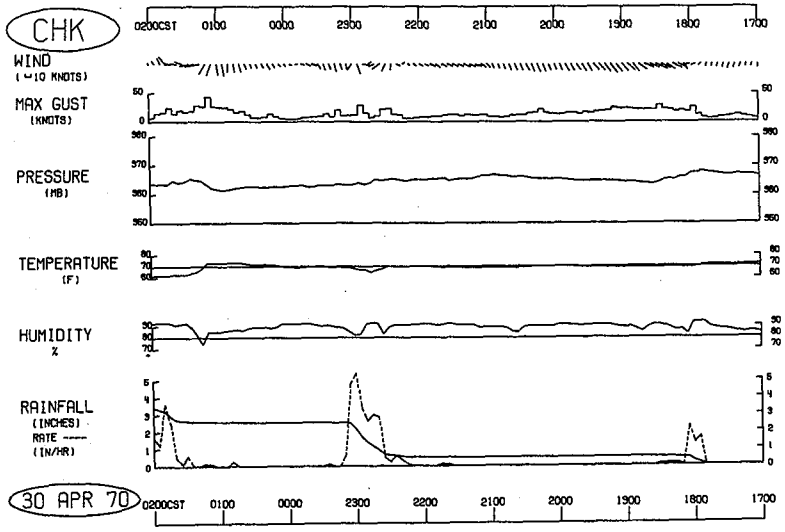
CHK
0200CST 0100 0000 2300 2200 2100 2000 1900 1800 1700
WIND
(10 KNOTS)
MAX GUST
(KNOTS)
PRESSURE
(MB)
TEMPERATURE
(F)
HUMIDITY
%
RAINFALL
(INCHES)
RATE ----
(IN/HR)
30 APR 70

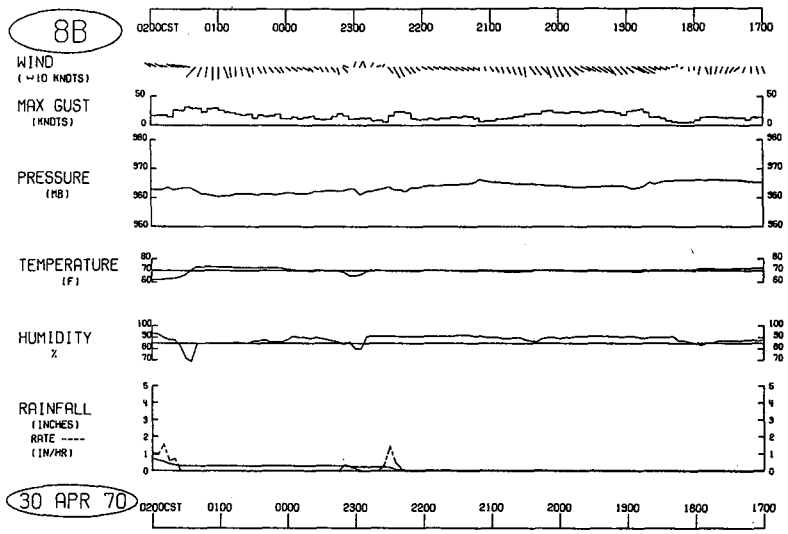
8B
0200CST 0100 0000 2300 2200 2100 2000 1900 1800 1700
WIND
(↵10 KNOTS)
MAX GUST
(KNOTS)
PRESSURE
(MB)
TEMPERATURE
(F)
HUMIDITY
%
RAINFALL
(INCHES)
RATE ----
(IN/HR)
30 APR 70

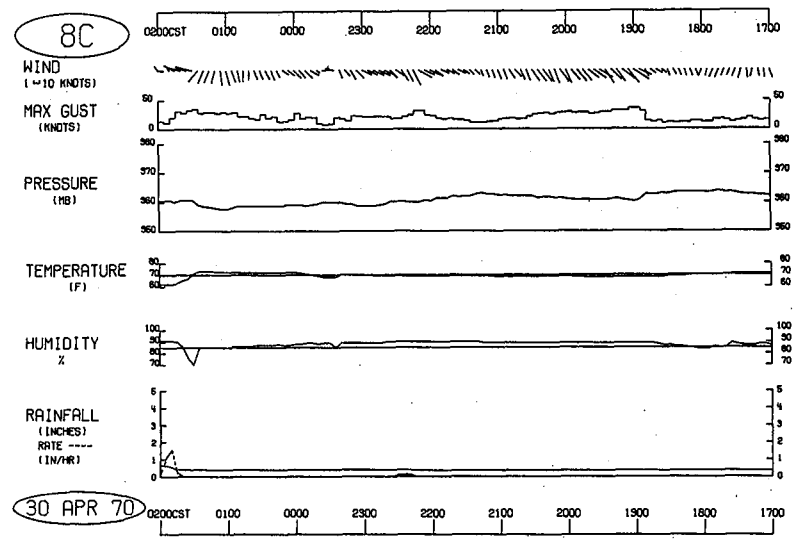
8C
0200CST 0100 0000 2300 2200 2100 2000 1900 1800 1700
WIND
(↵10 KNOTS)
MAX GUST
(KNOTS)
PRESSURE
(MB)
TEMPERATURE
(F)
HUMIDITY
%
RAINFALL
(INCHES)
RATE ----
(IN/HR)
30 APR 70

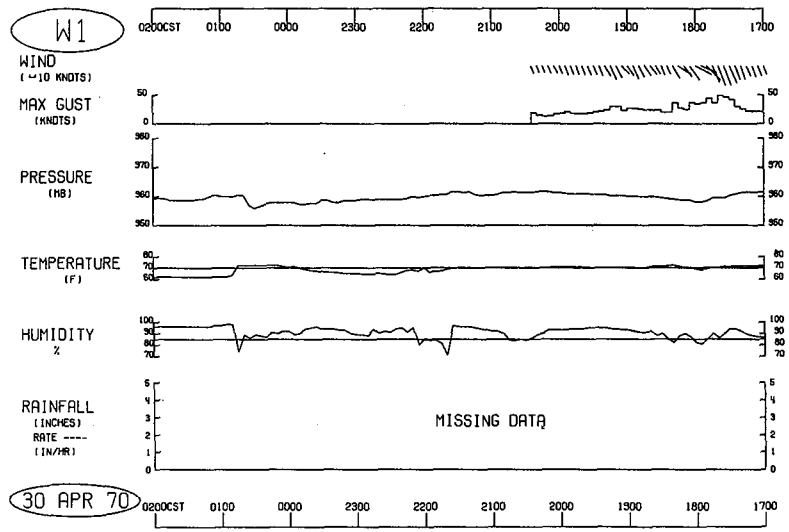
W1
0200CST 0100 0000 2300 2200 2100 2000 1900 1800 1700
WIND
(↵10 KNOTS)
MAX GUST
(KNOTS)
PRESSURE
(MB)
TEMPERATURE
(F)
HUMIDITY
%
RAINFALL
(INCHES)
RATE ----
(IN/HR)
MISSING DATA
30 APR 70

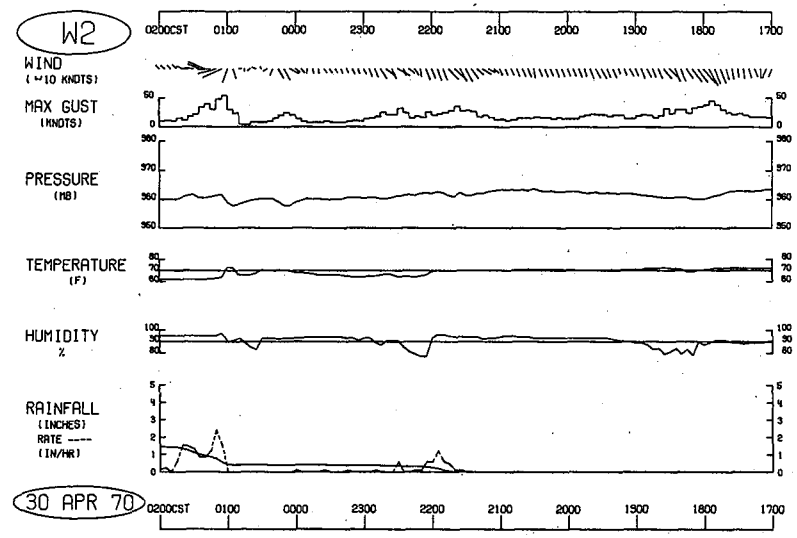
W2
0200CST 0100 0000 2300 2200 2100 2000 1900 1800 1700
WIND
(↵10 KNOTS)
MAX GUST
(KNOTS)
PRESSURE
(MB)
TEMPERATURE
(F)
HUMIDITY
%
RAINFALL
(INCHES)
RATE ----
(IN/HR)
30 APR 70

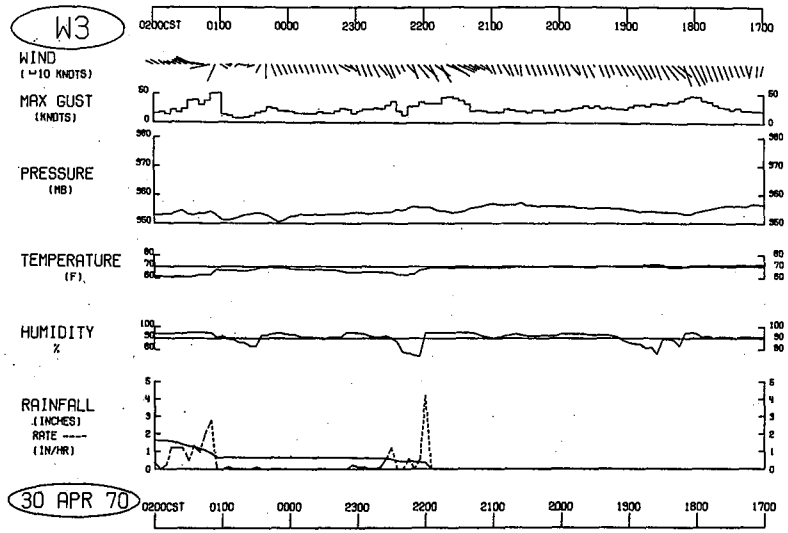
W3
0200CST 0100 0000 2300 2200 2100 2000 1900 1800 1700
WIND
(≥10 KNOTS)
MAX GUST
(KNOTS)
PRESSURE
(MB)
TEMPERATURE
(F)
HUMIDITY
%
RAINFALL
(INCHES)
RATE ----
(IN/HR)
30 APR 70

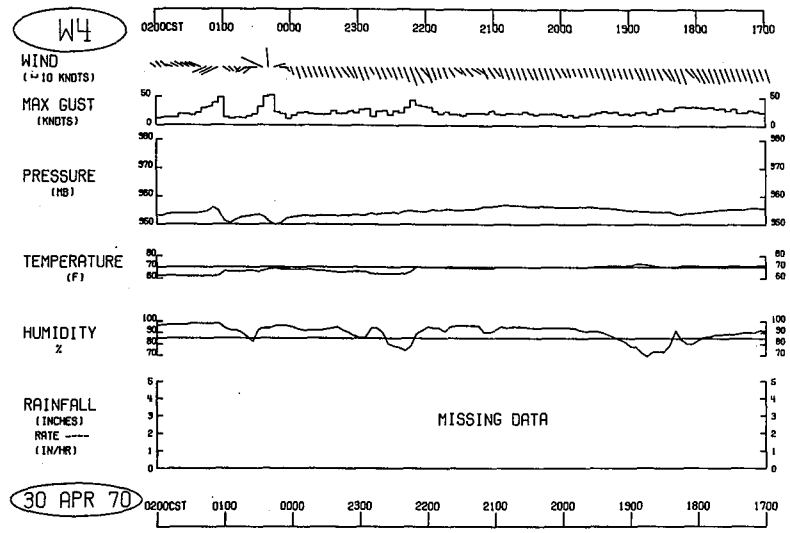
W4
0200CST 0100 0000 2300 2200 2100 2000 1900 1800 1700
WIND
(≥10 KNOTS)
MAX GUST
(KNOTS)
PRESSURE
(MB)
TEMPERATURE
(F)
HUMIDITY
%
RAINFALL
(INCHES)
RATE ----
(IN/HR)
MISSING DATA
30 APR 70

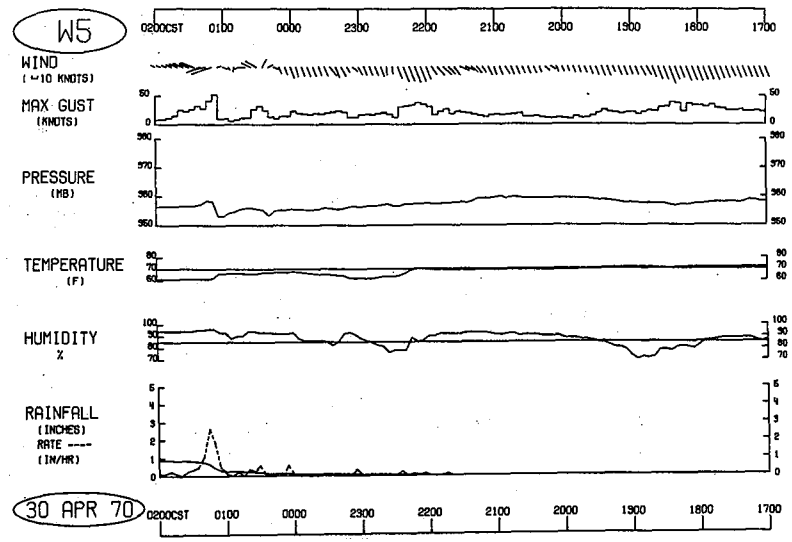
W5
0200CST 0100 0000 2300 2200 2100 2000 1900 1800 1700
WIND
(≥10 KNOTS)
MAX GUST
(KNOTS)
PRESSURE
(MB)
TEMPERATURE
(F)
HUMIDITY
%
RAINFALL
(INCHES)
RATE ----
(IN/HR)
30 APR 70

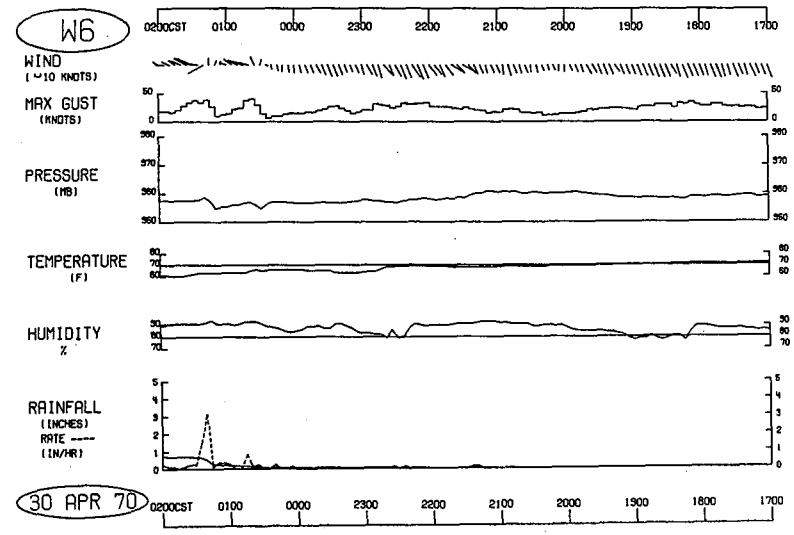
W6
0200CST 0100 0000 2300 2200 2100 2000 1900 1800 1700
WIND
(≥10 KNOTS)
MAX GUST
(KNOTS)
PRESSURE
(MB)
TEMPERATURE
(F)
HUMIDITY
%
RAINFALL
(INCHES)
RATE ----
(IN/HR)
30 APR 70

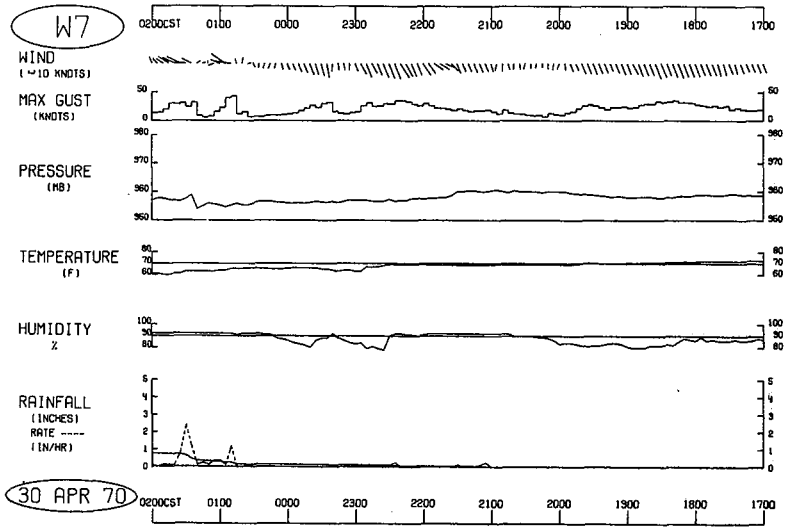
W7
WIND
(~10 KNOTS)
MAX GUST
(KNOTS)
PRESSURE
(MB)
TEMPERATURE
(F)
HUMIDITY
%
RAINFALL
(INCHES)
RATE ----
(IN/HR)
30 APR 70
0200CST 0100 0000 2300 2200 2100 2000 1900 1800 1700

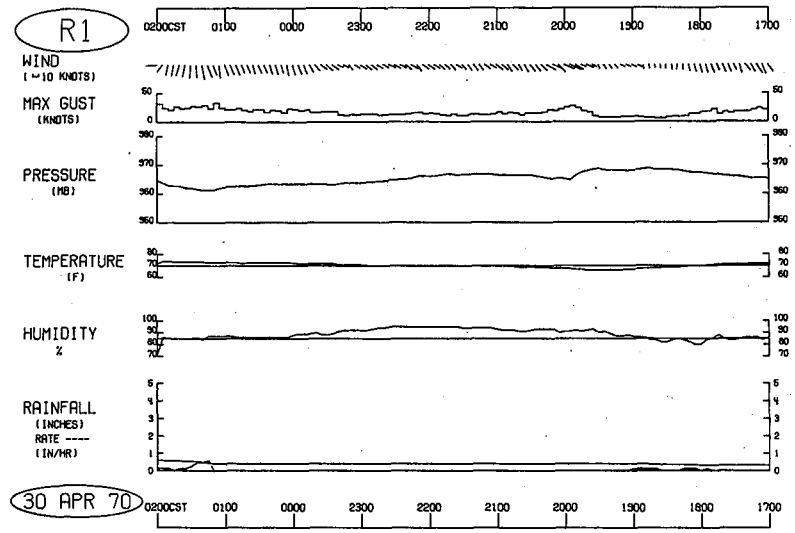
R1
WIND
(~10 KNOTS)
MAX GUST
(KNOTS)
PRESSURE
(MB)
TEMPERATURE
(F)
HUMIDITY
%
RAINFALL
(INCHES)
RATE ----
(IN/HR)
30 APR 70
0200CST 0100 0000 2300 2200 2100 2000 1900 1800 1700

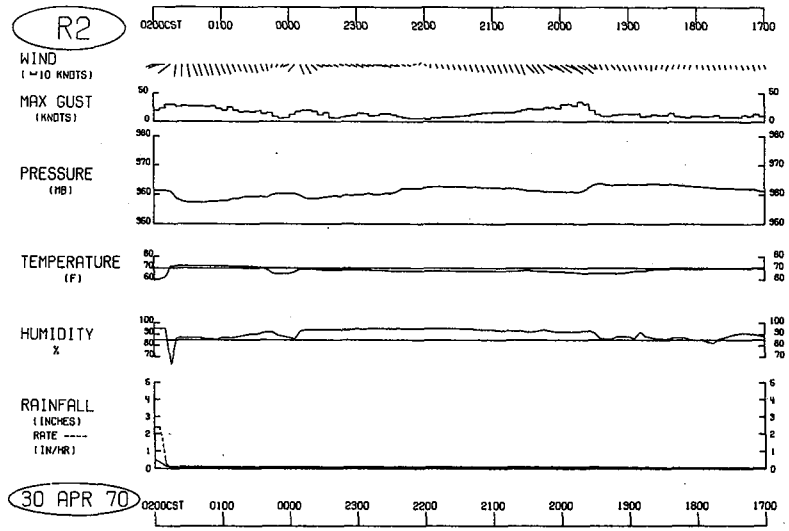
R2
WIND
(~10 KNOTS)
MAX GUST
(KNOTS)
PRESSURE
(MB)
TEMPERATURE
(F)
HUMIDITY
%
RAINFALL
(INCHES)
RATE ----
(IN/HR)
30 APR 70
0200CST 0100 0000 2300 2200 2100 2000 1900 1800 1700

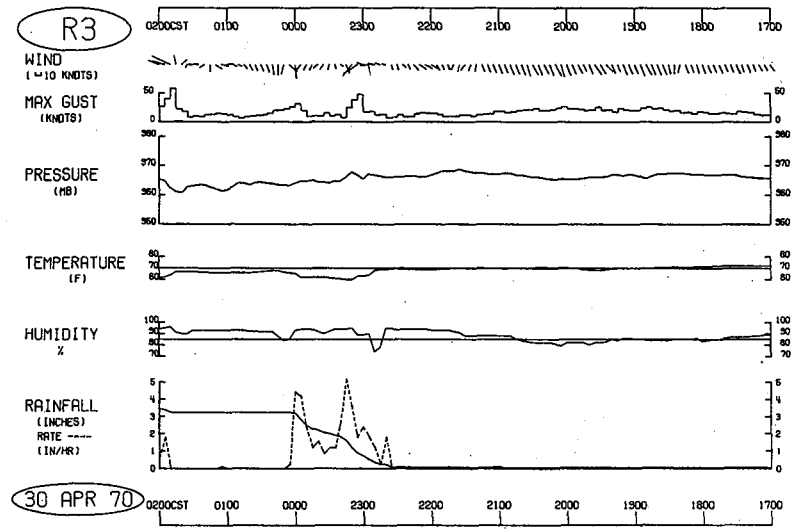
R3
WIND
(~10 KNOTS)
MAX GUST
(KNOTS)
PRESSURE
(MB)
TEMPERATURE
(F)
HUMIDITY
%
RAINFALL
(INCHES)
RATE ----
(IN/HR)
30 APR 70
0200CST 0100 0000 2300 2200 2100 2000 1900 1800 1700

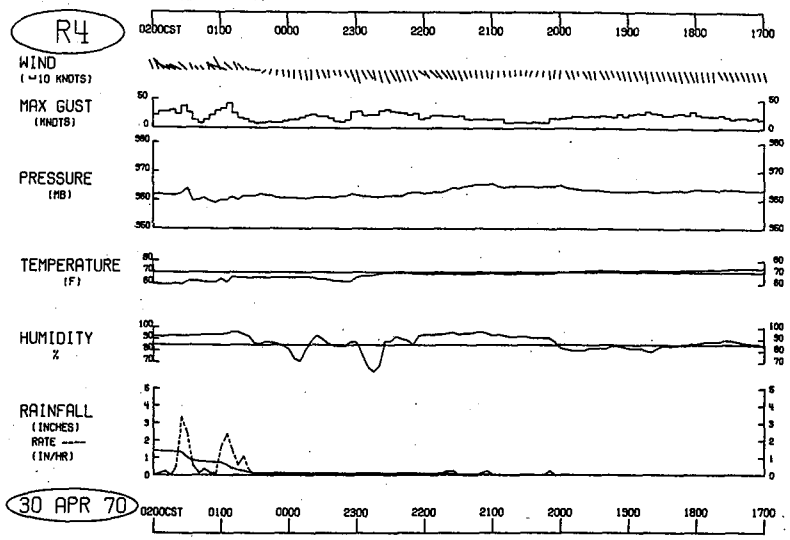
R4
0200CST 0100 0000 2300 2200 2100 2000 1900 1800 1700
WIND
(~10 KNOTS)
MAX GUST
(KNOTS)
PRESSURE
(MB)
TEMPERATURE
(F)
HUMIDITY
%
RAINFALL
(INCHES)
RATE ----
(IN/HR)
30 APR 70

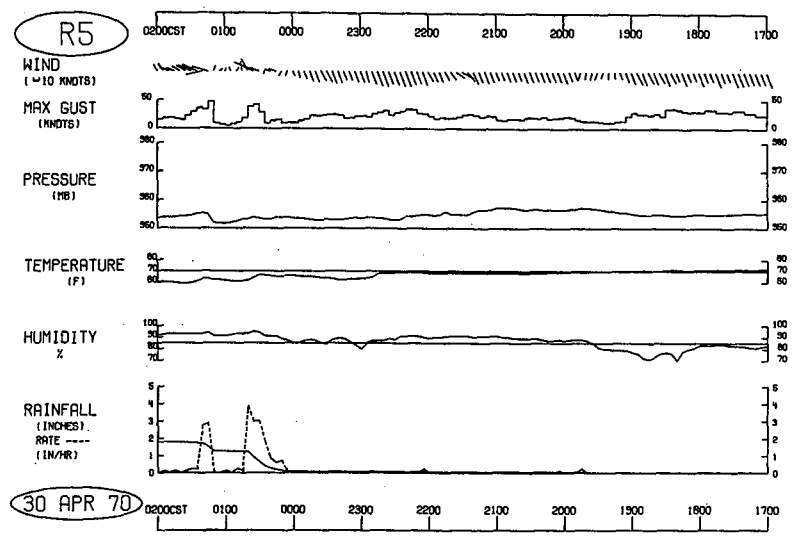
R5
0200CST 0100 0000 2300 2200 2100 2000 1900 1800 1700
WIND
(~10 KNOTS)
MAX GUST
(KNOTS)
PRESSURE
(MB)
TEMPERATURE
(F)
HUMIDITY
%
RAINFALL
(INCHES)
RATE ----
(IN/HR)
30 APR 70

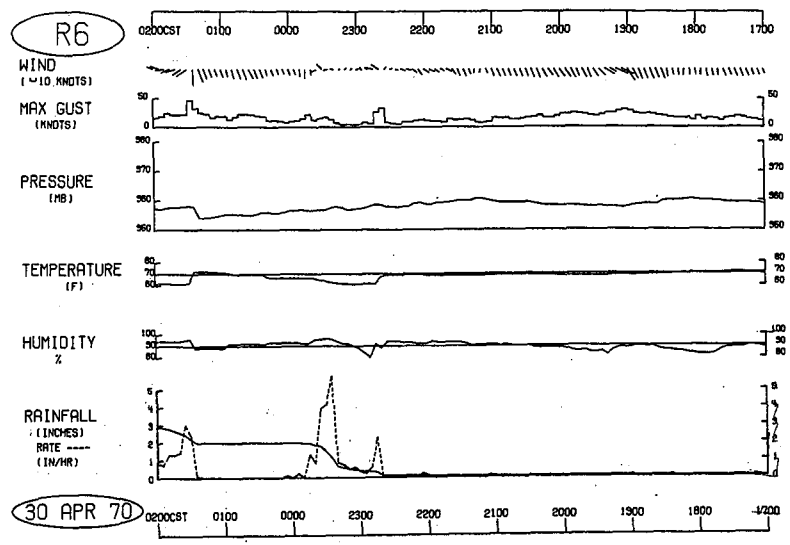
R6
0200CST 0100 0000 2300 2200 2100 2000 1900 1800 1700
WIND
(~10 KNOTS)
MAX GUST
(KNOTS)
PRESSURE
(MB)
TEMPERATURE
(F)
HUMIDITY
%
RAINFALL
(INCHES)
RATE ----
(IN/HR)
30 APR 70

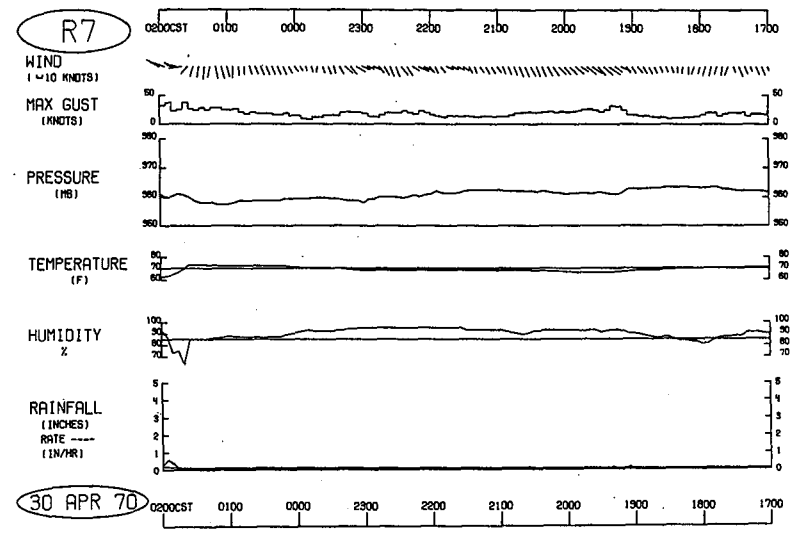
R7
0200CST 0100 0000 2300 2200 2100 2000 1900 1800 1700
WIND
(~10 KNOTS)
MAX GUST
(KNOTS)
PRESSURE
(MB)
TEMPERATURE
(F)
HUMIDITY
%
RAINFALL
(INCHES)
RATE ----
(IN/HR)
30 APR 70

5. SURFACE ANALYSES

Map analyses of surface observations (section 4) and radar digital reflectivities are displayed on the following pages at selected times covering the eight-hour period storms were in or near the NSSL surface mesonetwork. On each page we present eight maps of surface measured parameters surrounding a radar echo map, all to the same scale.

These analyses are produced by a time-to-space conversion technique tuned to resolve variations whose scale is larger than 20 n miles wavelength (Barnes, 1973). This is the approximate scale of many thunderstorm-related phenomena: high-low pressure couplets; echo size; divergence and vorticity patterns. Variations whose scale is only 10 n miles wavelength are resolved with two-thirds their actual amplitude and they have additional phase (position) uncertainty.

Network station locations (dots) are identified on the radar map. To facilitate comparison at different times, all maps are arrayed as shown in figure 12 (page 52). Each illustration page is identified by map time (CST) at the lower left. Parameter values at grid points 3.175 km apart are printed in units designated in figure 12. Distributions are indicated by letter shading between contours hand inked for emphasis. Streamlines and isotachs are computed from u- and v- component analyses and are drawn by a computer-driven drum plotter. Radar digital data are plotted as coded numbers scaled from 0 to 9. Corresponding reflectivities are listed in table 4. The digit distribution is hand contoured based on general knowledge of the video echo configuration. Data are truncated inside the 20 n mile range circle because ground clutter and automatic sensitivity time control (STC) calibration produce unreliable values therein (Wilk and Kessler, 1970).

In section 4, we noted that differences in mean pressure from station to station mainly reflect altitude differences. Altitude effects, pressure changes due to movement of large (synoptic scale) pressure systems, and instrument biases are removed by subtracting from observed pressure each station's linear trend pressure determined by regression analysis. Maps depict areal distributions of the resulting mesoscale perturbations.

Calculation of θ_w requires absolute pressure rather than relative pressure, but conveniently, the computation is insensitive to small errors in pressure. The pressure we used for this purpose is the grid-analyzed perturbation pressure plus the network mean pressure, $\overline{P}_{net}$ (section 4). From this pressure, adjusted temperature and adjusted humidity (discussed in section 4), θ_w computes by an approximate method similar to that developed by Prosser and Foster (1966).

Teten's formulation (1930) determines saturation vapor pressure from temperature

$$e_s = 6.1078 \exp[(17.26939\ T)/(T+237.3)]. \qquad (6)$$

Table 4. Equivalent Reflectivity[a] of Coded Digital Radar Data. For Comparison with Observed Rain Rates, the $Z = 200R^{1.6}$ Equivalent Radar Rain Rates Also Are Tabulated.

Code	log Z_e	Rain Rate (inches hr^{-1})
1	1.5	.01
2	2.2	.03
3	3.2	.14
4	3.9	.39
5	4.5	.93
6	4.9	1.66
7	5.2	2.55
8	5.7	5.24
9	6.2	10.77

[a]These reflectivities are unadjusted for digital interval truncation bias (Sirmans and Doviak, 1973). Consequently, rain rates greater than one inch hr^{-1} are underestimated about 30 percent.

Table 5. Polynomial Coefficients[a] (10) Approximating Temperatures Along Three Moist Adiabats (θ_w).

θ_w	C_o	C_1	C_2	C_3
10C	-135.01805	0.33800929	-2.889×10^{-4}	9.6×10^{-8}
20C	-102.40678	0.29999	-2.764×10^{-4}	9.9×10^{-8}
30C	-56.5666	0.1973568	-1.705×10^{-4}	5.98×10^{-8}

[a]Horace R. Hudson, National Severe Storms Forecast Center, Kansas City, Missouri (personal communication).

Relative humidity and (6) combine to give actual vapor pressure

$$e = e_s(RH/100). \tag{7}$$

Substituting actual vapor pressure on the left in (6) yields dew point temperature (T_d) when solved for T. Temperature (TLCL) and pressure (PLCL) of air lifted to its saturation level are given by these formulas (Barnes, 1968):

$$TLCL = T_d - (0.001296T_d + 0.1963)(T-T_d) \tag{8}$$

and

$$PLCL = P(TLCL/T)^{7/2}. \tag{9}$$

Temperatures[1] at the condensation pressure level corresponding to moist adiabats θ_w = 10, 20 and 30C are approximated by third-order polynomials:

$$TMA = C_o + C_1 \cdot (PLCL) + C_2 \cdot (PLCL)^2 + C_3 \cdot (PLCL)^3. \tag{10}$$

Coefficients C_o, C_1, C_2, C_3, listed in table 5 for the three moist adiabats, are useful to 400 mb. Air parcel θ_w is obtained by linearly interpolating TLCL between the appropriate TMA values.

Wet-bulb potential temperature is that temperature air would have if cooled by expansion (lifting) until saturated, then warmed by compression (descent) while maintaining saturation until its pressure equals 1000 mb. This temperature is a conservative property of air through condensation and evaporation processes. When mixed, air with different thermal properties reaches θ_w-value intermediate to the values before mixing. Atmosphere capable of sustaining severe thunderstorms characteristically has minimum θ_w at mid-tropospheric levels (4-7 km altitude) and maximum value in low troposphere. Other distributions found near thunderstorms indicate massive air movements vertically--the updrafts and downdrafts.

As Storm A enters the network area at 1745, no significant θ_w centers or gradients develop. Values of θ_w range from 19 to 22C and air from mid-levels ($\theta_w \sim$ 16C) doesn't yet reach the surface in large quantities. Rainfall from Storm A accumulates to 0.3 inches, but its 1.1 inches hr^{-1} rain rate diminishes rapidly after 1745. Perturbation pressure ranges from -2.5 to +1.5 mb in ridges and troughs elongated northeast-southwest.

---

[1]All temperatures in formulas (6) through (10) are expressed in degrees Celsius, except in (9) absolute values are required.

Peculiarly strong pressure gradient (2.1 mb/10 km) beneath dying Storm A produces winds in excess of 30 knots (five-minute average!) and results in strong divergence (10^{-3} sec^{-1}). Nelson and Barnes discuss probable causes (page 93). Flow deflects around echo A's weak downdraft, but winds no longer reveal A's decaying updraft expected near Station 7A at 1805. Weak convergence (10^{-4} sec^{-1}) remains southeast of the echo in the vicinity of R7, 7C and 8C, but moisture convergence cannot be found anywhere in the network area. Relative to the moving storm (table 2), surface air approaches from the northeast and deflects westward beneath the echo in a strong moisture divergence region (40 x 10^{-7} sec^{-1}).

After Storm A dissipates, surface flow establishes from the southeast 10 to 15 knots. Pressure range diminishes -1.5 to +1.5 mb and gradients weaken (1.5 mb/10 km). At 1930, Storm D lying west of the network causes weak moisture convergence and confluent relative flow near ELR, but there are few other interesting details. Several small echoes develop, but they produce little surface rain. Throughout the period prior to 2200, vorticity remains weak (10^{-4} sec^{-1}) and has no recognizable storm-related pattern.

Between 2200 and 0000 the large storms E_1 and E_2 pass through the network with interesting effects. In the southwest at 2210, the first significant amount of mid-level air (θ_w = 16C) arrives with E_1's rainy downdraft, revealing itself in the flow pattern as a "source." Adjacent on the east is E_1's updraft (near 6C) characterized by a line "sink" in the surface streamlines, by moisture convergence (-18 x 10^{-7} sec^{-1}), and by low pressure. E_1's well-organized nature is further indicated by the divergence-convergence couplet, both of order 10^{-3} sec^{-1}. On the other hand, vorticity has no apparent relationship to the storm. Vorticity centers develop near other storm-related features, but don't conserve their relationships in time. A broad pressure ridge now extends beneath the echo which is raining at rates exceeding 2 inches hr^{-1}. The storm's fast movement (48 kt) limits precipitation accumulations to less than two inches.

Storm E_1 progresses northeastward and carries described features with it, indicating (1) the storm's quasi-steadiness, (2) an 11-km spaced station network's ability to detect thunderstorm's salient attributes, and (3) the analysis technique's ability to resolve them. Changes in quasi-steady features do occur from time to time. For example, by 2250 E_1's rain rate is over 4 inches hr^{-1}, pressure excess reaches 2 mb, and downdraft air (now θ_w = 15C) spreads over all but the southeast area. Surface air rises into E_1 and E_2 along a boundary (pseudo front) which is clearly indicated by closely spaced θ_w isotherms and a moisture convergence band in confluent (relative) flow--the line along which winds converge. This front has many characteristics of the thunderstorm "gust front" (Charba, 1972) except that it doesn't propagate away from the storms. One different factor in Charba's study is the upper air flow; in his case mean flow was more westerly (262° at 10 m sec^{-1} versus 208° at 32 m sec^{-1} this case).

Reed et al. (page 171) compute average rain rate 1.6 cm hr^{-1} for E_2. From surrounding soundings they find E_2's vapor influx is 2.8 cm (gm) hr^{-1}. Precipitation efficiency computes to 57 percent, a value close to estimates by other investigators of Great Plains thunderstorms.

By 0000, moisture divergence prevails again, θ_w isotherms extend generally west-east and pressure distribution flattens between exiting E2 and oncoming Storm F.

Storm F's tornadic updraft, the evening's first (0020), exhibits cyclonic wind pattern in the "sink" area and significant vorticity (10^{-3} sec^{-1}) that conserves its identity, although diminishing. Large and deep mesolow pressure (-3 mb) advances ahead of the "sink," accelerating surface air into the "sink." A θ_w gradient becomes established in the west behind F's trailing pseudo front. Downdraft air passes mostly northwest of the network as does the heaviest rain. Moisture converges into the mesocyclone, along the pseudo front and beneath the rainy downdraft. Ellrod (1973) computes F's precipitation efficiency at 62 percent which compares nicely with the 57 percent computed for Storm E2. Storm F moves rapidly out of the area, and by 0050 winds in the west turn toward the largest, most destructive storm of the night, Storm G.

Behind G's pseudo front westerly winds, spreading over the entire network area, gust in excess of 50 kt partly in response to strong pressure gradient (3 mb/10 km) all along the front. This front's leading edge is several kilometers ahead of the precipitation echo at the surface, and it possesses Charba's "gust front" characteristics: wind shift and pressure rise precede peak gust and temperature drop; a thin line radar echo precedes the main precipitation echo.

Flow relative to Storm G enters from the northeast, but now deflects toward the south rather than west as in earlier storms. Moisture convergence is maximum behind G's mesocyclonic "sink" and covers the heavy rain area as far south as the developing tornadic cell on G's flank (near 5A at 0110). The tornadic cell rapidly sweeps the gust front northeastward (0140). Far behind G's stormy front, moisture convergence continues even in areas of relatively light precipitation (<0.25 inch hr^{-1}).

Wet-bulb potential temperature. Isotherms 0.5C; printed values 0.1C.	Surface wind relative to storm (knots). Moisture divergence centers (10^{-7} sec^{-1}) are boldly numbered. Relative maxima are underlined; convergence areas are shaded.	Kinematic divergence. Isopleths 50 x 10^{-5} sec^{-1}; printed values 10^{-5} sec^{-1}.
Pressure perturbation (from 8-hr trend). Isobars 0.5 mb; printed values 0.1 mb.	Radar echo: hand-contoured digital reflectivity data (coded; see Table 4). Data inside 20 n mile range suppressed due to ground clutter and fall-off in sensitivity time control (STC) calibration curve.	Surface wind (knots). Streamlines and isotachs are drawn by computer plotter.
Accumulated rainfall (by storm). Isohyets 0.5 inches; printed values 0.01 inches.	Rain rate calculated for previous 5-min period. Isopleths 0.5 inches hr^{-1}; printed values 0.001 inches hr^{-1}.	Relative vorticity about vertical axis. Isopleths 50 x 10^{-5} sec^{-1}; printed values 10^{-5} sec^{-1}.

TIME (CST)

Figure 12. Schematic map layout, parameter identifications and units. Illustrations are identified by time at lower left.

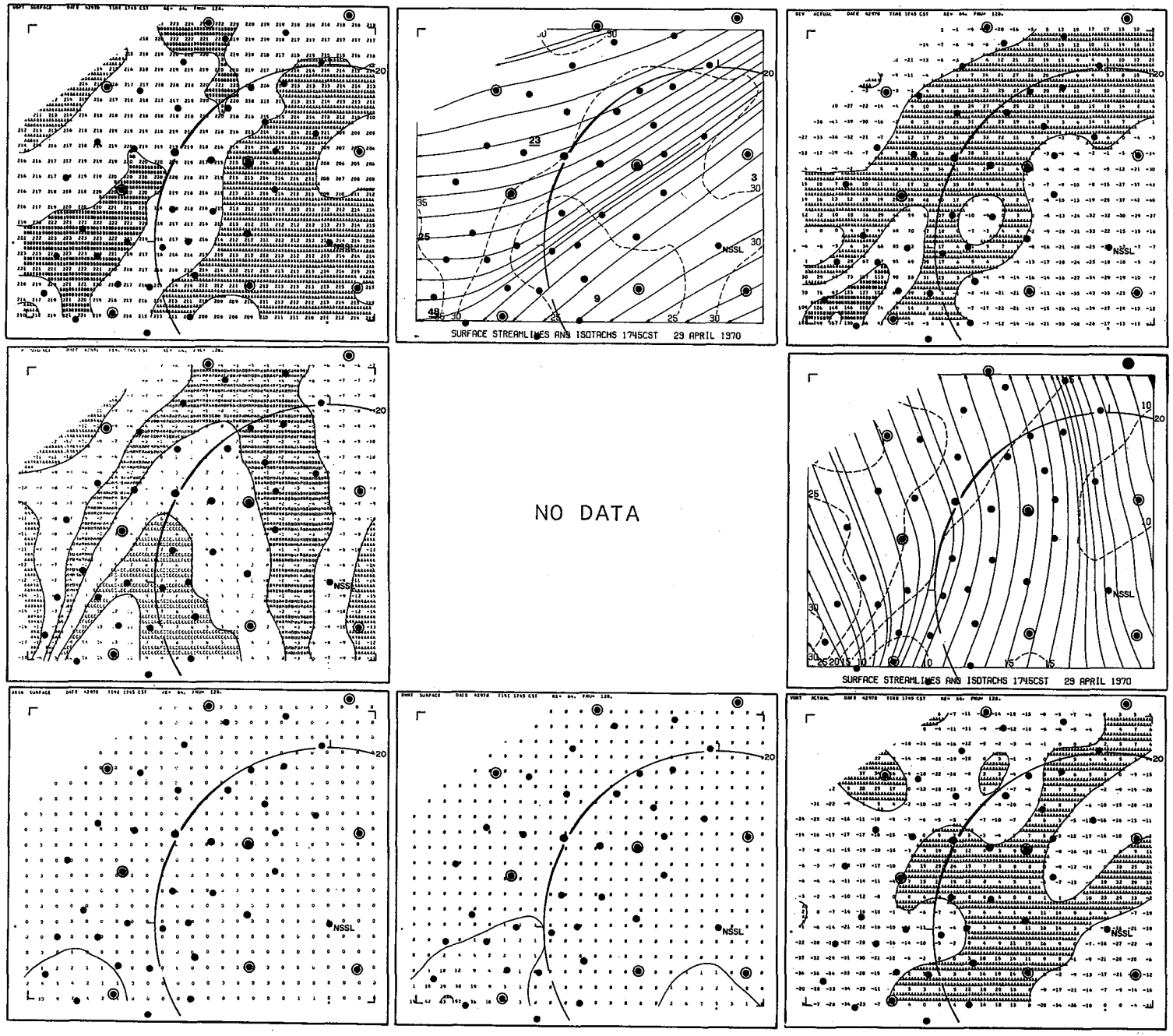
SURFACE STREAMLINES AND ISOTACHS 1745CST 29 APRIL 1970
NO DATA
NSSL
1745

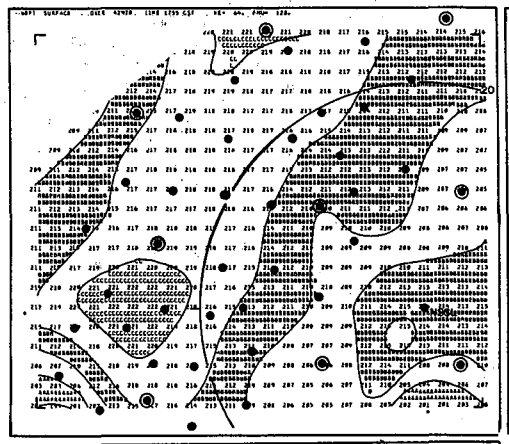

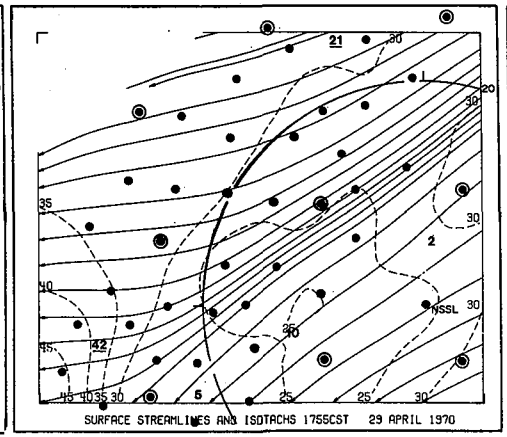
SURFACE STREAMLINES AND ISOTACHS 1755CST 29 APRIL 1970

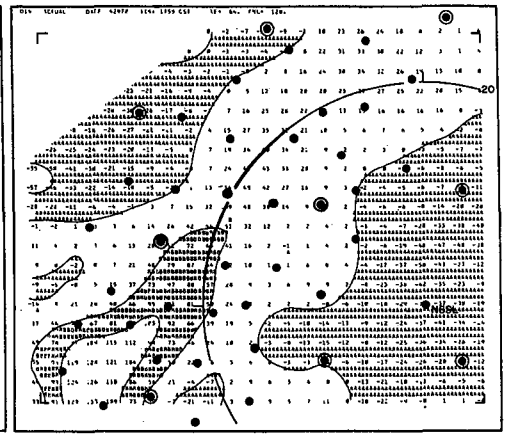

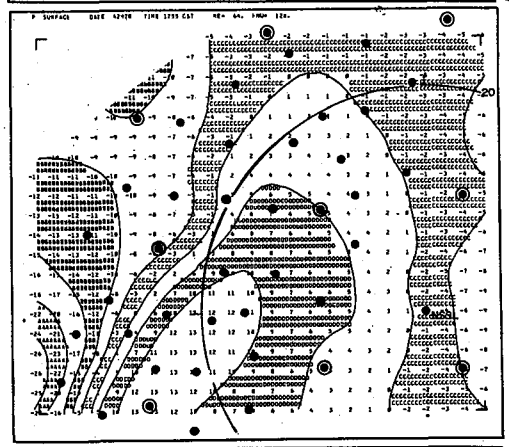

NO DATA

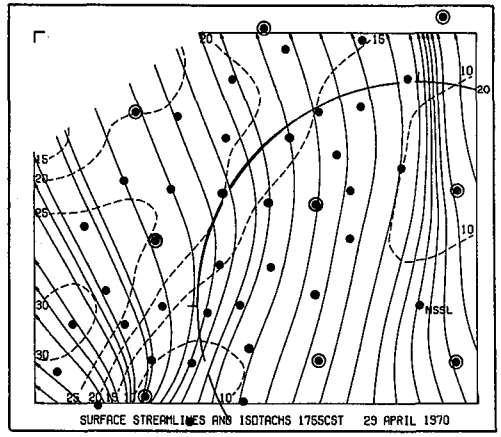
SURFACE STREAMLINES AND ISOTACHS 1755CST 29 APRIL 1970

1755

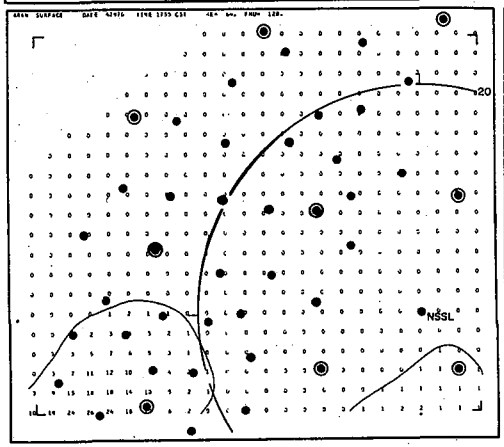

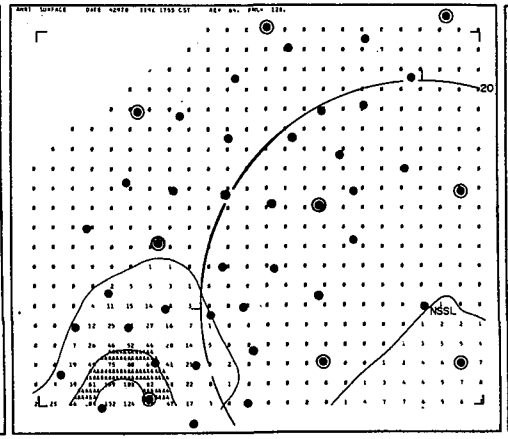

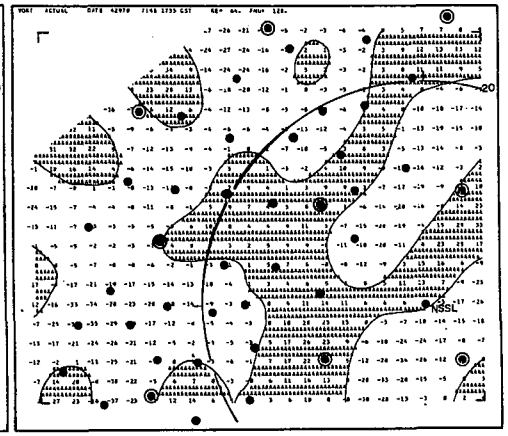

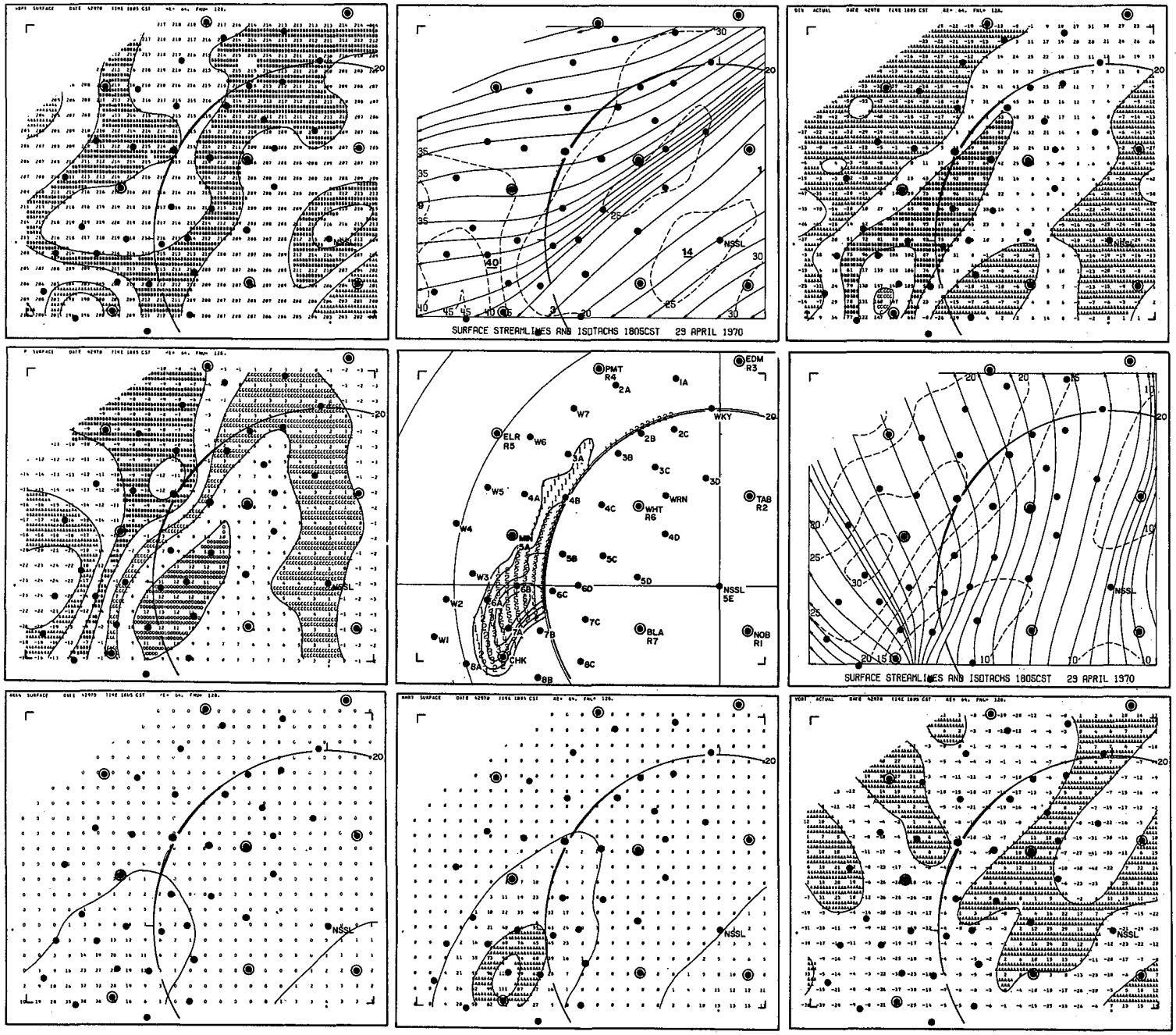
SURFACE STREAMLINES AND ISOTACHS 1805CST 29 APRIL 1970
SURFACE STREAMLINES AND ISOTACHS 1805CST 29 APRIL 1970
NSSL
PMT R4
EDM R3
ELR R5
WKY
WHT R6
WRN
TAB R2
NSSL 5E
BLA R7
NOB R1
CHK

1805

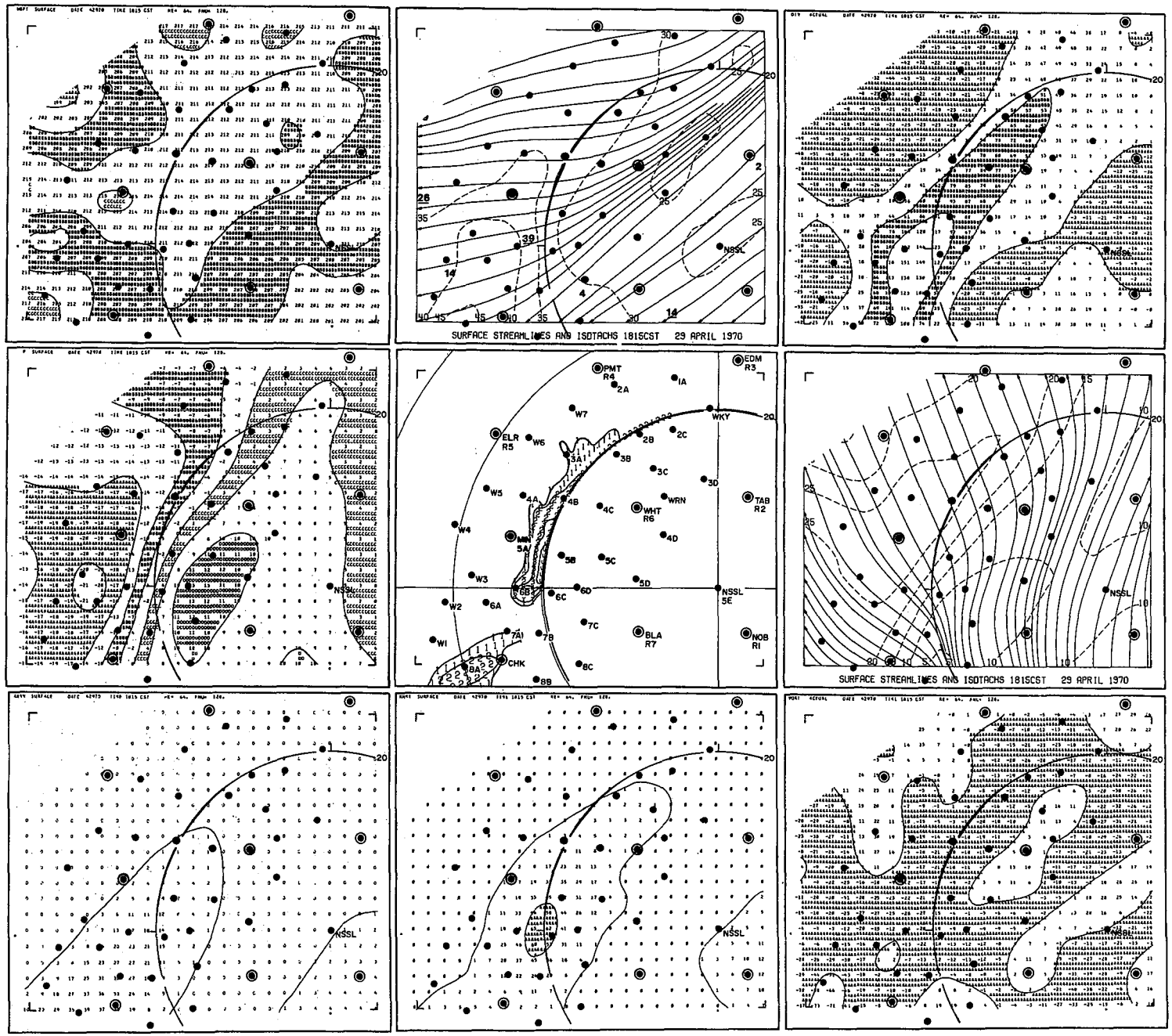
SURFACE STREAMLINES AND ISOTACHS 1815CST 29 APRIL 1970
SURFACE STREAMLINES AND ISOTACHS 1815CST 29 APRIL 1970
NSSL
PMT R4
2A
1A
W7
ELR R5
W6
WKY
2B
2C
3A
3B
3C
3D
W5
4A
4B
4C
WRN
WHT R6
TAB R2
W4
MW 5A
4D
5B
5C
W3
5D
NSSL 5E
W2
6A
6B
6C
6D
7C
BLA R7
NOB R1
W1
7A
7B
CHK
8A
8B
8C
EDM R3

1815

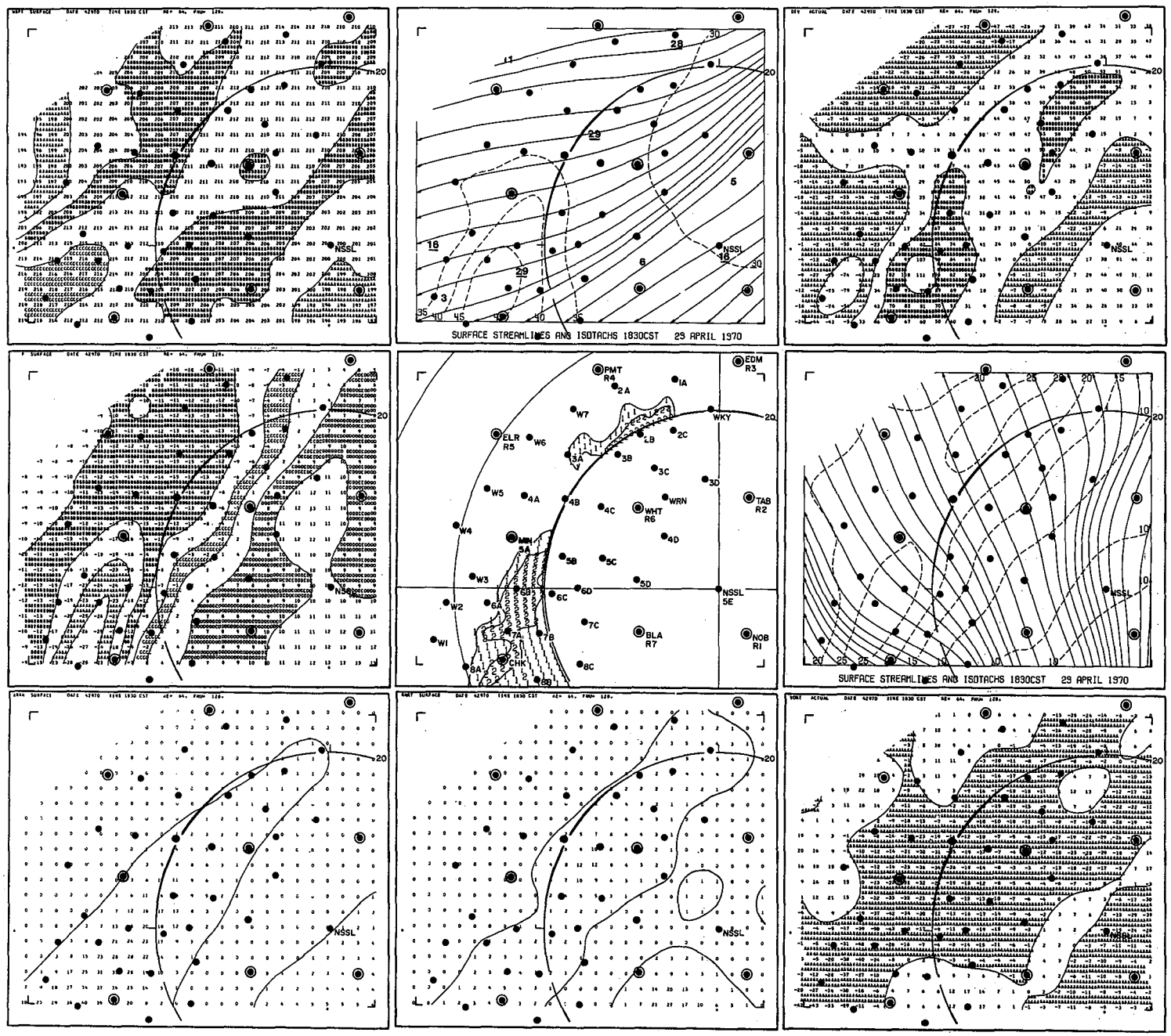
SURFACE STREAMLINES AND ISOTACHS 1830CST 29 APRIL 1970
SURFACE STREAMLINES AND ISOTACHS 1830CST 29 APRIL 1970
NSSL
PMT R4
EDM R3
ELR R5
WKY
TAB R2
WHT R6
NSSL 5E
BLA R7
NOB R1
CHK

1830

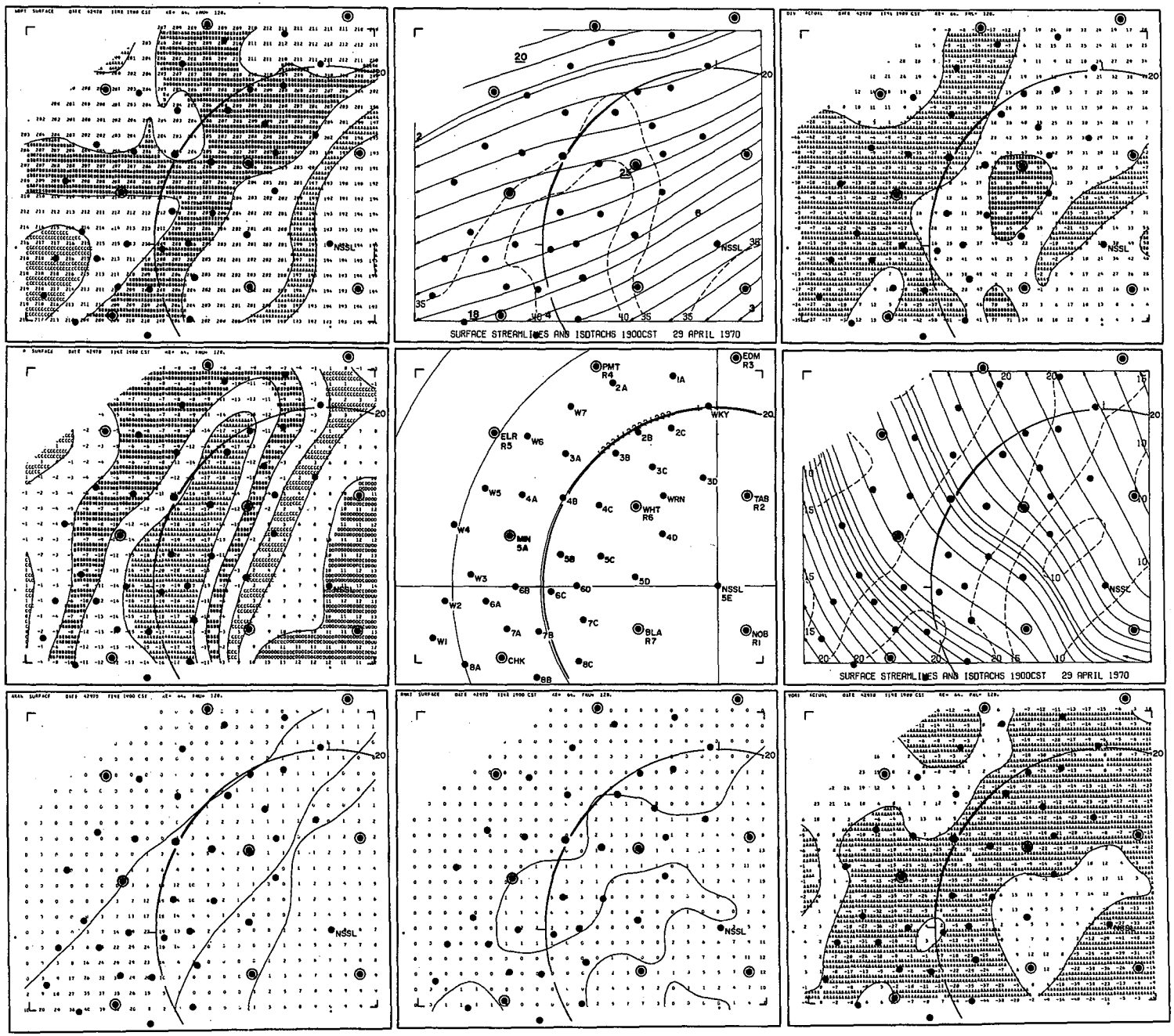
SURFACE STREAMLINES AND ISOTACHS 1900CST 29 APRIL 1970
SURFACE STREAMLINES AND ISOTACHS 1900CST 29 APRIL 1970
NSSL
PMT R4
EDM R3
ELR R5
WKY
TAB R2
WHT R6
MIN 5A
NSSL 5E
BLA R7
NOB R1
CHK

1900

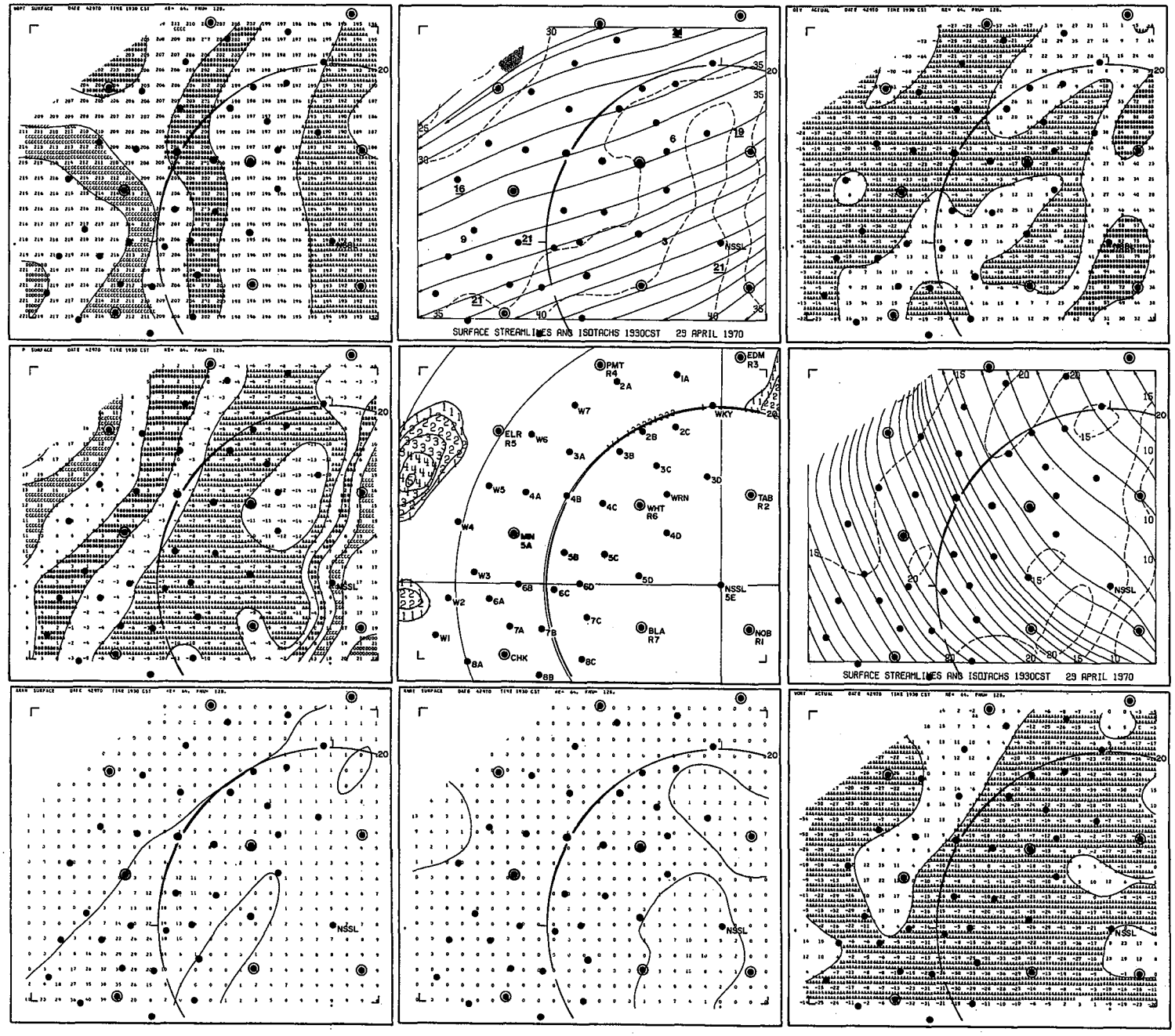
SURFACE STREAMLINES AND ISOTACHS 1930CST 29 APRIL 1970
SURFACE STREAMLINES AND ISOTACHS 1930CST 29 APRIL 1970
NSSL
PMT R4
EDM R3
ELR R5
WKY
TAB R2
WHT R6
MIN 5A
NSSL 5E
BLA R7
NOB R1
CHK

1930

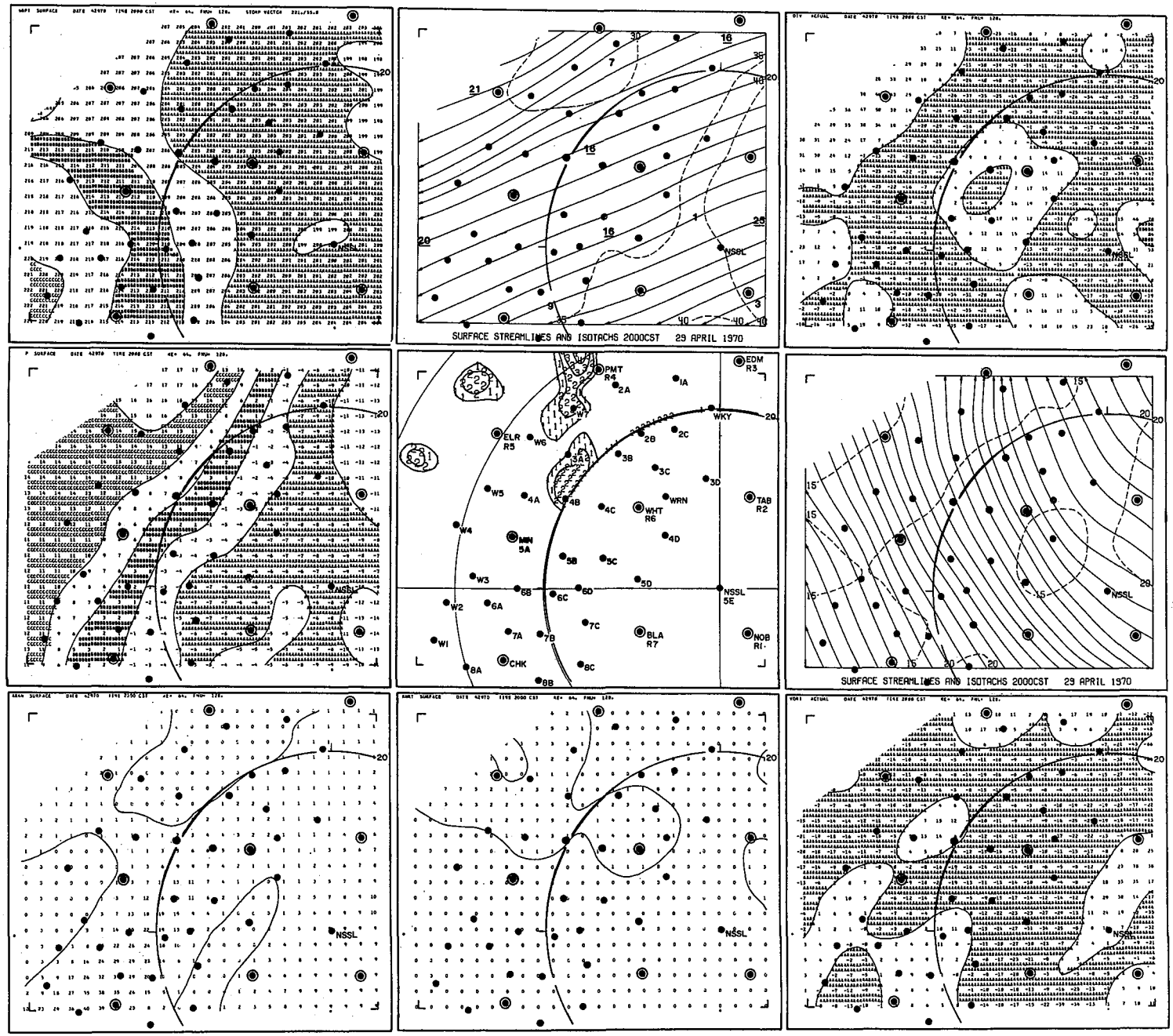
SURFACE STREAMLINES AND ISOTACHS 2000CST 29 APRIL 1970
SURFACE STREAMLINES AND ISOTACHS 2000CST 29 APRIL 1970
NSSL
PMT R4
EDM R3
ELR R5
WKY
TAB R2
WHT R6
MIN 5A
NSSL 5E
BLA R7
NOB
CHK

2000

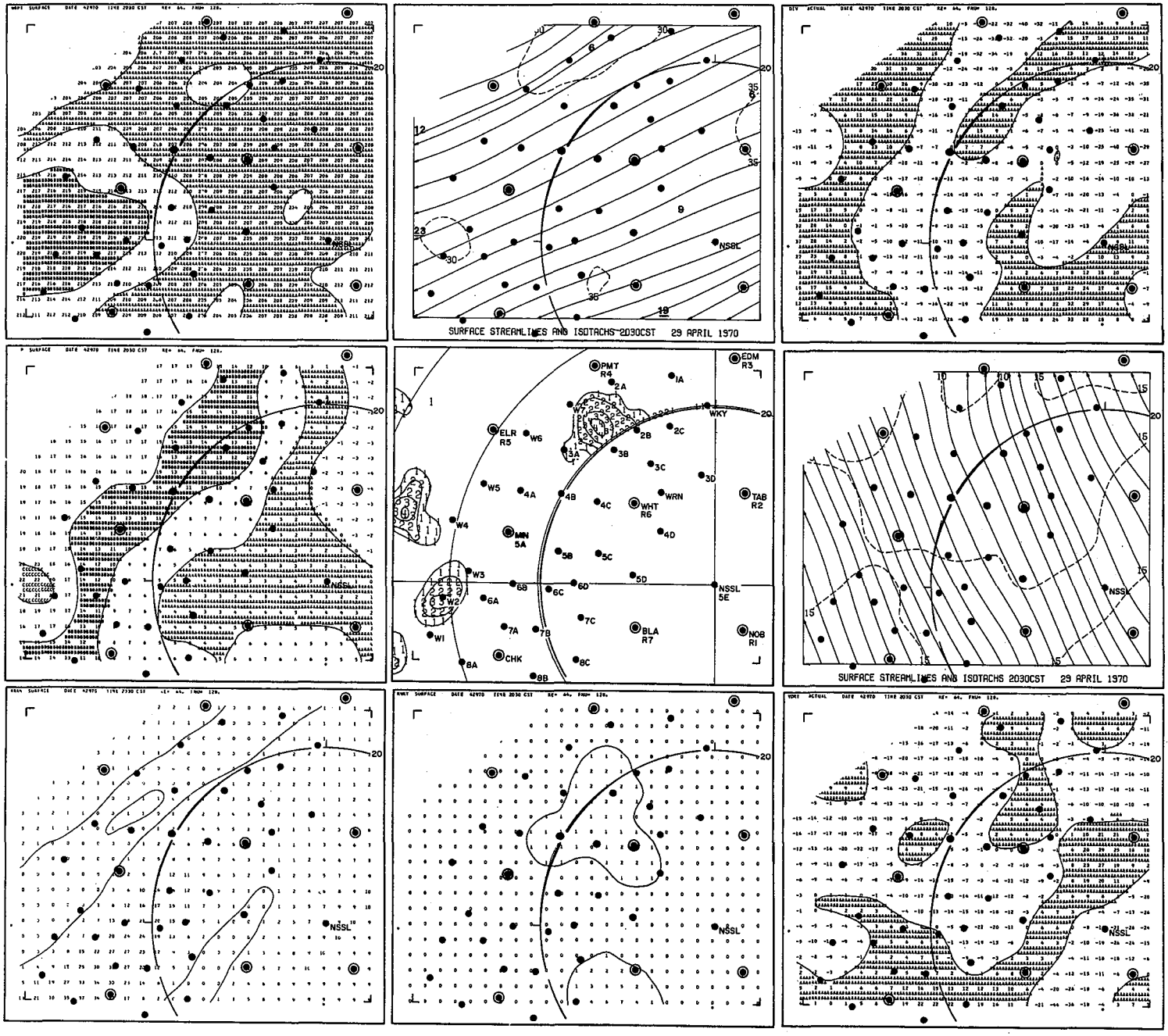
SURFACE STREAMLINES AND ISOTACHS 2030CST 29 APRIL 1970
SURFACE STREAMLINES AND ISOTACHS 2030CST 29 APRIL 1970
NSSL
PMT R4
EDM R3
WKY
ELR R5
TAB R2
WHT R6
MIN 5A
NSSL 5E
BLA R7
NOB RI
CHK

2030

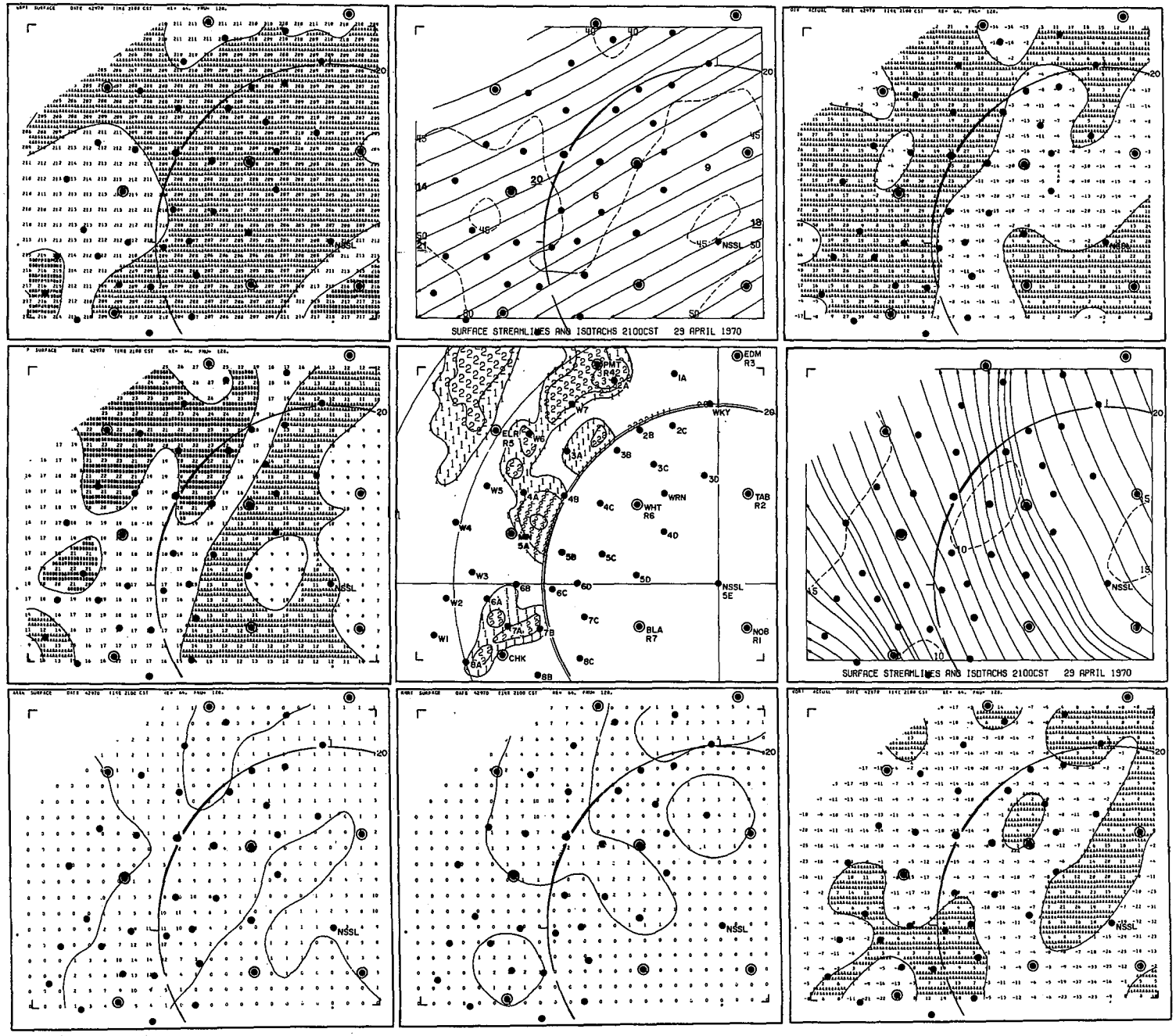
SURFACE STREAMLINES AND ISOTACHS 2100CST 29 APRIL 1970
SURFACE STREAMLINES AND ISOTACHS 2100CST 29 APRIL 1970
NSSL
EDM R3
TAB R2
NSSL 5E
NOB R1
BLA R7
WHT R6
WRN
WKY
ELR R5
CHK
IA
W1
W2
W3
W4
W5
W6
W7
2A
2B
2C
3A
3B
3C
3D
4A
4B
4C
4D
5A
5B
5C
5D
6A
6B
6C
6D
7A
7B
7C
8A
8B
8C

2100

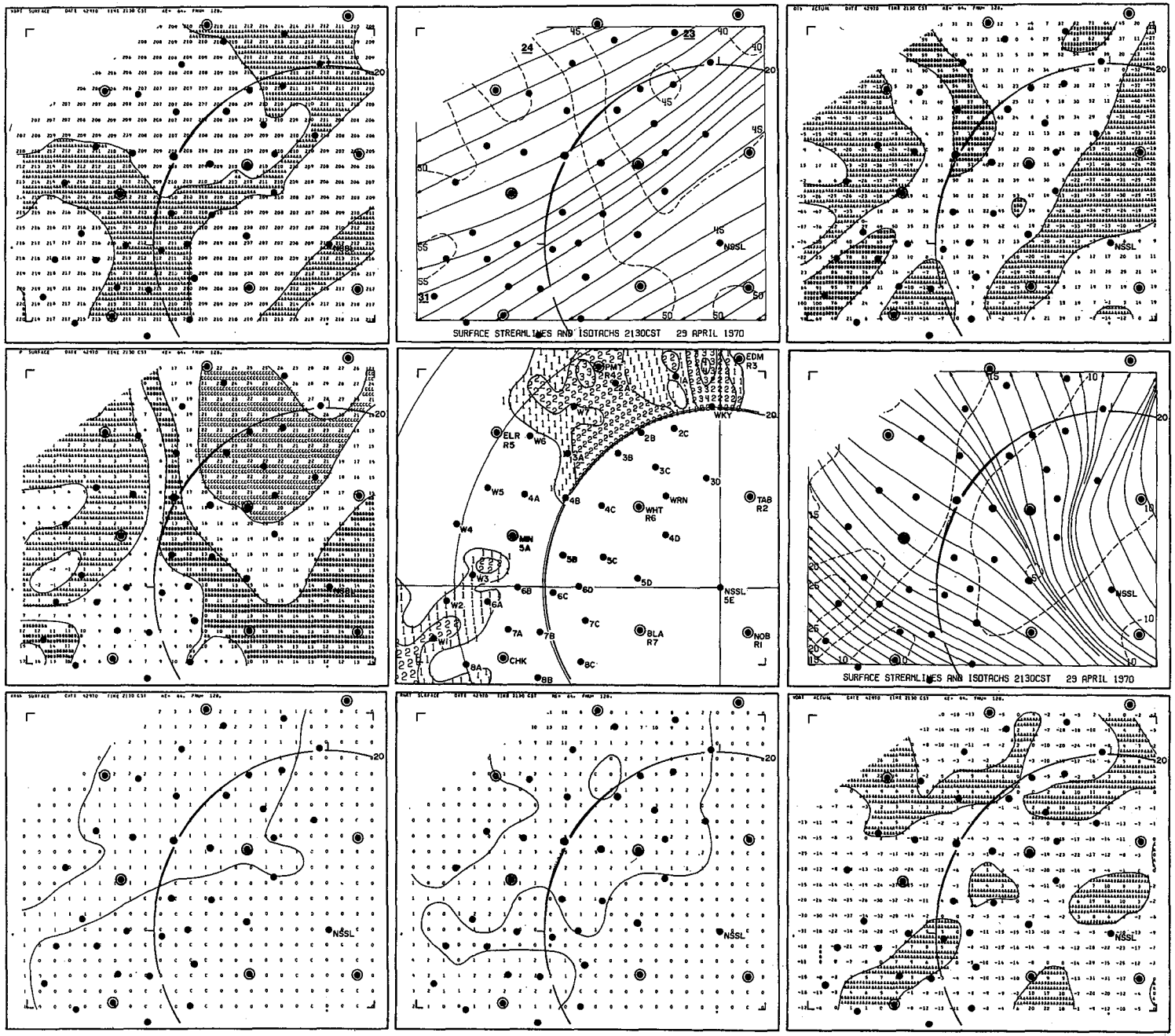
SURFACE STREAMLINES AND ISOTACHS 2130CST 29 APRIL 1970
SURFACE STREAMLINES AND ISOTACHS 2130CST 29 APRIL 1970
NSSL
EDM R3
WKY
ELR R5
WHT R6
TAB R2
NSSL 5E
BLA R7
NOB R1
CHK

2130

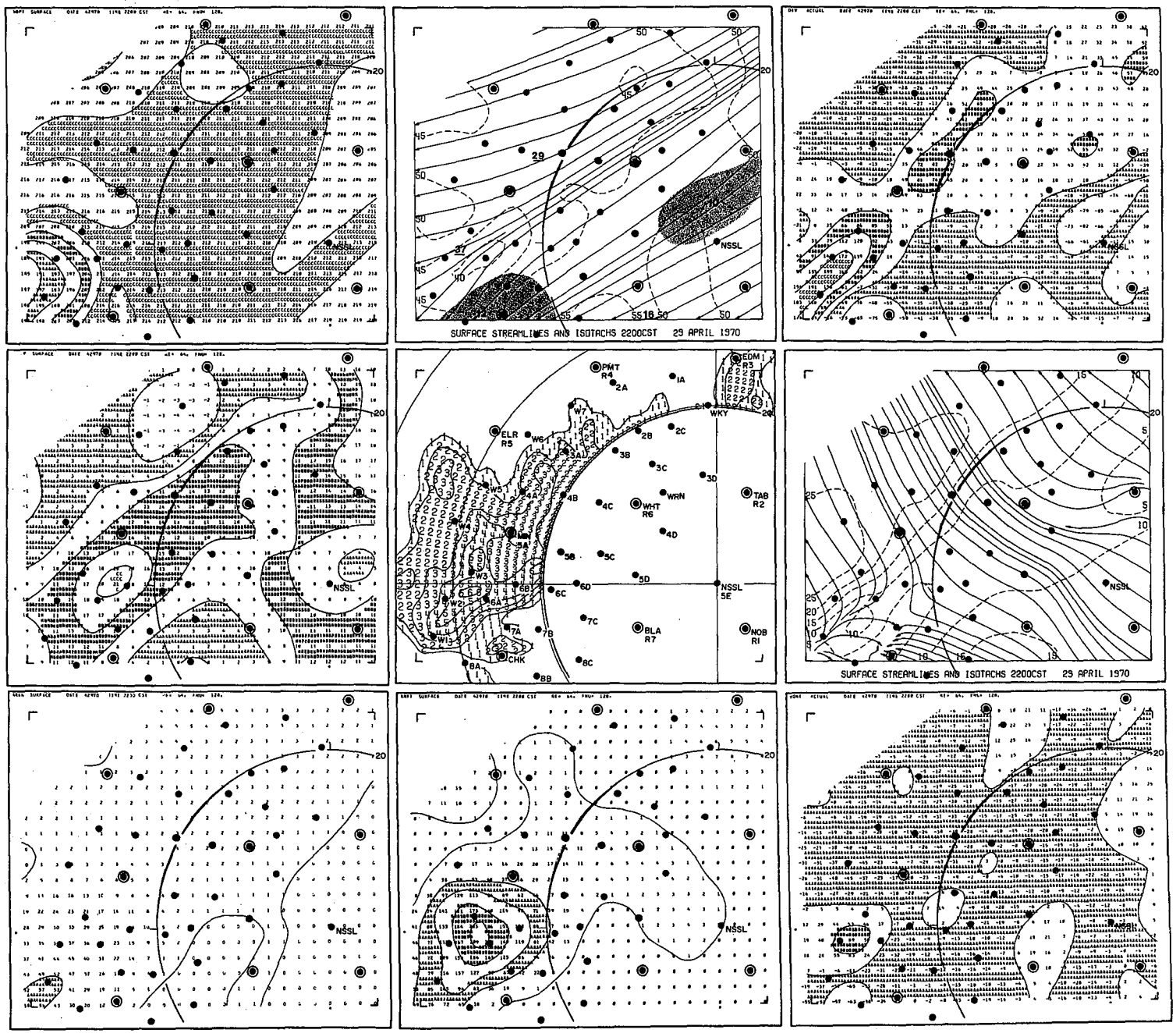
SURFACE STREAMLINES AND ISOTACHS 2200CST 29 APRIL 1970
NSSL
PMT R4
2A
1A
ELR R5
WKY
2B
2C
3B
3C
3D
WRN
TAB R2
4B
4C
WHT R6
4D
5B
5C
5D
6C
6D
NSSL 5E
7C
BLA R7
NOB R1
7B
8C
8B
CHK
SURFACE STREAMLINES AND ISOTACHS 2200CST 29 APRIL 1970

2200

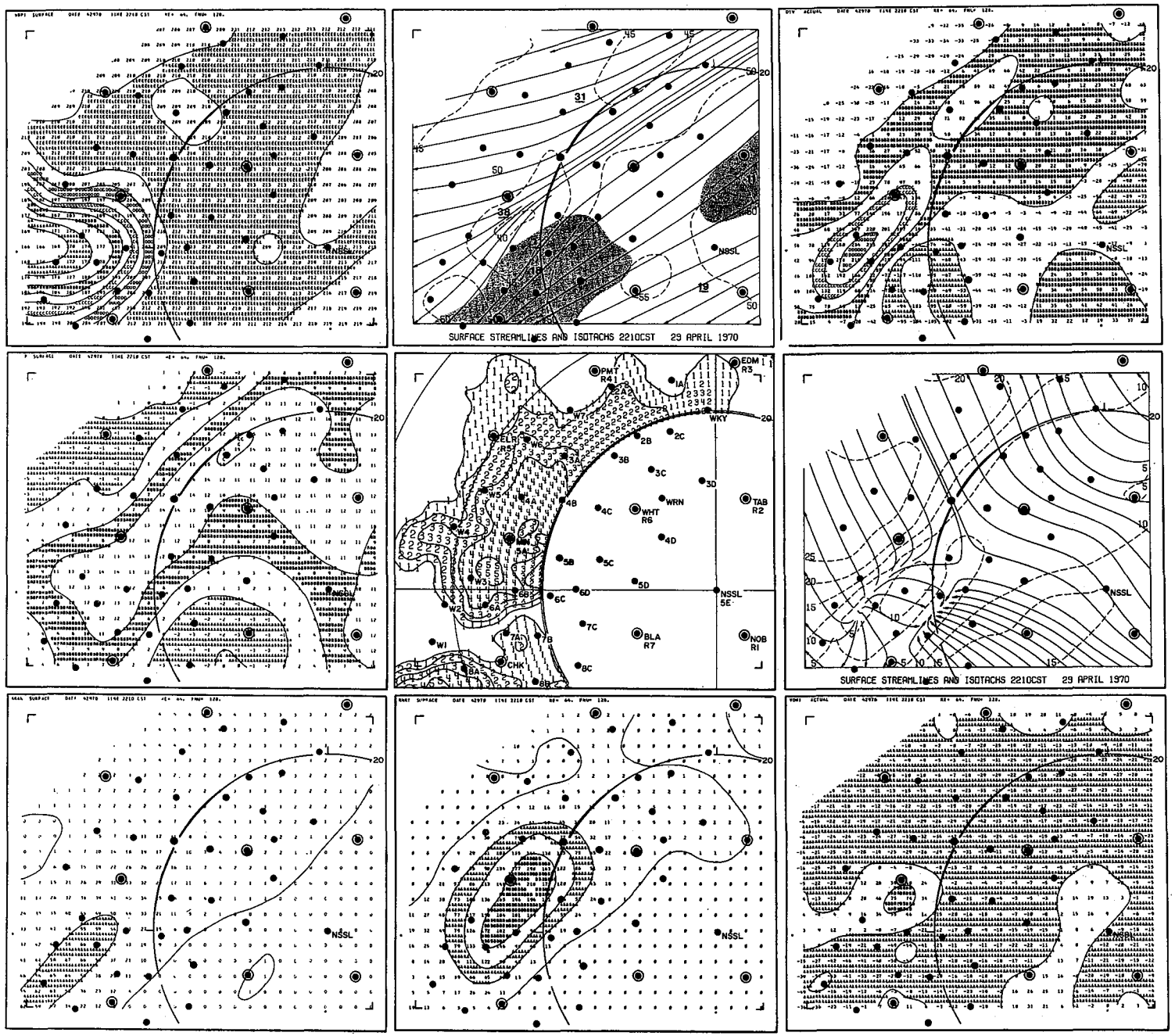
SURFACE STREAMLINES AND ISOTACHS 2210CST 29 APRIL 1970
SURFACE STREAMLINES AND ISOTACHS 2210CST 29 APRIL 1970
NSSL
PMT R4
EDM R3
WKY
ELR R5
WHT R6
WRN
TAB R2
NSSL 5E
BLA R7
NOB R1
CHK

2210

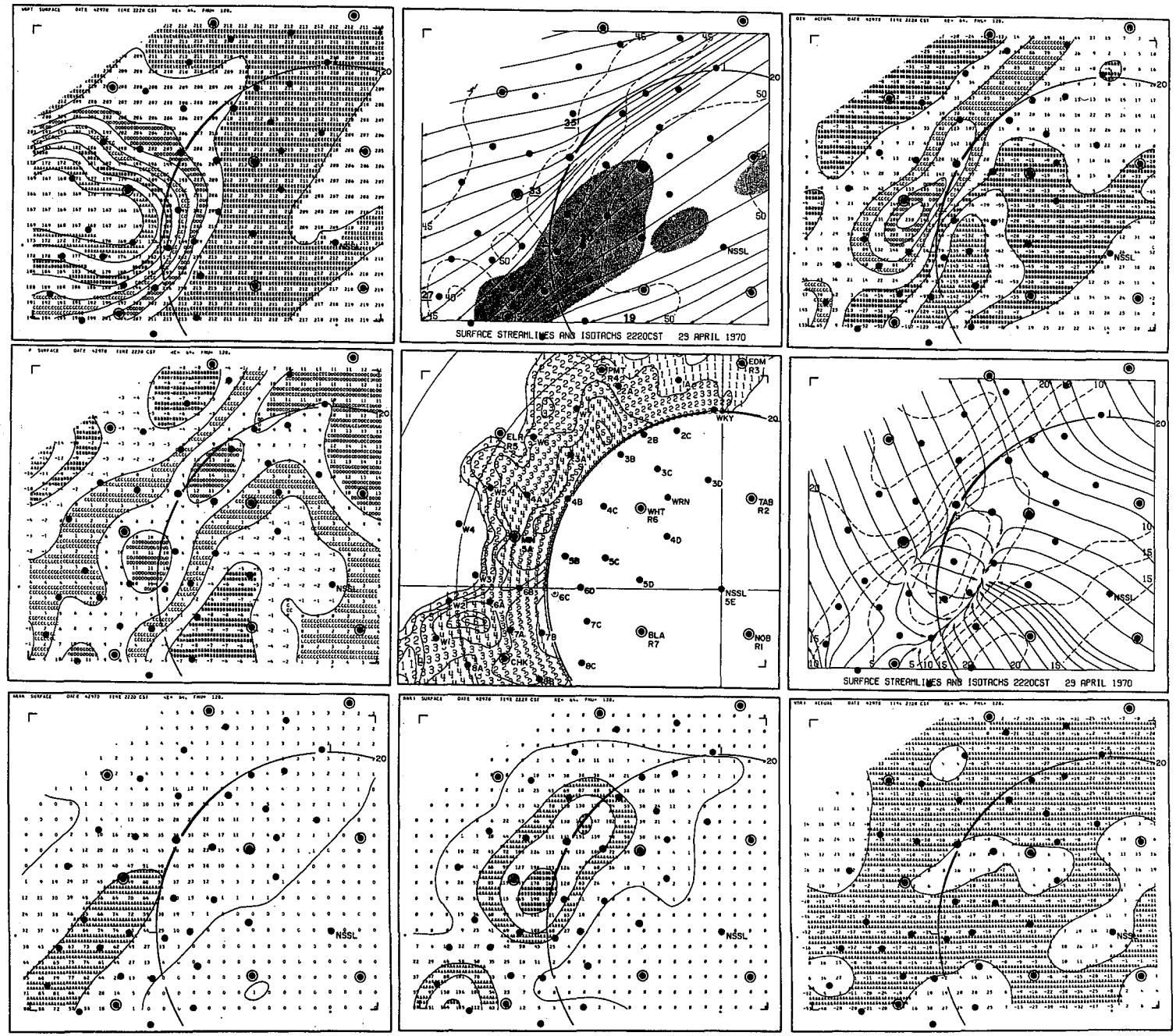
SURFACE STREAMLINES AND ISOTACHS 2220CST 29 APRIL 1970
SURFACE STREAMLINES AND ISOTACHS 2220CST 29 APRIL 1970
NSSL
EDM
R3
PHT
R4
ELR
R5
WKY
WRN
WHT
R6
TAB
R2
NSSL
5E
BLA
R7
NOB
R1
CHK

2220

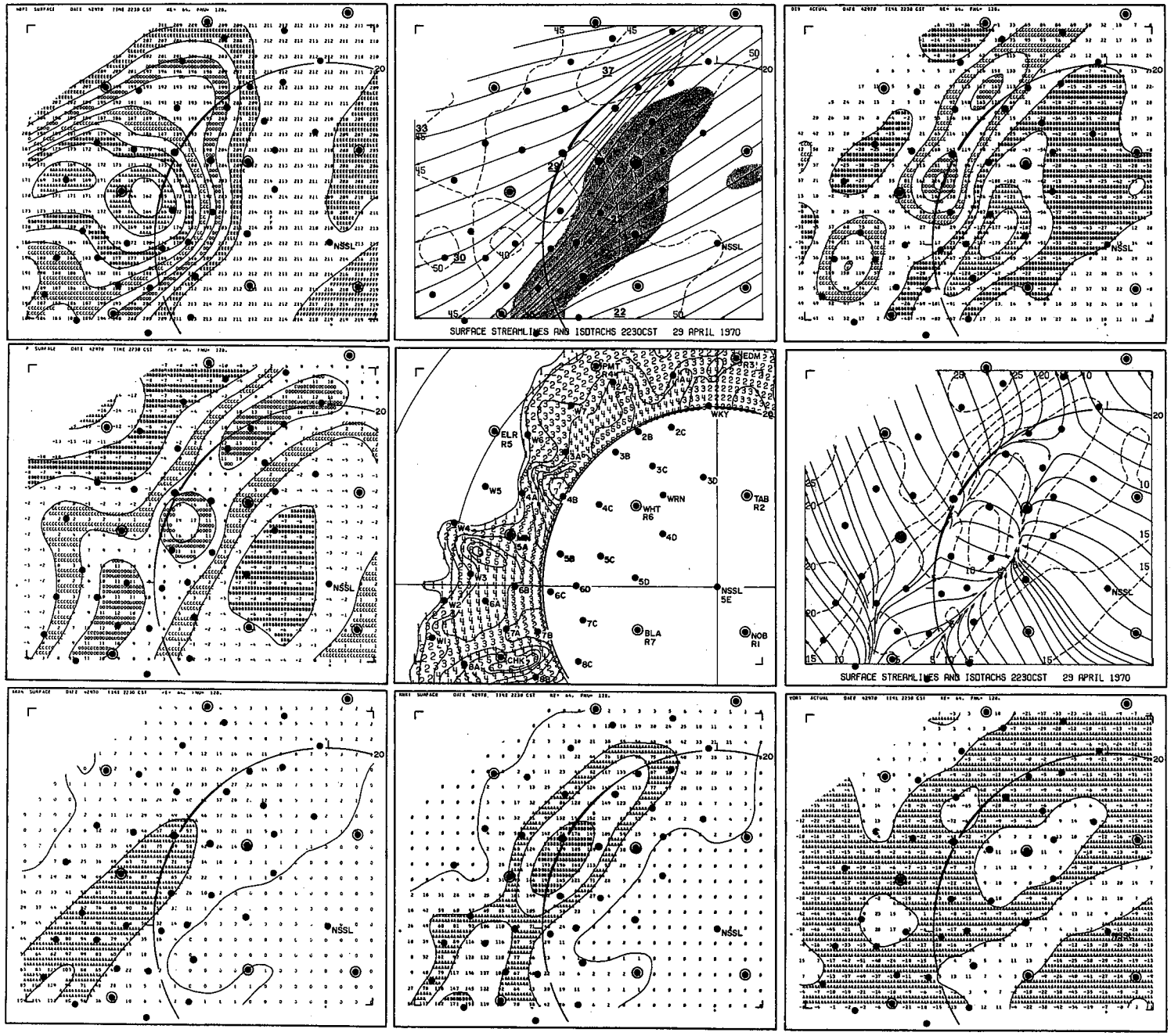
SURFACE STREAMLINES AND ISOTACHS 2230CST 29 APRIL 1970
SURFACE STREAMLINES AND ISOTACHS 2230CST 29 APRIL 1970
NSSL
ELR
R5
W8
W5
W4
W3
W2
W1
4A
4B
4C
WHT
R6
WRN
4D
TAB
R2
2B
2C
3B
3C
3D
5A
5B
5C
5D
6A
6B
6C
6D
7A
7B
7C
8A
8B
8C
BLA
R7
NSSL
5E
NOB
R1
PMT
EDM
WKY
CHK1

2230

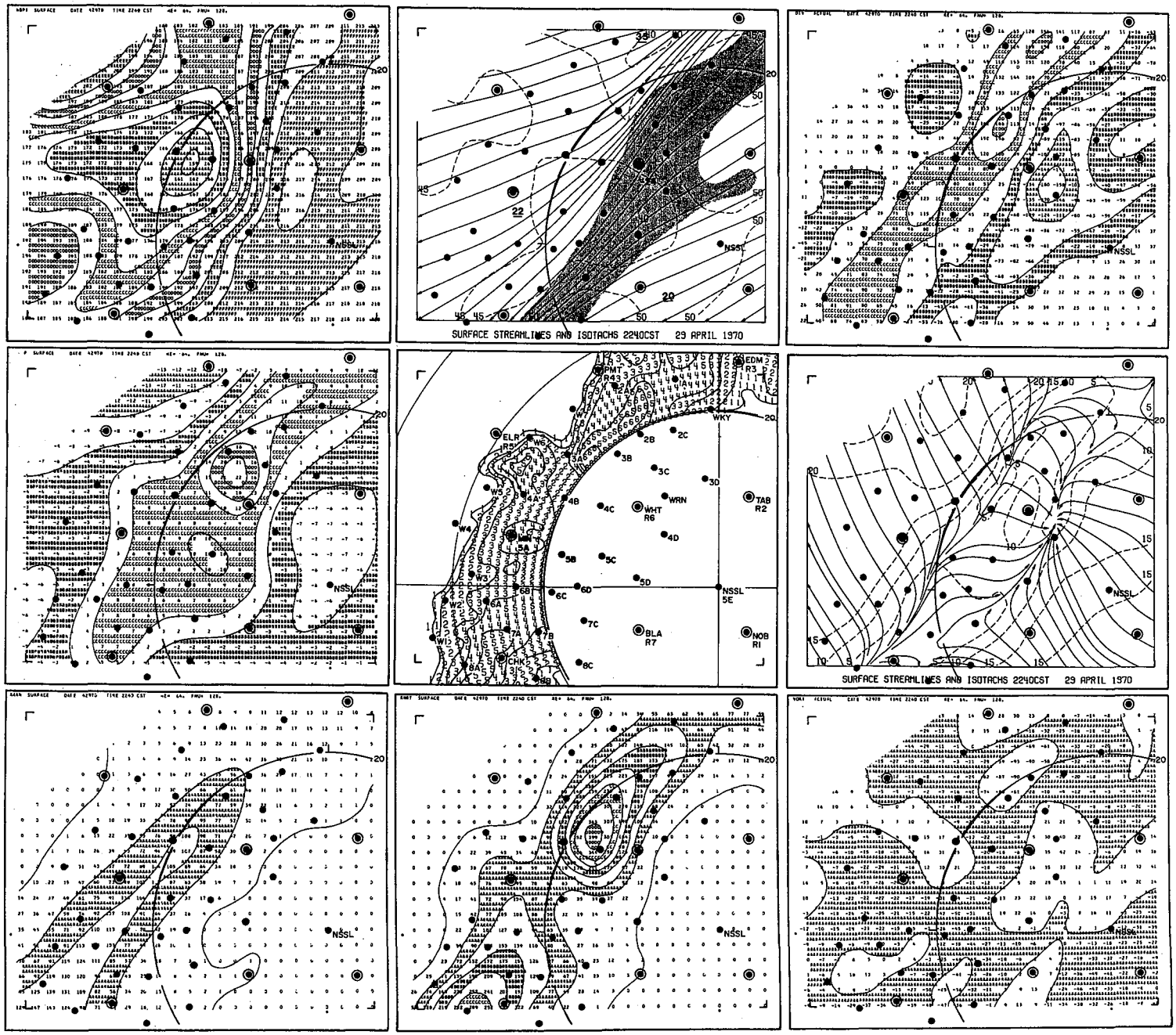
SURFACE STREAMLINES AND ISOTACHS 2240CST 29 APRIL 1970
NSSL
WKY
EDM
R3
PMT
R43
ELR
R5
2B
2C
3B
3C
3D
WRN
TAB
R2
WHT
R6
4B
4C
4D
5B
5C
5D
6C
6D
NSSL
5E
7C
BLA
R7
NOB
R1
8C
CHK
R8
W4
W5
W2
W3
SURFACE STREAMLINES AND ISOTACHS 2240CST 29 APRIL 1970

2240

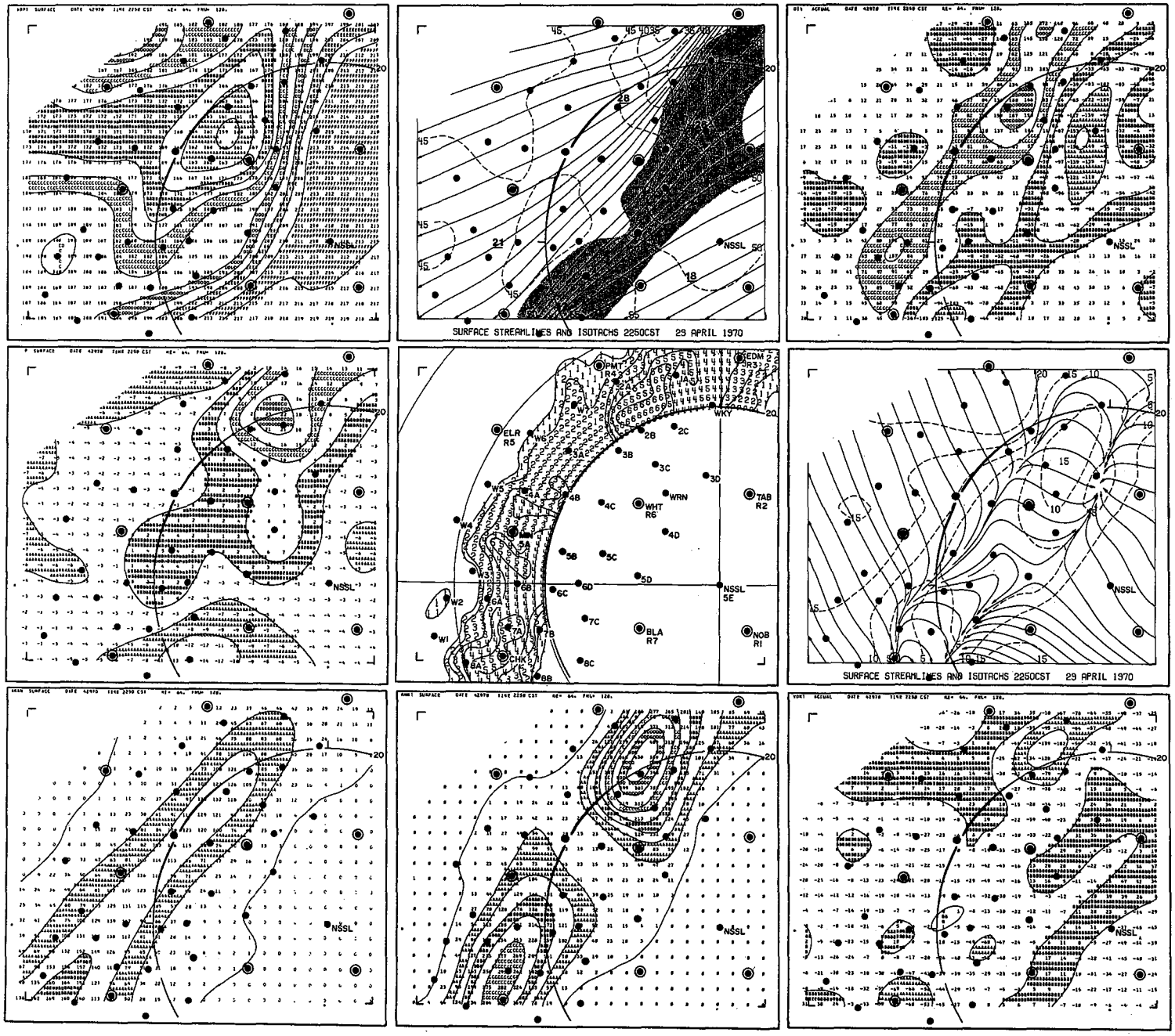
SURFACE STREAMLINES AND ISOTACHS 2250CST 29 APRIL 1970
SURFACE STREAMLINES AND ISOTACHS 2250CST 29 APRIL 1970
NSSL
ELR R5
WKY
TAB R2
WHT R6
WRN
BLA R7
NOB R1
NSSL 5E
EDM
PHT
CHK

2250

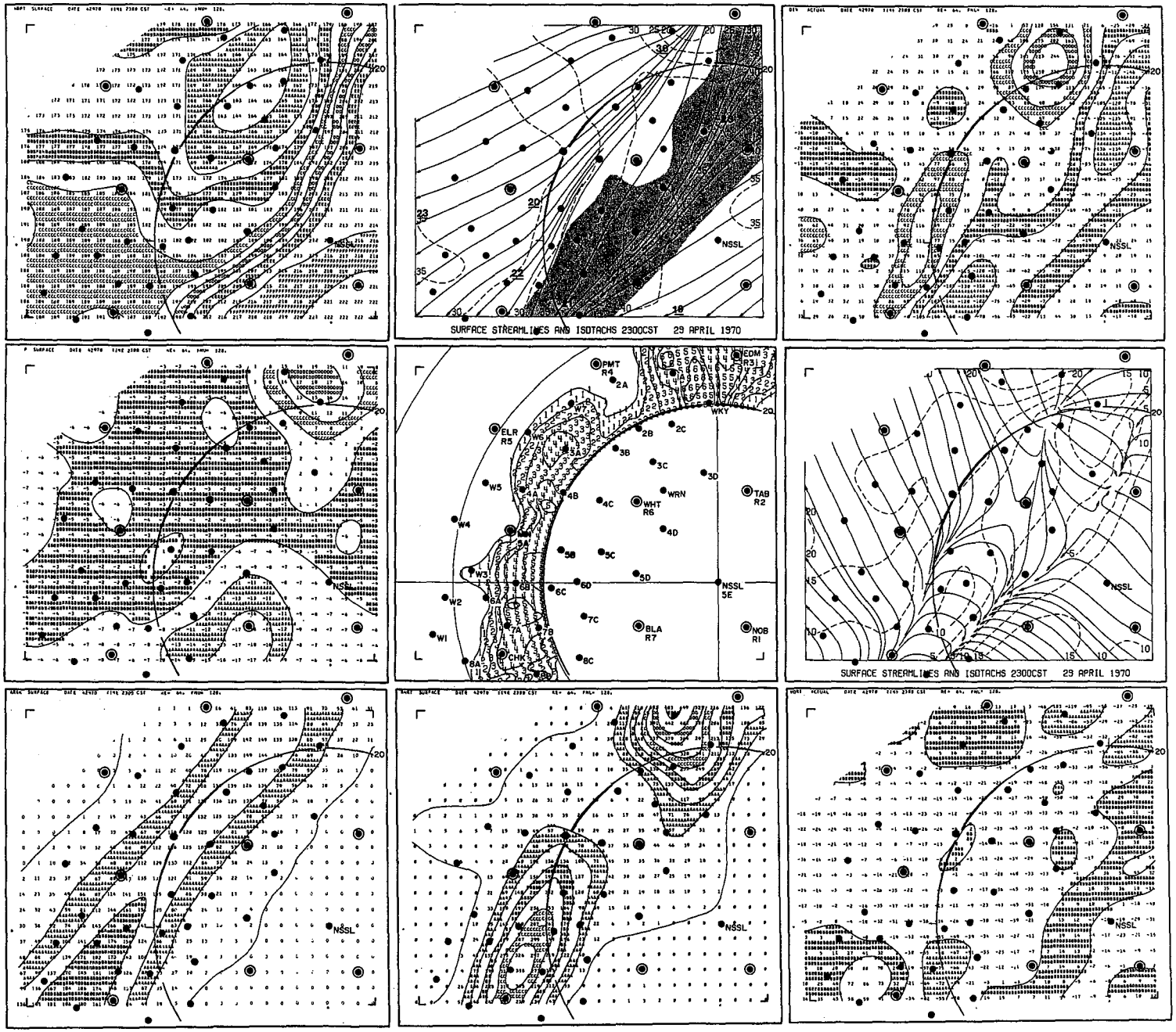
SURFACE STREAMLINES AND ISOTACHS 2300CST 29 APRIL 1970
SURFACE STREAMLINES AND ISOTACHS 2300CST 29 APRIL 1970
NSSL
PMT R4
ELR R5
WRN
WHT R6
TAB R2
BLA R7
NOB R1
CHK
WKY
EDM R3
2300

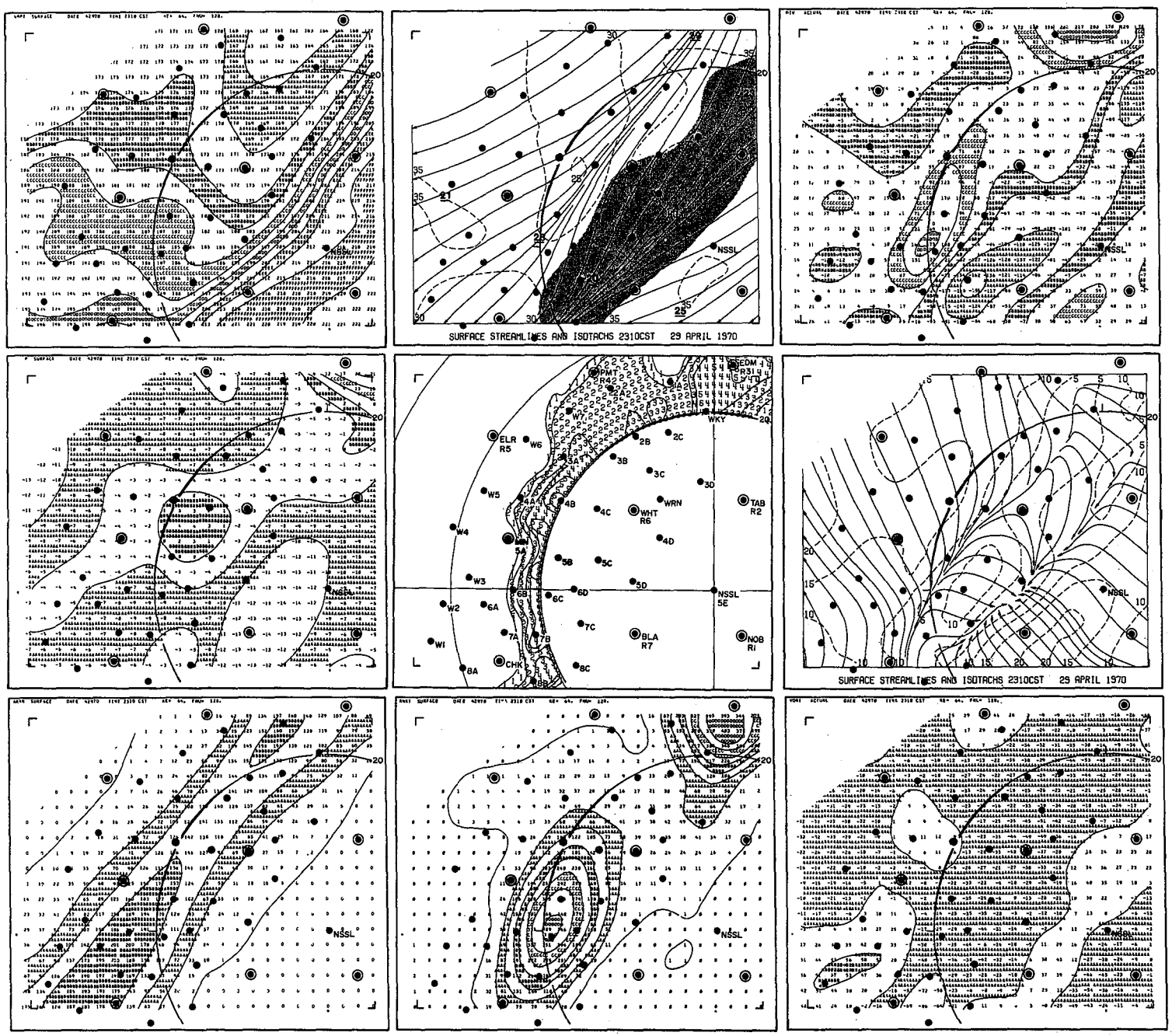
SURFACE STREAMLINES AND ISOTACHS 2310CST 29 APRIL 1970
SURFACE STREAMLINES AND ISOTACHS 2310CST 29 APRIL 1970
NSSL
ELR
R5
W6
W5
W4
W3
W2
W1
CHK
8A
8B
PM
R4
W7
EDM
WKY
2B
2C
3B
3C
3D
3A
4B
4C
WRN
WHT
R6
TAB
R2
4D
5A
5B
5C
5D
6B
6C
6D
6A
7A
7B
7C
8C
BLA
R7
NSSL
5E
NOB
R1

2310

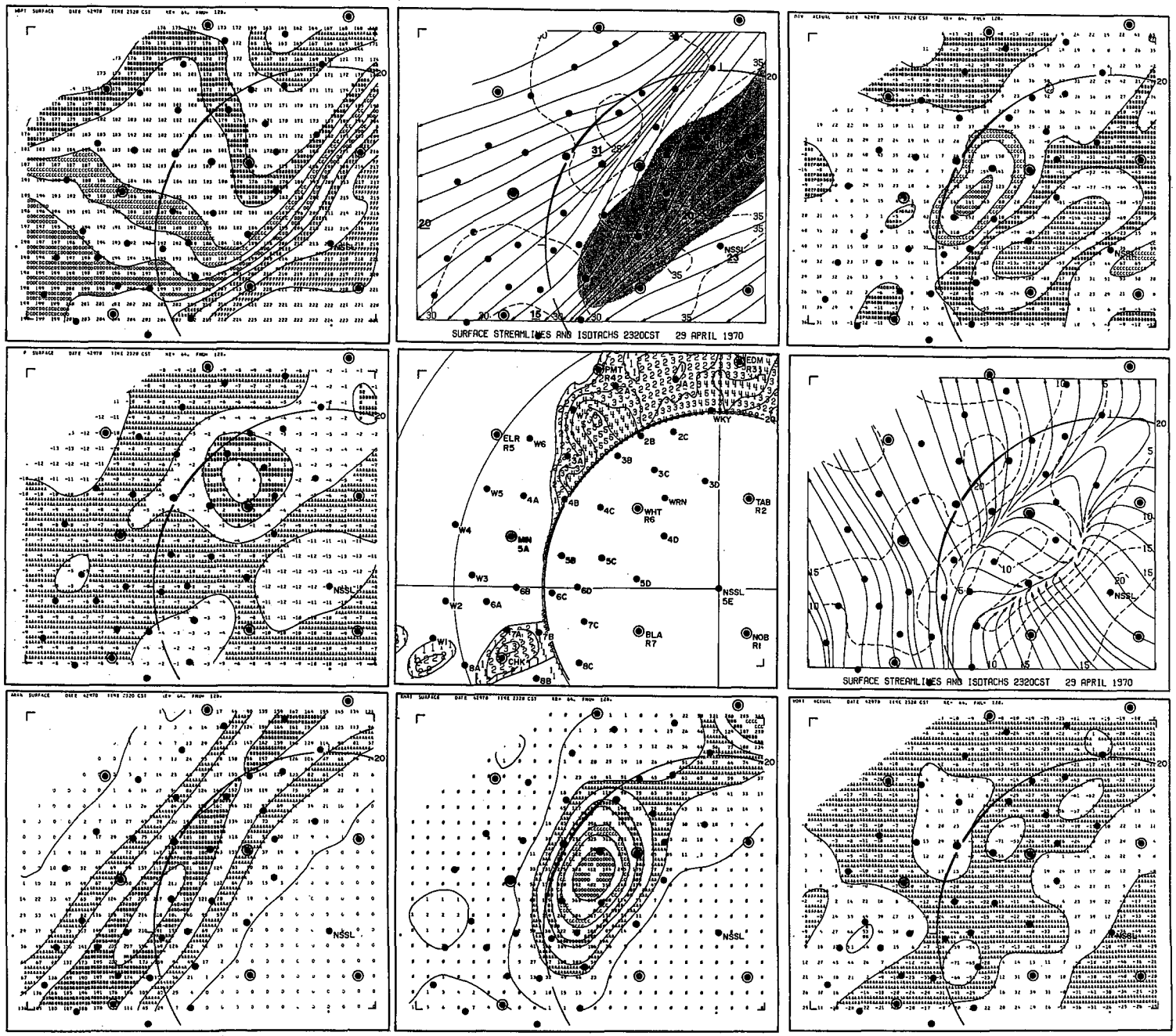
SURFACE STREAMLINES AND ISOTACHS 2320CST 29 APRIL 1970
SURFACE STREAMLINES AND ISOTACHS 2320CST 29 APRIL 1970
NSSL
ELR R5
W6
W5
4A
W4
MIN 5A
W3
W2
6A
6B
6C
6D
5A
5B
5C
5D
4B
4C
4D
3A
3B
3C
3D
2B
2C
WHT R6
WRN
TAB R2
WKY
NSSL 5E
BLA R7
NOB R1
7A
7B
7C
8A
8B
8C
CHK
W1
20
30
35
15
10
5

2320

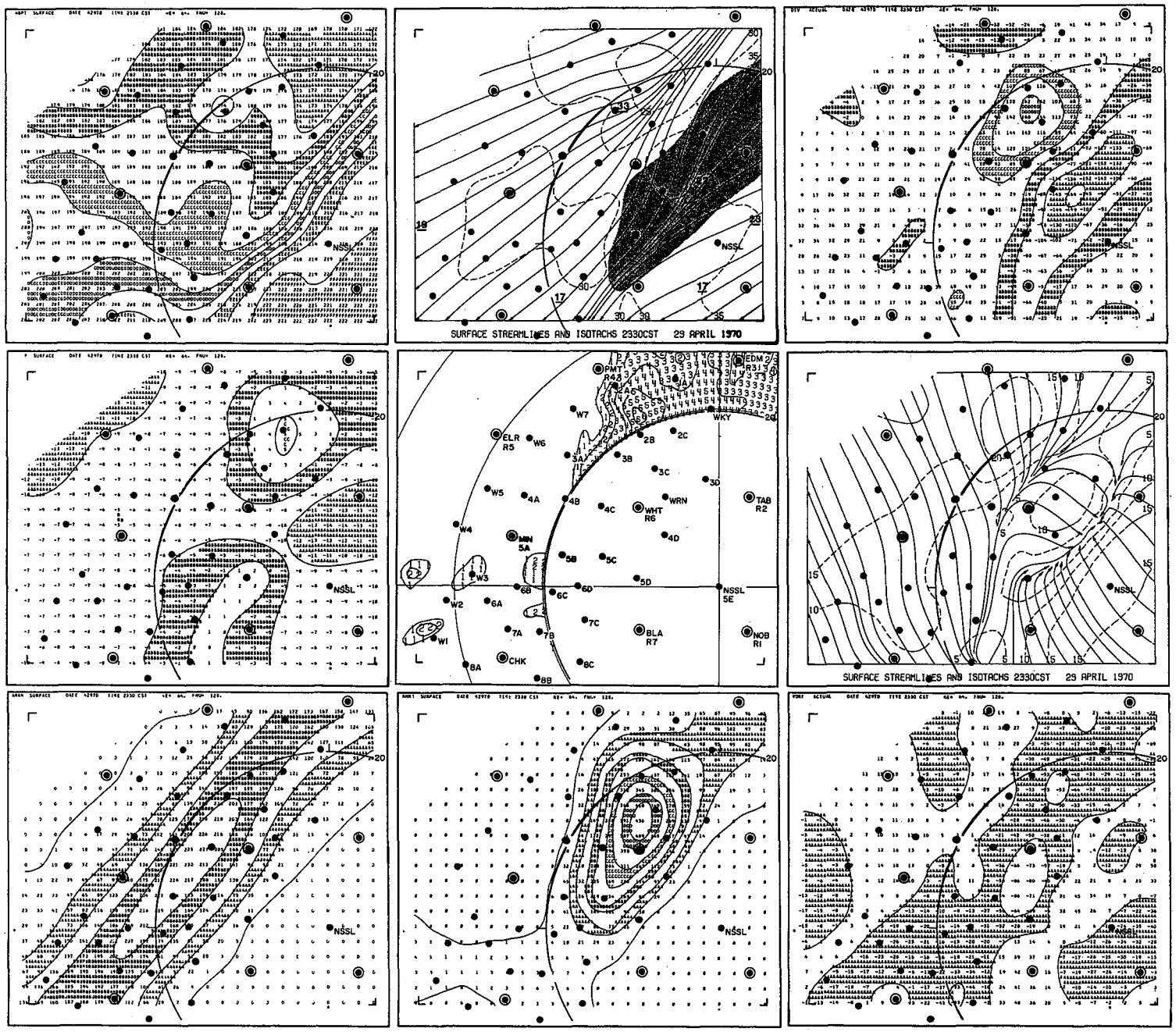
SURFACE STREAMLINES AND ISOTACHS 2330CST 29 APRIL 1970
SURFACE STREAMLINES AND ISOTACHS 2330CST 29 APRIL 1970
NSSL
ELR R5
W6
W7
PMT
EDM
WKY
2B
2C
3A
3B
3C
3D
W5
4A
4B
4C
WHT R6
WRN
TAB R2
W4
MIN 5A
4D
5B
5C
5D
W3
6B
6C
6D
NSSL 5E
W2
6A
7A
7B
7C
BLA R7
NOB R1
W1
CHK
8A
8B
8C

2330

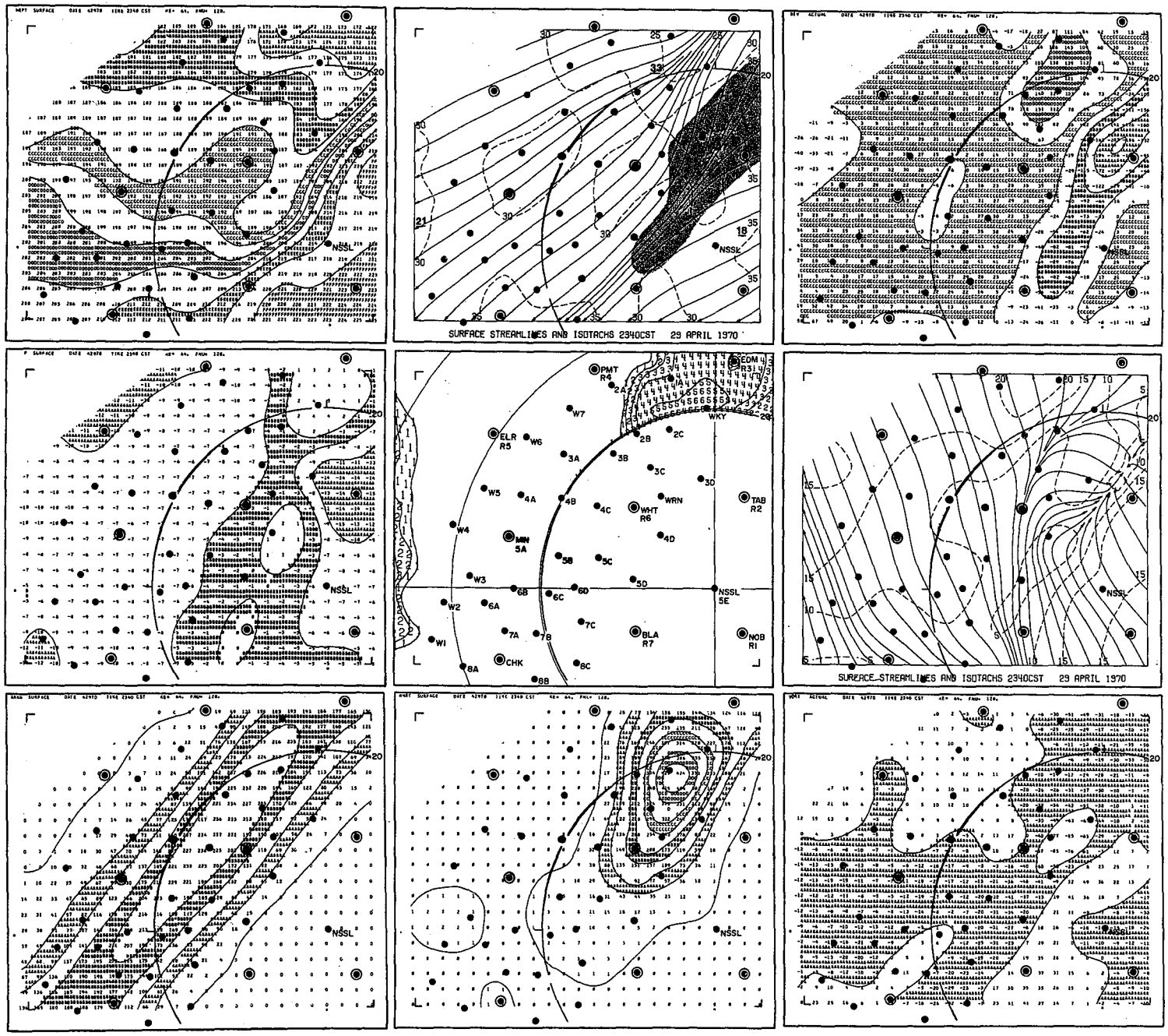
SURFACE STREAMLINES AND ISOTACHS 2340CST 29 APRIL 1970
SURFACE STREAMLINES AND ISOTACHS 2340CST 29 APRIL 1970
NSSL
PMT R4
EDM R3
WKY
ELR R5
W6
W7
2A
2B
2C
3A
3B
3C
3D
W5
4A
4B
4C
WRN
WHT R6
TAB R2
W4
MIN 5A
4D
5B
5C
W3
6B
6C
6D
5D
NSSL 5E
W2
6A
7C
BLA R7
NOB R1
W1
7A
7B
CHK
8A
8C
8B

2340

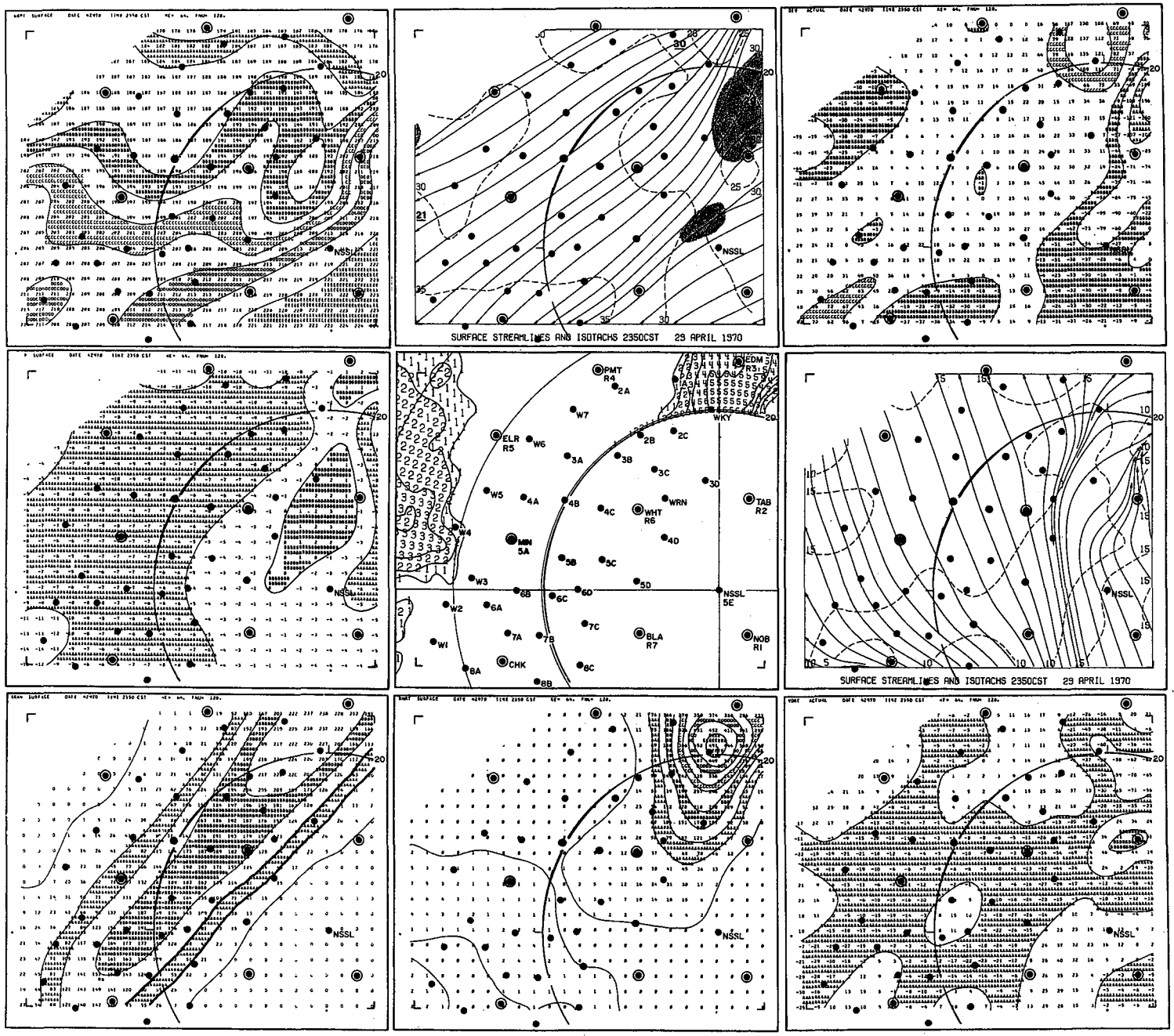
SURFACE STREAMLINES AND ISOTACHS 2350CST 29 APRIL 1970
SURFACE STREAMLINES AND ISOTACHS 2350CST 29 APRIL 1970
NSSL
PMT R4
EDM R3
WKY
ELR R5
TAB R2
WHT R6
MIN 5A
NSSL 5E
BLA R7
NOB R1
CHK

2350

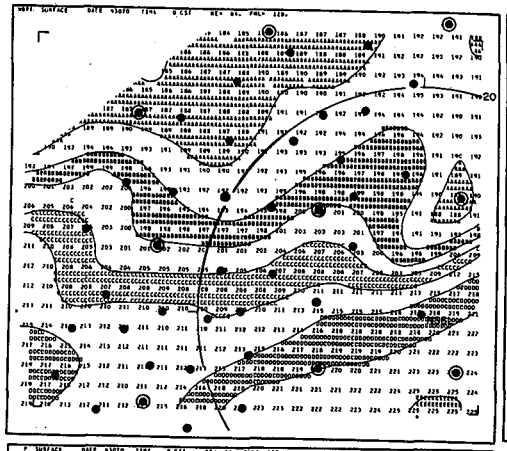

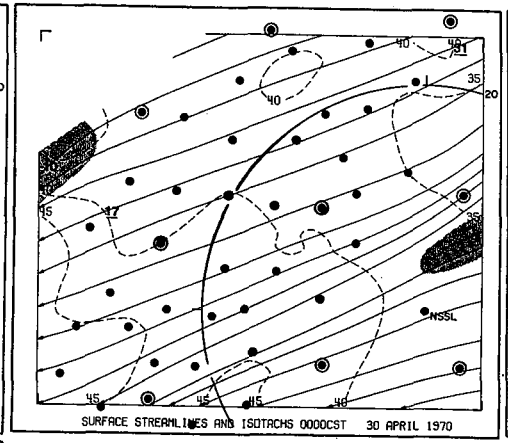
NSSL
SURFACE STREAMLINES AND ISOTACHS 0000CST 30 APRIL 1970

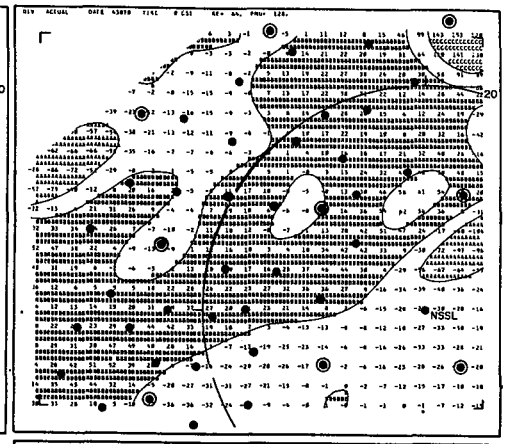
NSSL

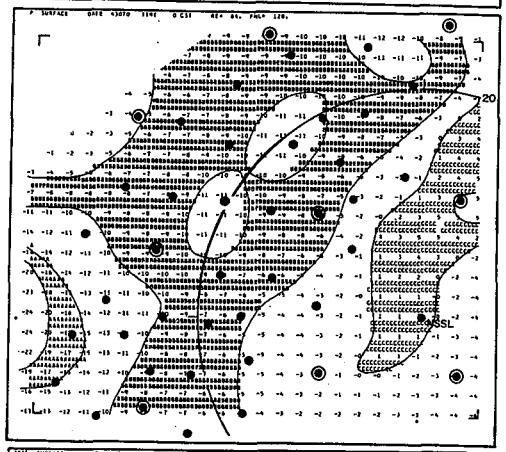
NSSL

NO DATA

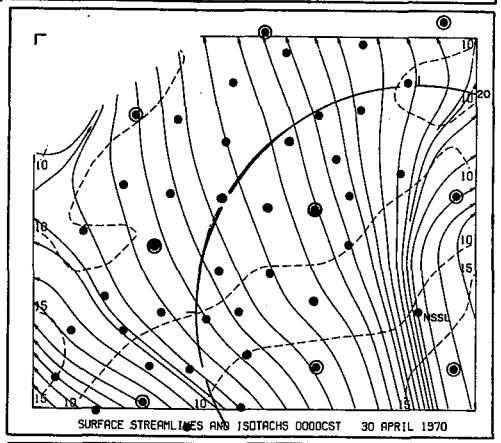
NSSL
SURFACE STREAMLINES AND ISOTACHS 0000CST 30 APRIL 1970

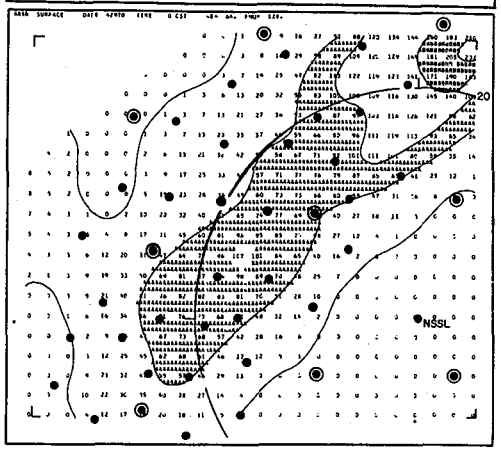
NSSL

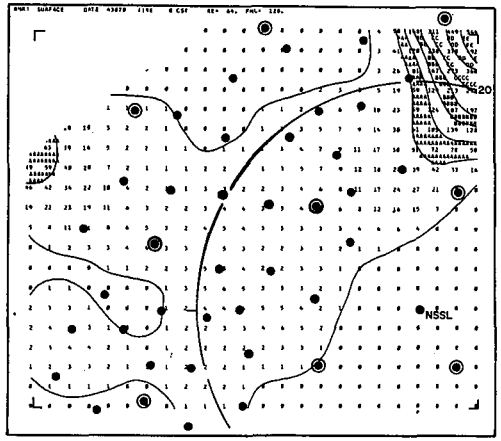
NSSL

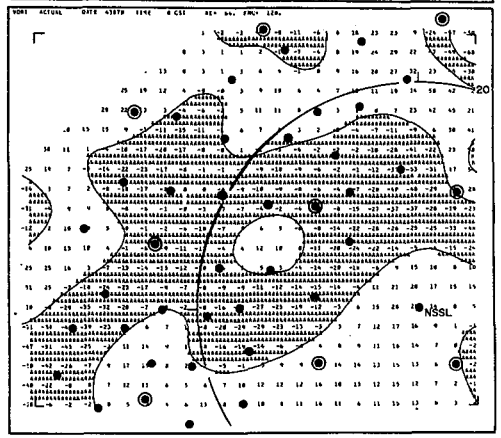
NSSL

0000

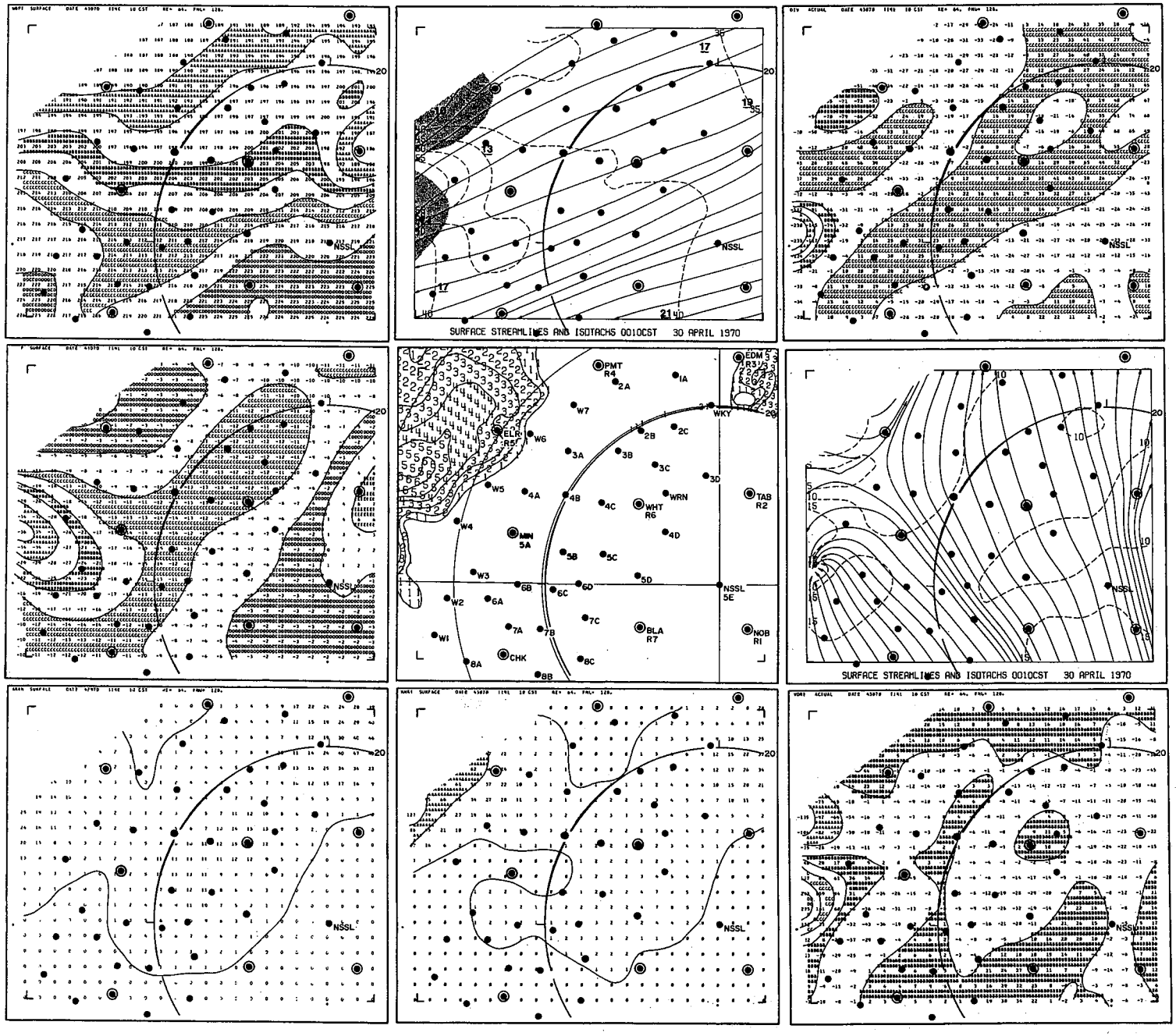
SURFACE STREAMLINES AND ISOTACHS 0010CST 30 APRIL 1970
NSSL
PMT R4
IA
2A
W7
WKY
ELR R5
W6
2B
2C
3A
3B
3C
3D
W5
4A
4B
4C
WHT R6
WRN
TAB R2
W4
MIN 5A
4D
5B
5C
W3
6B
6C
6D
5D
NSSL 5E
W2
6A
7C
7A
7B
BLA R7
NOB RI
W1
CHK
8A
8C
8B
EDM R3

0010

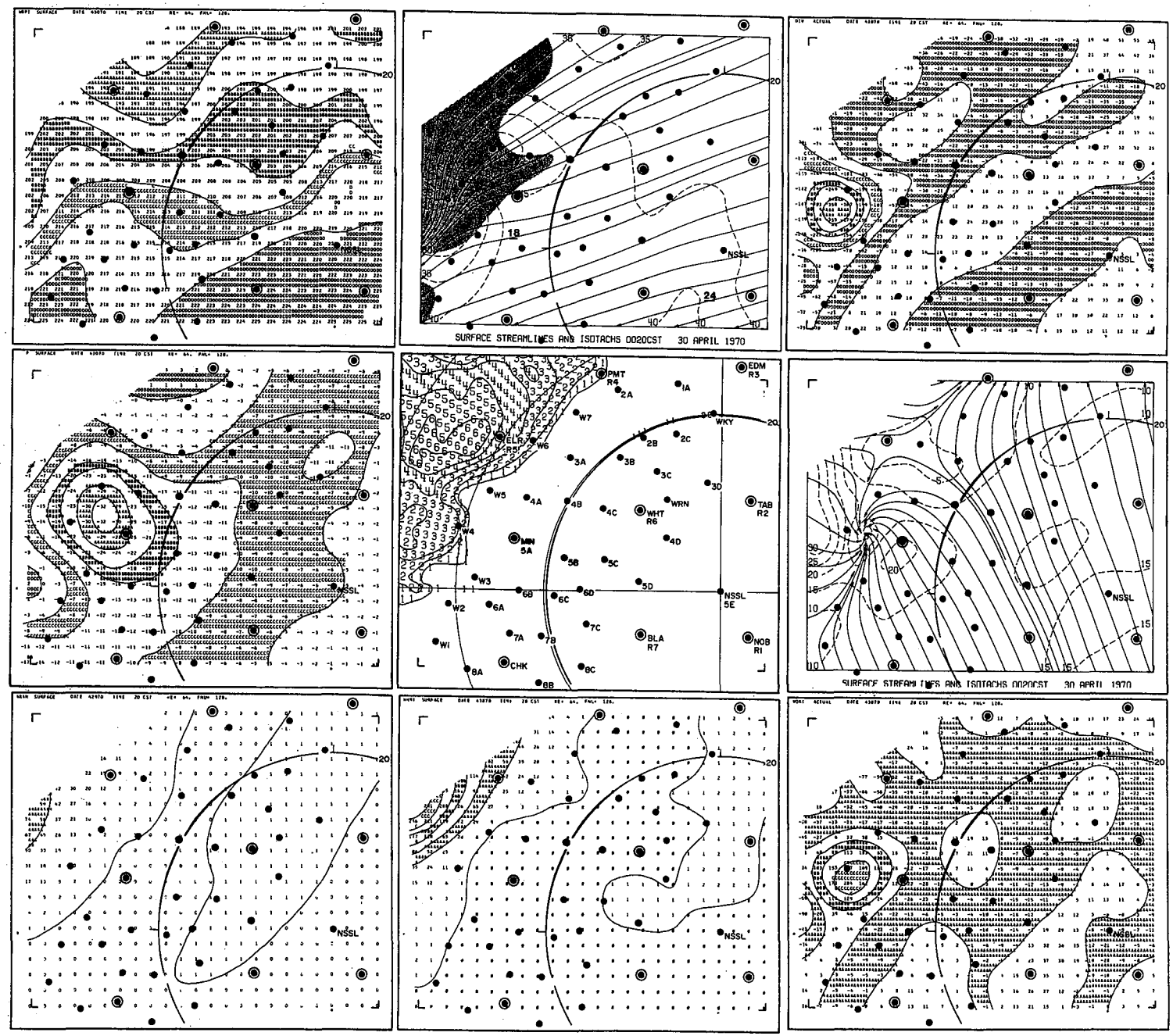
SURFACE STREAMLINES AND ISOTACHS 0020CST 30 APRIL 1970
SURFACE STREAMLINES AND ISOTACHS 0020CST 30 APRIL 1970
NSSL
PMT R4
EDM R3
WKY
TAB R2
WHT R6
BLA R7
NOB R1
CHK
MIN 5A
ELR R5
W6
W7
W5
W4
W3
W2
W1
1A
2A
2B
2C
3A
3B
3C
3D
4A
4B
4C
4D
5A
5B
5C
5D
6A
6B
6C
6D
7A
7B
7C
8A
8B
8C
WRN
NSSL 5E

0020

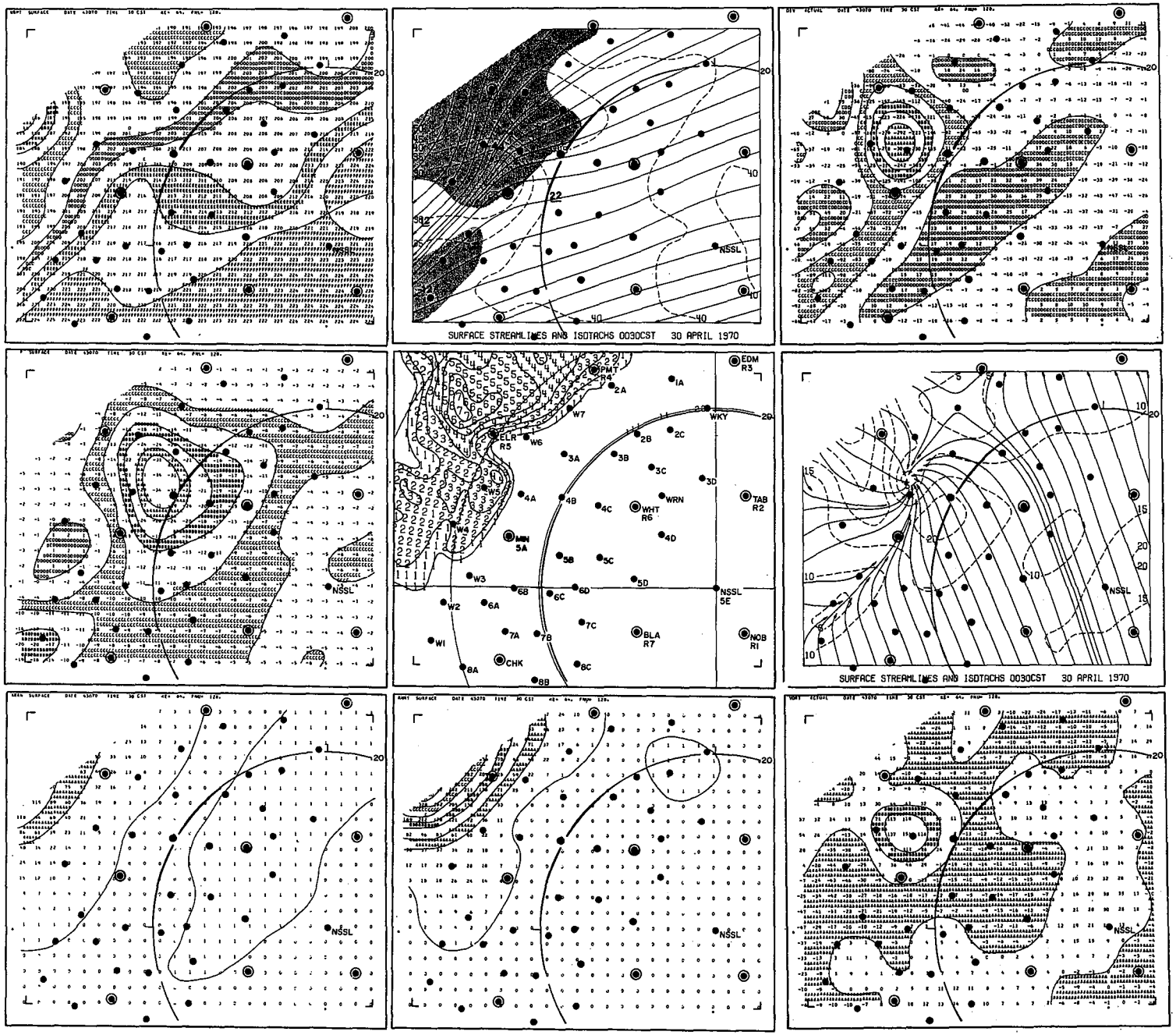
SURFACE STREAMLINES AND ISOTACHS 0030CST 30 APRIL 1970
SURFACE STREAMLINES AND ISOTACHS 0030CST 30 APRIL 1970
NSSL
EDM R3
PMT R4
WKY
ELR R5
TAB R2
WHT R6
MIN 5A
NSSL 5E
BLA R7
NOB R1
CHK

0030

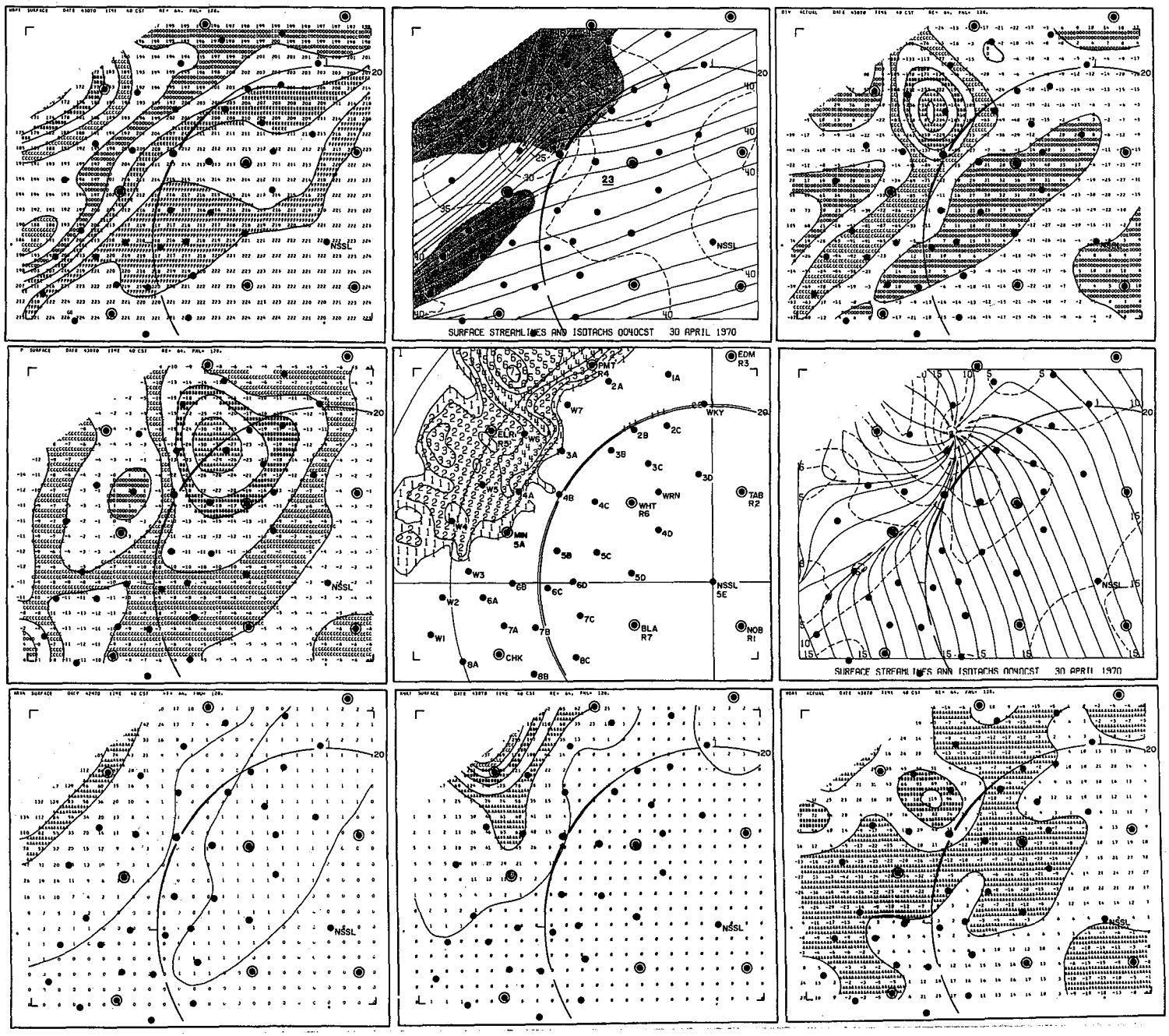
SURFACE STREAMLINES AND ISOTACHS 0040CST 30 APRIL 1970
SURFACE STREAMLINES AND ISOTACHS 0040CST 30 APRIL 1970
NSSL
EDM R3
WKY
TAB R2
NOB R1
BLA R7
WHT R6
CHK
ELR
MIN 5A
PMT
0040

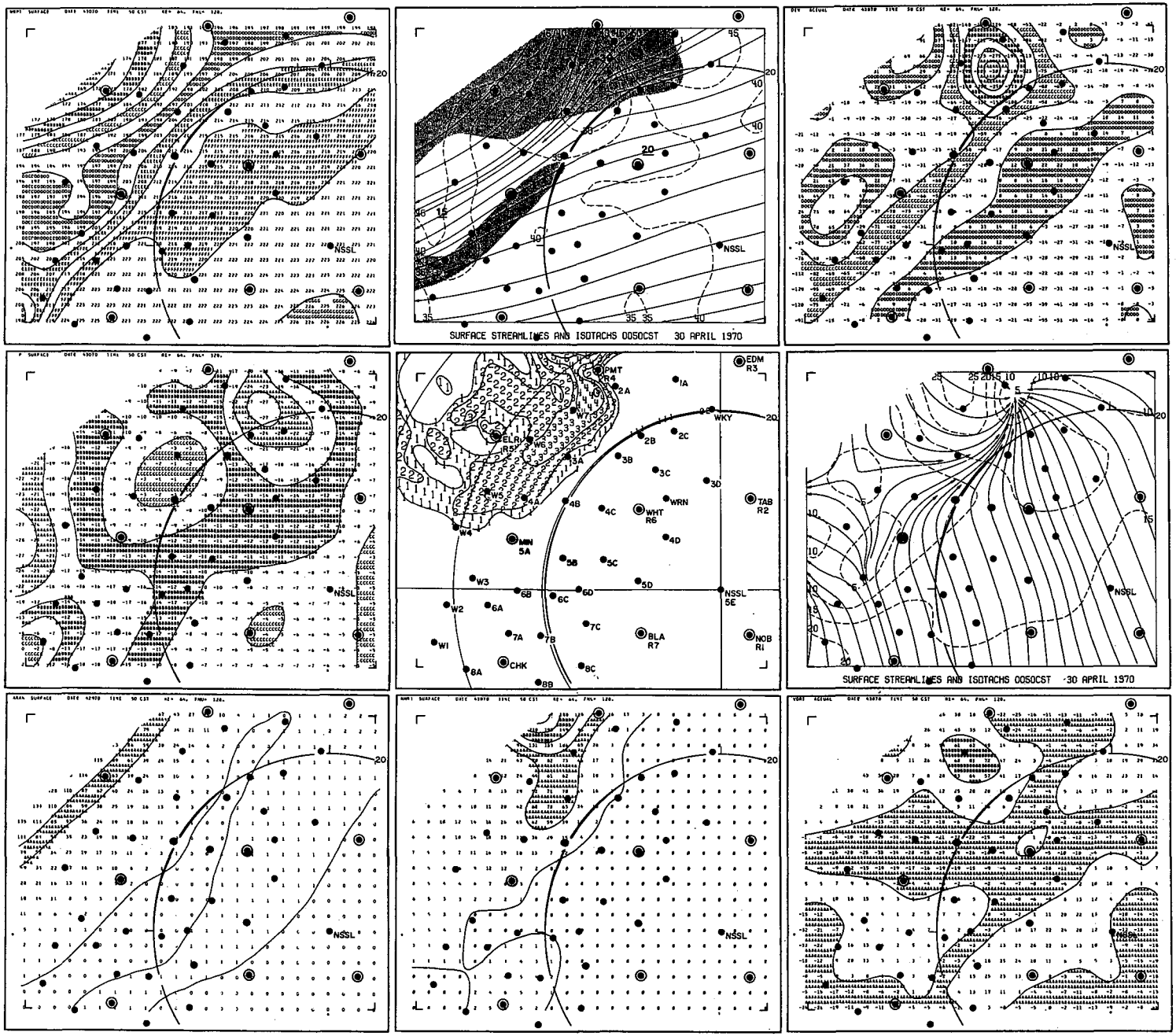
SURFACE STREAMLINES AND ISOTACHS 0050CST 30 APRIL 1970
SURFACE STREAMLINES AND ISOTACHS 0050CST 30 APRIL 1970
NSSL
EDM R3
PMT R4
IA
WKY
ELR R5
TAB R2
WHT R6
WRN
MIN 5A
NSSL 5E
BLA R7
NOB R1
CHK

0050

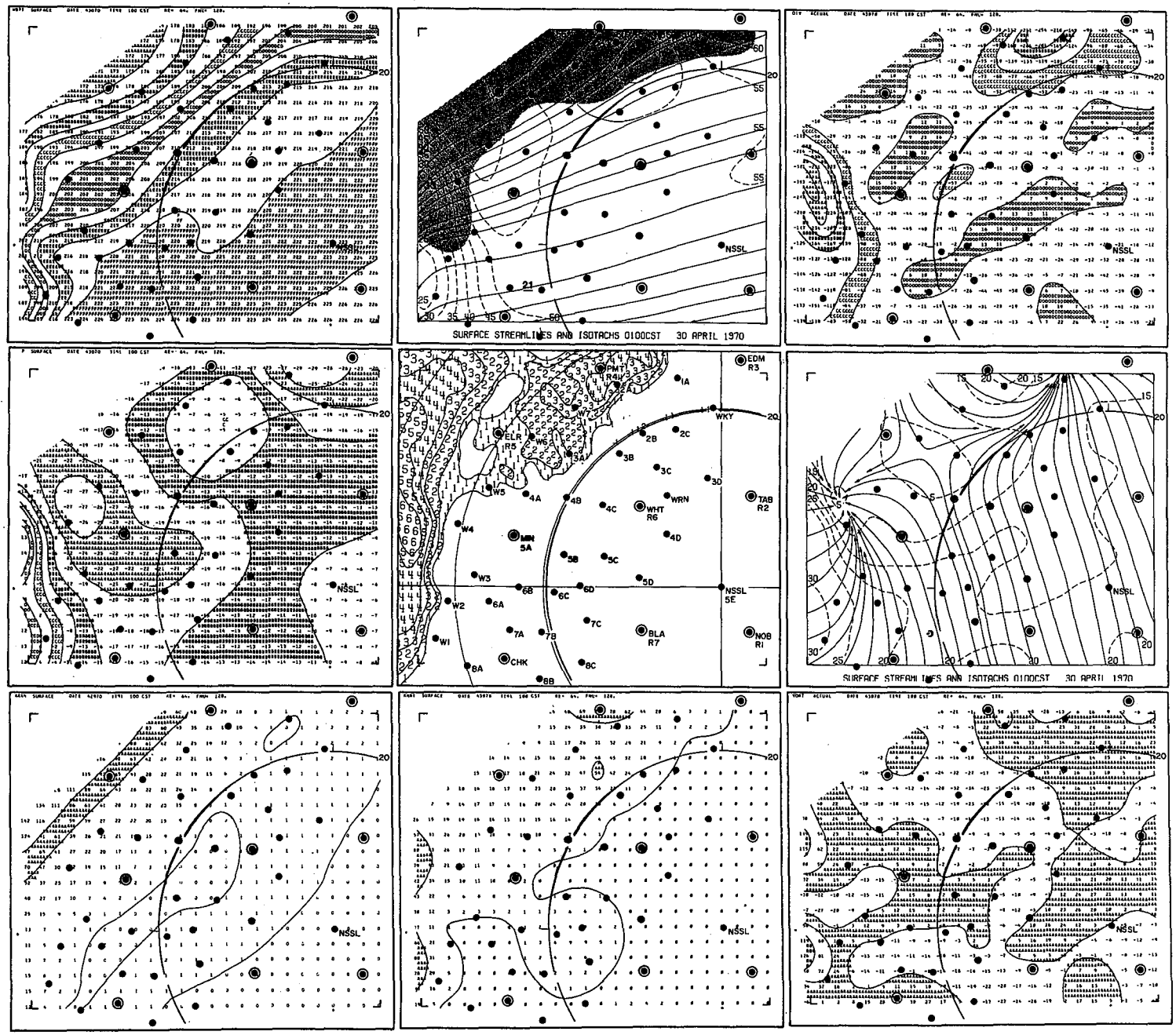
SURFACE STREAMLINES AND ISOTACHS 0100CST 30 APRIL 1970
SURFACE STREAMLINES AND ISOTACHS 0100CST 30 APRIL 1970
NSSL
EDM R3
PHT R4V
WKY
ELR R5
TAB R2
WHT R6
MIN 5A
NSSL 5E
BLA R7
NOB R1
CHK

0100

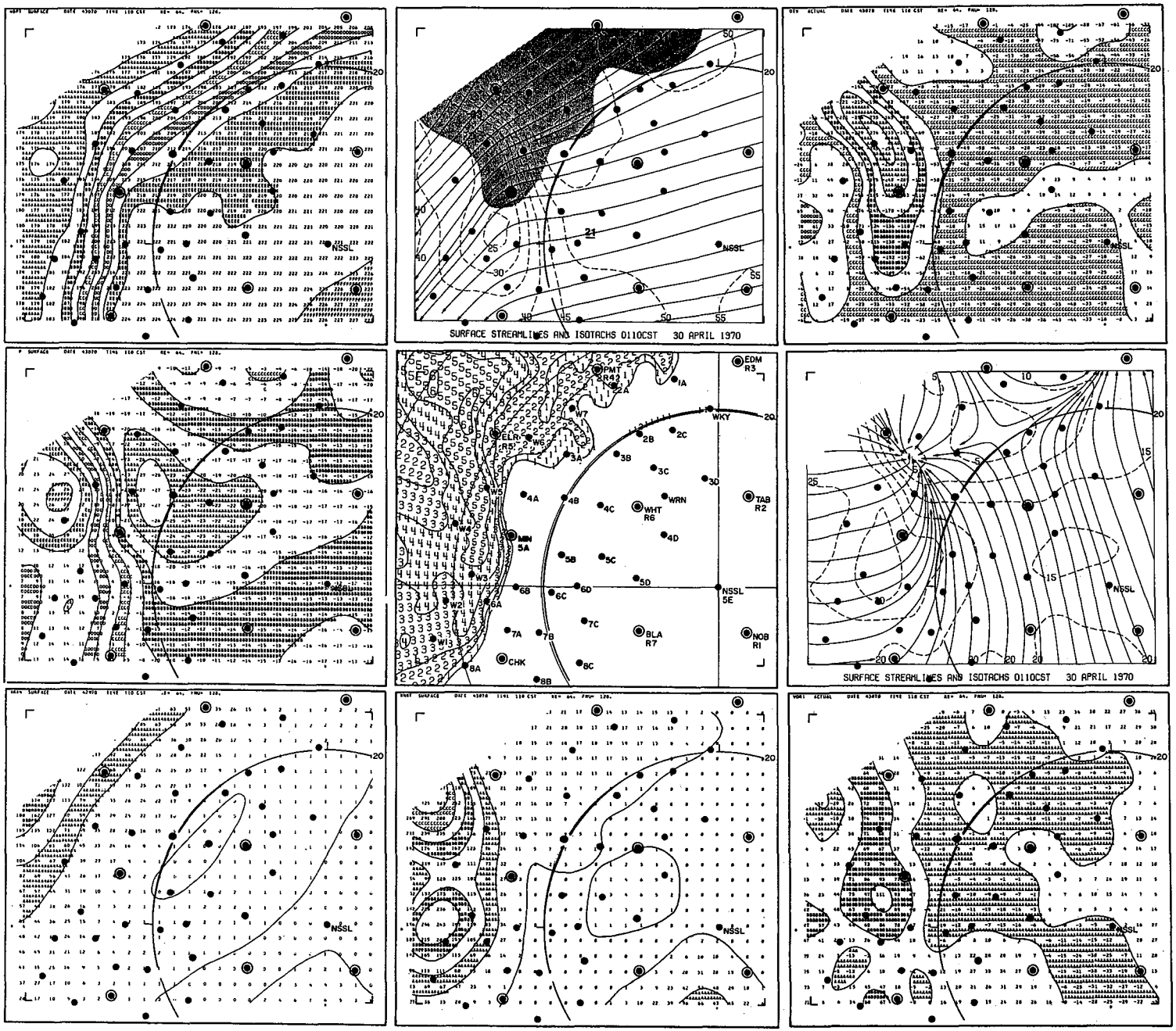
SURFACE STREAMLINES AND ISOTACHS 0110CST 30 APRIL 1970
SURFACE STREAMLINES AND ISOTACHS 0110CST 30 APRIL 1970
NSSL
EDM R3
WKY
TAB R2
WHT R6
WRN
NSSL 5E
BLA R7
NOB R1
CHK
MIN 5A
ELR
PMT R42

0110

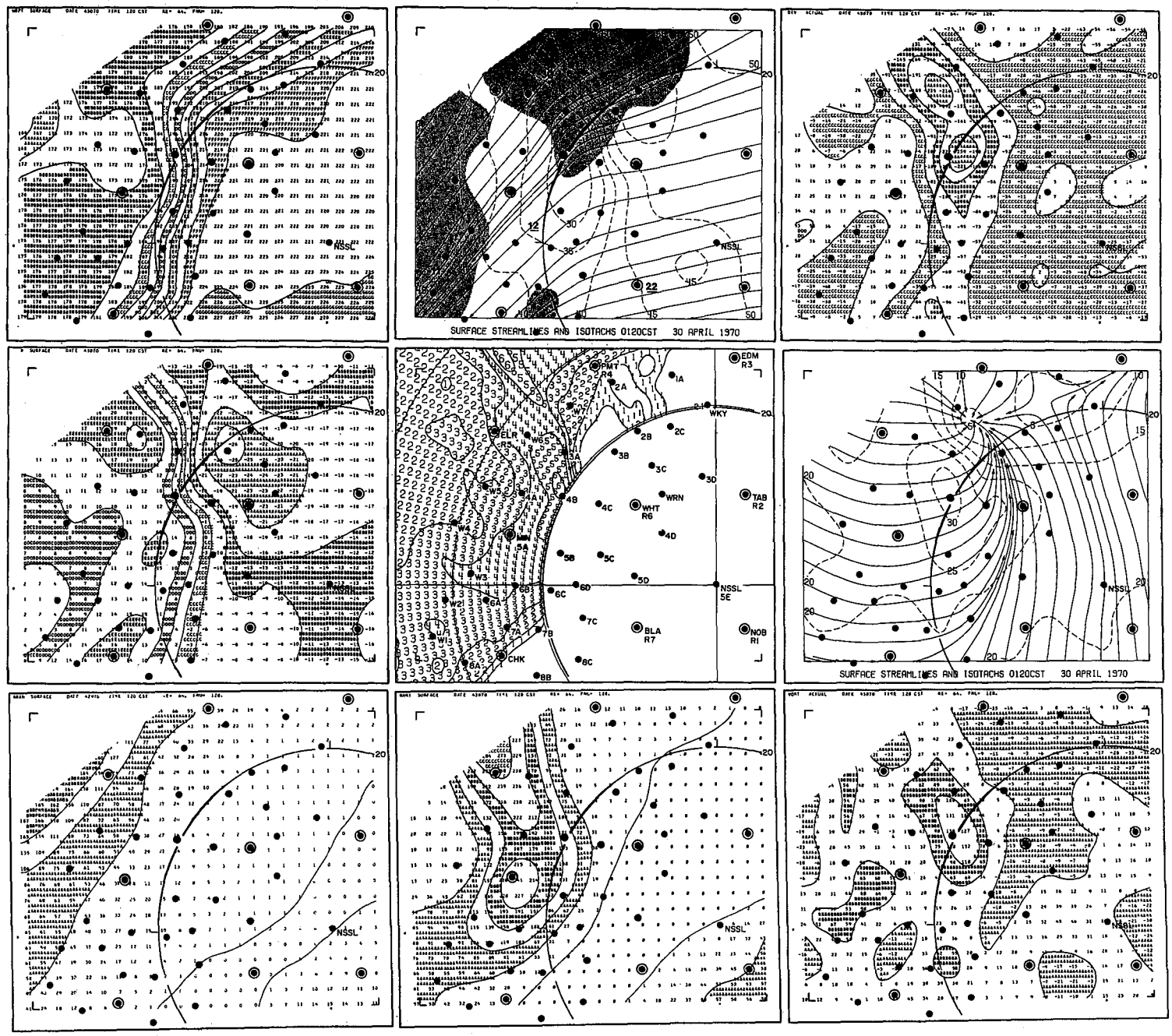
SURFACE STREAMLINES AND ISOTACHS 0120CST 30 APRIL 1970
SURFACE STREAMLINES AND ISOTACHS 0120CST 30 APRIL 1970
NSSL
EDM R3
TAB R2
NSSL 5E
NOB R1
BLA R7
WHT R6
WKY
CHK
0120

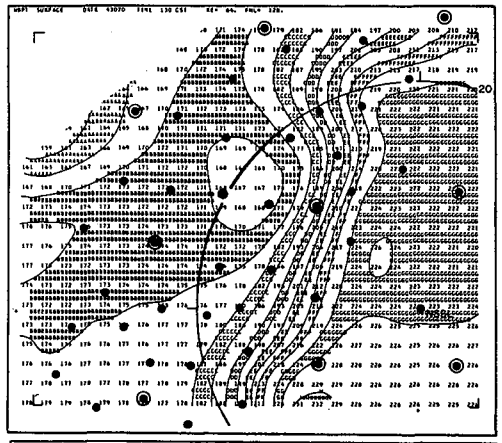

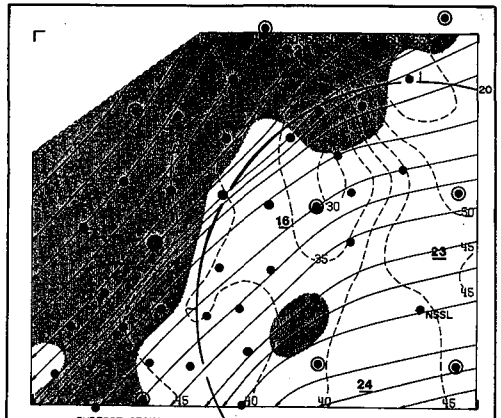

SURFACE STREAMLINES AND ISOTACHS 0130CST 30 APRIL 1970

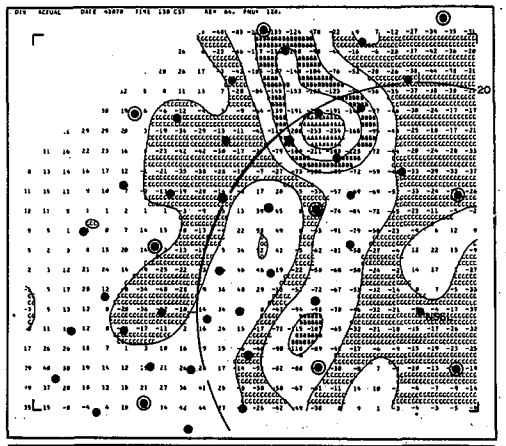

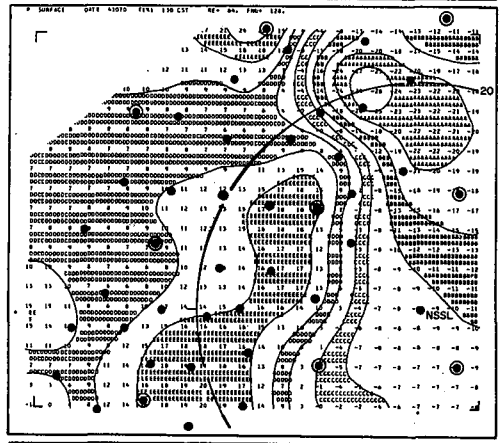

NO DATA

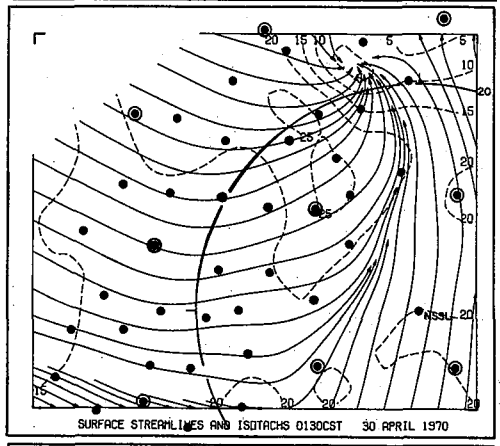

SURFACE STREAMLINES AND ISOTACHS 0130CST 30 APRIL 1970

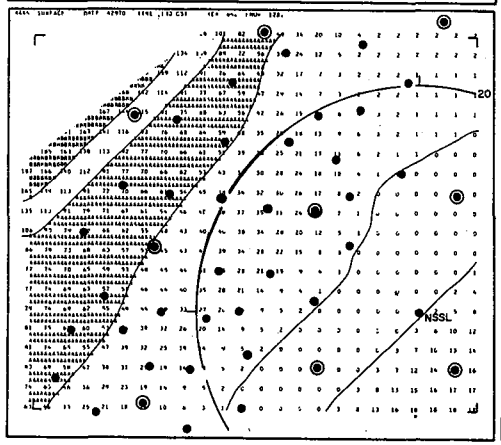

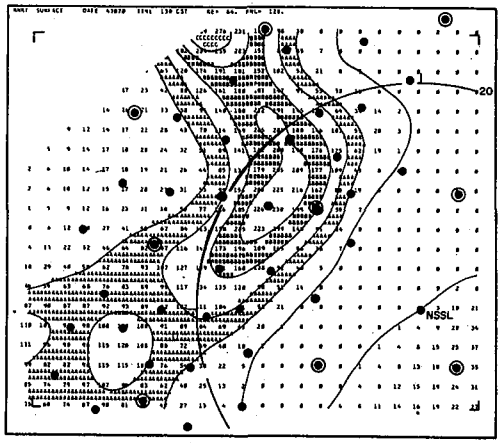

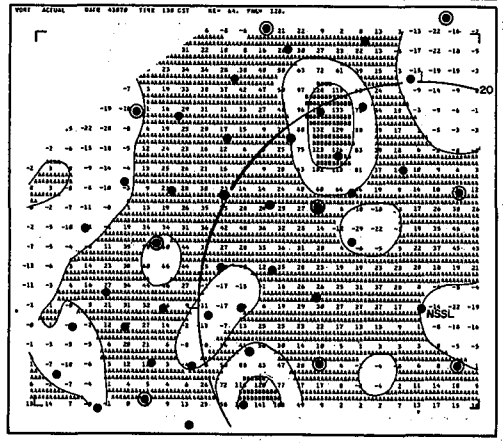

0130

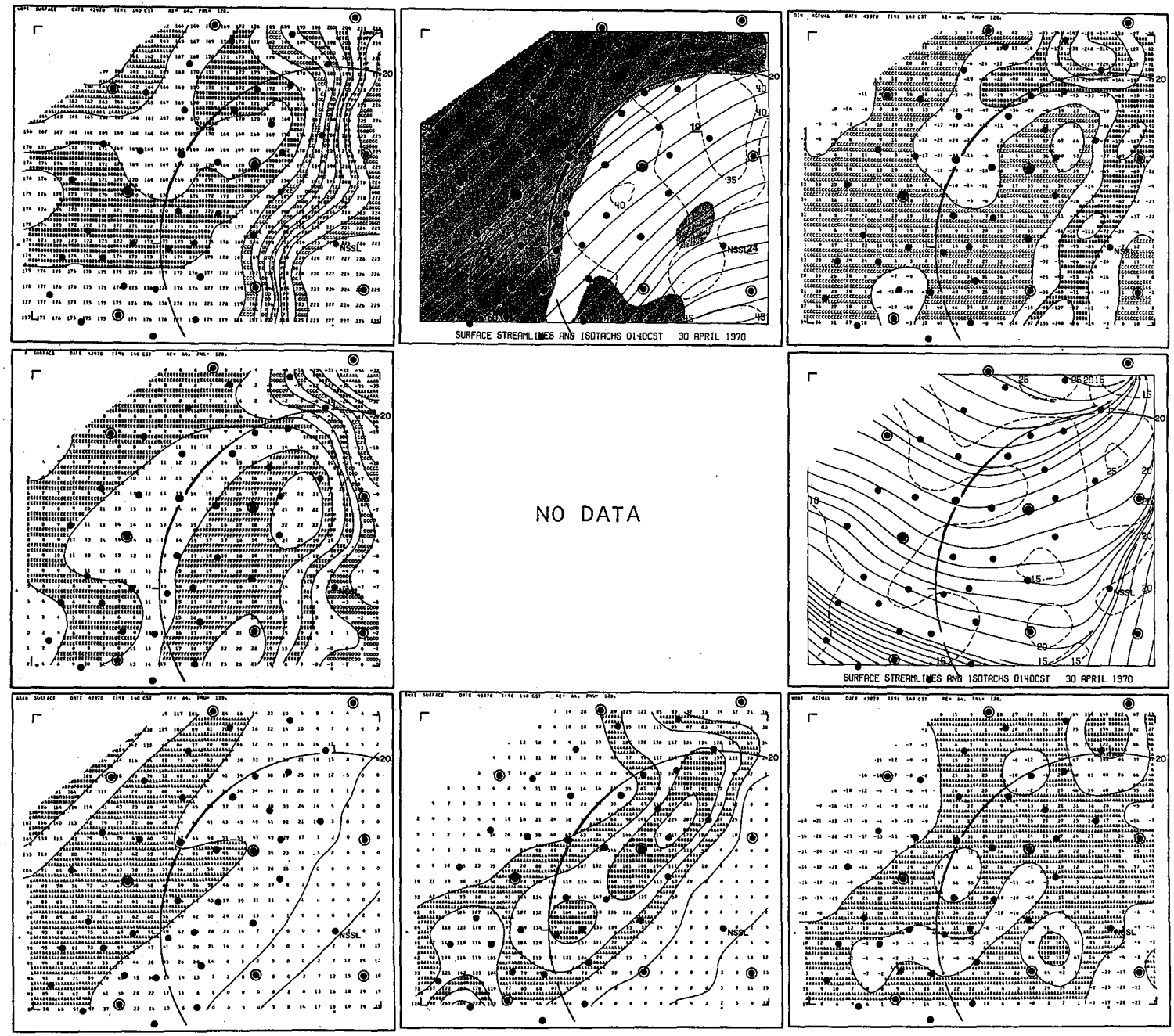
SURFACE STREAMLINES AND ISOTACHS 0140CST 30 APRIL 1970
NO DATA
SURFACE STREAMLINES AND ISOTACHS 0140CST 30 APRIL 1970
NSSL

0140

6. CONCLUSIONS

Five-minute data from surface instruments spaced 11 km adequately record passage and evolution of thunderstorm-related features such as mesocyclones, pseudo fronts, downdraft-updraft couplets, and general rainfall patterns. In fact, station spacing may be increased slightly (from 11 to 15 km) without seriously degrading results (Barnes, 1974). Although individual stations may record "micro" features (such as tornadoes and the pseudo front's internal structure) measurements are generally too few to resolve these features by spatial analysis, and more closely arrayed instruments are required for their study.

Rainfall patterns generally agree with radar reflectivity patterns near the surface, but the analysis smears the rain rate distribution suggested by radar. On the other hand, the analyzed rain rate maxima for the observed severe thunderstorms are in every case larger than radar estimates (table 4 and pages 65 - 75). This long-recognized discrepancy (Wilk and Kessler, 1970) points to the need for further work on NSSL's radar calibration for rainfall estimates such as recently published by Brandes (1974). Neither the digital radar reflectivity plots nor the corresponding video integrated displays resolve important details with the clarity of the log contour display. For example, the twin tornado cyclones accompanying Storm G (pages 141-151) are not detectable in either the video or digital integrated data. Clearly, finer resolution in the integrated data formats is desirable for severe storm morphological studies.

During the 1970 storm season, rawinsonde teams operated with flexibility. Their objective was simply to obtain as many soundings as feasible while storms were in the network. Soundings were limited to 400 mb altitude (7 km) and were released essentially without timing control. An analysis technique for such irregular measurements had not been developed in 1970. When later it was decided to position soundings relative to moving storms rather than assemble (in true geographic positions) all soundings taken during a given (small) time span, we found that the time-to-space adjustments produced data redundancy in some regions and data voids in other regions.

The devised objective analysis assumes data are distributed continuously over two-dimensional space. Results are good when data are spaced uniformly or are distributed more densely than the size of smallest interesting features. We believe that our ensemble soundings might have yielded more information had attention been paid to their spacing relative to the storms, and improved data acquisition procedures to accomplish this are now under development.

A measure of instrument altitude independent of pressure is required before the full significance of in-storm soundings can be determined. No economically feasible combination of rawinsondes will ever resolve flow patterns and thermodynamic structure <u>within</u> severe thunderstorms, but synthesis of details can be realized from internal flow mapping by dual-Doppler radar systems, ambient soundings tied together horizontally by aircraft measurements, and from dynamically consistent analyses that make physical interpretation more obvious.

7. ACKNOWLEDGMENTS

Computer software for plotting Stüve sounding diagrams, individual station graphs, and digital radar reflectivity maps were developed by Mr. J. H. Henderson, NSSL. Calculation and plotting of streamlines and isotach maps were accomplished by Dr. G. L. Achtemeier while on a National Research Council Post-doctoral Fellowship at the NSSL.

Thanks are extended to the staffs of NSSL's Computer and Data Processing Group and Graphic Arts Unit for preparing the illustrations.

8. REFERENCES

Barnes, S. L., 1968: An empirical shortcut to the calculation of temperature and pressure at the lifted condensation level. J. Appl. Meteor., 7, 511.

_____, 1973: Mesoscale objective map analysis using weighted time-series observations. NOAA Tech. Memo. ERL-NSSL-62, 60 pp.

_____, 1974: Mesonetwork array: its effect on thunderstorm flow resolution. (To be published.)

_____, J. H. Henderson and R. J. Ketchum, 1971: Rawinsonde observations and processing techniques at the National Severe Storms Laboratory, NOAA Tech. Memo. ERL-NSSL-53, 246 pp.

Brandes, E. A., 1974: Radar rainfall pattern optimizing technique. NOAA Tech. Memo. ERL-NSSL-67, 16 pp.

Browning, K. A., 1964: Airflow and precipitation trajectories within severe local storms which travel to the right of the winds. J. Atmos. Sci., 21, 634-639.

Charba, J., 1972: Gravity current model applied to analysis of squall-line gust front. NOAA Tech. Memo. ERL-NSSL-61, 58 pp.

Ellrod, G. P., 1973: Time variation of latent heat release during the evolution of Oklahoma thunderstorms as estimated from radar observations. Report 73-1 on NSF Grant No. GI-31278X, Dept. of Meteor., Univ. of Wisconsin, Madison, 52 pp.

Operations Staff, 1971: The NSSL surface network and observations of hazardous wind gusts. NOAA Tech. Memo. ERL-NSSL-55, 20 pp.

Prosser, N. E., and D. S. Foster, 1966: Upper air sounding analysis by use of an electronic computer. J. Appl. Meteor., 5, 296-300.

Sirmans, D., and R. J. Doviak, 1973: Meteorological radar signal intensity estimation. NOAA Tech. Memo. ERL-NSSL-64, 80 pp.

Teten, O., 1930: Ober einige meteorologische vegriffe. Z. Geophys., 6, 297-309.

Wilk, K. E., and E. Kessler, 1970: Quantitative radar measurements of precipitation. Meteor. Monograph, 11, No. 33, 315-329.

STUDY OF A DISSIPATING SEVERE STORM

Stephan P. Nelson and Stanley L. Barnes

National Severe Storms Laboratory
Norman, Oklahoma 73069

A small dying hailstorm entered the National Severe Storms Laboratory (NSSL) surface and upper air networks about 1800 CST on 29 April 1970. Structural details revealed by radar and network observations indicate the storm had supercell attributes at one time, but weak thermal instability, limited low-level moisture, and adverse upper winds prevented the storm from reaching the damaging proportions of later storms on this date. A surprising surface pressure distribution--high pressure center near the updraft and strong pressure gradient beneath the downdraft--suggests the storm interacted to its detriment with a large-scale, wave-like perturbation.

1. INTRODUCTION

During the afternoon and evening of 29-30 April 1970, central Oklahoma suffered an outbreak of severe storms. Five of these storms passed through the NSSL mesoscale surface and upper-air networks and are discussed in this volume. This report considers Storm A, the first to enter the networks about 1800 CST. The storm produced small hail and strong winds, but no funnels or significant damage. It is of interest because it dissipated within the network. Storm structure and factors leading to decay are described.

2. DATA

2.1 Radar

Film and digital 10-cm radar data are available from 1600 to 1815 CST. Due to a tape change, no digital data exists during a 14-min period from 1751 to 1805 CST when the storm entered the network. Radar system details are described by Wilk and Gray (1970). Analysis of storm structure is facilitated by computer-generated vertical cross sections and PPI maps of digitized reflectivities at 10-min intervals. The eight coded digital levels and their corresponding dBZ equivalents are shown in table 1.

2.2 Surface and Upper Air Network

Temperature, pressure, humidity, and wind data are available from the upper air and surface mesonetwork; surface rainfall is also measured. Data collection and analysis techniques have been described by Barnes et al. (1971) and Barnes (1973). Abstracted surface data and soundings are presented in another paper in this memorandum.

Table 1. Coded Digital Levels and Equivalent dBZ.

DIGITAL LEVEL	dBZ	DIGITAL LEVEL	dBZ
1	15	5	45
2	22	6	49
3	32	7	52
4	39	8	57

3. LIFE CYCLE

3.1 Radar Characteristics

Storm A evolved from a large area of light to moderate rain downwind of and contiguous with a larger storm (Storm C). Echo centroid movement was from 221° at 35 kt (18 m sec^{-1}). Echo history is presented from 1602 until 1815 CST when the storm entered the NSSL ground clutter (fig. 1). The storm grew steadily from 1620 until 1740 CST at which time it possessed reflectivities between 52 and 57 dBZ. Although small in size, the echo formed supercell characteristics between 1730 and 1740 (overhang east of a tight gradient region in the right rear quadrant, beginnings of a hook, fig. 1, 1745 CST). Cross sections reveal a weak echo region (WER) updraft signature from 1710 until the storm entered the ground clutter. However, the WER (fig. 2) was never very distinct nor bounded (i.e., the WER was not, in plan view, completely encircled by higher reflectivities). After 1740 CST the storm decayed rapidly; maximum reflectivity and overall storm dimensions decreased. This change is shown by two cross sections through the core perpendicular to storm motion (fig. 3).

3.2 Surface Characteristics

The storm entered the surface network at 1745 CST, at least five minutes after it began to decay. Analyses of surface parameters and the associated radar echoes are in another part of this report (pages 17-88). Strong divergence characterized the wind field near the echo (maximum value 1.6 x 10^{-3} sec^{-1} at 1805 CST) with the exception of weak convergence (-10^{-4} sec^{-1}) in the area just east of the echo where the updraft is usually expected (pages 111-123 and pages 125-139). Interestingly, although local mass convergence is indicated here, there is no <u>moisture</u> convergence in the entire network area during the period 1745 to 1830 CST.

Lowest wet-bulb potential temperatures (θ_w) associated with the downdraft air near the precipitation core are only 19.5C at 1805 CST (near CHK). After 1815 CST, no values less than 21C can be found. Soundings near this storm

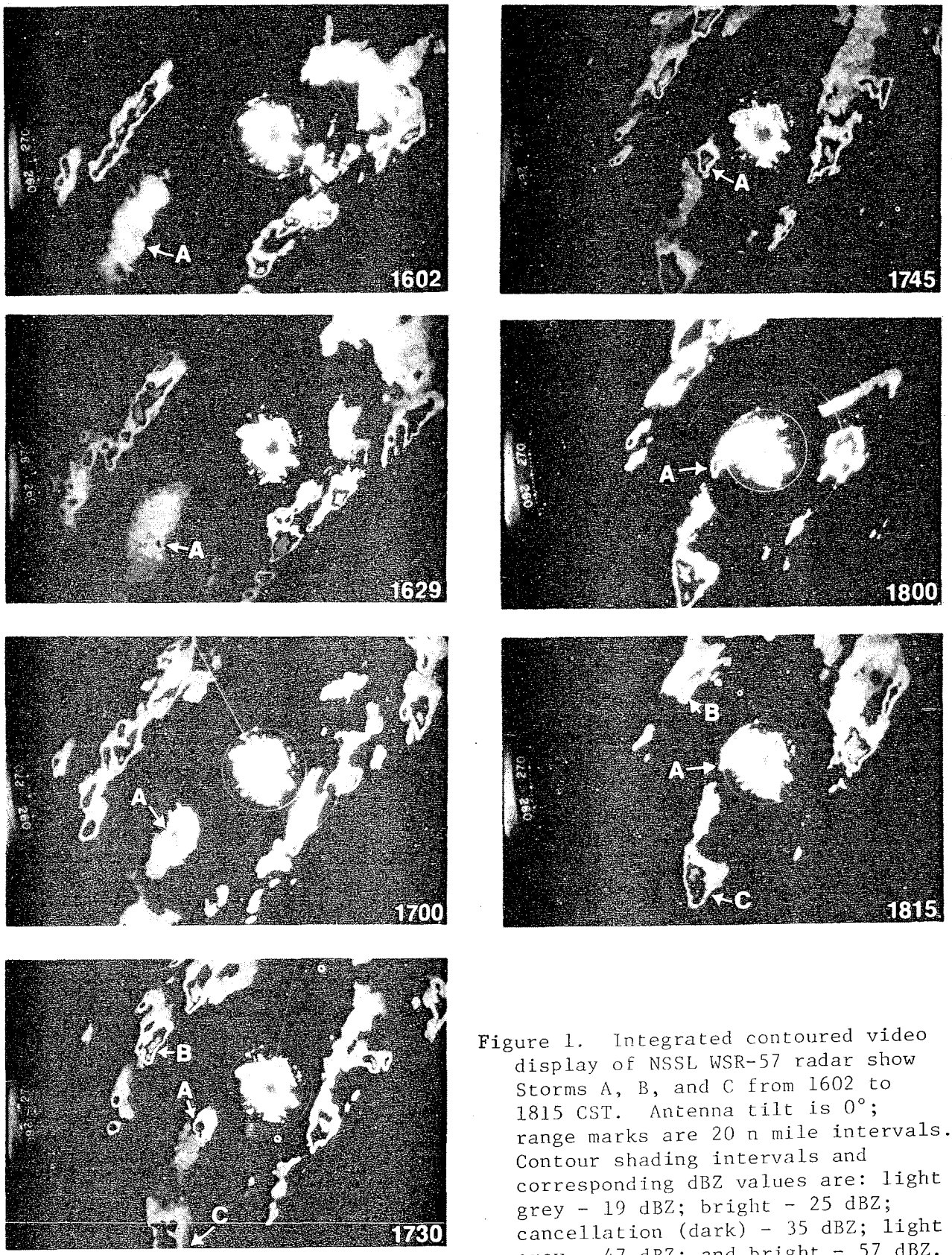

Figure 1. Integrated contoured video display of NSSL WSR-57 radar show Storms A, B, and C from 1602 to 1815 CST. Antenna tilt is 0°; range marks are 20 n mile intervals. Contour shading intervals and corresponding dBZ values are: light grey - 19 dBZ; bright - 25 dBZ; cancellation (dark) - 35 dBZ; light grey - 47 dBZ; and bright - 57 dBZ.

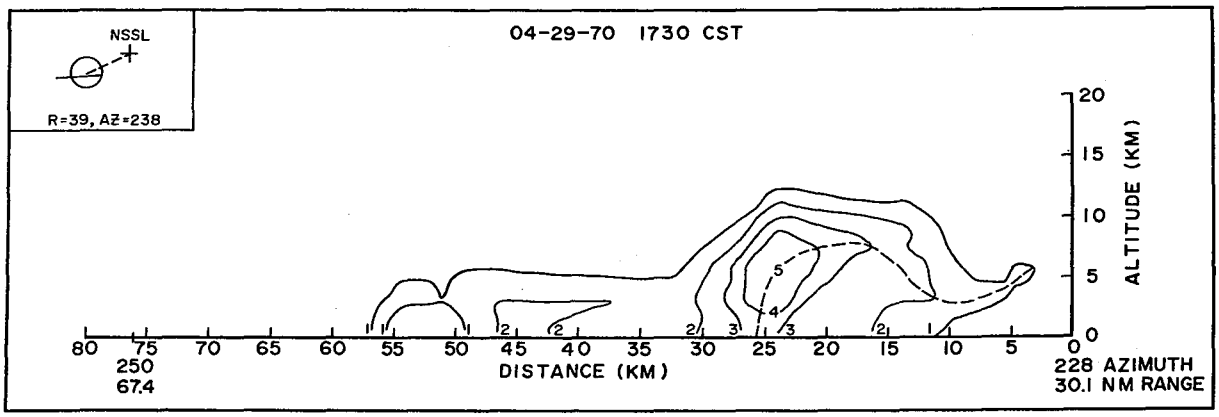

Figure 2. Cross section of Storm A's range normalized reflectivity. Dashed line denotes maximum reflectivity axis whose configuration suggests a weak echo region (WER) at 20 km. Insert shows Storm A (circle) position relative to radar (NSSL), and the orientation and length of cross section (solid straight line). Range (n mile) and azimuth in the insert are to the echo centroid. The range and azimuth to end points of the cross section are indicated below distance scale which measures from end point nearest radar.

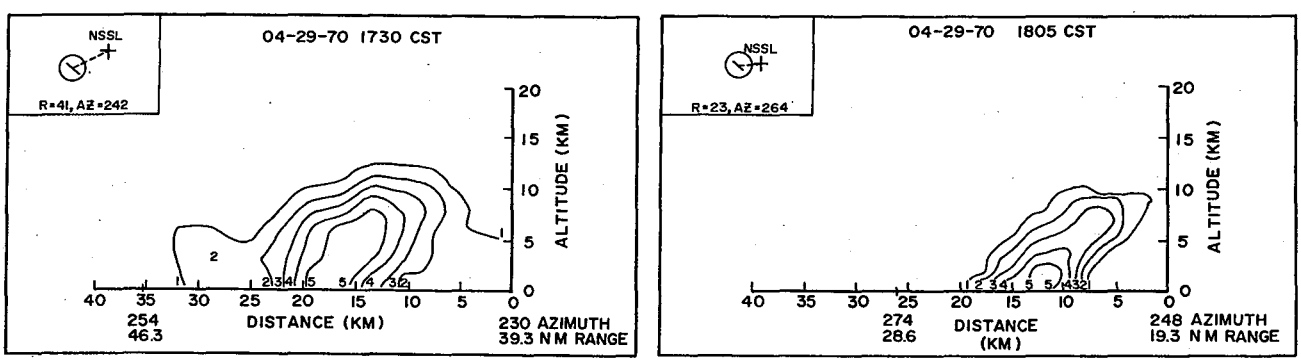

Figure 3. Cross sections through storm core and perpendicular to storm motion at 1730 and 1805 CST reveal decrease in storm size and intensity. See figure 2 for further explanation.

indicate minimum θ_w = 18C from 2.5 to 3 km MSL. This suggests that the mid-level air was not reaching the surface or, more likely, that the dying storm was thoroughly mixing updraft air (θ_w = 21C) with mid-level air to produce marginal negative buoyancy which only weakly contributes to downward acceleration. Precipitation drag mostly sustained this branch of the storm's circulation. Rainfall rates in excess of 1 inch hr^{-1} were analyzed at 1805 CST, 20 to 25 min after the storm intensity had begun to diminish. Individual stations (7A and CHK; pages 41-42) recorded five-minute rainfall rates over 2 inch hr^{-1}. Small hail was reported by the Chickasha sounding crew as the storm passed overhead approximately 1800 CST.

The pattern of pressure deviation from the eight-hour linear trend (pages 55-56) is unusual in that pressure excess normally found with the divergent downdraft here is associated with the convergence area that marks the dying updraft. The weak downdraft diverges in a maximum pressure gradient region with largest deficit pressures west of the echo. The cause of this peculiar pressure distribution only can be speculated, but the pattern between 1745 and 2000 CST suggests a wave-like perturbation--an elongated trough and ridge oriented in the direction of upper flow (southwest to northeast) gradually traversed the network from west to east. Because the time and space scales of this perturbation are considerably larger than Storm A, it is unlikely that the storm produced this pressure field.

Strong winds experienced on the northwest side of dying Storm A (averaging greater than 30 kt over five minutes) are believed caused mainly by the remarkable surface pressure gradient beneath the cloud and only partly by the downdraft, although the downdraft influence in the surface wind pattern is evident in the spreading of streamlines near the storm at 1815 CST (page 56).

4. CAUSES OF STORM DECAY

Why this storm died so soon after formation (about 2 hr) while others later in the evening (Storms E, F, and G) lasted much longer is not known, but several factors are suggestive. Tropospheric thermal structures were compared. Figure 4 reveals a marked decrease in Lifted Index (Galway, 1956) during the evening from about -2 to -7 when the tornadic storms occurred. The major reason for this change is the deepening and increase in low-level moisture (fig. 5).

Increase in low-level moisture was accompanied by increase in low-level winds. Wind speeds in the 1.5 to 3 km layer nearly doubled prior to tornadic Storm F (fig. 6). Moreover, vertical wind shear changed remarkably during the evening. Storm A found itself in a strongly sheared environment with large direction shear between the layers 1.5 - 3.0 km and 3.0 - 4.5 km (table 2). On the other hand Storm F experienced strong shear in its lower environment, but relatively little shear at middle levels. Other studies also indicate that shear structure plays an important role in determining thunderstorm structure (Marwitz, 1972a, b, c). Plotted on the hodograph (fig. 6) are translation vectors of Storms A and F. Winds relative to these storms can be visualized by lines from terminal points of A and F to the respective hodograph curves. For Storm F the relative winds veer continuously from northeast through south to south-southwest, while for Storm A the

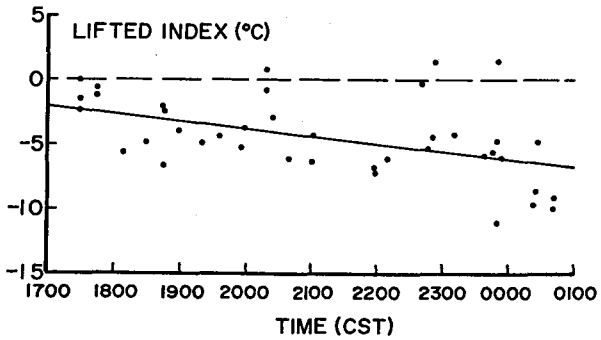

Figure 4. Lifted Index (Galway, 1956) versus time for environmental soundings (not in convection) from NSSL network stations on 29-30 April 1970. Regression line shows definite trend toward greater thermal instability from the time Storm A occurred (1700-1800) until time larger tornadic storms occurred (0000-0100).

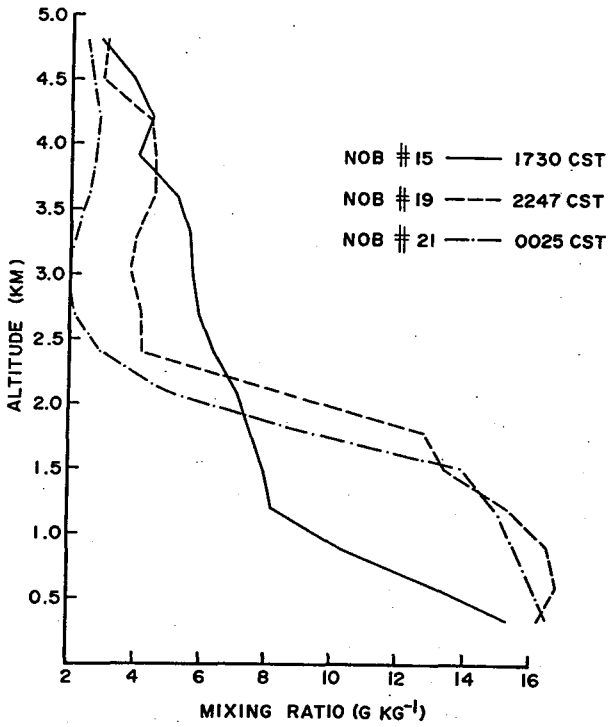

Figure 5. Mixing ratio versus height for three environmental soundings taken at Noble, Oklahoma, on 29-30 April 1970; 1730, 2247 and 0025 CST.

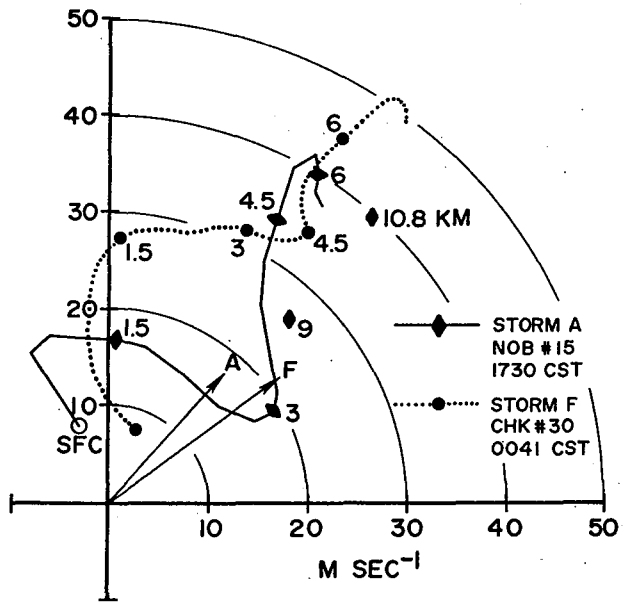

Figure 6. Environmental wind hodographs for Storms A and F. Vectors indicate the two storms' speeds and directions of motion. Note increase in low-level winds (1.5 - 3 km), change in mid-level speed shear (3 - 4.5 km) and change in direction shear relative to the two storms.

relative winds back from east-southeast through north to southwest. Storm F's relative wind structure is thought to favor development of a long-lived, quasi-steady updraft which systematically purges its precipitation load as it continuously propagates into the low-level moisture field (Marwitz, 1972a). Storm A, on the other hand, apparently was entraining drier air from the northwest at 3 km and did not have at cloud base (about 1.5 km) as large a flux of moisture into the updraft. Storm A's very large shear from 3 to 4.5 km altitude (table 2) may explain the north-south echo orientation (fig. 1). As the storm reached maximum height (∿ 13 km) at 1730 CST, the echo core expanded toward the northeast responding to upper level winds (see diamond marked 10.8 km in fig. 6). However, in order for the updraft to reach these precipitation-removing winds, it had to pass through an adversely sheared layer (6-9 km shear vector from 010°, 5 x 10^{-3} sec^{-1}).

Table 2. Comparison of Environmental Vertical Wind Shear Between the Small, Short-lived Storm A (1730 CST) and the Long-lived Tornadic Storm F (0041 CST). See Also Figure 6.

LAYER (KM)	VECTOR SHEAR STORM A	($10^{-3}sec^{-1}$) STORM F
1.5 - 3.0	295°/12.0	265°/8.7
3.0 - 4.5	180°/13.3	270°/4.0
4.5 - 6.0	220°/4.0	200°/7.0
6.0 - 9.0	010°/5.0	
9.0 - 10.8	220°/7.5	

Finally, the storm may have been influenced adversely by moving into an area where storm-induced pressure perturbations were insufficient to overcome the accelerations associated with the larger-scale wave-like disturbance. (Although this is speculative because we do not know the cause of the pressure wave, it is a point to check in studies of dissipating storms.)

5. SUMMARY

A small dissipating hailstorm that temporarily possessed supercell radar characteristics was sampled by the NSSL surface and upper air networks revealing the following information:

(a) Updraft roots in the moist surface air no longer existed. Weak mass convergence was indicated, but there was no moisture convergence or pressure deficit on the storm's inflow side (right side).

(b) A downdraft principally sustained by precipitation drag (rainfall in excess of 1 inch hr^{-1}) was found under the echo core, in a region of strong pressure gradient.

(c) The pressure perturbation field exhibited a wavelength larger than the storm and therefore is not believed caused by the storm. The pressure wave's cause is unknown but the resulting large pressure gradients superimposed upon the storm's downdraft momentum are believed responsible for the unusually strong winds (for a small dying storm) recorded in the area northwest of the echo. Peak gusts were near 50 kt and five-minute average values were stronger than 30 kt.

By comparison with environment conditions attendant to the tornadic storms occurring later in the evening, factors relating to this storm's decay are surmised to be (1) marginal thermal instability, (2) shallow moisture layer, and (3) a vertical wind shear regime that was not conducive to long-lived convective cells. Vector shear was on the order of 10^{-2} sec^{-1} in 1.5 km layers and marked direction shear existed throughout the cloud bearing layer.

6. ACKNOWLEDGMENTS

The assistance of Mr. Mike Weible, NSSL, in developing radar reflectivity cross sections is appreciated.

7. REFERENCES

Barnes, S. L., 1973: Mesoscale objective map analysis using weighted time-series observations. NOAA Tech. Memo. ERL-NSSL-62, 60 pp.

_____, J. H. Henderson and R. J. Ketchum, 1971: Rawinsonde observation and processing techniques at the National Severe Storms Laboratory. NOAA Tech. Memo. ERL-NSSL-53, 246 pp.

Galway, J. G., 1956: The Lifted Index as a predictor of latent instability. Bull. Amer. Meteor. Soc., 37, 528-529.

Marwitz, J. D., 1972(a): The structure and motion of severe hailstorms. Part I: Supercell storms. J. Appl. Meteor., 11, 166-179.

_____, 1972(b): The structure and motion of severe hailstorms. Part II: Multi-cell storms. J. Appl. Meteor., 11, 180-188.

_____, 1972(c): The structure and motion of severe hailstorms. Part III: Severely sheared storms. J. Appl. Meteor., 11, 189-201.

Wilk, K. E., and K. C. Gray, 1970: Processing and analysis used with the NSSL weather radar system. Preprints of Papers, 14th Radar Meteor. Conf., Tucson, Amer. Meteor. Soc., 369-374.

APPENDIX

Summary of 3-cm Doppler Radar Data Taken on 29 April 1970

Kenneth C. Crawford and Rodger A. Brown

National Severe Storms Laboratory
Norman, Oklahoma 73069

NSSL's 3-cm Doppler radar was converted from CW to pulsed mode in 1964-65 and subsequently used in various studies. It had been equipped in 1969 and early 1970 with an improved data acquisition system and was used intermittently during Spring 1970 at Chickasha, Oklahoma, 26 n miles southwest of NSSL.

During the evening of April 29th, data were acquired with this system from Storm A which approached the site from 221° at 18 m sec^{-1} and began passing almost directly overhead at 1745 CST. Data were collected in the Velocity-Azimuth Display (VAD) mode at 30°, 45° and 60° elevation angles using a gate spacing of 250 meters. Only data acquired during the 15-minute period from 1730 to 1745 have been reduced and this effort required three man-months.

Figure A1 shows the storm as it appeared on the WSR-57 radar at 1739 CST (see also fig. 1 on page 91). Figure A2 shows an example of the VAD-observed average speeds in gates 1-4; the first gate starts at a range delay of 5 μsec (750 m). Elevation angle is 30°.

If the horizontal wind V_h and precipitation fall speed V_f are uniform in the small scanned region, as they may be ahead of the storm core, then these quantities are defined by the VAD equations

$$V_h = \frac{\overline{V}_1 - \overline{V}_2}{2 \cos \alpha} \tag{1}$$

$$V_f = \frac{\overline{V}_1 + \overline{V}_2}{2 \sin \alpha} \tag{2}$$

where α is the elevation angle, $\overline{V}_1$ and $\overline{V}_2$ are the velocities measured in the direction of the wind (where speeds are maxima) (Battan, 1973). Application of (1) and (2) to the data plotted in figure A2 yields wind estimates of 12 m sec^{-1} from 190° at a height of 0.45 km (above ground level; 0.8 km MSL) and 17 m sec^{-1} from 180° at a height of 0.8 km (1.15 km MSL).

During the same time period, a rawinsonde 10 n miles north of the storm (MIN #22, page 25) measured winds 20.9 m sec^{-1}, 170° at 0.817 km (MSL) and 20.9 m sec^{-1}, 184° at 1.2 km. The Noble sounding (#15) was nearly 30 n miles northeast of the storm at 1730 CST and indicated 17.8 m sec^{-1}, 155° at 0.75 km, 17.1 m sec^{-1}, 173° at 1.2 km.

Data from all 10 range gates are plotted in plan view (fig. A3) with the CHK radar in the center. Average velocities are entered to the nearest m sec^{-1}. Negative values indicate motion toward the radar and conversely. The S-shaped velocity pattern is a consequence of vertical wind shear, and small scale irregularities indicate local wind variability.

Attempting to compute two-dimensional winds, thunderstorm reflectivity was depicted in vertical cross section relative to CHK and in the direction of movement (221-041°, fig. A4). During the data collection period, several locations relative to the storm were observed from both northeast and southwest and are shown (fig. A4) by the shaded region along the storm's leading edge. Such observation-pairs were vectorially added (assuming steady-state) to produce a two-dimensional wind in the vertical cross section plane. Basically, these motions (not indicated) were downward, indicating falling precipitation, and in the direction of storm motion. No significant features being noted, this part of the investigation was phased out.

Although the Doppler radar data collected in 1970 contributed little directly to our knowledge of storm morphology and dynamics, the 1970 Doppler project was an important step along the way toward present capability to process large amounts of immensely-revealing velocity data in real time (Sirmans and Doviak, 1973).

ACKNOWLEDGMENTS

We appreciate the careful and laborious efforts of Donald W. Burgess in extracting mean Doppler velocity values from the analog Doppler velocity spectra.

REFERENCES

Battan, Louis J., 1973: Radar Observation of the Atmosphere. University of Chicago Press, 324 pp (see pp 147-148).

Sirmans, Dale and R. J. Doviak, 1973: Pulsed-Doppler velocity isotach displays of storm winds in real time. J. Appl. Meteor., Vol. 12, No. 4, pp 694-697.

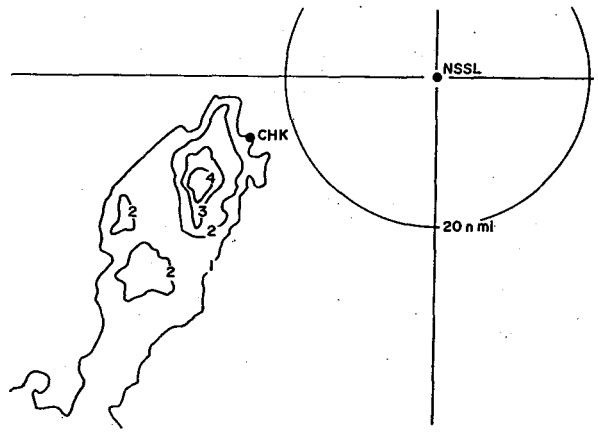

Figure A1. Isoecho contours for Storm A at 1739 CST, 0° antenna tilt. Reflectivities corresponding to coded values are 1 = 19 dBZ; 2 = 25 dBZ; 3 = 35 dBZ; and 4 = 47 dBZ.

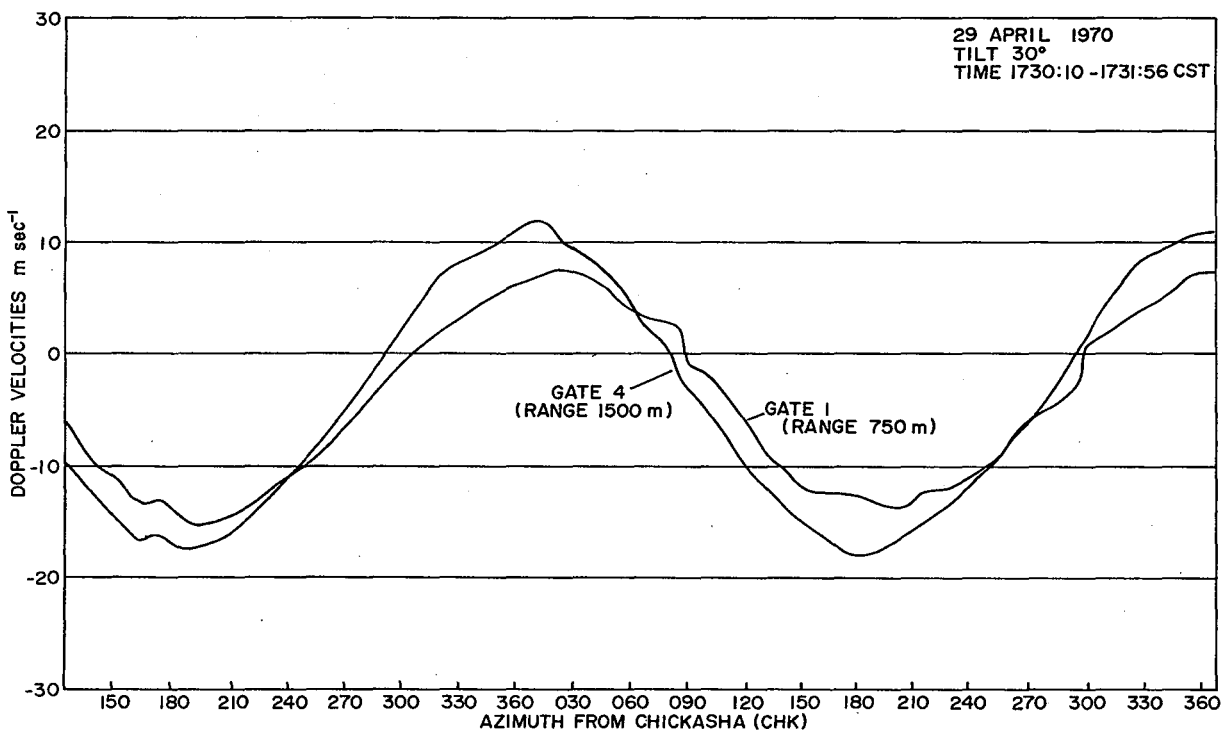

Figure A2. Velocity-Azimuth Display of Chickasha Doppler radar gates 1 and 4.

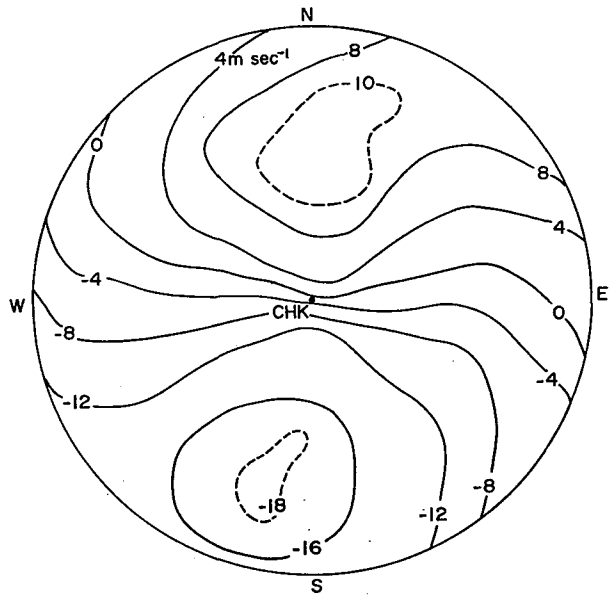

Figure A3. PPI-type display of average Doppler velocities. Positive values are away from CHK radar; time of last data scanned 1731 CST.

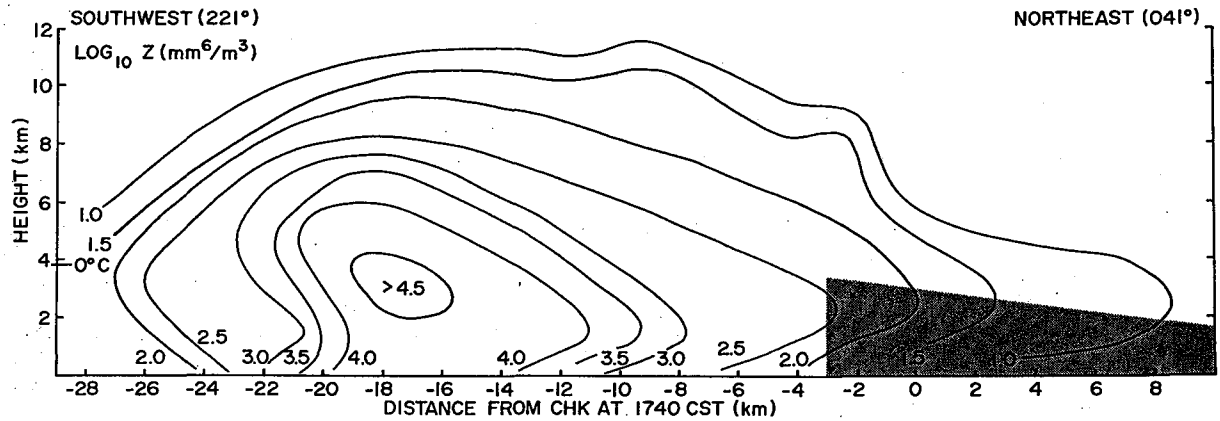

Figure A4. Constructed vertical cross section of reflectivity in direction of storm motion.

THE INTERNAL STRUCTURE OF A THUNDERSTORM AS REVEALED BY θ_w SURFACES

James H. Henderson

National Severe Storms Laboratory
Norman, Oklahoma

On the evening of 29 April 1970, a series of severe thunderstorms moved through the National Severe Storms Laboratory's nine-station meso-rawinsonde network. A total of 58 soundings were taken in and around the thunderstorms. One storm was sampled internally with a rawinsonde entering the storm near 1200 m and ejecting at 6750 m. Another balloon entered around 6500 m in the same storm a few minutes later. A profile of various thermodynamic properties of the storm has been studied. Results are discussed in the paper.

1. INTRODUCTION

During April and May 1970, the National Severe Storms Laboratory operated a network of surface and upper air stations in central Oklahoma as indicated in figure 1. The surface and upper air networks were operated in a manner described by Barnes et al. (1971). One special objective of the 1970 sounding program was to make a serious attempt at placing balloons in updrafts. It has been demonstrated by Barnes (1970) that useful information can be obtained from these updraft soundings. A total of 489 soundings were obtained during the period of operation, several of these being in updrafts.

During the evening of April 29, 1970, a series of eight thunderstorms of varying degrees of severity occurred in or near the network, including two storms which produced tornadoes in Oklahoma City. These data are being extensively studied and results will be reported at a later time. This paper reports the preliminary findings concerning an earlier, less severe storm which was sampled more thoroughly than the tornadic storms. A balloon from the Wheatland site (WHT) was successfully released into an updraft of this thunderstorm which moved northeastward across the middle of the network. Several environmental soundings were also taken around the edges of the thunderstorm at mid-levels.

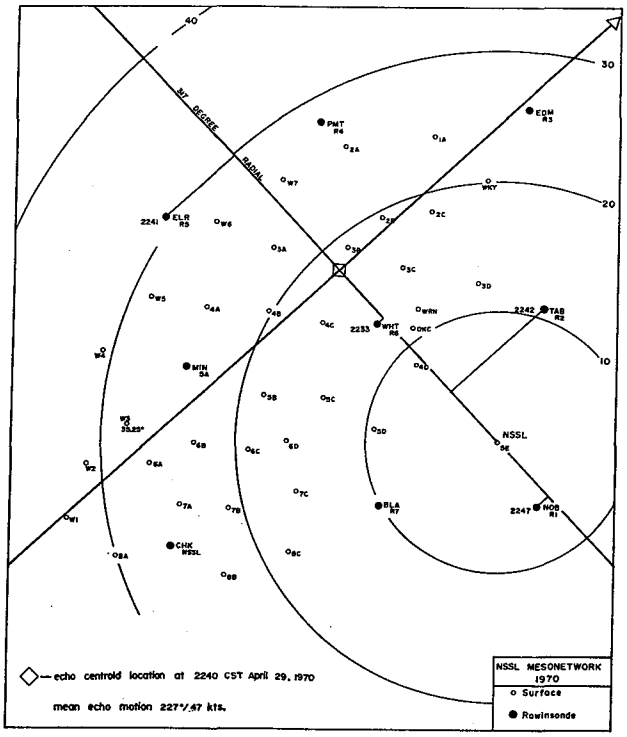

Figure 1. 1970 NSSL surface and upper air networks. Range marks are in nautical miles.

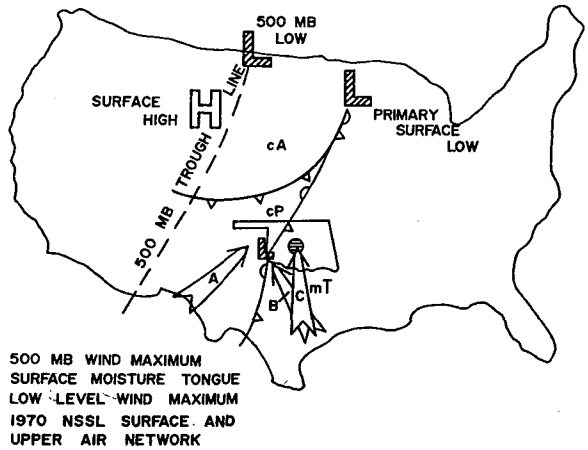

Figure 2. Composite map of synoptic features on evening of April 29, 1970.

2. SYNOPTIC AND MESOSCALE ENVIRONMENT

Figure 2 shows a composite of the synoptic features during the evening of the 29th. A sharp 500 mb trough line was located in western New Mexico with a wind maximum oriented NNE-SSW across eastern New Mexico. An old cP front, coincident with a dry line, was located in western Oklahoma. An open wave later developed along this front in the Texas panhandle. A surface moist tongue with dew points greater than 21°C was underneath a low-level jet with winds greater than 20 m sec^{-1}. The depth of the moist layer increased during the evening from an average of 50 at 1800 CST to 200 mb by 0100 CST on the 30th.

Figure 3 represents the environmental soundings on the right and left flanks of the thunderstorms. Noble, Oklahoma (NOB), is about 70 km SE of El Reno, Oklahoma (ELR). The NOB sounding is on the right flank of the storm and represents the environmental air interacting with the thunderstorm (Fankhauser, 1971). The NOB sounding is more moist and has a characteristic surface θ_W of 21°C. The soundings have very similar lapse rates above cloud base. The environmental winds show some signs of confluence and diffluence aloft. More is said on this subject using a quasi-natural coordinate system in a later section.

3. RADAR HISTORY AND REPRESENTATION OF STORM

The first echo from this storm appeared at 1748 CST at 245°/200 n miles from NSSL radar. About 1923 CST, the core echo split into two parts which by 2050 CST became two separate echoes. After separating, one echo appeared

Table 1.

Coded values of reflectivity and their Log Z_e equivalent. Log Z_e units (mm^6/m^3).

Code	Log Z_e	Code	Log Z_e
1	1	5	4
2	2	6	4.5
3	3	7	5
4	3.5	8	5.5

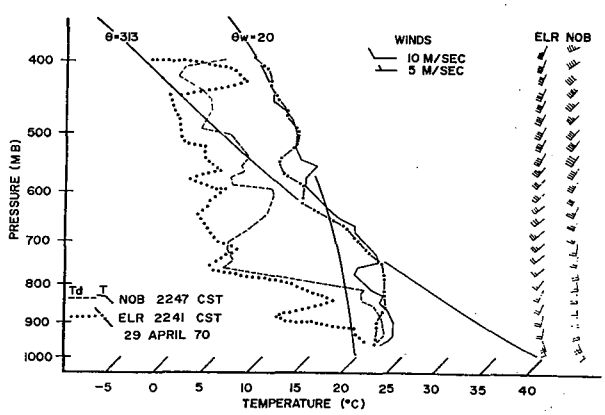

Figure 3. Skew T-Log P diagram of Noble and El Reno environmental soundings.

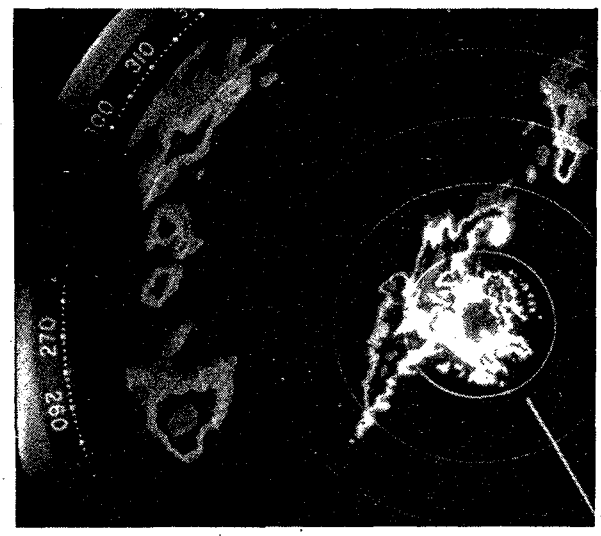

Figure 4. Photograph of NSSL's WSR-57 PPI radar scope at 0° tilt with integrated log contours of radar echo at 2240 CST April 29, 1970. Range marks are for every 20 n miles.

to rotate about the other until they formed a line as they tracked through the network. The northernmost storm is the subject of this study. The echo centroid's mean velocity was 227°/47 kt, along the path indicated in figure 1. Figure 4 shows the 2240 CST PPI representation of the storm (0° antenna tilt). The echo centroid was located at 317°/18 n miles. Figure 5 represents composite radar cross section along the 317° radial. The intensities indicated are coded and correspond to powers of ten in units of mm^6/m^3 as indicated in table 1. The radar contour and display is described by Wilk et al. (1968) and by Sirmans et al. (1970). Intensities were obtained by averaging digitally-recorded reflectivities in gates of one nautical mile over four cross sections through the echo centroid (normal to the storm path) and covering a 30-min period. During this period, the configuration of contours 4 through 7 were quasi-steady while contours 3 and less exhibited greater variability.

The OKC radar indicated a top of 16 km at 2145 CST and 15.5 km at 2245 CST. There was no damage reported with this storm. However, wind gusts to over 50 kt were recorded at several stations in the NSSL surface mesonetwork. Thirty-minute rainfall amounts exceeded 1.0 inches at several stations with some five-minute rates exceeding 6.0 inches/hour.

The composite echo shown in figure 5 has several striking features. There are two reflectivity maxima indicated. The westernmost maximum

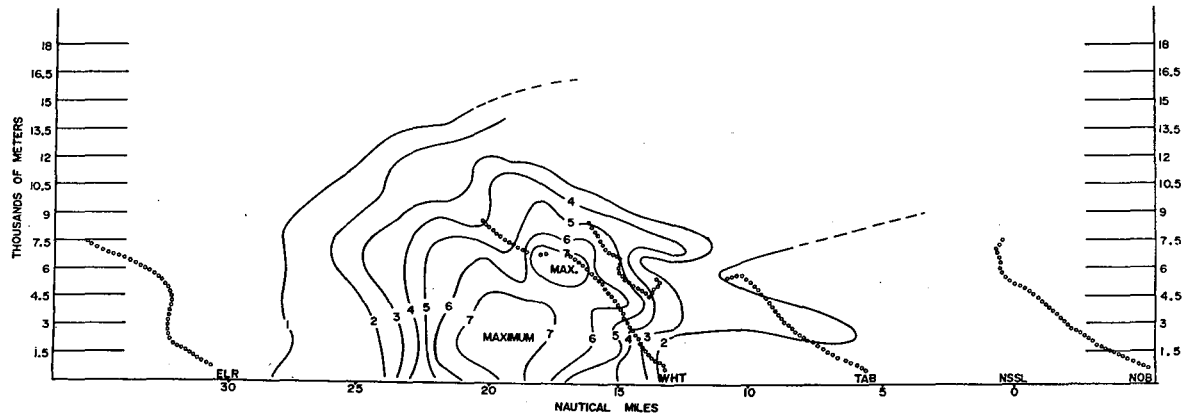

Figure 5. Average composite radar echo along 317° radial centered in time at 2240 CST. Circles indicate projections of balloon positions on 317° radial. See table 1 for explanation of reflectivity code.

associated with the downdraft is in very good agreement with the maximum rainfall pattern for the thirty minute period. The maximum aloft appears to be near the top of a quasi-steady updraft as indicated by the Wheatland (WHT) sounding to be discussed later. The echo gradient near the "wall" may extend closer to NSSL but detailed structure closer than 13 n miles is lost in the ground clutter.

4. THE UPDRAFT SOUNDINGS

4.1 Positioning the Data

A natural coordinate system was used to develop the cross sections. The origin was placed at 317°/18 n miles from NSSL, the position of the echo centroid at 2240 CST. The s-axis was aligned along the mean direction of the echo centroid movement (toward 47°). The n-axis is toward the right and along the 317° radial from NSSL. The horizontal displacements of the four balloons which sampled the storm were projected onto the 317° radial for every 150-m altitude (MSL). These points are indicated by circles in figure 5. A careful examination of the raw data indicated that each sounding had good signals and good tracking data.

4.2 Vertical Trajectories of the Balloons

The NOB and ELR soundings exhibit characteristics similar to other environment soundings obtained earlier and later except that both the balloons tend to move away from the radar echo above 6 km. This will be elaborated in a later section. The WHT sounding apparently entered the cloud base around 2 km. The balloon, which was in the radar echo from the start, accelerated upward from around 1500 m which was apparently 500 m below cloud base. The balloon continued at above-normal ascent rate (up to 24 m sec^{-1}) until rapid deceleration took place near the upper reflectivity maximum. The balloon then accelerated upward again (at 10 m sec^{-1}). Breakdown of the principal

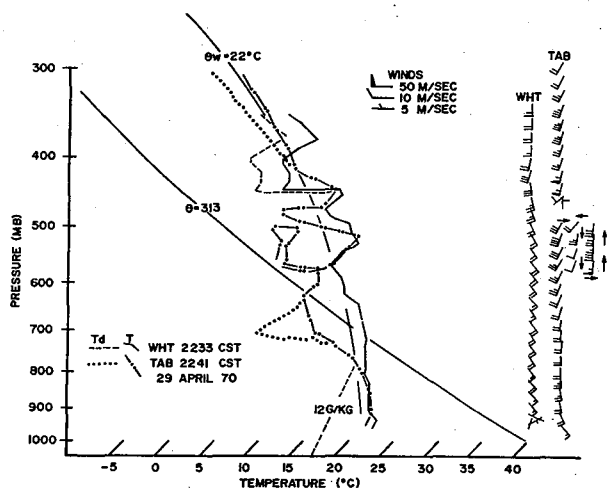

Figure 6. Skew T-Log P diagram of Wheatland and Tinker Air Base soundings inside thunderstorm. Moist adiabatic ascent is along the 23°C θ_w curve. Note the TAB soundings up and down path.

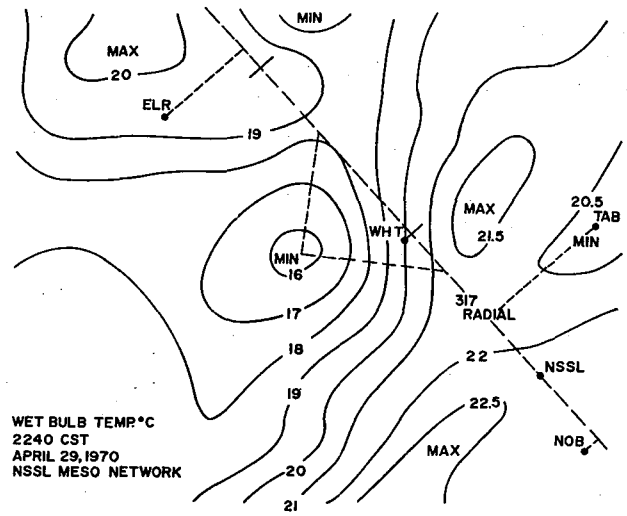

Figure 7. Surface pattern of θ_w across NSSL SFC network at 2240 CST, April 29, 1970. Bold lines along 317° radial represent right and left flanks of echo from figure 5. Jog in 317° radial was introduced to project θ_w min. onto radial.

updraft above 5 to 6 km altitude has been noted by several investigators including Barnes (1970), Marwitz and Berry (1971), Sinclair (1969), Steiner and Rhyne (1962).

Figures 5 and 6 reveal that the Tinker Air Base (TAB) sounding rises to 800 mb moist adiabatically along the 23°C θ_w curve. Calculations using this balloon's data revealed organized convergence from the overhang into the updraft up to 1.5 km. The lapse rate then changes from moist adiabatic to dry adiabatic up to 3.0 km. Figure 5 indicates balloon movement toward echo of higher reflectivity in this layer. Strong lateral movement toward the storm is indicated at around 5700 m. The trajectory of the balloon indicates a possible indirect circulation aloft driven by a branch of the main updraft. Examination of the TAB wind sounding (fig. 6) indicates speed in excess of 50 m sec^{-1} in this layer. The soundings at ELR and NOB both indicate speeds of 40 and 45 m sec^{-1}, respectively, at this level. This indicates strong mixing between the environment and the storm in this region. The fact that the balloon begins a rapid acceleration above this level with moist adiabatic ascent along θ_w = 22°C and the behavior of the WHT balloon indicate branches of the updraft persist in the upper portions of the echo.

5. WET-BULB POTENTIAL TEMPERATURE STRUCTURE OF THE RADAR ECHO

Figure 7 details an objective analysis of the surface pattern of wet-bulb potential temperature, θ_w, over the NSSL surface network (see fig. 1) at 2240 CST. The objective analysis makes use of a refinement of Barnes' (1964) technique which includes time-to-space conversion of five-minute observations weighting each observation according to its distance from a grid point and

the difference between observations time and map time.

The pattern reveals an area of $\theta_w > 21°C$ which is associated with the updraft. Air with $\theta_w \leq 16°C$ is considered to be downdraft air. The two short lines perpendicular to the 317° radial represent the right and left edges of the radar echo.

The problems involved in displaying a four-dimensional phenomena in two dimensions are candidly illustrated in figure 7. The 16°C values associated with the downdraft do not lie along the 317° radial. In order to illustrate this major feature of the storm, the θ_w minimum was projected onto the cross section shown by figure 8. Otherwise, the surface values were taken along the 317° radial. Figure 8 reveals a striking resemblance to Newton's schematic model (Newton, 1966). The downdraft air has θ_w of 18°C or less with a core of 16°C. The updraft core has a value of 22°C or greater.

The cross section of θ_w was analyzed independent of the radar echo and the two patterns were then superimposed. Slight adjustments of the θ_w pattern were accomplished using the radar echo and figure 9 (an analysis of the u component of velocity).

5.1 The Updraft

Air having $\theta_w \geq 22°C$ is found in a 1 km deep layer on the right flank in the NOB sounding 35 km from the base of the tilted updraft. This layer deepens to 2 km as air approaches the echo (TAB sounding). In the radar echo, air with $\theta_w \geq 22°C$ coincides nicely with the apparent echo weak region.

The updraft as described by the θ_w surfaces shows two distinct branches based on the WHT and TAB soundings. Both branches appear slightly above and tilting toward areas of maximum radar reflectivity. Air with $\theta_w < 23°C$ between the two branches may be evaporationally cooled air from above which has descended into the region of maximum water load. This is also suggested by the fact that the WHT balloon experienced downward motion in this area (-6 m sec^{-1}).

It is interesting to speculate on the small-scale features in the right edge of the radar echo. Minimum θ_w (< 18°C) indicates ambient air inside the echo overhang. Above the overhang, $\theta_w > 20°C$ indicates air that has been associated with the updraft has moved laterally out of the intense echo region.

Around 5700 m on the right edge, the TAB balloon appears to be involved in a rotary type of motion as it is brought into a more intense portion of the echo. Wind speeds, echo contours, and θ_w values indicate that this sub-circulation is a real phenomenon. The change in value of θ_w from 18 to 24°C and acceleration upward (to 19 m sec^{-1}) reveal that the balloon was entrained into updraft air.

5.2 The Downdraft

The θ_w structure of the downdraft shown in figure 8 involves more speculation than the updraft due to lack of data. However, following the guidance of previous researchers in this field (Hookings, 1965; Newton, 1966),

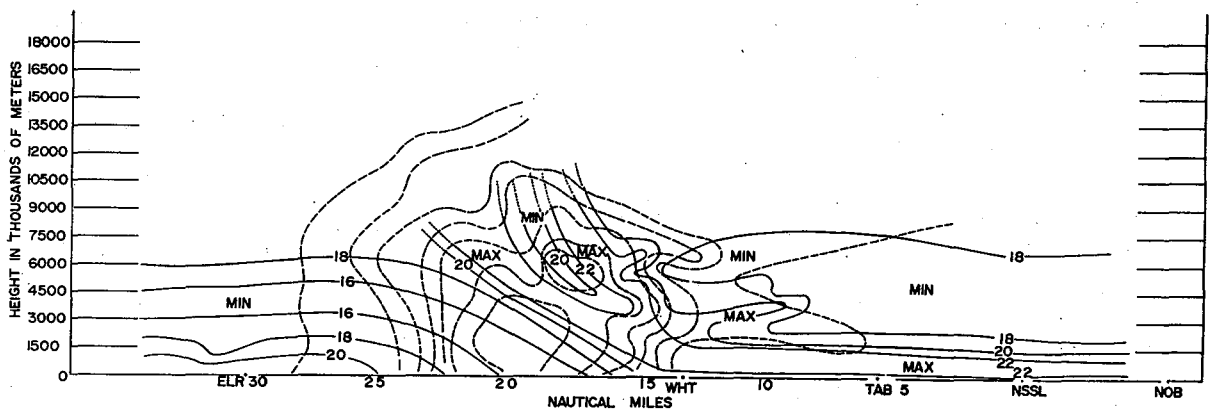

Figure 8. θ_W pattern along cross section of average composite radar echo. Maximum values of $\geq 22°C$ indicate updraft air. Minimum values $\leq 18°C$ indicate downdraft air. Note two branch updraft with reflectivity maximum in between.

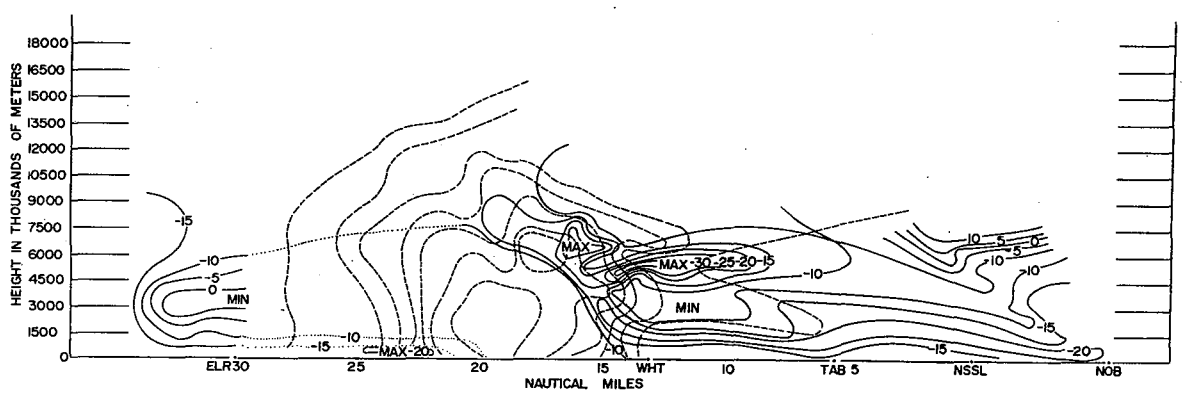

Figure 9. U-component along cross section of average composite radar echo (-u) values indicate air moving toward left edge of cross section. Values are in m sec^{-1}. Note that -20 m sec^{-1} max along right flank of echo into the echo-weak region of the radar composite agrees nicely with θ_W of > 22°C.

the area of minimum values 18°C or less found near the downdraft at the surface and the mid-level band of 18°C or less found at ELR are connected. In support of this, the u component of velocity (fig. 9) shows evidence of air moving toward the radar echo in the same layer, and an analysis of the v component (not included here) indicates that this air is moving in the s-direction with about the same speed as the echo.

The tight gradient between updraft and downdraft air is an extrapolation of the surface analysis and represents conceptually continuous regeneration of the updraft due to mechanical lifting of warm moist air along the

convergence zone on the right flank of the echo. An objective analysis of the surface wind field at 2240 CST (not shown) depicts a convergence-divergence couplet which supports this idea.

6. KINEMATIC FEATURES OF THE RADAR ECHO

6.1 Winds

Wind speeds and directions at WHT (fig. 6) show a very marked deviation from those at the other three stations. The direction is consistently southeast at speeds of 15 - 20 m sec^{-1} until the balloon exits one branch of the updraft (see fig. 8).

Speeds and directions in the updraft are similar to the speeds and directions of the subcloud layer on the right flank of the echo (see figs. 3 and 6 for the low-level winds at TAB and NOB). This is simply a verification of the concept that the undiluted updraft is a very efficient mechanism for vertical transport of low-level momentum. The fact that the wind speed and direction change to resemble more closely the ambient winds above 6 km is a further indication of the breakdown of the main core of the updraft.

Note from figures 5 and 8 that as the WHT balloon encounters the second branch of the updraft the wind direction backs to again resemble the flow near the subcloud layer. This fact, coupled with the increase in θ_w, supports the analysis of a second branch of the updraft along the echo weak region of the storm.

6.2 U-Component of Flow

In order to better represent the flow pattern in the plane of the cross section, the wind components were calculated in the natural coordinate system. Figure 9 is an analysis of the u-component along the plane of the cross section. The v-component is not presented here for lack of space.

Because of inadequate data along the s-direction, it is difficult to make specific arguments as to the actual divergence-convergence pattern. However, if one makes the assumption that the flow into the cross section is constant at any given point, i.e. $\partial v/\partial s = 0$, then the divergence is given by $\partial u/\partial n = -\partial w/\partial z$. The $\partial w/\partial z$ term was calculated for the four soundings over 300 m layers. These values were then used to subjectively adjust the analysis of the u-component. This approach worked nicely in the area of the environmental soundings at low and mid-levels, but the two patterns were somewhat inconsistent above 6 km suggesting that $\partial v/\partial s$ is possibly non-zero.

Examination of figure 9 reveals the following:

a. The right flank of the echo is characterized by convergence except for small areas of divergence associated with the overhang and the "rotor" aloft.

b. On the left flank there is divergence in the lowest km, convergence is implied over a 2 km thick layer and then divergence above 3 km.

7. CONCLUDING REMARKS

A rather consistent pattern of storm structure emerges from this analysis of mesoscale data from radar, surface and upper air networks. The radar reflectivity pattern was characterized by features now thought to be indicative of large severe thunderstorms, i.e., low-level echo wall or horizontal gradient maximum, and overhanging precipitation on the right flank, weaker echo regions associated with the updraft air entering from the right flank and a reflectivity maximum below and to the left of the updraft (viewed along the storm's path). In addition, a second reflectivity maximum was observed at higher altitude, possibly located between two branches of the updraft. The composite data also suggest strong interaction with the right flank in the form of large horizontally-rolling circulations, possibly driven by the updraft. The three-dimensional nature of these circulations is not clear, nor is their degree of steadiness.

The updraft structure compares very nicely with that of other investigations. The data suggest a single updraft at low levels which branches at mid-levels and eventually breaks down into a highly turbulent regime. Downdraft air is apparently entrained laterally (along the cross section) from the mid-level air sweeping along with the storm, descending to the surface near the precipitation core.

Many details are still lacking, however. The origin of overhanging precipitation along the right flank is not understood. The anvil characteristics went largely unobserved by either soundings or radar. Structure along the storm path was not observed.

8. ACKNOWLEDGMENTS

The author wishes to thank Dr. S. L. Barnes who provided the guidance for this study.

9. REFERENCES

Barnes, S. L., 1964: A technique for maximizing details in numerical weather map analysis. J. of Appl. Meteor., 3, 396-409.

_____, 1970: Some aspects of a severe right-moving thunderstorm deduced from mesonetwork rawinsonde observations. J. Atmos. Sci., 27, 634-648.

_____, J. H. Henderson, and R. J. Ketchum, 1971: Rawinsonde observation and processing techniques at the National Severe Storms Laboratory. NOAA Tech. Memo., ERL NSSL-53, 246.

Fankhauser, J. C., 1971: Thunderstorm-environment interaction determined from aircraft and radar observations. Monthly Weather Review, 99, 171-192.

Hookings, G. A., 1965: Precipitation-maintained downdrafts. J. Appl. Meteor., 4, 190-195.

Marwitz, J. D., and E. X. Berry, 1971: The airflow within the weak echo regions of an Alberta hailstorm. J. Appl. Meteor., 10, 487-492.

Newton, C. W., 1966: Circulation in large sheared cumulonimbus. Tellus, 18, No. 4, 699-713.

Sinclair, P. C., 1969: Vertical motion and temperature structure of severe convective storms. Preprints of Papers, 6th Conf. on Severe Local Storms, Chicago, Amer. Meteor. Soc., 346-350.

Sirmans, D., W. L. Watts, and J. Horwedel, 1970: Weather radar signal processing and recording at the National Severe Storms Laboratory. JEEE Trans. Geosci. Electron., GE-8, 88-94.

Stiener, R., and R. H. Rhyne, 1962: Some measured characteristics of severe storm turbulence. NSSP Rept. 10, U. S. Weather Bur., Washington, D. C., 17.

Wilk, K. E., and Edwin Kessler, 1968: Radar measurements of precipitation for hydro-logical purposes. World Meteor. Org (IHD), Report No. 5, 30-46.

A DETAILED DESCRIPTION OF THE INTERNAL STRUCTURE OF A THUNDERSTORM

James H. Henderson

National Severe Storms Laboratory
Norman, Oklahoma 73069

During the evening of 29 and 30 April 1970, one large non-tornadic thunderstorm, growing in the wake (northeast) of an equally large storm, was sampled internally on three different occasions as it traversed the NSSL surface and upper air mesonetwork. Thermodynamic and kinematic details of this echo are revealed by superimposing the radiosonde data on digitally-produced CAPPI displays. Cells originate at the right rear and dissipate near the left front in agreement with concepts by Hitschfeld, Marwitz and Berry. Adverse vertical wind shear prevented these large storms from attaining typical supercell characteristics, inducing instead a multi-celled structure. The effect of precipitation loading the updraft is made particularly evident by a sounding launched into the wake storm. Encountering high liquid water amounts at 4 to 6 km, the balloon decelerated, even though in air with temperature excess +5C.

1. INTRODUCTION

During the evening of April 29, 1970, a series of eight thunderstorms of varying degrees of severity moved through central Oklahoma, the National Severe Storms Laboratory surface and upper air network. Henderson (1971) has described that synoptic situation. One non-tornadic storm complex moving northeastward was sampled by no less than 23 rawinsonde ascents during a three hour period. Data were obtained on all flanks and inside the storm.

Surface and upper air network operations were reported by Barnes et al. (1971); the radar display, explained by Wilk and Gray (1970). Computer programs displayed digital radar reflectivities as CAPPI maps (Marshall, 1957) on scales compatible with surface and upper air maps. RHI displays were fabricated by rearranging the data from 12 PPI scans (four minutes) obtained as the antenna was tilted from 0 to 20 degrees. The surface analyses were accomplished in an objective manner on the CDC 6400 at MSC-NASA, Houston, Texas (Barnes, 1973).

Of 23 soundings only four are discussed here since they most closely relate to the storm of interest. The four soundings combined with a myriad of surface and radar data reveal some of the complex kinematic and thermodynamic structure of this thunderstorm, particularly its updraft.

2. RADAR HISTORY, ITS RELATION TO SURFACE FEATURES

Figures 1 through 4 show the digital PPI echo representation at 20-minute intervals from 2200 CST to 2300 CST. Part of the echo is obscured due to range delay and ground targets. (Figures 3 and 4 candidly illustrate difficulties with having a research radar near the middle of the surface and upper air networks.) The reflectivity intensities, figures 1 through 4, correspond to powers of ten in units of mm^6/m^3, table 1.

Table 1. Coded Values of Reflectivity and Their Equivalent Log Z_e Units (mm^6/m^3).

CODE	LOG Z_e	CODE	LOG Z_e
1	1.5	5	4.5
2	2.2	6	4.9
3	3.2	7	5.2
4	3.9	8	5.7

Growth and dissipation of new cells within the echo complex agreed with other researchers (Hitschfeld, 1971; Marwitz and Berry, 1970) in that new cells originated at the right rear and dissipated near the left front. Figure 1 shows cell "A" (arrow) on the right rear flank of the echo complex. This cell developed just prior to entering the network and by 2200 CST has attained intensity level 6 with tight gradient on its right rear flank. By 2220 CST (fig. 2) this cell A expands and moves away from the region of tight gradient. RHI data (not shown) indicate by 2220 CST a new cell develops aloft and south of the tight gradient area.

By 2240 CST, the newly-developed cell "B" dominates the northernmost echo complex, but the WER (Weak Echo Region after Chisholm, 1970) and details of the intense echo gradients are lost due to ground targets. However, these will be seen later in the CAPPI presentations. Figure 3 also shows the southernmost echo complex directly upstream. Implications of its effect on the northernmost echo are discussed later. By 2300 CST (fig. 4), cell B shrinks and decreases intensity.

The lifetime of this cell has been about 40 min. Finally note, the multicellular characteristics of both echo complexes during passage through the network (fig. 1 through 4). Large cells in the echo complex are more intense and long-lived than the small cells whose lifetimes were near 20 min and whose sizes were of a spatial scale too small to be observed by the NSSL surface network.

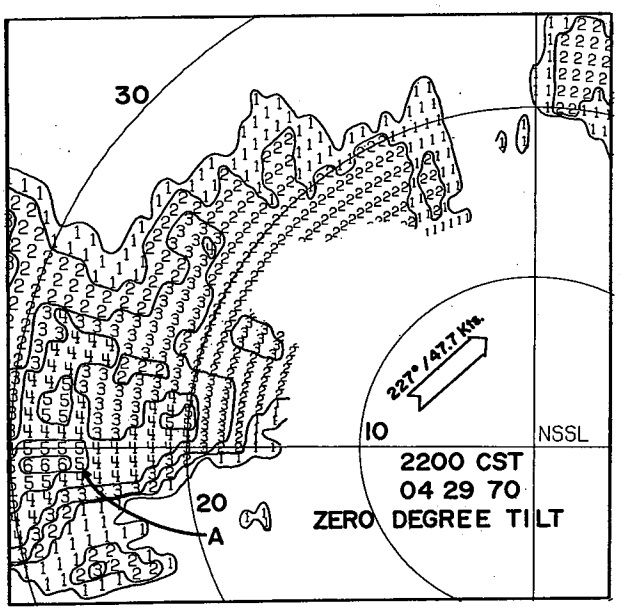

Figure 1. Digital SFC radar echo (coded), average storm motion was 227°/47.7 kt. Contours were hand analyzed.

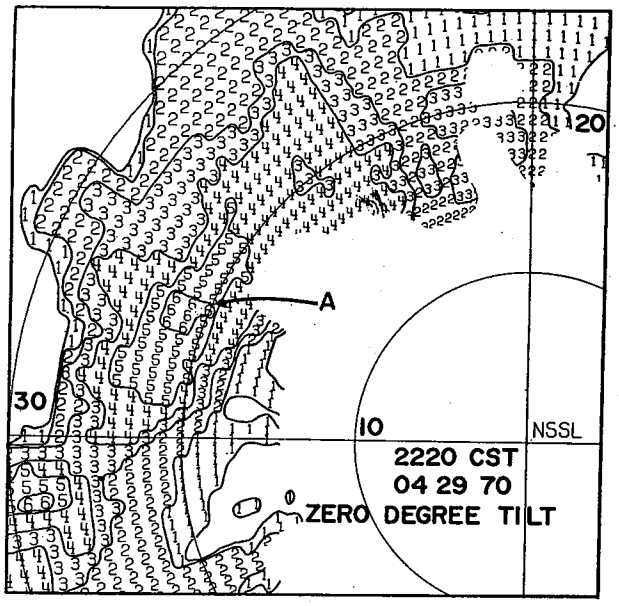

Figure 2. Cell A in mature state. New development occurring southeast of cell A.

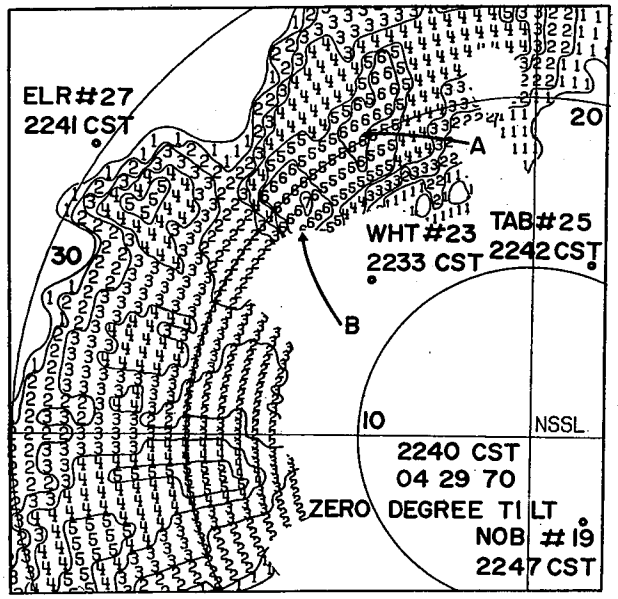

Figure 3. Note new cell B. Dots are radiosonde sites. Time of launch pertinent to this study are shown.

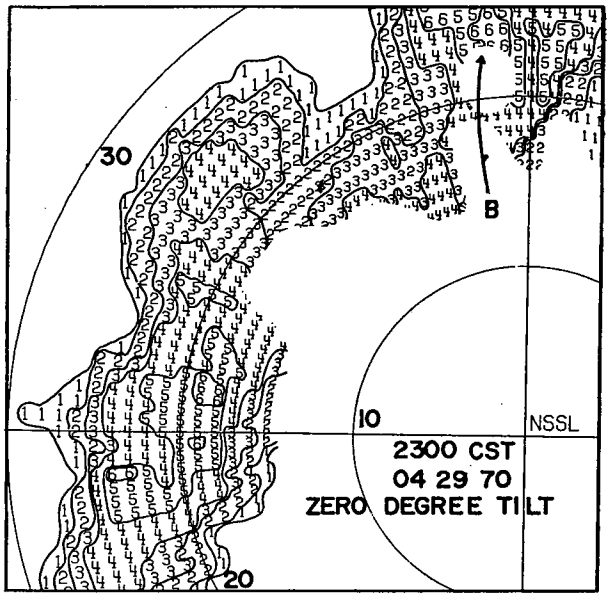

Figure 4. Network now dominated by southernmost echo complex. Note multicellular characteristics of both echo complexes.

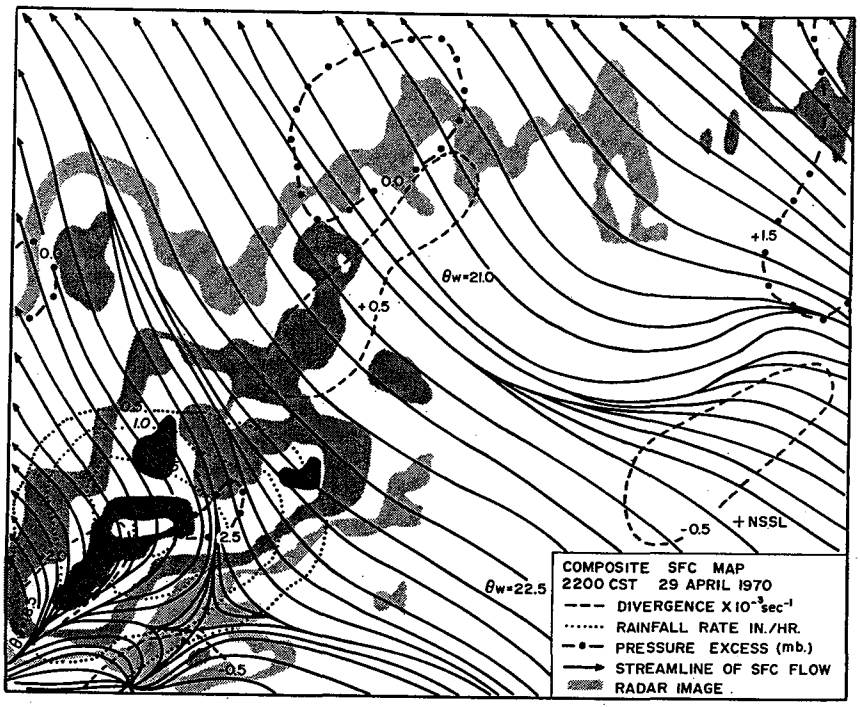

Figure 5. A composite of objective analysis maps at 2200 CST. Radar image is taken from figure 1.

Figure 5 is a 2220 CST composite of important surface features associated with the storm. The shaded image represents the radar echo corresponding to figure 1. Important features found were similar to those of other researchers (Fujita, 1963; Stout, 1957; Charba and Sasaki, 1971). These features were excess[1] pressure and maximum rainfall rates near the echo core, divergence along the middle of the echo with a maximum centered near the southwest corner relative to the storm's motion, convergence and deficit pressure near the updraft region. In the streamline flow pattern, sources were associated with the echo core while sinks were found near the updraft. Col areas usually located the transition from source to sink.

The 2200 CST composite map (fig. 5) shows that a line source in the streamline flow pattern is enclosed by a divergence center in excess of 2.0×10^{-3} sec^{-1}. Moreover, the echo associated sink is enclosed by convergence center with a maximum value near -0.5×10^{-3} sec^{-1}. Rainfall rates are above 2 inches hr^{-1} while excess pressure shows a center over 2.5 mb. Other maps (not shown) identical to figure 5 were analyzed from 2100 CST until 0000 CST at five-minute intervals. These results are discussed below.

[1]Deficit and pressure centers were determined in the manner described by Barnes (1972).

The updraft associated sink in the streamline pattern remained a steady state feature during its passage through the network. The area under the sink's influence gradually increased until 2240 CST. The convergence center showed the same trend reaching a maximum of -1.8×10^{-3} sec^{-1} at 2235 CST and thereafter it decreased. The increase in convergence is associated with the new cell development (Cell B, fig. 3).

Recall from figure 5 that a line source is present along the echo center at 2200 CST. At 2205 CST a point source appears in the flow pattern along the southwest edge of the echo. This point was to the rear of the divergence center and apparently is separate from the descending air associated with the "rainy downdraft." This feature moved with cell A (fig. 2) until 2235 CST when it disappeared. The outflow from the echo went back to the form of a line source. The disappearance of the point source coincides with a decrease in the divergence pattern to a minimum value below 1.8×10^{-3} sec^{-1}. At 2235 CST, RHI data indicates cell B attained its greatest height and maximum reflectivities aloft began to descend. The divergence values at the surface began to increase, reaching a maximum of 2.4×10^{-3} sec^{-1} by 2255 CST. Five minutes prior to this, the source point reappeared in the streamline pattern. Disappearance and reappearance implications of the source point relate to the growth and dissipation of this echo and are discussed later.

Rainfall rates associated with echo A did not exceed 2.5 inches hr^{-1}. The rate with echo B (fig. 3) increased rapidly after 2235 CST. A maximum rate near 5 inches hr^{-1} was reached prior to the echo moving out of the network at 2300 CST.

Echoes A and B had associated pressure excess centers. Though rainfall rates were much heavier with echo B, both cells had maximum pressure excesses near 2.5 mb. Centers of deficit pressure were different than that found by other researchers (e.g., Stout, 1957) in that the centers were found to the right of the sink and maximum convergence area associated with the updraft. This was a consistent feature during the passage of the storm through the network. The maximum deficit pressure was -1.5 mb at 2235 CST.

Finally, the reader notes that the vorticity patterns have been left out of the surface composite map. Most vorticity centers associated with this storm were small and their values were of order 10^{-4} sec^{-1}. Contrast Barnes (1972) results for the two tornadic storms which occurred later this night.

3. UPPER AIR ENVIRONMENT

Figure 6 shows the hodograph of the Edmond #23 rawinsonde launched at 2018 CST. This sounding represents the environmental flow during the early evening. The average movement of the echo (fig. 1) was to the right of all the environmental winds. Winds in the first 3 km veered as flow typical of a Great Plains thunderstorm often does (Fankhauser, 1971; Marwitz, 1972). Above 3 km, there is strong backing indicated up to 7.5 km. This is not a typical shear pattern. As evening progressed, the shear structure changed (Barnes, 1972) to resemble a more typical supercell storm environment.

Though once considered to be detrimental to convection, shear is now thought to play a significant role in intensifying and prolonging convective systems (Marwitz, 1972). The ability of the environmental winds to erode the clouds and precipitation sheath from around updraft cores thus keeping them from becoming surrounded by high concentrations of liquid water which would collapse them (Hitschfeld, 1959) is an important consideration in this paper. If the shear mechanism is altered, then updrafts would more resemble those of the thunderstorm project (Byers and Braham, 1949).

Figure 7 soundings represent the ambient thermodynamic field. NOB (Noble) represents the environment on the right flank of the echo. Though somewhat modified by the echo itself, the sounding is convectively unstable (Lifted Index, -7) and typical of a tornado-producing air mass (Miller, 1967). On the other hand, ELR (El Reno) has a more stable sounding on the left flank. This air is dryer at all levels.

Figure 8 identifies balloon positions at 1.5 km levels. Wind velocities are in m sec^{-1} at the heights indicated. A striking feature, also noted in a previous paper (Henderson, 1971), is the movement of the NOB and ELR balloons away from opposite flanks of the echo above 4.5 km. Recall in figure 3, the larger echo complex southwest and upwind of the storm under study. This echo complex moved from 217°/35.7 kt or 10° left of the northernmost echo. Objective analyses of the 23 soundings (not shown) reveal diverted flow aloft around this southernmost echo. The flow in the vicinity of the northernmost echo resembles wake flow behind an obstacle. The flow should then be a mixture of the updraft and ambient air. Therefore, updraft rising into this modified air experiences less shear. The net effect of this altered flow on the storm structure is discussed in the next section.

4. INTERNAL STRUCTURE OF THE RADAR ECHO

After Barnes (1970) demonstrated that useful information could be obtained from in-storm soundings, one primary objective of the 1970 observation program was to make a serious attempt at placing balloons into thunderstorm updrafts. As the radar echo entered the southwestern corner of the network, it began to take on characteristics identified with organized updrafts (Marwitz et al., 1972). On the right rear flank, there was a concavity open to the subcloud winds, and a steep echo gradient immediately adjacent to the weak echo notch. Extrapolating the movement of these features, it was determined that the most favorable chance to launch into the updraft would occur at the WHT (Wheatland) site. The condition for launch was the arrival of a wind shift which indicated that outflow from the storm was influencing the station. The balloon rose to the southeast in the outflow until about 1 km above the surface where it encountered the updraft. The balloon then turned northwestward and moved perpendicular to the storm's motion into the echo gradient.

Along this trajectory, moist-adiabatic ascent (θ_w = 23 C) occurred up to 4.5 km (fig. 9). The WHT balloon experienced maximum vertical velocity[2]

[2]These vertical velocity profiles were obtained by the simple differencing technique $\Delta Z/\Delta t$ over a ΔZ of 300 m. The profiles shown are with the average balloon ascention rate in the lowest 1.5 km removed. Accuracy is assumed to be $\pm$ 1 m sec^{-1}.

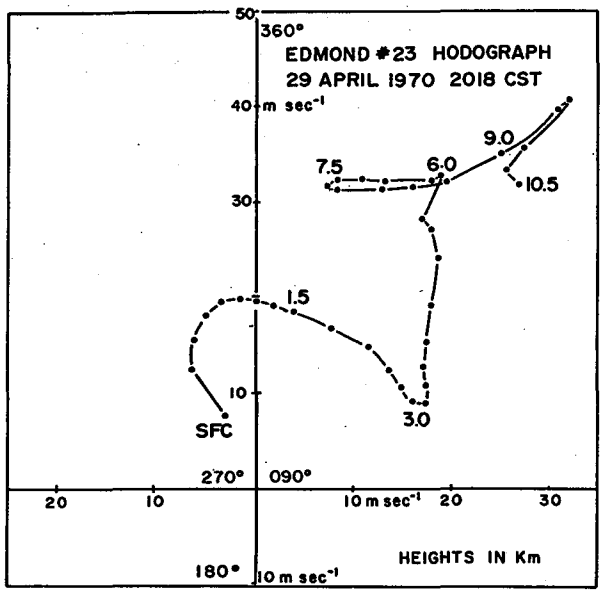

Figure 6. Hodograph representing environmental flow early in the evening. Note the strong backing from 3 - 7.5 km.

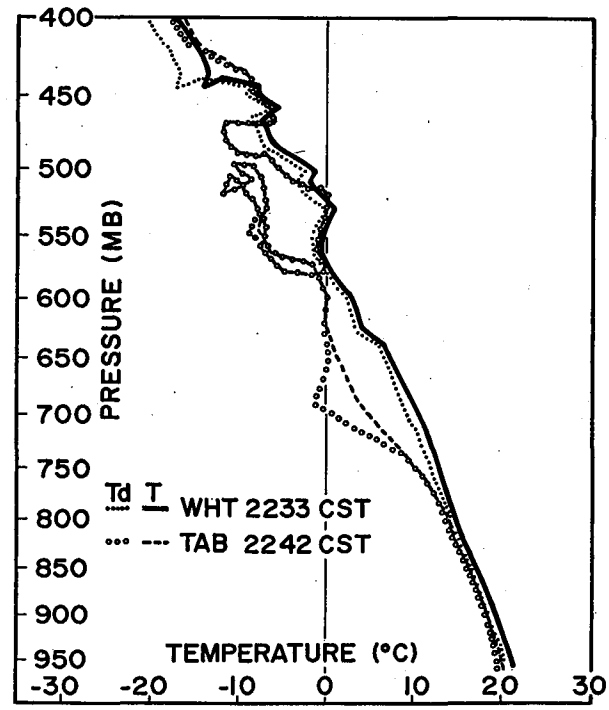

Figure 7. Environmental soundings. NOB is a right flank sounding while ELR was launched on the left flank.

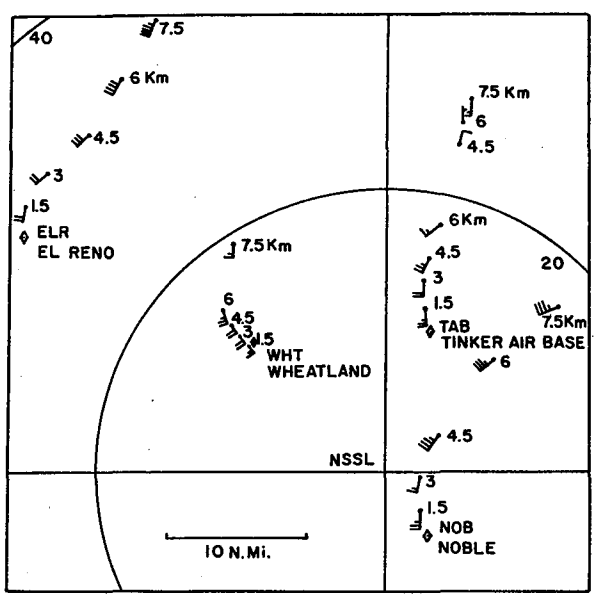

Figure 8. Position of balloons used to describe upper flow. Times of launch are those given in figure 3.

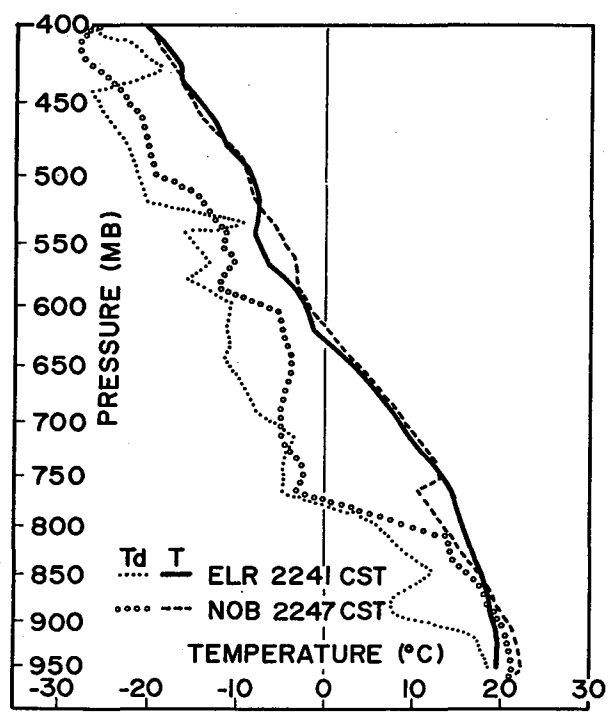

Figure 9. In-storm soundings. Note up and down behavior of TAB balloon. WHT balloon sinks then rises near 7 km.

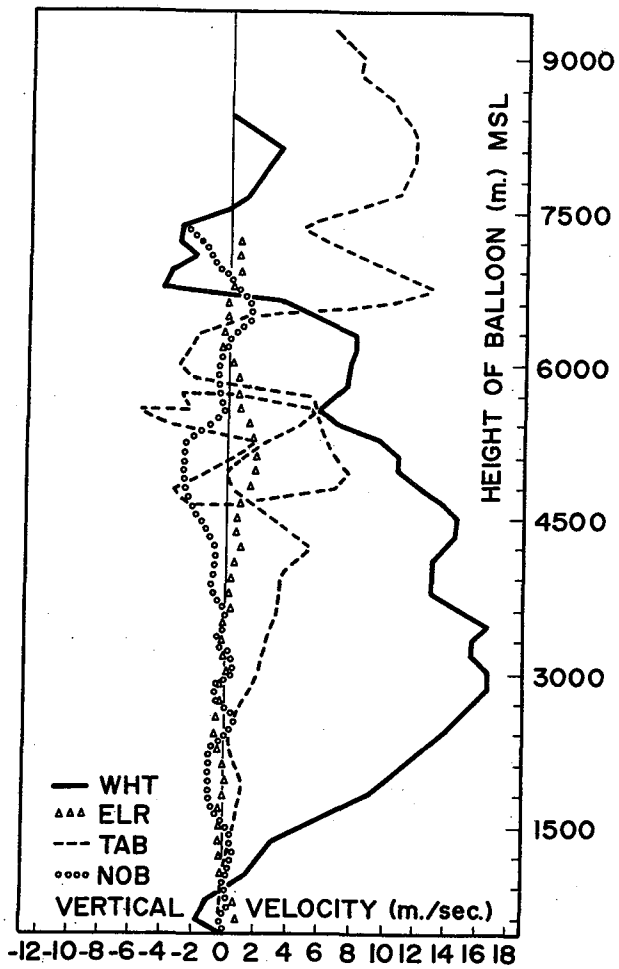

Figure 10. Vertical velocity profiles of the radiosondes--balloon vertical velocity subtracted.

(17 m sec^{-1}) between 3 and 4 km (fig. 10). Note that the first marked deviation from moist-adiabatic ascent (fig. 9) occurred above this level.

Figure 11a through e show the positions of the WHT balloon in relation to the CAPPI echo at the altitudes indicated Echo patterns for heights 1.5, 3.0, and 4.5 km at 2230 CST and 2240 CST were averaged to produce the pattern at 2235 CST (digital data for the scan at 2235 CST was not available). The balloon moved upward into a region of strong echo indicating maximum water load in the updraft. The temperature field at 4 km (not shown) revealed updraft temperature excess of +5.1C. Many convection models (e.g., Kessler and Bumgarner, 1971) indicate that the updraft should continue to accelerate, yet the observation indicates just the opposite.

One possible explanation of this paradox relates to the previous discussion of storm ventilation by a sheared environment. Because the flow separates around the southernmost storm, the shear mechanism less effectively removes water from the updraft column. This water mass reduces the effective buoyancy of the updraft. One other effect of this reduction in shear would be to increase the precipitation efficiency of the storm. This probably happened with echo B which produced the highest rainfall rates of the evening over the northern portion of the network.

An alternative argument to the above explanation might be that the balloon left the updraft, thereby experiencing a decrease in vertical velocity. However as previously pointed out, a large temperature excess still existed above 4 km and figure 8 shows the WHT wind speeds and directions up to 6 km are similar to those found in the subcloud layer on the right flank of the echo. This then would be a confirmation of the concept that the undiluted updraft is a very efficient mechanism for vertical transport of low-level momentum.

Near 6 km (fig. 11d) the WHT balloon exits the southwest portion of the intense echo gradient. This exiting is marked by temperature fluctuation and a rapid falloff in vertical velocity (fig. 10). This then would represent the area of strong mixing in the sheath surrounding the updraft core.

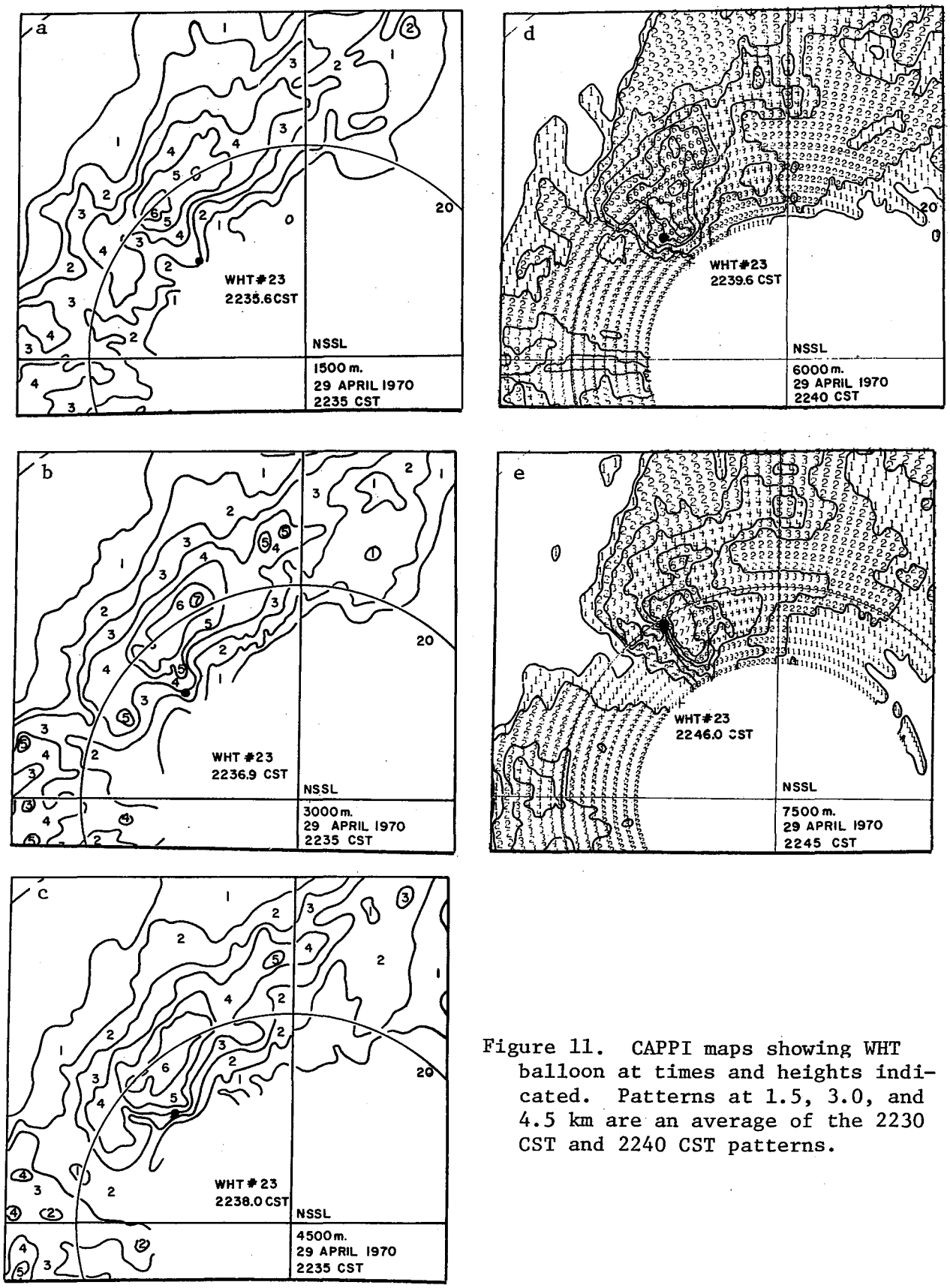

Figure 11. CAPPI maps showing WHT balloon at times and heights indicated. Patterns at 1.5, 3.0, and 4.5 km are an average of the 2230 CST and 2240 CST patterns.

The fact that the balloon did exit the updraft near 6 km may be attributed to any of several causes. Theory suggests that an adverse pressure gradient will cause a transition from laminar to turbulent flow, thus destabilizing the velocity profile. Adverse pressure gradient may come about from several causes. Among these are the thermally-induced pressure excess in the updraft at altitude (Barnes, 1970; Davies-Jones and Ward, 1971), pressure effects from the accumulated water and dynamic pressure effect.

Between 6 and 7.5 km, the balloon entered a weak echo region (fig. 11e) whereupon it descended briefly (-5 m sec^{-1}), encountered super-adiabatic lapse rate and unsaturated air. These events indicate precipitation falling into clear air which chills, then negatively buoyant, sinks. Link this to the appearance of mid-level air (θ_w 16C) at the surface some ten minutes afterward on the southwest side of the echo. θ_w values in the "rainy downdraft" associated with the storm core were higher than 16C indicating a mixture of ambient mid-level and updraft air. This is taken as the mechanism which produces localized gustiness away from the principal downdraft and gust front. Probably a mechanism of this type produced a 65 kt gust at station 7A on the southwest side of the southernmost echo.

Figure 12a through g are CAPPI presentations showing a later in-storm sounding when cell B was dissipating. The TAB sounding was released under the cirrus shield on the right front flank of the echo. In the lowest 2 km (fig. 9) moist-adiabatic ascent occurs. Above this level the lapse rate decreases to dry adiabatic indicating a well-mixed layer. Soon after the balloon begins to experience rising motion and reaches a maximum of 5 m sec^{-1} near 4.5 km (fig. 10).

Above 4.5 km the balloon is caught up in the storm circulation (fig. 12d). RHI data indicates the balloon became involved with a higher reflectivity core and sank. Beyond this point figure 12e and g show the balloon is involved with weak echo and other maximum reflectivity regions. Figure 10 shows alternate areas of rising and sinking motion. The echo and entrained balloon had moved out of the surface network by 2300 CST and it is difficult to relate the erratic behavior to previously described features. The updrafts encountered may have had their roots at the surface but one can only speculate. Certainly a very complex structure is revealed in the echo at this stage.

5. CONCLUDING REMARKS

Previously Henderson (1971) had published a study of the storm. However, additional surface and detailed radar data revealed some different, more complex conclusions than those reported in the first analysis.

The character of this storm differs somewhat from earlier interpretations. Though the echo contains structure similar to that reported by other researcher i.e., low-level echo wall, overhanging precipitation, WER associated with the updraft entering from the right flank, there are significant exceptions. The maximum vertical velocity occurs at a level below that supported by cloud modelers. The environment in which the echo developed was more that of a mixture because the southernmost echo diverted the flow. This blocking is thought to hinder the ventilation of the northernmost echo thereby causing

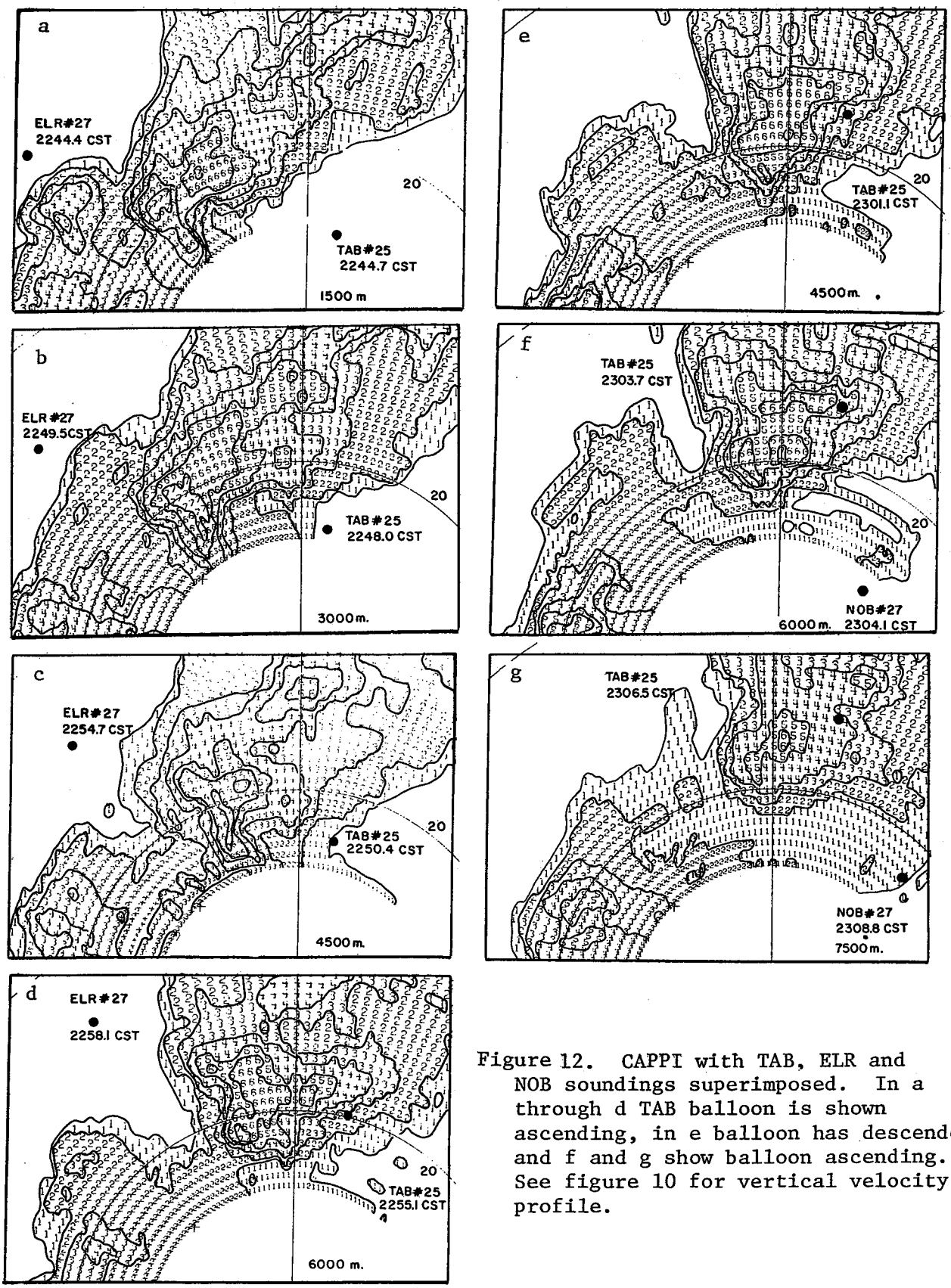

Figure 12. CAPPI with TAB, ELR and NOB soundings superimposed. In a through d TAB balloon is shown ascending, in e balloon has descended, and f and g show balloon ascending. See figure 10 for vertical velocity profile.

water to load the updraft leading to its demise.

The typical surface features associated with this echo are similar to those found by other researchers. The greatest single difference showed in the surface point surface. Hypothetically, the appearance and disappearance of this feature was independent of the "rainy downdraft" and was associated with the dissipating stage of the echo. Detailed observations of this phenomena in other storms could shed some light on its importance.

6. ACKNOWLEDGMENTS

The author wishes to thank Drs. Stanley L. Barnes and John D. Marwitz, who provided very stimulating discussion. Also to Messrs. Mike Weible and Bill Bumgarner who helped generously with the programming of the radar data.

7. REFERENCES

Barnes, S. L., 1970: Some aspects of a severe right-moving thunderstorm deduced from mesonetwork rawinsonde observations. J. Atmos. Sci., 27, 634-648.

_____, 1972: Morphology of two tornadic storms: an analysis of NSSL data on April 30, 1970. Preprints of Papers, 15th Radar Meteor. Conf., Champaign, Amer. Meteor. Soc., 69-76.

_____, 1973: Mesoscale objective map analysis using weighted time-series observations. NOAA Tech. Memo. ERL-NSSL-62, 60 pp.

_____, J. H. Henderson and R. J. Ketchum, 1971: Rawinsonde observation and processing techniques at the National Severe Storms Laboratory. NOAA Tech. Memo. ERL-NSSL-53, 246 pp.

Byers, H. R. and R. R. Braham, Jr., 1949: The Thunderstorm. Washington, D.C., U. S. Govt. Printing Office, 287 pp.

Charba J., and Y. Sasaki, 1971: Structure and movement of the severe thunderstorms of 3 April 1964 as revealed from radar and surface mesonetwork data analysis. J. Meteor. Soc., of Japan, 49, 191-214.

Chisholm, A. J., 1970: Alberta hailstorms: a radar study and model. Ph.D. Thesis, McGill Univ., 237 pp.

Davies-Jones, R. P., and N. B. Ward, 1971: Comments on "Some aspects of a severe right-moving thunderstorm deduced from mesonetwork rawinsonde observations." J. Atmos. Sci., 28, 652-653.

Fankhauser, J. C., 1971: Thunderstorm-environment interaction determined from aircraft and radar observations. Monthly Weather Rev., 99, 171-192.

Fujita, T., 1963: Analytical mesometeorology: a review. Meteor. Mono., 5, 77-125.

Henderson, J. H., 1971: The internal structure of a thunderstorm as revealed by θ_w surfaces. Preprints of Papers, 7th Conf. Severe Local Storms, Kansas City, Amer. Meteor. Soc., 234-239.

Hitschfeld, W. F., 1959: The motion and erosion of convective storms in severe vertical wind shear. Sci. Rept. MW-29, Storm Weather Group, McGill Univ., Montreal, 48 pp.

_____, ed. 1971: Hail research at McGill 1956-1971. Sci. Rept. MW-68, McGill Univ., 48 pp.

Kessler, E., and W. C. Bumgarner, 1971: Model of precipitation and vertical air currents NOAA Tech. Memo., ERL-NSSL-54, 93 pp.

Marshall, J. S., 1957: The constant-altitude presentation of radar weather patterns. Proc. 6th Weather Radar Conf., Boston, Amer. Meteor. Soc., 321-324.

Marwitz, J. D., 1972: The structure and motion of severe hailstorms. Part III: Severely sheared storms. J. Appl. Meteor., 11, 189-201.

_____, A. H. Auer, Jr., and D. C. Veal, 1972: Locating the organized updraft in severe thunderstorms. J. Appl. Meteor., 11, 236-238.

_____, and E. X. Berry, 1970: The weak echo region and updrafts of a severe hailstorm. Proc. 14th Radar Meteor. Conf., Tucson, Amer. Meteor. Soc., 43-47.

Miller, R. C., 1967: Notes on analysis and severe storm forecasting procedures of the Military Weather Warning Center. Tech. Rept. No. 200, Air Weather Service, USAF, 156 pp.

Stout, C. E., 1957: Mesometeorological systems from dense network stations. Presented at IUGG Meeting in Toronto.

Wilk, K. E. and K. C. Gray, 1970: Processing and analysis used with the NSSL weather radar system. Preprints of Papers, 14th Radar Meteor. Conf., Tucson, Amer. Meteor. Soc., 369-374.

MORPHOLOGY OF TWO TORNADIC STORMS: AN ANALYSIS OF NSSL DATA ON APRIL 30, 1970

Stanley L. Barnes

National Severe Storms Laboratory
Norman, Oklahoma

Surface, upper air, and radar data from the National Severe Storms Laboratory reveal the mesoscale structure of two severe thunderstorms that struck Oklahoma City within one hour of each other. At the surface both supercell storms were characterized by mesocyclonic sinks near the main updrafts with convergence values greater than 10^{-3} sec^{-1} and vorticity half as large or less. Lowest pressure preceded the mesocyclones several nautical miles; highest pressures were found near the rainy cores, but not coincident. Mid-level air descended practically unmixed on the southwest (rear) flanks and produced local accelerations in the cold air behind the gust fronts that may link to a tornadogenesis mechanism. Changes in characteristics of damage from three tornadoes seem closely related to evolution of mesoscale convergence/vorticity couplets. Soundings measure both dry adiabatic ascent aloft and descent near the surface just ahead of one storm's main updraft. This destabilization mechanism prepares a deep layer (6 km) for more energetic overturning and may partly explain the quasi-steady nature of such storms.

1. INTRODUCTION

On the night of April 29-30, 1970, five thunderstorms passed over the NSSL-operated 44-station surface network in central Oklahoma. Collected were more than eight hours of autographic recordings, upper air soundings from nine network stations, and digital radar data. This paper presents a descriptive analysis of two tornadic storms which traveled nearly parallel paths through Oklahoma City and caused over $6.3 million in damage within a one-hour period. Paths of both supercell storms were essentially straight and 25 to 30 degrees right of the mean wind to 7 km (208°, 32 m sec^{-1}). The first storm's speed was about 10 m sec^{-1} slower than the mean wind; the second was only 2 m sec^{-1} slower. Echo tops reached above 16 km (55,000 ft).

Soundings to 400 mb were obtained within 30 km on the right flanks of the two storms as they entered the network. These soundings were characterized by a deep moist layer (to 800 mb), strong static instability (Showalter Index, -8 to -10) and 20 to 30 m sec^{-1} vector shear in the cloud layer below 7 km.

Directional shear mainly was confined to the lower 2 to 3 km.

2. DATA

Surface stations five nautical miles apart recorded continuously while hourly ascents were made from sounding sites at 15 n mile intervals, and quantized radar reflectivity scans were made every 20 sec. Surface data abstracted at five-minute intervals (averaged over the preceding interval in the case of winds), upper air data analyzed at 750-m height intervals (see Barnes et al., 1971) and radar data (Wilk and Gray, 1970) displayed every five minutes (or whenever available in the case of CAPPI and RHI maps) provide the basis for defining the storm's quasi-steady characteristics.

3. ANALYSIS METHOD

Surface and upper air maps of temperature, moisture, wind and the parameters therefrom derived were developed through an objective interpolation that incorporates (1) time-to-space conversion which positions observations relative to the moving storms and (2) individual observations weighted both according to their distance from grid points and also according to their age (relative to the reference map time). Thus, grid point value, g is determined from observed values, f_i, according to the relationship

$$g(x,y,t) = \sum_{i=1}^{N} \eta_i f_i \ (x,y,t) / \sum_{i=1}^{N} \eta_i \qquad (1)$$

where

$$\eta_i = \exp\left(- \frac{r_i^2}{RE} - \frac{t_i^2}{FNU}\right). \qquad (2)$$

Arbitrary parameters RE and FNU are chosen on the basis of data distribution and scale size of the phenomena analyzed (Barnes, 1973).

Careful attention is paid to superpositioning information from all sensors. Balloon positions are computer-plotted, interpolated fields are computer-printed at grid points with contour shading, and radar intensities are plotted to scale using a computer-driven plotter. Where figures show hand-drawn contours, in every case they are based on computer-derived results.

Wet-bulb potential temperature, θ_w, is evaluated by polynomial approximation (Prosser and Foster, 1966). Pressure excess (deficit) is calculated by subtracting the eight-hour linear trend of station pressure as determined by a regression analysis for each individual station. Thus, instrument biases and elevation effects are removed automatically from the pressure analyses. (Pages 33 - 35 explain surface data processing.) Storm translation vectors are obtained by visually estimating positions of echo centroids ($Z_e > 10^{-3}$ mm^6 m^{-3} at zero antenna tilt) over several hours. Storm direction derives from a linear regression line fit to positions; the average of displacements between five-minute fixes determines storm speed.

4. SURFACE FEATURES

Surface maps at five-minute intervals indicate clearly the quasi-steady character of these storms and relationships among wind, pressure, rainfall, thermodynamic variables, and "signatures" in radar echo structure. Two chosen times illustrate the type of details observed. Other results are displayed on pages 75 - 86.

4.1 Storm F

The first tornadic storm (Storm F) at 0040 CST shows a radar pattern weak echo notch and strong gradient (fig. 1a near W7), now familiar indicators of an updraft region (Browning, 1964; Booker et al., 1969; Marwitz, 1972). In this case the hook structure just south of W7 reveals a cyclonic circulation also evident in the surface wind pattern (fig. 1d). Centers of convergence (3×10^{-3} sec^{-1} in fig. 1e) and vorticity (1×10^{-3} sec^{-1} in fig. 1f) associate with this mesocyclone. The convergence zone does extend along the wind shift line southwest of the cyclone center, but no other significant vorticity centers are noticed. Surface θ_w values (fig. 1b) are 20 to 21C east and northeast of the updraft. Across the wind shift line, θ_w decreases only 2 to 3C. Air descended from mid-troposphere is in evidence only near ELR where θ_w = 16C.

Most interestingly, the lowest pressure (fig. 1c) does not coincide with the mesocyclone center, but locates nearly four nautical miles east. Shaw (1931) points out that the center of lowest pressure does not coincide with a vortex core (kinematic center) when the vortex is imbedded in a larger scale pressure gradient. According to Shaw's analysis, the surface pressure center is displaced in the direction of higher superposed pressure a distance $L = V/(f + \zeta)$ where f is Coriolis parameter $2\omega \sin \phi$, ζ is relative vorticity, and V is translation velocity of the spinning system (treated as though in solid rotation). Storm F's mesocyclone moves at slightly over 25 m sec^{-1}. Substituting the known displacement between mesocyclone and pressure centers (about 8 km) and recognizing that $\zeta >> f$ in a tornado cyclone, we can evaluate Shaw's relationship yielding $\zeta = 3 \times 10^{-3}$ sec^{-1}. This magnitude is quite reasonable for above-the-surface air near a tornado cyclone, particularly when one considers observed surface vorticity equals 10^{-3} sec^{-1} near this cyclone (fig. 1f). In slower moving systems, the pressure center probably would not be displaced so far from the cyclone center. This may explain why other investigators of tornado cyclones report no significant separation of wind and pressure centers.

Surface pressure gradients are significant enough to turn the ahead-of-storm winds from southeasterly to northeasterly producing a col in the streamline field (fig. 1d). Also, the 20 kt maximum isotach southeast of the cyclone center may be attributed to acceleration by the mesolow.

The tornado in this storm is imbedded within the mesocyclone circulation centered north of Station 3A. Damage is neither wide nor intensive. Although ground survey team made no path measurements, this tornado ranked apparently in the F1 or F2 category (defined by Fujita et al., 1971). The pressure disturbance associated with the tornado's circulation is not seen in these maps because of its small time-space scale relative to station distribution.

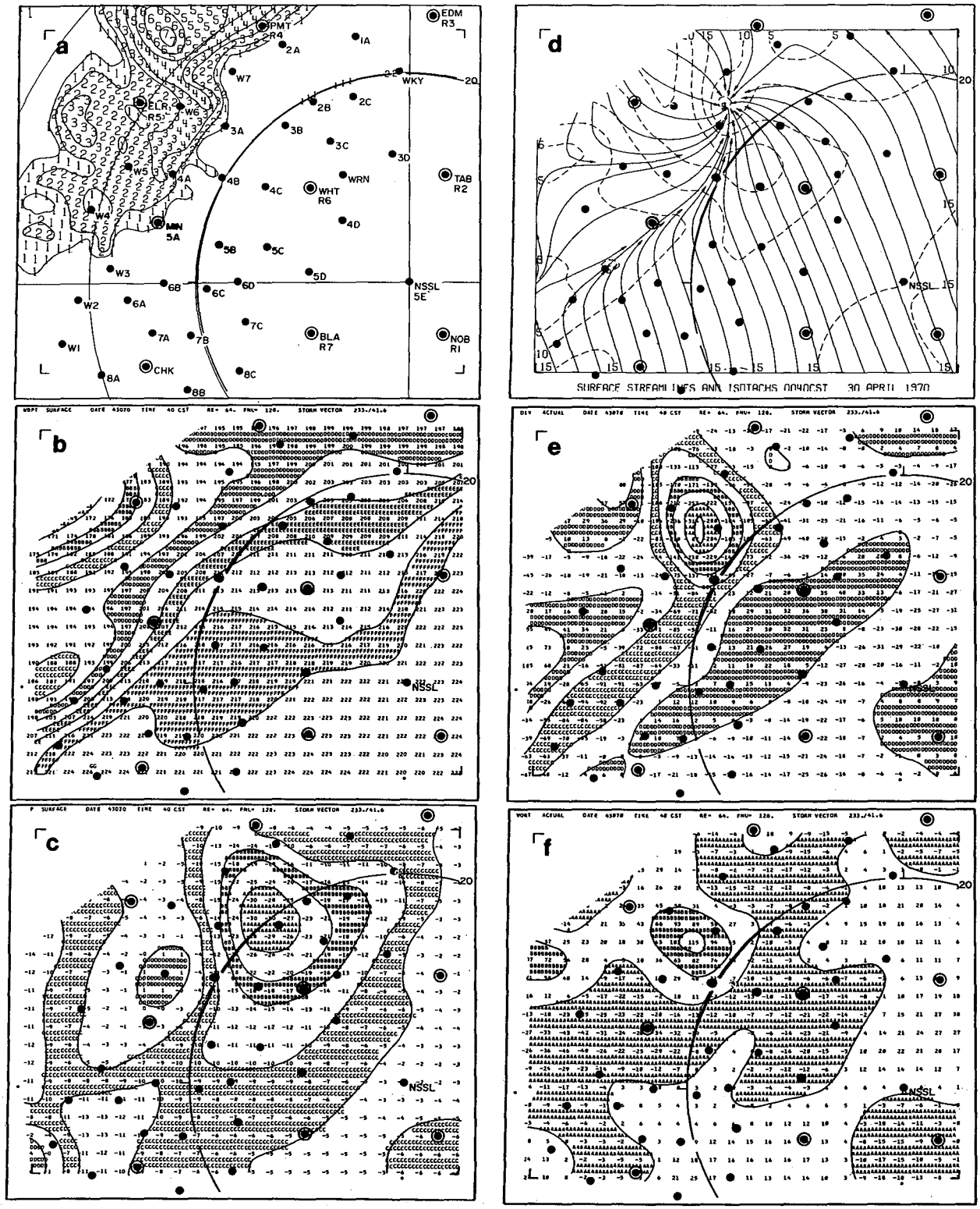

Figure 1. Storm F 0040 CST surface analyses: (a) coded radar reflectivity; (b) wet-bulb potential temperature in tenths Celsius; (c) pressure excess in tenths millibars; (d) streamlines and isotachs in knots; (e) divergence and (f) relative vorticity in units 10^{-5} sec^{-1}. Surface stations (dots) and sounding stations (circled) are identified in (a). Range circle is 20 n miles.

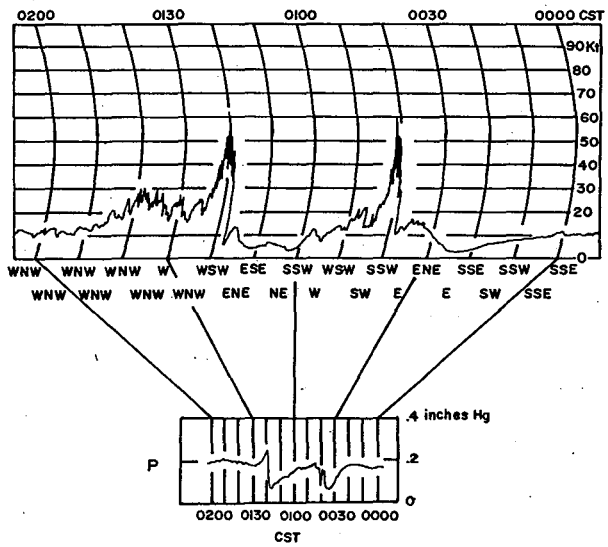

Figure 2. Wind speed and pressure traces for Station 3A located about one-half nautical mile right of first tornado damage path. Instantaneous wind directions are at five-minute intervals. Pressure recorded in inches Hg (1 mb - .03 inch). At 0041 CST, 60 kt gust and sharp "V" in pressure trace mark the tornado passage.

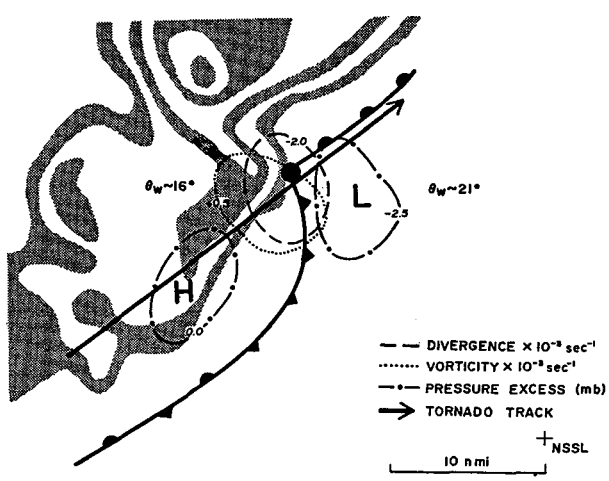

Figure 3. Storm F surface features composited at 0040 CST.

However, the vortex is clearly evident in the individual wind and pressure recording for Station 3A (fig. 2). It is important to realize that the tornado vortex follows behind the mesolow.

Storm F's composited surface features (fig. 3) show a relationship between three entities: the mesocyclone center (large dot); the tornado on or near the outflow boundary south of the mesocyclone center; and the mesolow center four nautical miles east. The separation of mesocyclone and mesolow centers has not been discovered in previous thunderstorm studies, and this fact's implications to storm dynamics are not fully understood. The convergence and vorticity centers nearly coincide with the mesocyclone in this case, and their relative magnitudes confirm that flow near the ground is more radial than tangential on this scale. Finally, all of these features lie at the radar hook echo's leading edge.

4.2 Storm G

A second severe storm (G) entered the network on Storm F's heels and produced two tornadoes. Although Storm G's radar appearance is that of a squall line (page 22), in fact Storm G is taller and larger than other cells in the line and exhibits distinct supercell characteristics (Browning, 1964; Browning and Donaldson, 1963). Line cells nearest Storm G rapidly develop and merge with G's main updraft, suggesting the cells are feeder clouds (Dennis et al., 1970). Bates (1962) observed tornado development beneath a cumulus congestus "street" on the southwest flank of a large thunderstorm.

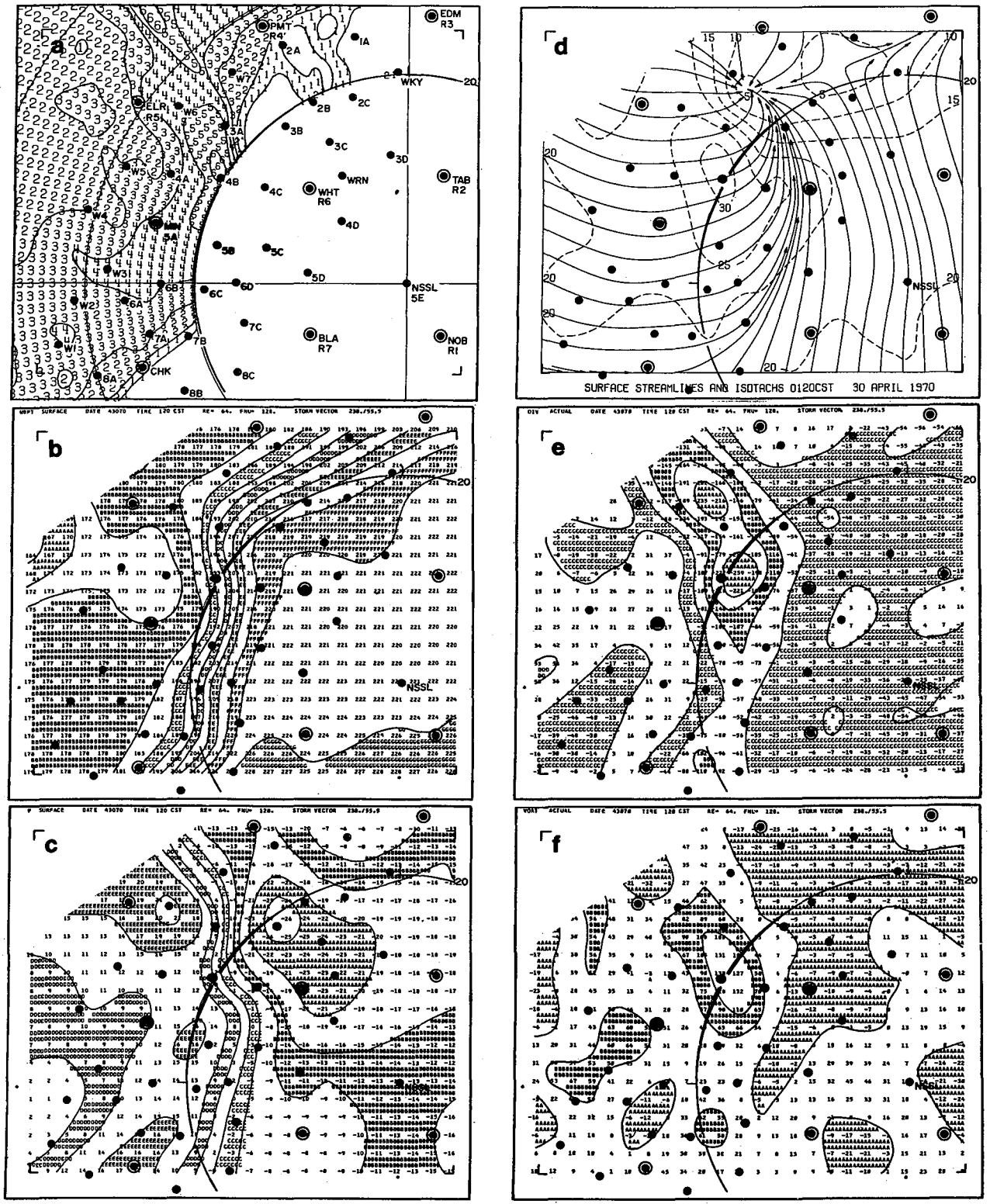

Figure 4. Storm G surface analyses at 0120 CST. Reflectivity inside 20 n miles is not analyzed due to ground clutter. Figure 1 caption has explanation.

One flanking tower (shown over 4B in fig. 4a) produces Storm G's first tornado! At 0120 CST, this tornado sweeps within one-half nautical mile of Station 4C which is some 10 n miles from G's main updraft identified by the mesocyclonic "sink" in the surface wind field (fig. 4d). Additional details on this tornado's character and the one which accompanied Storm G's main updraft are described on pages 141-151 and 153-165 in this memorandum. Here our concern is with this storm's mesoscale structure.

An important feature in the flow field (fig. 4d) is its high velocity just southwest of the mesocyclone. This air, recently having descended from mid-troposphere (θ_w = 17C in fig. 4b), has a larger component toward the northeast than adjacent surface air, locally accelerating the gust front. Two resulting effects are believed important to tornado cyclone development: (1) increasing convergence along the gust front's leading edge triggers new cell growth; and (2) horizontal shear increases vorticity's vertical component such that cyclonic (positive) shear results on the downdraft jetlet's left side (viewed in direction of its flow)--the side toward which upper winds will carry the growing convective cell. Such conditions also may produce the environment in which tornadoes themselves can develop (pages 147-150).

Two convergence centers in excess of 2 x 10^{-3} sec^{-1} appear at 0120 CST (fig. 4e), one with the surface mesocyclone and the other with the developing tornadic cell. Vorticity, half as great as convergence, now positions near the existing tornado rather than near the surface mesocyclone as in Storm F. Although this tornado's mesocyclonic circulation does not reach into the surface air, its presence aloft manifests as a well-developed hook echo signature (page 143).

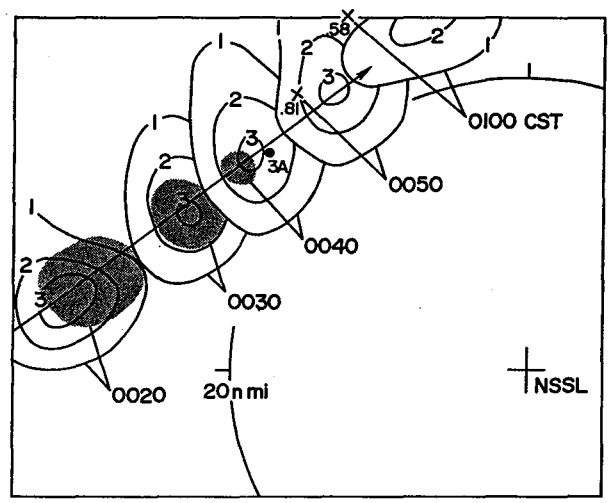

Figure 5. Evolution of Storm F's convergence and vorticity centers as storm crossed network area. Convergence is contoured in 10^{-3} sec^{-1} intervals; maximum closely follows mesocyclone center. Vorticity exceeding 10^{-3} sec^{-1} is shaded. At 0050 and 0100 CST, maximum vorticity values are shown at X's. Tornado moved along path (arrow) close to Station 3A (dot), passing there at 0041 CST.

Surface air convergence into Storm F remains nearly constant during its traverse across the network, but vorticity diminishes by nearly a factor of four (fig. 5). At 0020 CST vorticity is maximum (2.04 x 10^{-3} sec^{-1}) near the center of convergence. Storm F's tornado (path shown by arrow in fig. 5) passes near Station 3A at 0041 CST (fig. 2), and the convergence center also passes 3A shortly after 0040 CST (fig. 5). From this we conclude the tornado and convergence center nearly coincide. According to damage path survey (pages 153-165), the tornado apparently lifts or

dissipates soon after reaching its 0050 CST position. By 0100 CST, vorticity decreases to 0.58 x 10^{-3} sec^{-1} and no longer associates with the convergence center (fig. 5).

Storm G's evolving convergence (fig. 6) enters as an elongated band, then splits into two centers as the major tornado cyclone develops and becomes the dominant center. An area of increasing vorticity overtakes the maximum convergence area. Damage from G's first tornado occurs soon after it enters the network in the vicinity of Stations W2, W3 and 6A (locations are shown in fig. 4a). About 0123 CST, the storm passes near Station 4C, doing considerable damage as it rips northeastward through Oklahoma City and, apparently lifting, exits the network about 0140 CST. Shortly after 0130 CST, a third tornado briefly touches down to the northwest of the major tornado's path just as vorticity increases in the vicinity of the surface mesocyclone.

As Storm G passes over the northern part of the network, another cell in the flanking line passes over the southeastern corner near NSSL. Although this cell could not be detected in the radar ground clutter, its presence is revealed by 10^{-3} sec^{-1} convergence center (fig. 6) and rain rate maximum (page 86). This non-tornadic cell also has an associated vorticity maximum which lags behind the convergence center by seven nautical miles. These facts imply that updrafts cannot support tornado development in the surface air until ambient vorticity reaches some threshold value. Insufficient surface layer vorticity may also mean the updraft isn't rotating significantly, but we cannot determine this from these observations alone.

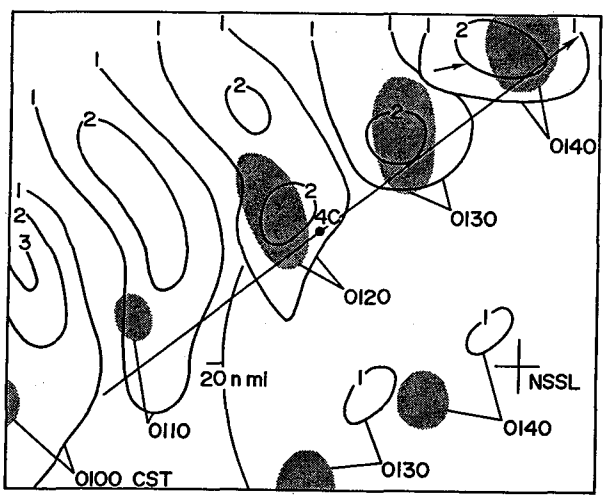

Figure 6. Evolution of Storm G's convergence and vorticity centers. At 0120 CST, northernmost convergence center corresponds to location of surface mesocyclone and main updraft. Newly-developed cell about 10 n miles south has associated vorticity center and contains a tornado that passes near Station 4C (0123 CST). Third tornado (short arrow) developed briefly about 0133 CST northwest of main tornado track (long arrow). Note: Convergence and vorticity centers do not coincide in non-tornadic cell passing near NSSL.

From the available data, we surmise these relationships: (1) tornadic damage may occur even though the larger mesocyclonic circulation (in which tornadoes are commonly found) doesn't extend completely to the surface; (2) both ambient vorticity and convergence of order 10^{-3} sec^{-1} are necessary to support tornadoes in the surface layer; (3) these minimum conditions may occur anywhere along the gust front (flanking line or squall line) where the flow is accelerated locally in response to as yet incompletely understood forces--they occur most commonly beneath developing cumulus towers near the principal updraft of larger, quasi-steady thunderstorms.

Wind and pressure traces for Station 4C show that Storm F's outflow

boundary never did pass 4C (fig. 7); the wind remained from the SSE until shortly after 0120 CST when G's first tornado cyclone caused a 95 kt gust from the WSW. The pressure trace at this time exhibits an 8 mb drop and, immediately thereafter, an 11 mb rise. As in the earlier Storm F, G's tornado is on the back side of the mesolow (fig. 4c).

Storm G's mesolow center stayed several miles ahead of and between the surface mesocyclone and flanking tornadic cell (fig. 8). Two high pressure centers are found within the rain area. Orientation of lines connecting these centers with the mesolow suggests a physical relationship from the fact that the twin tornado cyclones eventually merged (pages 141-151).

5. UPPER AIR FEATURES

Although the density of soundings obtained during the passage of these storms far exceeds previous atmospheric samplings near severe thunderstorms, the scale of observations actually is gross in relation to storm structures. Furthermore, a combination of unfortunate circumstances prevented obtaining the sounding density of which the network is capable. Only 12 soundings were obtained in and immediately ahead of Storm F, and only one sounding to an altitude of 1 km was taken during the passage of Storm G.

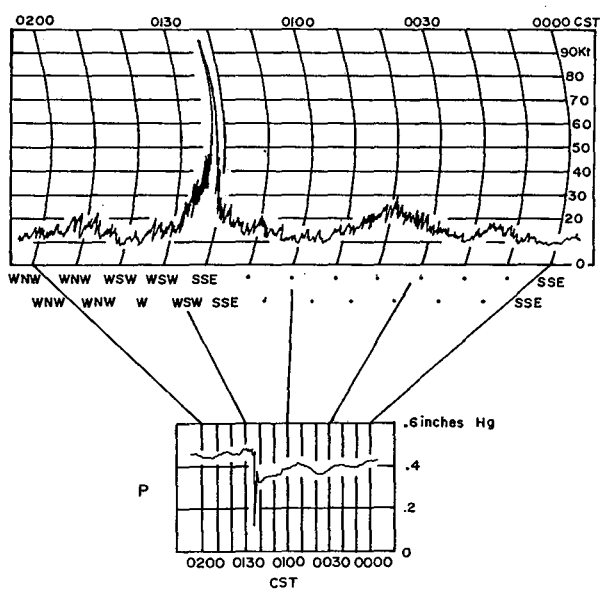

Figure 7. Wind speed and pressure traces at Station 4C located near the damage path of Storm G's first tornado. Dots indicate no change in wind direction. Tornado produced 95 kt gust at 0123 CST and pressure trace "V" just after mesolow center passed.

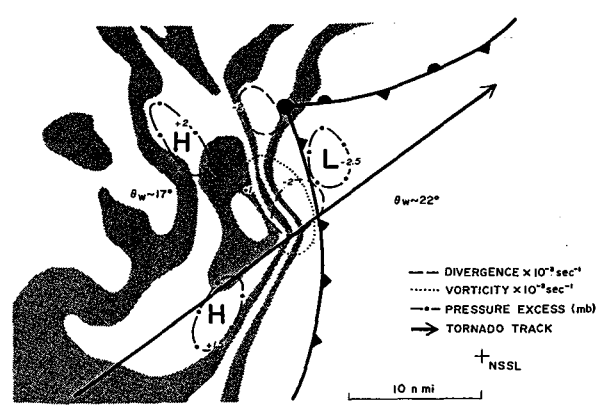

Figure 8. Storm G surface features composited at 0120 CST. Main body of storm is out of picture at top; only a small finger of the precipitation core extends toward the mesocyclone (large dot). Newly-developed, tornado-producing cell is at center; another tornado developed later near the mesocyclone.

The 0030 CST reflectivity, temperature, wind and vertical motion distributions are displayed at five levels 1500 m apart (fig. 9). Eleven balloons' positions are indicated by black dots with full wind barbs equalling 10 m sec^{-1}. Air temperature[1] is plotted to the upper right and the balloon's vertical velocity (m sec^{-1}) in excess of that due to its own buoyancy is plotted at the lower right. Soundings A, B, C, and D refer to ascents indicated and are discussed later. The fiducial X southeast of the storm core indicates the updraft position near the surface and provides perspective in each figure part. Dashed streamlines show flow relative to the moving storm.

The region of particular interest (fig. 9) lies just east of "X". Low altitude air (1.5 km) is 1 to 2C warmer than the rest of the storm's environment, while air at 6 km is significantly colder. A tentative explanation follows. The surface mesolow accelerates air toward the updraft (near "X") and thereby creates a divergence zone ahead of the storm (fig. 1e) resulting in weak subsidence in the lower atmosphere. Compare in figure 10 temperature and dew point profiles for soundings C (WHT No. 24) and D (CHK No. 30). The saturated layer at D subsides and drys in the vicinity of C. Aloft, a stable dry layer near 6 km at D (CHK in fig. 10) lifts at C. Corroborative evidence of lifting near C is the 3.9 m sec^{-1} excess balloon ascent rate (WHT No. 24 in fig. 11, also C in fig. 9b).[2]

The cause of this dry ascent aloft hasn't been determined, but likely it is forced lifting by a storm-induced perturbation. With subsidence in the lower layers, the combined effect stretches air vertically and decreases static stability. Thus, the supercell storm prepares the atmosphere just ahead to release its energy more violently.

---

[1]The reader may note that isotherms do not exactly fit reported temperatures. These objectively interpolated results (fig. 9) consider the observations' distribution, non-simultaneity, and uncertainty (Barnes, 1973). Balloons released from the fixed network sites reach specific altitudes at irregular intervals. The analysis scheme adjusts each balloon's real position to a storm-relative one under the assumption that the storm is translating steadily in a known direction. We don't know, a priori, the scale of important variations in a storm's near environment--we assume observations reveal perturbations whose size (distance between relative extrema) is twice the station spacing (approximately 32 n miles). Amplitudes of smaller scale perturbations are smoothed inversely proportional to their size. Furthermore, we suspect the storm's environment changes as the storm interacts with ambient air, but we don't know the time scale of these changes. Even though a storm's radar echo and visual cloud frequently indicate overall steadiness, individual storm portions undergo more rapid transitions and may initiate changes in their immediate environment. Rapid temporal changes are suppressed. Finally, we recognize observational uncertainty may be as much as $\pm$1C. Considering all of the above, the quasi-steady assumption is considered justified when analyzed values at data points fit the ensemble observations to within 1C (root-mean-square difference).

[2]The accuracy of these vertical motion estimates is judged to be 0.5 to 1.0 m sec^{-1} but is dependent upon assuming that the ascent rate in the surface layer is due solely to the balloon's buoyancy.

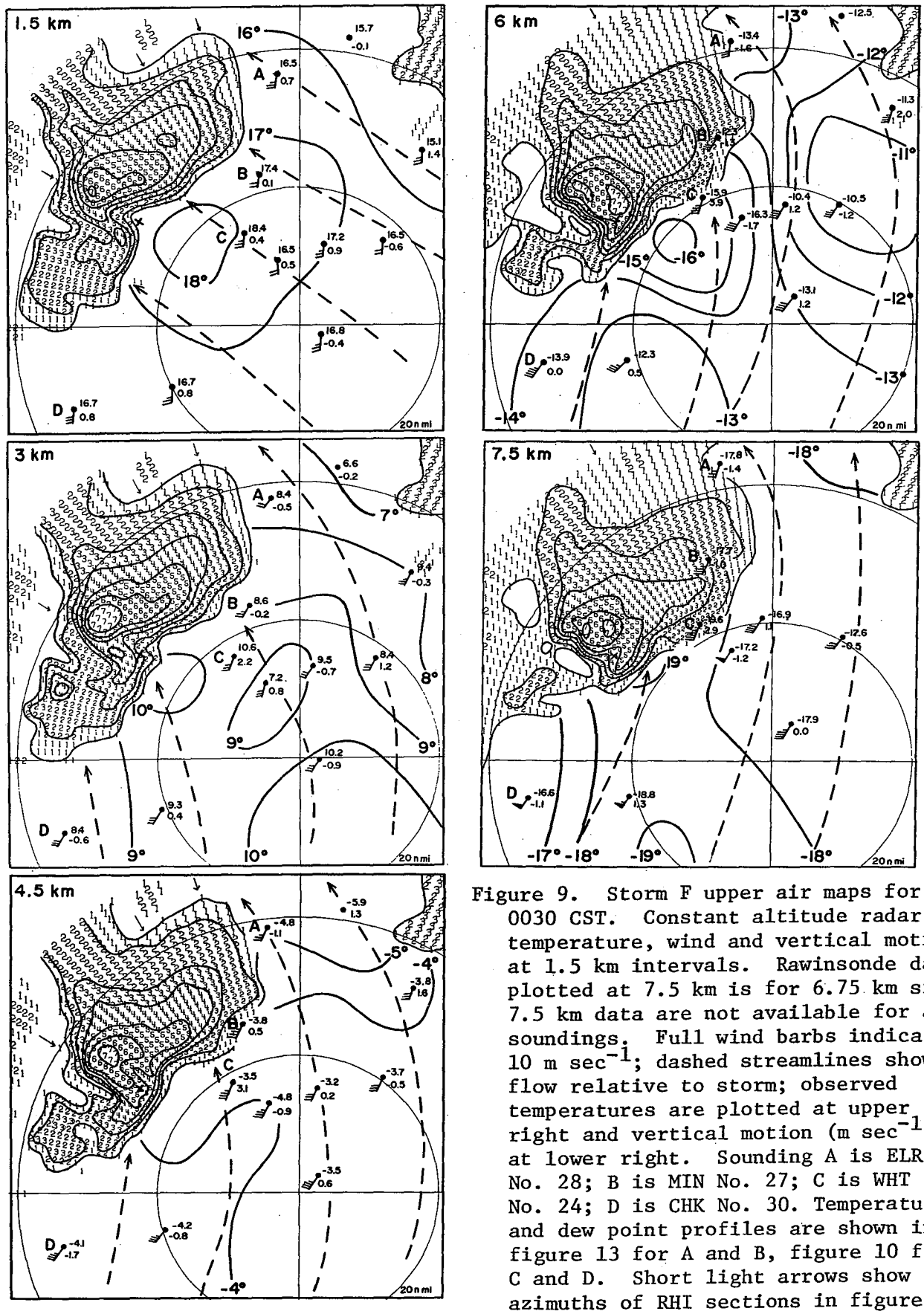

Figure 9. Storm F upper air maps for 0030 CST. Constant altitude radar, temperature, wind and vertical motion at 1.5 km intervals. Rawinsonde data plotted at 7.5 km is for 6.75 km since 7.5 km data are not available for all soundings. Full wind barbs indicate 10 m sec^{-1}; dashed streamlines show flow relative to storm; observed temperatures are plotted at upper right and vertical motion (m sec^{-1}) at lower right. Sounding A is ELR No. 28; B is MIN No. 27; C is WHT No. 24; D is CHK No. 30. Temperature and dew point profiles are shown in figure 13 for A and B, figure 10 for C and D. Short light arrows show azimuths of RHI sections in figure 12.

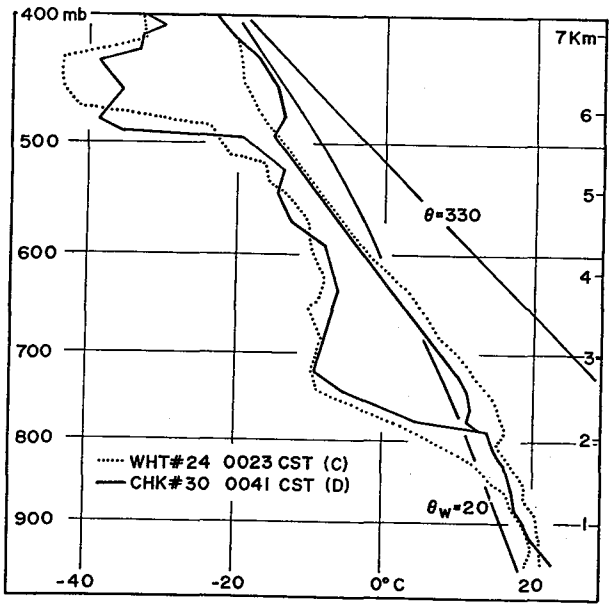

Figure 10. Stüve diagram of sounding C near updraft) and D (undisturbed environment). Ascents began at times shown.

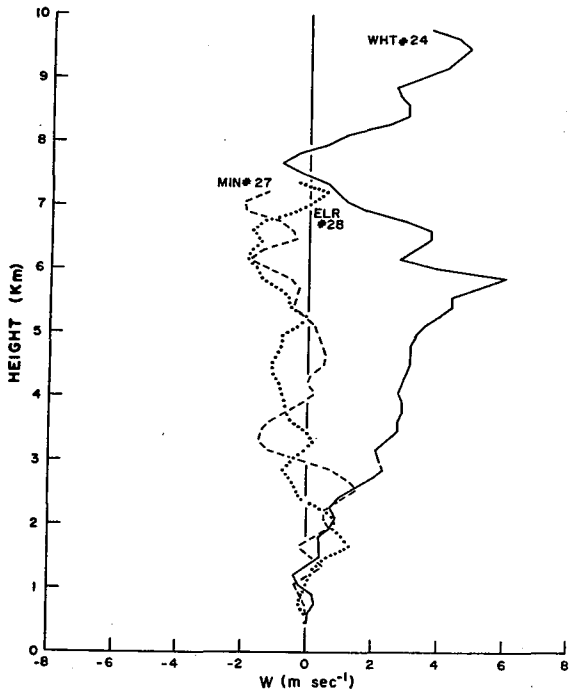

Figure 11. Balloon ascent rate in excess of that due to buoyancy for soundings A, B, and C in figure 9. (See fig. 10 also.)

Between 7 and 8 km in the WHT sounding, vertical motion decreases to near zero (fig. 11). Balloon C encounters light precipitation in this layer (fig. 12b) which near the bottom is unsaturated but at the top approaches saturation (see page 32). Above 8 km the air is saturated with respect to ice, and the vertical velocity (fig. 11) again increases to near 4 m sec^{-1} (supposedly responding to latent heat release).

The anvil region of Storm F was sounded by balloons A and B (fig. 9). The ELR sounding (A) skirted the precipitation shield while the MIN sounding (B) penetrated the anvil just below the reflectivity core aloft (fig. 12c). Both balloons experienced weakly descending air (fig. 11) up to 2 m sec^{-1}. Thermal structure (fig. 13) reveals somewhat colder surface air at ELR and then up to 4.5 km remarkably similar profiles. The stable layer sensed at 5 km by the ELR balloon is recorded at a slightly higher altitude in the MIN sounding. On the whole the MIN sounding indicates slightly more moisture, probably a result of evaporating rain.

The winds sensed by balloon C in the 6 to 7.5 km layer vectorially are intermediate to the ambient winds and the 1.5 km winds (fig. 14). In this part of the storm, low-level and ambient air mix. This supports Marwitz' (1972) supercell storm model: that is, the updraft air found on the right forward flank originates from levels well above the surface (e.g., cloud base).

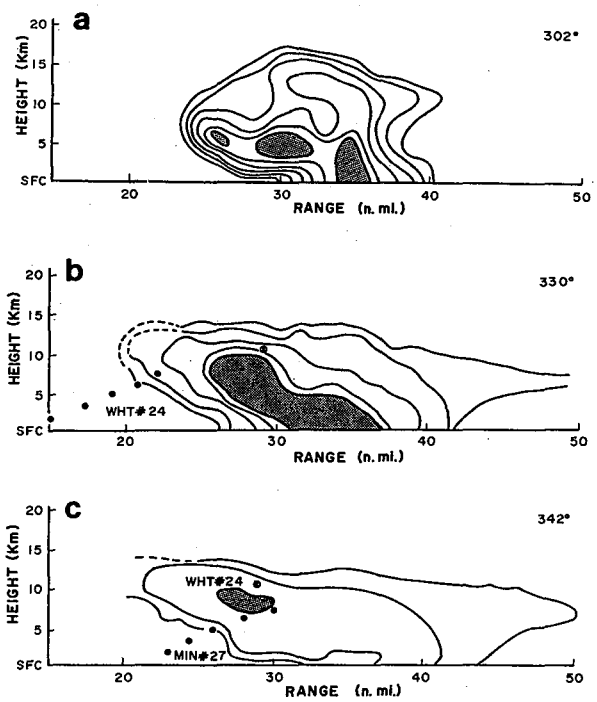

Figure 12. Selected range-height displays for Storm F at 0030 CST based on digital reflectivities: (a) through the main updraft along azimuth just counter-clockwise from that marked by "X" in figure 9; (b) along sounding C azimuth in figure 9; (c) along sounding B azimuth in figure 9. Dots show balloon positions. Except for circled cross at 10 km in WHT sounding, all balloon positions are in azimuth planes shown. The WHT 10 km position is along azimuth 342, but is shown also in (b) for reference.

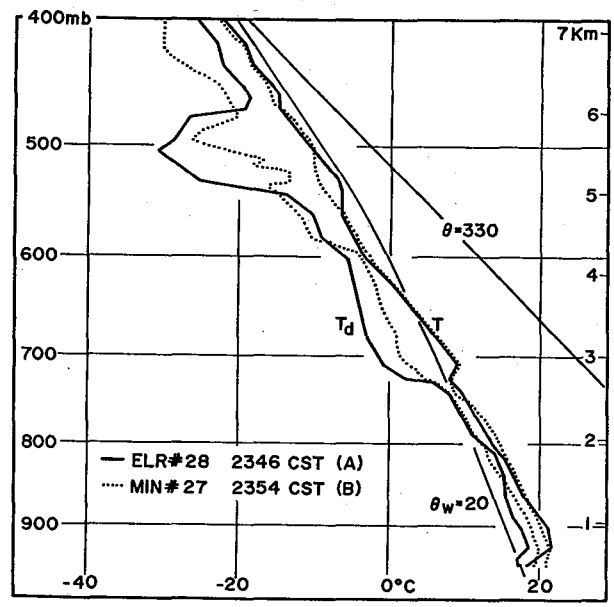

Figure 13. Stüve diagram of soundings A and B (through anvil).

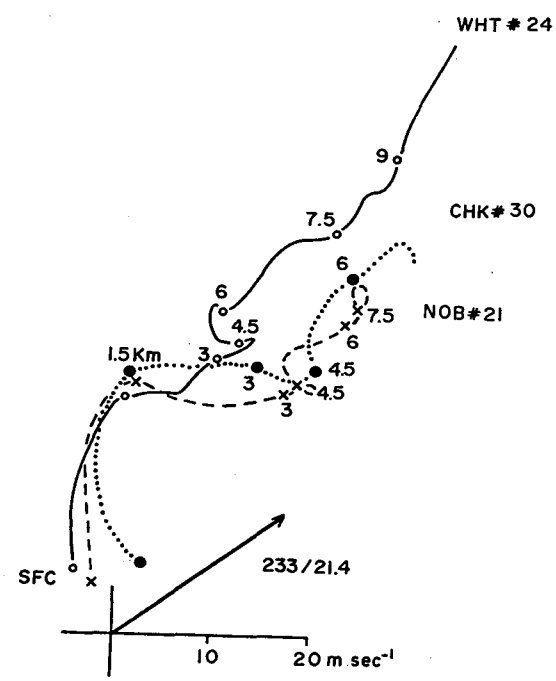

Figure 14. Hodographs of ambient winds (CHK and NOB) and in-storm winds (WHT). Storm F vector (heavy arrow) is 15 degrees to the right of ambient winds at 4.5 km.

In Marwitz' model, this structure is attributed to observations that almost all direction shear occurs in the lower atmosphere (as in fig. 14).

Above 7.5 km, balloon C moves rapidly to the northeast responding to strong winds (70 m sec^{-1}) just above the heaviest precipitation core (fig. 12b and 12c). Speed shear in this layer is of the order 10^{-2} sec^{-1}.

Air nearer the surface moving more westward is expected to tilt the updraft toward the storm core (part of Marwitz's model and Browning's model, 1964). Storm F's three-dimensional radar structure provides clues which, considered with well-defined surface features, reasonably picture flow in and about this storm. At low levels the main updraft manifests itself as a weak echo region giving way to an overhanging vault at 4.5 km (fig. 9). At 6 and 7.5 km, the updraft's main branch (that which produces the highest cloud top) rises between two reflectivity maxima and extends to an echo top beyond 16 km (fig. 12a). Although no sounding reached this part of Storm F, probably this vigorous updraft is characterized by moist-adiabatic ascent up through at least 5 km altitude (Barnes, 1970), rises in some degree shielded from the shearing ambient flow and is rotating cyclonically about a vertical axis.

At 6 and 7.5 km (fig. 9), closely-spaced reflectivity contours on the storm's southwest (upwind) side indicate juxtaposition of dry ambient air and the precipitation-laden updraft. Speculating that evaporating precipitation chills this dry air, it descends to the surface without significant mixing. How this air interacts with the storm's dynamics isn't completely understood, but considering momentum conservation principles, surface winds produced by this mechanism could influence strongly (and asymmetrically) the nearby surface sink (mesocyclone).

Mid-level air that does mix with updraft air increases its θ_w and, therefore, is not as negatively buoyant. This air intrudes farther into the storm core tending to separate around the updraft. Two reflectivity contour indentations on both sides of the reflectivity core (fig. 9; 6 and 7.5 km) support such interpretation. Then entrained air may become part of the rainy downdraft which descends most rapidly near the storm cores. This impression is amplified by Henderson's results (pages 111-123) and by observed weakly descending air in and under the rain shield (soundings A and B in fig. 9; also fig. 11).

6. CONCLUDING REMARKS

This paper describes the NSSL observations of a series of tornadic storms. Some interpretations are offered, but others may be as compelling and valid; the reader is invited to test other concepts against the data.

Many facts found here corroborate details previous investigators surmised with less complete data. Other details, such as uniqueness of mesocyclone and mesolow centers, occurrence of tornadoes near to but behind the mesolow, and dry ascent ahead of the updraft, are newly found. Contributions to our knowledge of severe thunderstorm dynamics will be subjected to future study.

7. ACKNOWLEDGMENTS

I am indebted to Dr. Edwin Kessler, NSSL's Director, for bringing to my attention Shaw's early work on rotating wind and pressure systems, and for his many other helpful suggestions.

8. REFERENCES

Barnes, S. L., 1970: Some aspects of a severe, right-moving thunderstorm deduced from mesonetwork rawinsonde observations. J. Atmos. Sci., 27, 634-648.

_____, 1973: Mesoscale objective map analysis using weighted time-series observations. NOAA Tech. Memo., ERL-NSSL-62, 60 pp.

_____, J. H. Henderson, and R. J. Ketchum, 1971: Rawinsonde observation and processing techniques at the National Severe Storms Laboratory. NOAA Tech. Memo., ERL-NSSL-53, 246 pp.

Bates, F. C., 1962: Tornadoes in the Central United States. Transactions Kansas Academy of Science, 65, 215-246.

Booker, D. R., D. C. Hall, H. E. Hart, and L. W. Cooper, 1969: Evidence of severe storm rotational characteristics obtained from superpressure balloon trajectories. Preprints of Papers, 6th Conf. on Severe Local Storms, Chicago, Amer. Meteor. Soc., 32-37.

Browning, K. A., 1964: Airflow and precipitation trajectories within severe local storms which travel to the right of the winds. J. Atmos. Sci., 21, 634-639.

_____, and R. J. Donaldson, Jr., 1963: Airflow and structure of a tornadic storm. J. Atmos. Sci., 20, 533-545.

Dennis, A. S., C. A. Schock, and A. Koscielski, 1970: Characteristics of hailstorms of Western South Dakota, J. Appl. Meteor., 9, 127-135.

Fujita, T. T., J. T. Tecson, and L. A. Schaal, 1971: Preliminary results of tornado watch experiment 1971. Preprints of Papers, 7th Conf. on Severe Local Storms, Kansas City, Amer. Meteor. Soc., 255-261.

Marwitz, J. D., 1972: The structure and motion of severe hailstorms. Part 1: Supercell storms. J. Appl. Meteor., 11, 166-179.

Prosser, N. E., and D. S. Foster, 1966: Upper air sounding analysis by use of an electronic computer. J. Appl. Meteor., 5, 296-300.

Shaw, N., 1931: Meteorological Calculus: Pressure and Wind. Manual of Meteorology, Vol. IV, Cambridge University Press, London, pp 259-261.

Wilk, K. E., and K. C. Gray, 1970: Processing and analysis used with the NSSL weather radar system. Preprints of Papers, 14th Radar Meteor. Conf., Tucson, Amer. Meteor. Soc., 369-374.

RADAR-OBSERVED MERGER OF TWIN HOOK ECHOES

Stanley L. Barnes

National Severe Storms Laboratory
Norman, Oklahoma 73069

National Severe Storms Laboratory radar film reveals twin hook echoes on the southeast flank of a tornadic thunderstorm which struck Oklahoma City on 30 April 1970. The circulation from only one of these tornado cyclones (nearest the radar core) reached the surface; both produced tornadoes. As the two hook echoes merged into one larger hook, the tornadoes left the surface. Divergence (2.5×10^{-3} sec^{-1}) calculated from surface wind measurements shows an overall decrease in updraft strength during the merger, but there is some question about how closely the surface flow was coupled with that at cloud base. Maximum vorticity (1.5×10^{-3} sec^{-1}) followed the developing hook echo and increased slightly. Local acceleration of the thunderstorm gust front in response to a downdraft impulse from the storm's southwest flank is the apparent cause of the new cell development and vorticity maximum.

1. INTRODUCTION

Multiple tornado funnels beneath the same rotating parent cloud occur often enough that they cannot be considered "freaks" of nature. Such a storm was documented by Fujita et al. (1970), based on a series of photographs taken by Mr. Paul Huffman, Staff Photographer of the Elkhart Truth. A single tornado was observed to split into twin funnels, each rotating about a common point between them. Ward (1970) studied this phenomenon in a laboratory vortex chamber and found that multiple vortices commonly form when the inflow angle (arctangent of the tangential component over the radial component) is large. The inflow angle critical for multiple vortex formation depends upon the ratio of converging layer depth to convection radius.

Another class of multiple vortices has been reported by Bates (1968), and Golden (1973). These tornadoes (waterspouts in the latter case) occur beneath growing cumulus congestus clouds which form along the shear zone separating warm, moist air on the forward flank of a larger cumulonimbus

from the cooler downdraft air which flows outward from the storm's rainy core. Unlike multiple vortices which form in one parent updraft, these vortices are independent initially.

The multiple tornadoes reported here formed along a shear line, but moved on converging paths until they merged (came in close proximity). Thus, the case contains aspects of both classes of multiple tornadoes.

2. DATA

Shortly after midnight on 30 April 1970, two large thunderstorms moved across northwestern Oklahoma City within a one-hour period. Both were tornadic and apparently supercell type with smaller convection cells extending southwestward from the main updraft region. Because their tracks lay across the 44-station mesonetwork operated by the National Severe Storms Laboratory, a detailed record of their passage was obtained. The first of these storms (Storm F) was thought to have been responsible for residential damage in the extreme northwestern edge of Oklahoma City (Barnes, 1972; Storm Data, 1970). However, newspaper accounts place the damage more closely in time to the second storm (Storm G) which traveled a path nearly parallel to Storm F's. This conclusion is confirmed by the discovery of Storm G's twin hook echoes and two damage paths.

From continuous analog recordings of surface parameters, data were analyzed at five-minute intervals using an objective technique (Barnes, 1973). Five nautical mile station spacing does not allow us to resolve individual tornado features, but the parent tornado cyclone and gust front are easily detected in the time series data.

Although 57 rawinsondes were launched from nine stations during an eight-hour period, only two rose near Storm G, and one of these reached only 1 km altitude.

Except for two brief power failures, continuous 10-cm radar data (WSR-57) were recorded in several formats at a rate of three azimuthal scans per minute.

3. RADAR OBSERVATIONS

The evolution of twin hook echoes and their subsequent merger was discovered in the radar film sequence reproduced as figure 1. The sequence of frames spans the period 0113 CST to 0149 CST when power at NSSL failed completely. At 0113 CST, Storm F is just leaving the metropolitan Oklahoma City area while Storm G is approaching from the west. A line connecting the three dots labeled Mustang, May Ave. - US 66, and WKY defines the first tornado's path through the city. Mustang, a small community southwest of Oklahoma City, was the first to experience intensive damage from this funnel. WKY denotes the site of a tall television tower instrumented by NSSL; it is just north of the last severely damaged structures along this tornado's path. The Camelot Addition was the only area experiencing severe

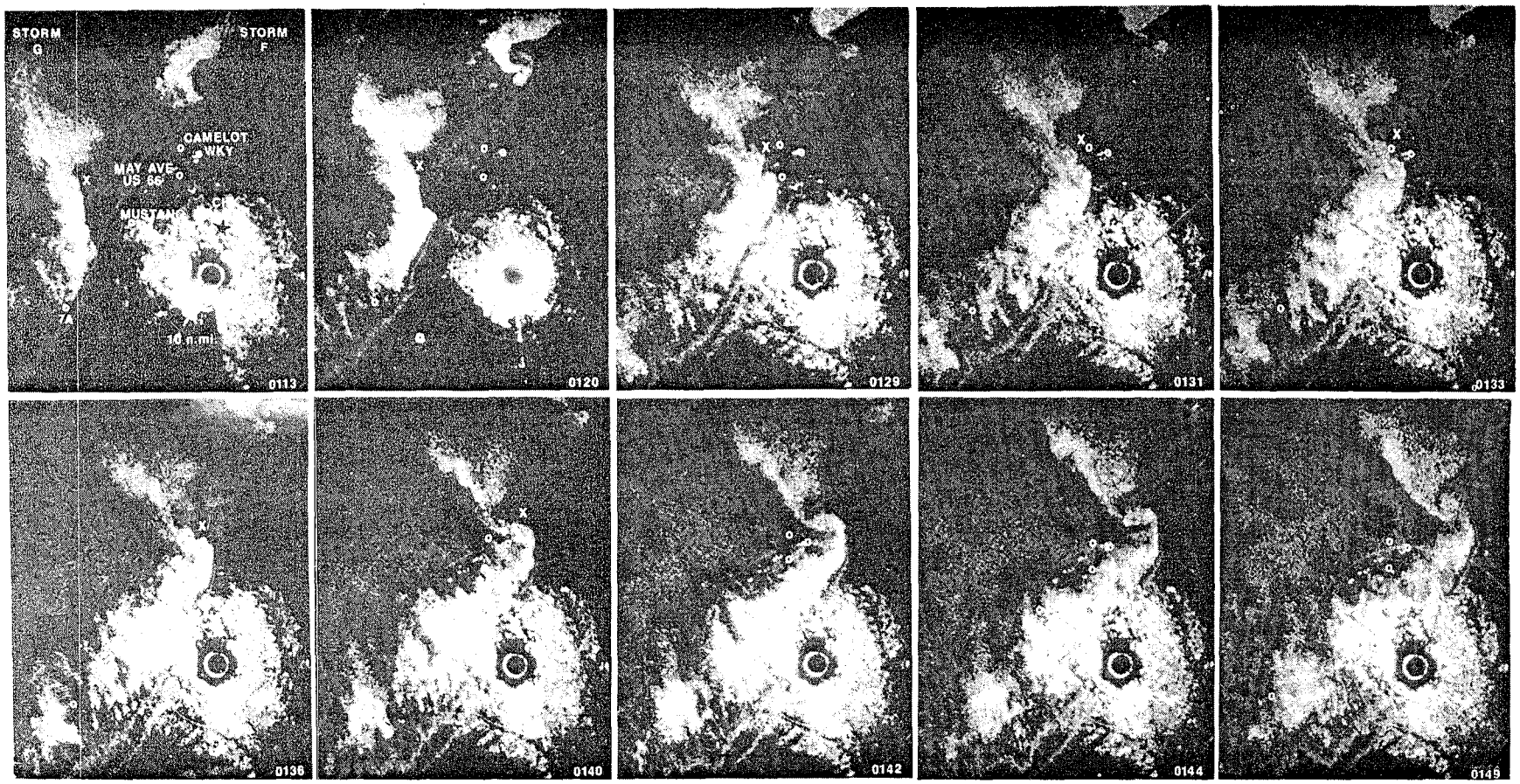

Figure 1. Twin hook echo evolution and merger observed by NSSL's WSR-57 (10 cm) radar. First video level corresponds to reflectivity 19 dBZ; second, brighter level is 39 dBZ. Times (lower right) are CST; antenna tilt is 0° except 1° at 0120; range marks are 10 n mile intervals. Surface mesocyclone position is indicated by "X" (see also fig. 2). Twin hook echoes (tornado cyclones) are about six nautical miles apart at 0129 on the southeast flank of the large supercell Storm G. First extensive damage occurred at Mustang (0120) as a result of a tornado that developed from a growing cell along Storm G's gust front (thin line echo in frames 0129 through 0149). This tornado caused intensive, but spotty damage along a line passing just south of WKY, then it lifted. About 0136, a tornado developed from a second hook echo near the surface mesocyclone and touched down briefly in the Camelot Addition. The sounding (star) labeled CHK No. 30, positioned relative to Storm G, was released at 0041 CST from Chickasha, Oklahoma, which is about three nautical miles south of mesonetwork station 7A.

damage from Storm G's second tornado.[1]

By 0120 the first tornado cyclone produced a hook echo pattern and approached Mustang about 10 n miles from Storm G's main updraft (X). This tornado cyclone developed from a cumulonimbus cell growing among others along the gust front that accompanied the larger Storm G. Its hook echo signature, not obvious in the integrated digital radar data (Barnes, 1972), is clearly defined by the WSR-57's log contour display.

The second hook echo developed during the five-minutes following 0120 CST near Storm G's main updraft (near X) and is clearly visible at 0129 CST. The twin tornado cyclones continued northeastward and by 0131 CST the first tornado struck the May Ave. - US 66 area. Five minutes later (0136 CST), the second tornado cyclone passed directly over the Camelot Addition.[2]

As the tornadoes moved past the WKY tower, damage was less intense, as though the funnels had lifted. The radar echoes from 0140 through 0149 CST suggest the twin cyclones merged, but the available information does not show whether the two circulations became one larger cyclone, or whether the two retained their identities and simply moved in circular paths relative to a point between them. In either case, they interacted strongly.

4. SURFACE WIND FIELD

During the period 0100 to 0140 CST the surface wind pattern changed little relative to Storm G. Figure 2 presents computer-drawn streamlines based on five-minute averaged wind data. Notable features include a sinklike mesocyclone inferred to be the root of Storm G's main updraft, the wind shift line extending from the mesocyclone in an arc southward, and the col northeast of the mesocyclone. At 0100 CST the mesocyclone associated with Storm F's updraft is just leaving the analysis area.

The position of Storm G's surface mesocyclone center is indicated by X in the frames of figure 1. This surface feature relates most closely with the Camelot hook echo, leading it by two to four nautical miles. From this mesocyclone northeastward, the wind field is highly deformed along an axis of dilatation that extends to Storm F's mesocyclone. Air just ahead of Storm G's mesocyclone turns from its original direction of travel (from the south-southeast) towards the updraft as a result of an intense mesodepression (L). The axis of dilatation, along which this mesocyclone moved, is not the boundary separating Storm F's cold surface air from the moist air to the southeast. That boundary's 0100 CST position is indicated in figure 2 by a dashed line which also indicates the southeastmost penetration of Storm F's gust front. At 0100 CST winds along this zone have turned back towards the northwest in response to Storm G's approaching mesodepression.

---

[1] Storm F also produced a tornado which struck Yukon, Oklahoma, located west of the May Ave. - US 66 junction and north of Mustang. However, this storm passed three nautical miles or more from Camelot, and at least 30 min prior to the time of damage reported in Oklahoma City newspapers.

[2] At 0137 CST the power failed at Lake Hefner filtration station one mile southwest of Camelot Addition.

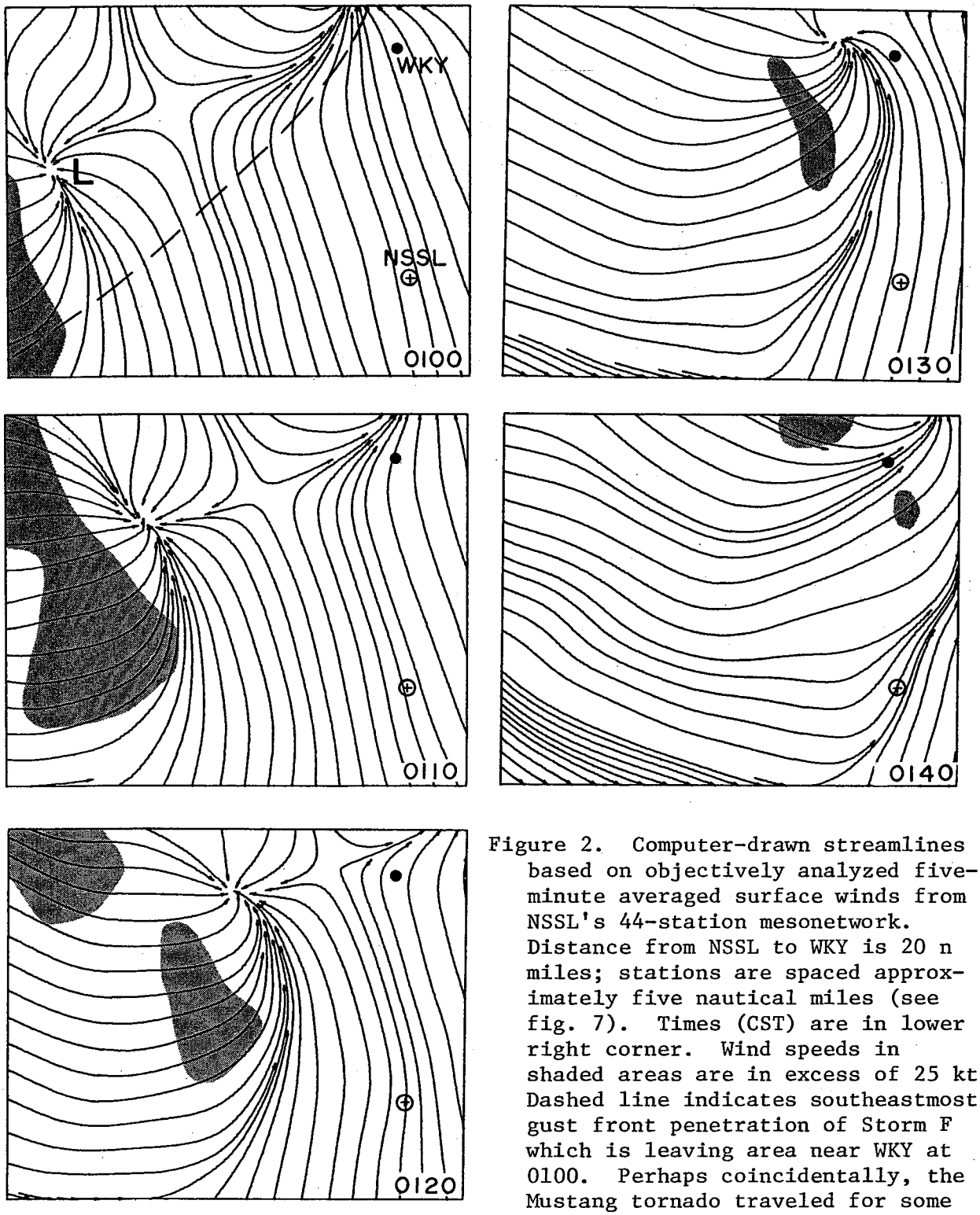

Figure 2. Computer-drawn streamlines based on objectively analyzed five-minute averaged surface winds from NSSL's 44-station mesonetwork. Distance from NSSL to WKY is 20 n miles; stations are spaced approximately five nautical miles (see fig. 7). Times (CST) are in lower right corner. Wind speeds in shaded areas are in excess of 25 kt. Dashed line indicates southeastmost gust front penetration of Storm F which is leaving area near WKY at 0100. Perhaps coincidentally, the Mustang tornado traveled for some distance along this same path. Storm G's mesodepression centered at "L" causes air behind this cold air boundary to retreat northwestward.

The Mustang hook echo, the first to form, traveled along a path nearly coincident with Storm F's old gust front. This hook echo produced the more destructive tornado, but wind data indicate no cyclonic circulation at the surface, at least on a scale detectable in observations separated by five nautical miles. However, the smaller tornadic funnel(s) associated with this hook echo must have been on or very near the surface to cause several millions of dollars damage.

Qualitatively viewing the streamline pattern's time sequence (fig. 2), the mesocyclone first appears to have relatively little rotational component; mostly it is characterized by convergence and deformation. With time, the streamlines near the center take on more curvature giving the impression of a growing rotational component. A time composite of convergence and vorticity centers (fig. 3) reveals at 0110 CST an elongated convergence area in excess of 2×10^{-3} sec^{-1} that later splits into two centers. The northernmost of these associates with the surface mesocyclone and eventually diminishes. Vorticity in excess of 1×10^{-3} sec^{-1} first appears in two small areas, one of which lags the convergence area. In time this center grows and catches up with the convergence center.

These trends are borne out by a quantitative analysis based on the objectively analyzed fields of divergence and vorticity. From maps analyzed at five-minute intervals, areas of convergence in excess of 10^{-3} sec^{-1} and in class intervals of 0.5×10^{-3} sec^{-1} were measured by planimeter. These areas were then weighted and summed to produce a parameter that is roughly proportional to the mass transported vertically by the updraft. Similarly, vorticity areas in excess of 0.5×10^{-3} sec^{-1} were measured, weighted and summed. The results (fig. 4) verify that convergence diminished by a factor of two between 0100 CST and 0135 CST, and then remained essentially constant, while vorticity was trending slightly upward during the same period.

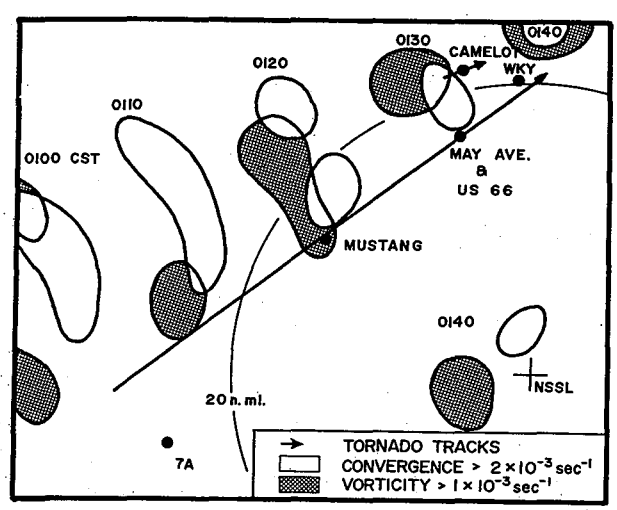

Figure 3. Time sequence of Storm G's convergence and positive vorticity centers based on objectively analyzed surface winds shown in figure 2. Maximum vorticity first (0100 CST) associates with cell producing Mustang-WKY tornado, but later (0130) appears with Camelot cyclone as the two updrafts begin to merge. Convergence near the surface mesocyclone center diminishes until the merger (see also figure 4). The convergence and vorticity centers near NSSL are associated with cell that produced "V" pressure trace at 7A. Note that they are not coincident; nor was any damage reported between 7A and NSSL.

Figure 4. Time variation of area-weighted convergence and vorticity associated with Storm G's twin tornado cyclones. Ordinate units are arbitrary, representing the sum of planimetrically-measured areas between 0.5×10^{-3} sec^{-1} contours computed from objectively analyzed surface winds times the lower bounding contour value. Positive vorticity, mostly in the cold air behind the gust front, remains relatively constant while convergence diminishes by a factor of two. This marked change in the ratio of convergence to vorticity is thought to be related to the observed larger rotation radius of Storm G's hook echo after the twin cyclones merged (see Ward, 1970).

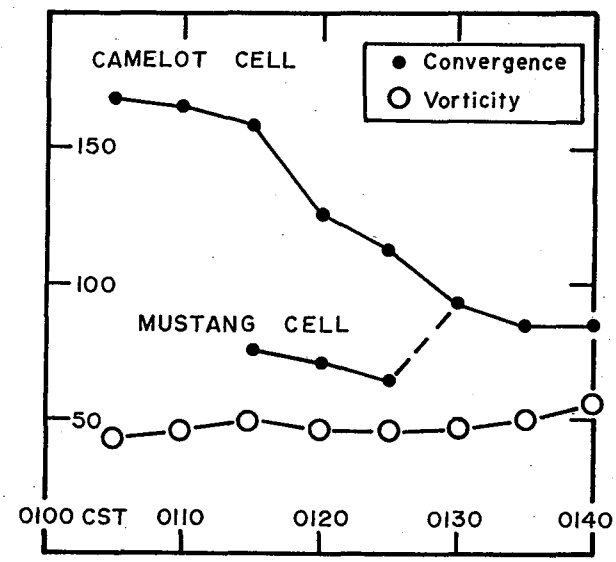

Keep in mind that the motion scale to which these results apply is larger than individual tornadoes. The larger (5 n miles) tornado cyclone circulations are among the smallest features that correlate well in the time series data from adjacent stations, but only their approximate characteristics are represented in the analyses.

It is encouraging that these results and the manner in which the two tornado cyclones interacted are in qualitative agreement with Ward's (1970) laboratory findings. When convergence dominates over the rotational component of flow into an updraft, only small-scale vortices form. When vorticity increases relative to the convergent component, a larger vortex may form containing several smaller vortices within it.

Soon after the twin tornado cyclones merged (fig. 5), Storm G stopped producing tornadoes. Only sporadic damage reports were noted from the area northeast of WKY, and it is not clear whether Storm F or Storm G caused these.

5. TORNADOGENESIS

The configuration of twin hook echoes (0129 CST, fig. 1) is strongly reminiscent of unstable Kelvin-Helmholtz waves which occur on horizontal surfaces separating fluids of different density and across which there is a considerable shear in horizontal velocities. Barcilon and Drazin (1971) have suggested that multiple dust devils observed to lie in the same vertical plane may be caused by a type of flow instability in an unstably stratified fluid-perhaps as a combination of Kelvin-Helmholtz and Rayleigh-

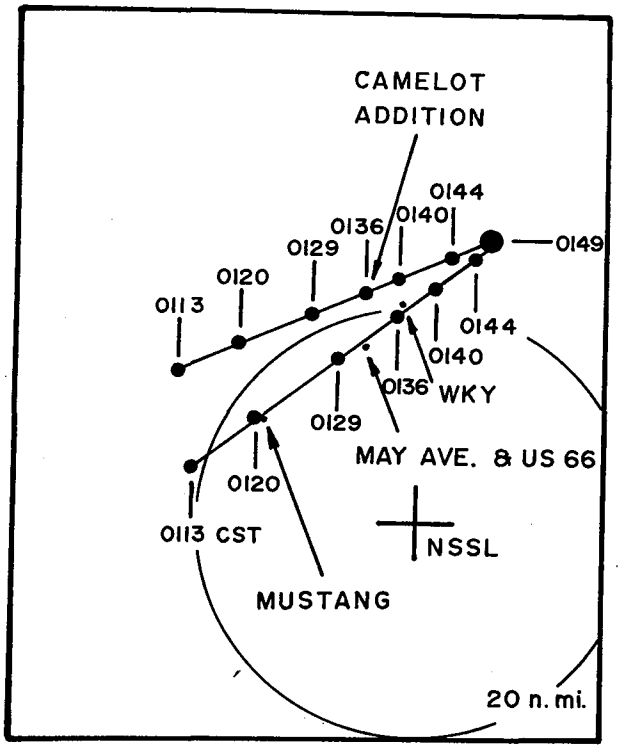

Figure 5. Tracks of twin hook echoes from figure 1 radar displays.

Taylor instabilities. Treating a simple linear case, they were able to demonstrate that large amplification is possible when gravitational-shearing forces are coupled with convective-rotational forces.

The density interface separating thunderstorm outflow air from less dense air feeding the updraft is tilted, but this may not be important to the physics of the phenomenon. Components of gravity and wind shear normal to the interface are still present, and may act to amplify perturbations.

Multiple dust devils and tornadoes (or waterspouts) frequently have been observed along shear zones caused by thunderstorm gust fronts. It is only a slight conjecture to assume that if one or more of these vortices becomes coupled (entrained) into a convective updraft, the vortex will either grow as an entity, or add its vorticity to that of the updraft. Lemon's analysis[3] of another severe thunderstorm case observed in the NSSL network indicates that when flanking cells are entrained into the quasi-steady updraft of supercell-type storms, they lose their identity and add their physical properties to those of the main updraft.

Can this be a reasonable mechanism for initiating rotation on the scale of the tornado cyclone? Suppose wind shear across the gust front interface reaches a critical value and produces instabilities resulting in vortices. Vorticity thus generated and entrained into updrafts is concentrated by vertical stretching. If updraft rotation develops on a large enough scale, it may be "self-sustained" by concentrating vorticity from the ambient atmosphere. Subsequent smaller vortices transported into this favorable regime may retain circulation about their own axes and grow.

The described mechanism is not meant to describe all tornadic storms, but may have some relevance to the sequence of events accompanying supercell storms which have attendant flanking updrafts along their gust fronts.

In the present case, there is some evidence suggesting that still another tornado cyclone developed briefly to the south of the Mustang hook echo. In figure 1, a protrusion is noted at 0120 CST along the leading edge of the echo about 12 n miles southwest of Mustang. This radar echo feature developed

[3]Personal communication.

from a part of the storm which previously had passed close to station 7A where there was recorded a 3-mb "V" pressure trace coincident with a 50 kt squall as the wind shift line passed. Later, about 0140 CST, this echo portion passed just north of NSSL. Convergence and vorticity patterns indicated centers of 1.2×10^{-3} sec^{-1} and 1.3×10^{-3} sec^{-1} moved along this path, but the vorticity center lagged five nautical miles behind the convergence center (fig. 3).

6. THE DOWNDRAFT AIR

The air's motion behind the gust front is from westerly to west-northwesterly directions (fig. 2) in excess of 25 kt averaged over five minutes (shaded areas). These directions are not readily explainable on the basis of vertical momentum transports or the presence of synoptic-scale wind systems. A sounding released from Chickasha, Oklahoma, at 0041 CST (fig. 6) about 20 n miles ahead of Storm G (see 0113 CST frame of fig. 1) indicates no wind directions greater than 218° below 7 km (termination altitude). A deep upper level trough was approaching Oklahoma from the west, and winds aloft had backed during the previous six hours. At the surface, a stationary front was located in northwestern Oklahoma and no significant pressure systems were in the area. We must conclude, therefore, that the surface winds observed behind the gust front were produced largely by the storm itself.

Wet-bulb potential temperatures in the post-gust-frontal air are about 17C, suggesting this air came down from at least 3 km altitude. Average wind in the 3 to 6 km layer was from 215° at 63 kt. The first tornado cyclone moved from 233° at 62 kt. The vector difference is from 310° at 18 kt. The acceleration which causes this right-of-mean-flow movement has been variously attributed to Magnus effect on the rotating updraft or continuous propagation into the moisture field. To these effects, now add acceleration of downdraft air by surface pressure gradients.

An intense ridge of high pressure was observed in the rain area behind the gust front creating a 2 to 3 mb per 15 n mile pressure gradient directed mostly eastward (fig. 7). In five minutes, this acceleration is sufficient to turn air eastward by 4.8 kt, not considering the retarding frictional force.

The causes of thunderstorm pressure systems have not been extensively investigated because there is no easy way to measure or calculate from theoretical models three dimensional pressure distributions in and about them. These observations make it clear that horizontal pressure gradients play an important role in determining thunderstorm flow characteristics.

7. CONCLUDING REMARKS

Davies-Jones and Kessler (1973) have suggested that the mechanism proposed by Barcilon and Drazin (1971) explaining dust devil formation along the same vertical plane has application in larger scale convection. These observations of multiple tornado cyclones along the gust front of an exceptionally large supercell-type thunderstorm and the subsequent merger of two cyclones supports this suggestion. The data are insufficient to determine the entire tornadogenesis mechanism; nevertheless, the following partial explanation of tornadoes that develop beneath a supercell cumulonimbus updraft and its flanking convection cells emerges from these data.

Figure 6. Stüve diagram of Chickasha, Oklahoma, sounding released about 20 n miles east of Storm G's first hook echo at 0041 CST. Sloping dashed lines are mixing ratio; sloping solid line labeled 280 is potential temperature (K); 10C, 20C, and 30C wet-bulb potential temperature lines are curved. Right-hand heavy line is temperature profile; dew point profile is to left except in the saturated layer below 790 mb where they coincide. Circles designate elapsed time since release versus pressure and reveal balloon ascent rate; curve cycles back to zero for times greater than 15 min. Winds are plotted at right as vectors with north at top. Speeds corresponding to 10 m sec^{-1} are shown by line segment at bottom of wind plot. (This diagram was computer-plotted from NSSL archive sounding tapes.)

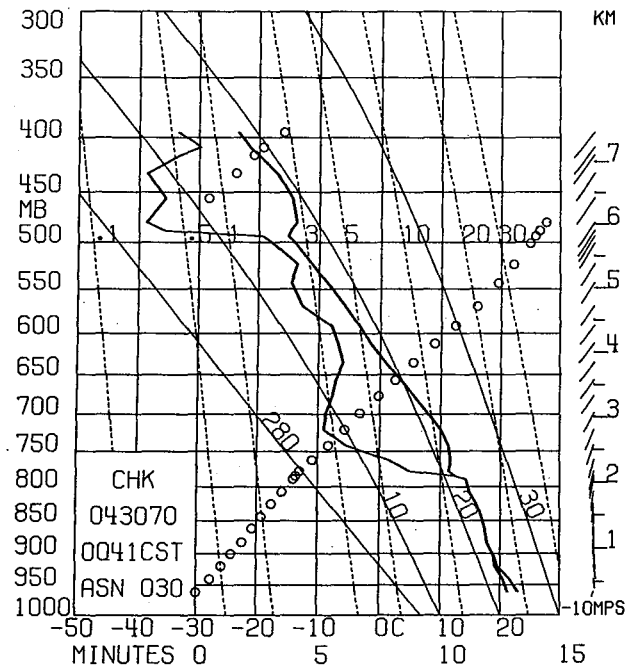

Figure 7. Surface pressure perturbation (from eight hour trend) at 0120 CST. Isobars at 0.5 mb intervals reveal strong eastward-directed gradient that may have contributed to Storm G's right-of-mean-flow movement by accelerating downdraft air in that direction. Intense mesodepression 20 n miles northwest of NSSL contributed to flow characteristics about col point in figure 2. NSSL's 44-station network is indicated by dots. Circled dots are sounding stations; Chickasha is in the southwest.

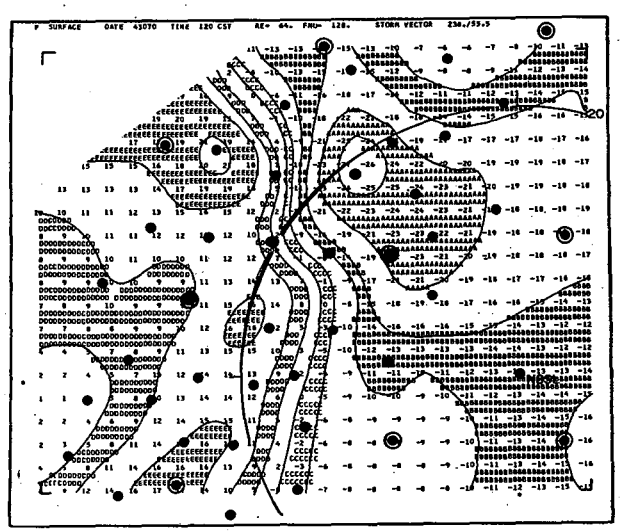

The intense mesodepression beneath a supercell updraft strongly accelerates sub-cloud air toward the updraft base. Potentially cold mid-tropospheric air brought to the surface by evaporative cooling provides the density interface necessary to support shearing-gravitational instabilities that manifest as roll vortices tilted upward along the gust front. Vorticity thus generated is stretched and concentrated by the updraft cells along the storm's flank. These updrafts eventually merge with the main updraft, adding their properties to it. In time, the supercell updraft may attain significant rotation (through this or some other source) so that subsequent smaller vortices (funnel clouds?) find themselves in an environment favoring their growth, that is, they become tornadoes.

The space and time scales required for these developments are yet unresolved, either through observations or theoretical considerations. Although not capable of resolving details within tornadoes, dual-Doppler radar data may eventually reveal the evolution of flow in rotating updrafts. Even then, we will need to understand through boundary layer studies how and why surface winds are apparently decoupled from the cloud circulations as they were in the Mustang tornado cyclone.

8. REFERENCES

Barcilon, A. I., and P. G. Drazin, 1971: Dust devil formation. Tech. Rep. 35 to Office of Naval Research, Geophysical Fluid Dynamics Institute, Florida State University, 16 pp.

Barnes, S. L., 1972: Morphology of two tornadic storms: an analysis of NSSL data on April 30, 1970. Preprints of the 15th Radar Meteorology Conference, Champaign-Urbana, Illinois, Amer. Meteor. Soc., Boston, Mass., 69-76.

_____, 1973: Mesoscale objective map analysis using weighted time-series observations. NOAA Tech. Memo ERL NSSL-62, 60 pp.

Bates, F. C., 1968: A theory and model of the tornado. Proceedings of the International Conference on Cloud Physics, Toronto, Amer. Meteor. Soc., Boston, Mass., 559-563.

Davies-Jones, R. P., and E. Kessler, 1973: Tornadoes. Weather and Climate Modification, Ed. W. Hess, John Wiley, New York, (in press).

Environmental Data Service, 1970: Storm Data, Vol. 12, No. 4, U. S. Government Printing Office, Washington, 26-46.

Fujita, T. T., D. L. Bradbury, and C. F. Van Thullenar, 1970: Palm Sunday tornadoes of April 11, 1965. Mon. Wea. Rev., 98, 26-69.

Golden, J. H., 1973: The life cycle of the Florida Keys waterspout as the result of five interacting scales of motion. Ph. D. dissertation, Florida State University, 370 pp.

Ward, N. B., 1970: The exploration of certain features of tornado dynamics using a laboratory model. NOAA Tech. Memo. ERL NSSL-52, 22 pp.

TORNADO CHARACTERISTICS IMPLIED FROM DAMAGE TRACKS

S. L. Barnes and B. L. Courtney

National Severe Storms Laboratory
Norman, Oklahoma 73069

Damage tracks surveyed by National Severe Storms Laboratory staff, and newspaper accounts of three tornadoes that struck the Oklahoma City area on April 30, 1970, reveal characteristics of these wind systems. Few details emerge from surveying the first tornado (Storm F) except that its path crossed mostly open country and passed several miles northwest of Oklahoma City. Twin tornado cyclones (Mustang and Camelot), observed an hour later in Storm G, apparently produced multiple funnels that moved rapidly (120 kt) around the southern half of larger cyclonic circulations (hook echoes). Maximum winds estimate less than 240 kt. Sporadic damage mostly at roof level suggests the tornadoes often did not extend to the ground. Typical noise heard from the Mustang tornado was a "bang" as opposed to the "roar of freight trains." Unusual electrical phenomenon occurred with only one tornado (Camelot).

1. INTRODUCTION

The April 29-30, 1970 storms spawned at least three tornadoes in Oklahoma. Considerable sporadic damage was evident as one tornadic storm travelled a path from 115 n miles southwest of Oklahoma City to northwest of the metropolitan area, and finally dissipated some 45 n miles northeast near Stillwater. Two other tornadoes were spawned from a storm that followed the first by one hour. One funnel, touching down about 35 n miles southwest of Oklahoma City, caused extensive damage through the City and surrounding communities. The second of these tornadoes touched down briefly in the City's extreme northwestern part and travelled a converging path toward the first tornado. As the two approached each other on the City's northeast edge, both lifted. The storm's last reported damage occurred 50 n miles northeast near Cushing. These storms travelled a rapid 30 to 55 kt along paths of 160 and 85 n miles long. Since they happened during the night, few people saw the funnels. NSSL radar and surface network measurements, damage photographs and newspaper accounts are the only information sources on the nature of these funnels. We take liberty to correct obvious errors in these reportings and to reassess the damage attributed to the various tornadoes based on more complete information than existed at that time.

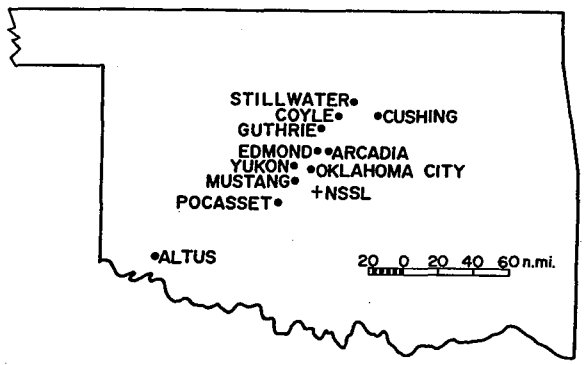

Figure 1. Locations of Oklahoma towns referred to in text.

2. STORM F (2225 to 0200 CST)

The first tornadic storm, identified as Storm F, produced a tornado near Altus, Oklahoma, 115 n miles southwest of Oklahoma City. Storm Data [1] reports the tornado formed approximately 2225 CST and then moved northeastward at around 39 kt before dissipating five n miles south of Stillwater at 0200 CST (fig. 1). The tornado was sighted on the ground several times along this path. A pilot who later flew over the storm's path from east of Guthrie to south of Stillwater reported the tornado was definitely on the ground at times. At one point, southwest of Coyle, the tornado picked up a trailer home and moved it 100-150 feet to the west while the storm itself continued in a northeast direction.

As this storm approached Oklahoma City about 0100 CST, radar detected a tornado cyclone five n miles southwest of Yukon. We believe this funnel evolved from the same tornado cyclone that struck the Altus area. Radar photographs support this belief (pages 21 - 22). NSSL's mesonetwork station at Cimarron Airport (three n miles southwest of Yukon) recorded wind and pressure traces indicating tornadic activity (page 129). NSSL personnel surveyed the damage path (fig. 2), but extent and type of damage was not recorded.

3. STORM G (0100 to 0245 CST)

3.1 Mustang Tornado

Storm Data [1] records this information on the major tornado with Storm G: the first damage ($10,000) occurred at a farmstead four n miles northwest of Pocasset (fig. 1). At Mustang, damage estimated at $500,000, was confined mainly to a shopping center and the City Hall in the north part of town. Two semi-trailer trucks, in the storm's path, were blown off Highway I-40 and turned on their sides while entering Oklahoma City from the west. Then the tornado moved along a path 1/2 n mile wide from southwest to northeast across Oklahoma City. In Oklahoma City, damage (estimated at $6.3 million) involved 1473 homes, 293 businesses, eight schools, 12 churches, and 300 signs. Southwestern Bell Telephone Company officials reported 30,000 telephones out of order, primarily in northwest Oklahoma City and in Mustang. Oklahoma Gas and Electric Company officials reported 215 poles downed. In several areas roofs were blown at right angles to the storm's path indicating a rotating column of air. After the storm left Oklahoma City, it extensively damaged a home and several outbuildings two miles west of Arcadia.

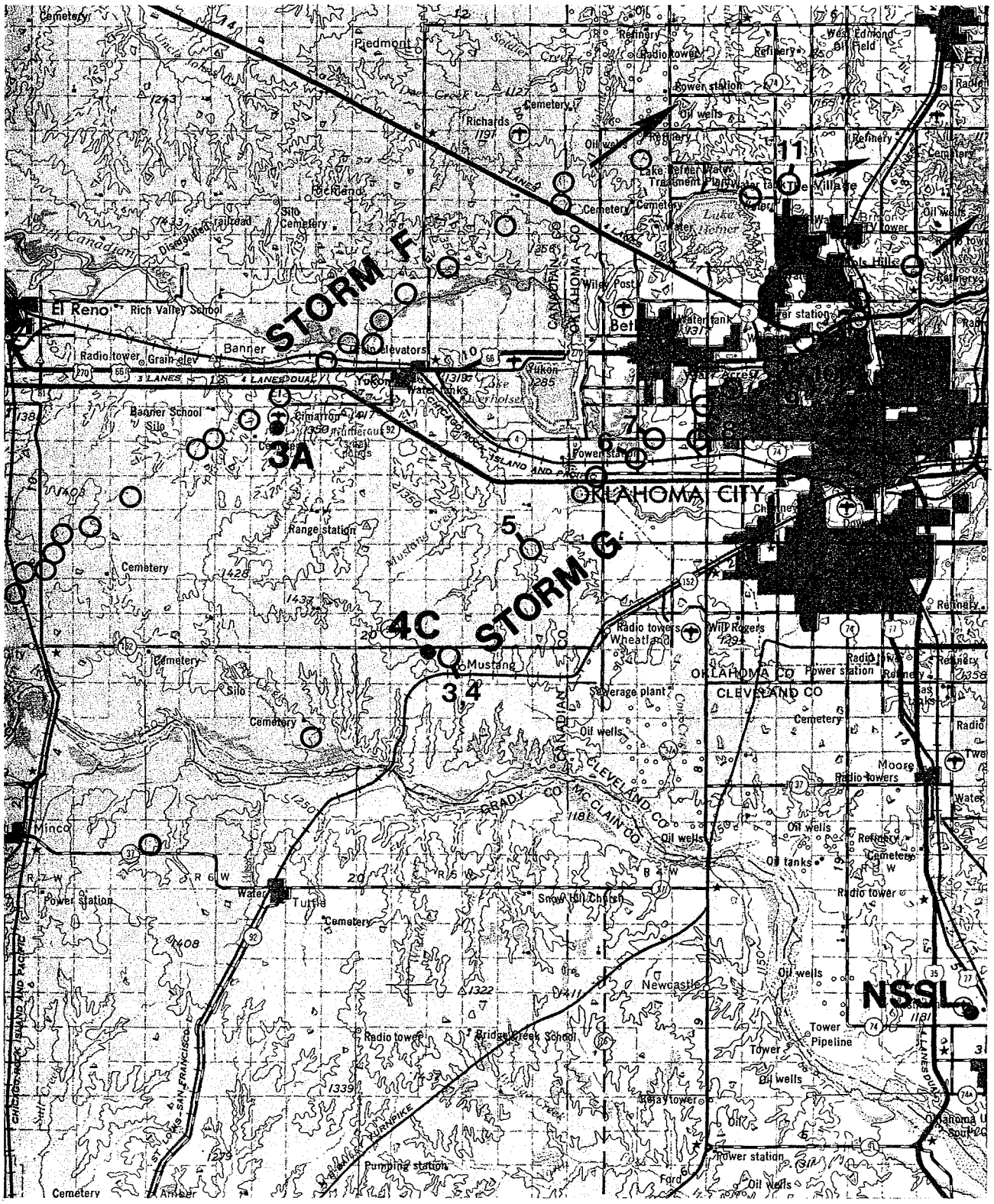

Figure 2. Damage tracks from three tornadoes crossing Oklahoma City area shortly after midnight April 30, 1970. Circles denote damage points surveyed by NSSL staff; numbered circles refer to damage photographs 3 - 11. Solid dots 3A and 4C locate NSSL meteorological recording sites. Light dashed lines show scale (one statute mile).

Damage characteristics at the Mustang, Oklahoma shopping center are shown in figure 3. Also damaged in this small community were the brick and steel city office building (fig. 4) and several lesser structures.

Travelling mostly across open country, the tornado next deroofed the Mustang Valley School (fig. 5) three miles northeast of the Mustang community. Two to four miles farther along, the storm struck a low density industrial section on Oklahoma City's southwest edge. One manufacturing building (fig. 6) was demolished, but 100 feet south a building of similar construction was undamaged! At least two other buildings in this area sustained severe damage. One man who witnessed the tornado from an apartment complex at 7145 Melrose Lane commented "When I saw part of the roof knock down that tree outside the bedroom window, I decided something was really wrong. It lasted just seconds...sucked glass out of the bedroom window" [2].

Continuing northeastward into Oklahoma City, this tornado dipped down sporadically. A car wash (fig. 7) on N. W. 10th and Whitman literally blew away. Other buildings in the area were tossed about and heavily damaged; trees were split or broken. Across the street from the car wash apartment dwellers woke up to an "exploding" sound but couldn't see much in the heavy rain. The apartments were virtually undamaged.

One mile east of this damage, the Southwestern College fieldhouse, 4700 N. W. 10th, was practically demolished ($200,000 damages). One wall and the roof were torn away and part of another wall crumpled [3].

In the vicinity of N. W. 23d and Meridian, the funnel battered homes, businesses, and apartment dwellings (fig. 8). "Damage appeared to be some of the most excessive in the estimated 100-block area over which the tornado travelled." The canopy roof and other debris from a small grocery store on Meridian landed nearly a block away in the front yard of a residence at 4400 N. W. 19th (also called Warren Avenue). Roofs were blown off two sections of the Windsor Hills Apartments, and the north wing of Gaslight Apartments incurred heavy damage [3].

The funnel was again on the ground at May Avenue and N. W. 39th (US 66 Highway). One million dollars damage was estimated at May Avenue Dodge (fig. 9). "Downtown Chevrolet lost the roof off its carport...the adobe wall of El Rancho Sanchez was caved in and the Taco Boy was an almost unrecognizable pile of rubble, except for the untouched sign." Several motels, apartment complexes and businesses were severely damaged along N. W. 39th (Habana, Tropicana, DeVille, Spanish Village, Richardson Ford, Watts Funeral Home). At the Habana Inn, the assistant manager heard a big bang. "I went to look and this guy was flying through the glass. I ran over to help him, but then the wind started howling so hard I got scared and climbed in a chimney. When the danger was finally over, we went over to see if the man was hurt. He was bleeding badly from his leg" [2].

Continuing its diagonal path across the city, the twister next came down west of Pennsylvania Avenue along 48th Street. An automobile from several houses away landed in the living room of a home at 2201 N. W. 48th. On the north side of 48th, four homes were heavily damaged (fig. 10), while homes

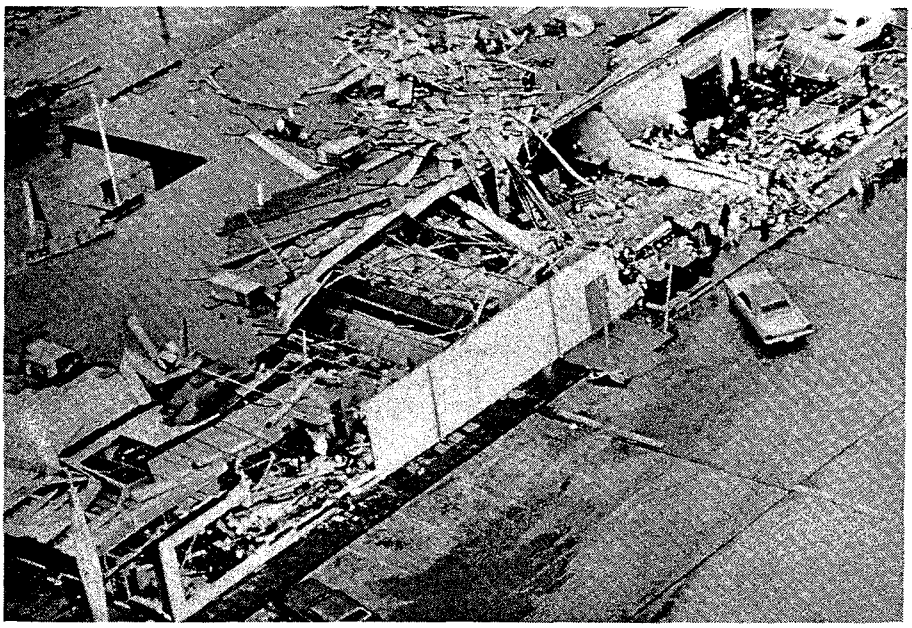

Figure 3. Tornado-wrecked Mustang Shopping Center viewed toward northeast. (Copyright 1970, Oklahoma Publishing Company, Oklahoma City Times, May 1).

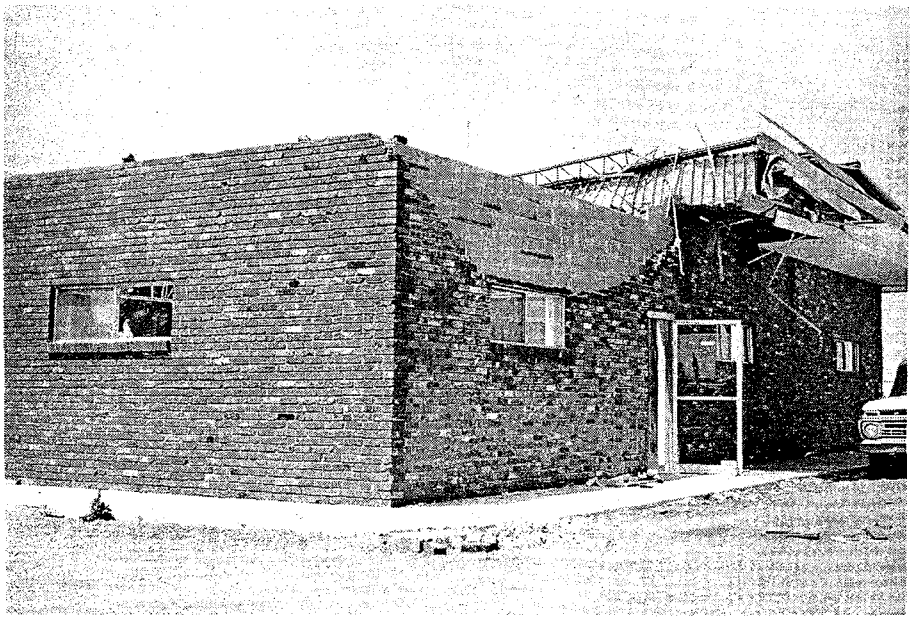

Figure 4. Southeast corner of the Mustang City Hall (NSSL photo).

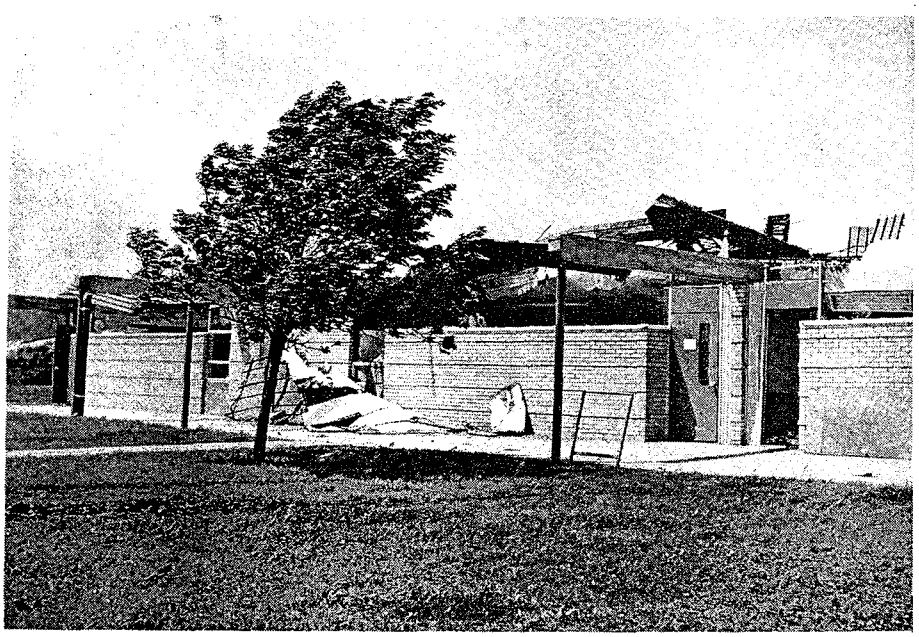

Figure 5. Mustang Valley School looking northwest (NSSL photo).

Figure 6. Demolished instrument manufacturing company, view northwest, (NSSL photo).

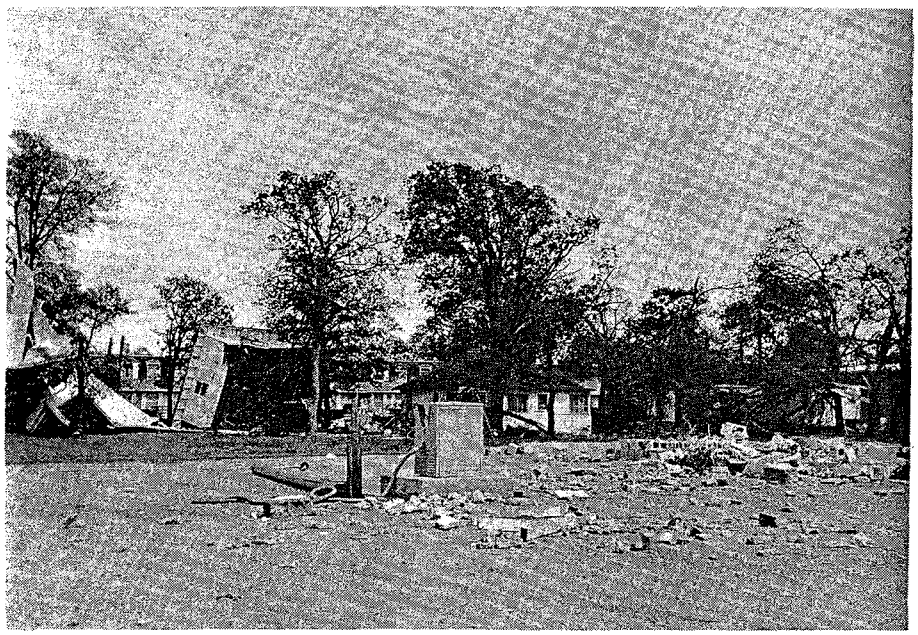

Figure 7. Site of car wash at N. W. 10th and Whitman. Original location of tilted building in background is undertermined (NSSL photo).

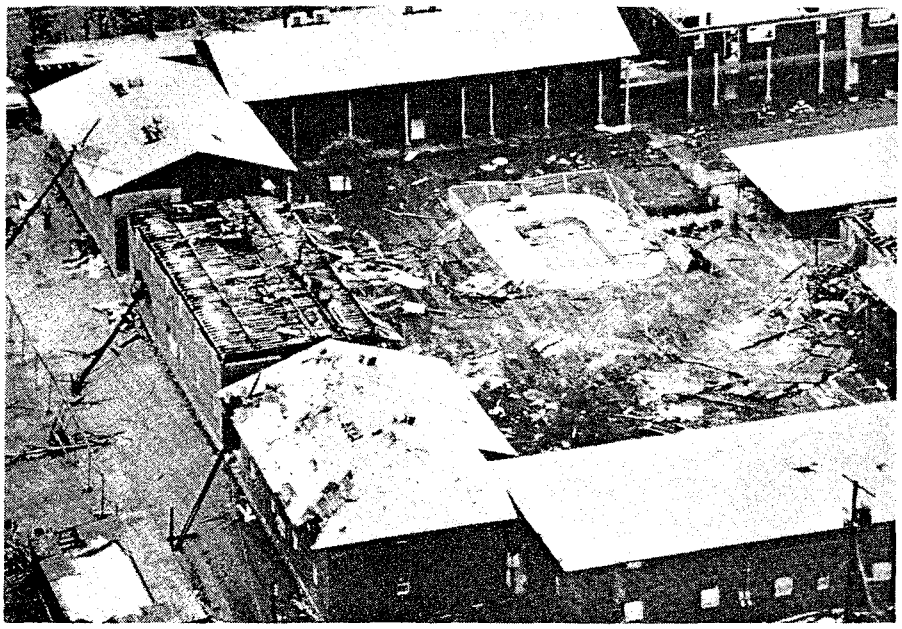

Figure 8. Apartment complex at N. W. 23d and Meridian. Telephone poles blown toward east. Tornado moved toward upper right heavily damaging the roof on the northeast apartments, but leaving adjacent roofs intact. Funnel apparently passed directly over single story structure near swimming pool without damaging it. (Copyright 1970, Oklahoma Publishing Company; from Oklahoma City Times, April 30).

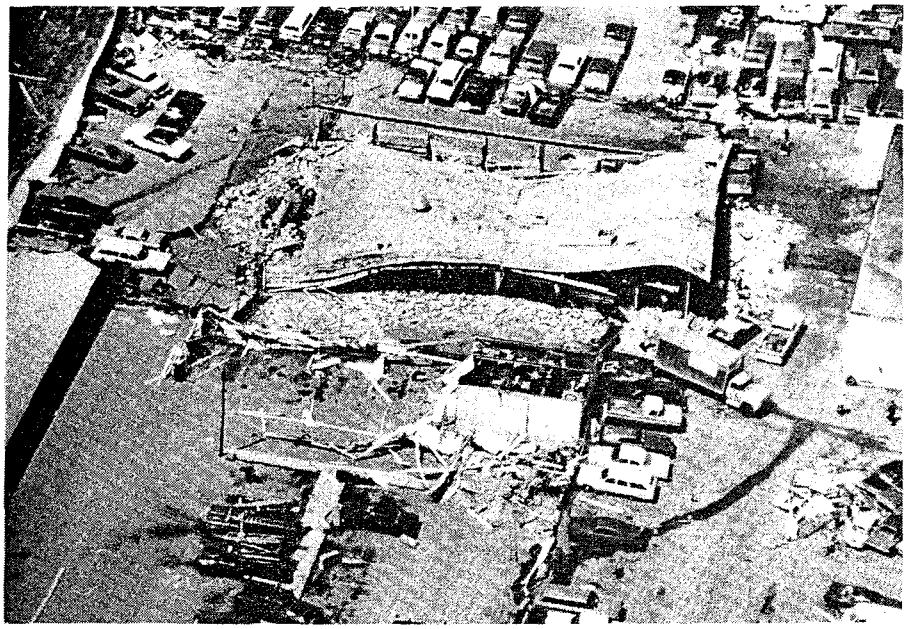

Figure 9. Collapsed garage at May Avenue Dodge. North is toward top. Funnel apparently travelled southeastward (toward lower right) across this building and then along N. W. 39th. (Copyright 1970, Oklahoma Publishing Company; from Daily Oklahoman, May 1).

Figure 10. One of four heavily damaged homes along the north side of N. W. 48th near Pennsylvania (NSSL photo).

on the south side remained untouched [2]. At N. W. 49th and Pennsylvania, one wing of the Temple B'Nai Israel School was demolished [3]. At nearby Belle Isle Apartments (N. W. 46th) a woman and her husband saw what appeared to be a funnel heading northeast straight toward the apartment complex. Nevertheless, the apartments sustained only minor damage: three trees uprooted, broken windows, and a piece of the roof missing [2].

Over the next two miles along the southeast edge of Belle Isle Lake, the tornado damaged considerably roofs and elevated structures. Near 50th and Western, part of the McGuiness High School gym roof and walls were ripped away. The principal said electric clocks in the school and at his nearby home stopped at 0133 CST. Much of the school debris was deposited at a home about one block northeast of the school. The resident, awakened by the storm, commented that the tornado announced itself with a loud report followed by a loud crash [2].

Along 62d street, the storm drove a steel beam through a home, moved half the house off its foundation, bowed the walls out and deposited part of the roof in a neighbor's yard. Again, the occupant of the dwelling reported that "it sounded like a great big gun fired" [2]. The tornado skipped a mile and then slammed into a new housing development, demolishing about four blocks of homes under construction and blasting debris into a nearby residential area. Only scattered minor damage resulted as the storm skimmed out of the city. On the Northeast Expressway, a cafe employee saw what he thought was a funnel approaching. "I jumped up to close the kitchen window. Then the thing hit" [2]. The wind unroofed a neighboring service station, blew out two cafe plate glass windows, and crushed a late model car parked outside.

The only other damage reported from this storm was in the Arcadia area and later near Cushing [1]: At 0245, a tornado touched down briefly causing considerable damage. Six homes, one car, and several garages were damaged. Trees were uprooted and utility lines were downed. Two persons received minor injuries. This damage point, eight n miles east of Cushing, lies 41 n miles from the northeast edge of Oklahoma City and a little to the right of the path taken by Storm G. At the rate Storm G was moving (about 55 kt), it could have easily reached the Cushing area within the hour after leaving Oklahoma City. Although radar continuity cannot be traced beyond the Arcadia area (power outage at NSSL), we feel that Storm G was strong enough to have inflicted further tornadic damage.

3.2 Camelot Tornado

About the time the Mustang tornado was striking N. W. 48th Street (0131 CST), another tornado developed about four n miles northwest and hit the Camelot Addition (fig. 11). Storm Data reports "the greatest damage along the storm path was in a residential area in the extreme northwest section of Oklahoma City. There, 30 homes valued at from $35,000 to $50,000 were either destroyed or damaged." But this damage incorrectly is attributed to Storm F's tornado. Studies of NSSL radar photographs and newspaper accounts clearly indicate that the Camelot damage occurred at least 30 minutes after Storm F had passed some three n miles farther to the northwest. One eye witness, Samual Bates, a Metro Security Patrolman watching the area, said

Figure 11. Damaged residences in the Camelot Addition, northwest Oklahoma City. Funnel travelled south of east in direction of arrow. (Copyright 1970, Oklahoma Publishing Company; from Oklahoma City Times, May 1).

the tornado appeared in a "brilliant green light, the most beautiful I've ever seen" [3]. "The twister touched down near 116th Street," Bates said, "cut its swath then skipped into the air, fishtailed around then headed toward Edmond." Radar information suggests that this storm later merged with the Mustang storm when it was east of Edmond (pages 141-151).

4. CONCLUSIONS

The separate damage tracks from Storms F and G with times of passage established by radar film data and power outages clearly indicate that three major tornado cyclones passed through the Oklahoma City metropolitan area after midnight on April 30, 1970. We cannot ascertain from available information whether each parent cyclone had one or more tornadoes either simultaneously or sequentially. Several eyewitnesses have established that there were funnels, although few details in the debris patterns suggest rotating wind systems. Perhaps this is explainable by the storm's very high forward speeds (over 55 kt). The one-half mile width of the Mustang tornado damage path suggests either a single large funnel, or multiple small funnels progressing around an arc in the larger cyclone system (hook echo signature). The latter seems more likely.

Near Belle Isle Lake, the severe damage path was rather narrow (less than 100 feet wide) and curved in a discontinuous arc eastward from N. W. 48th Street across the Classen traffic circle then northward to N. W. 62d Street (fig. 12). This arc began and ended on the tornado cyclone's straight path

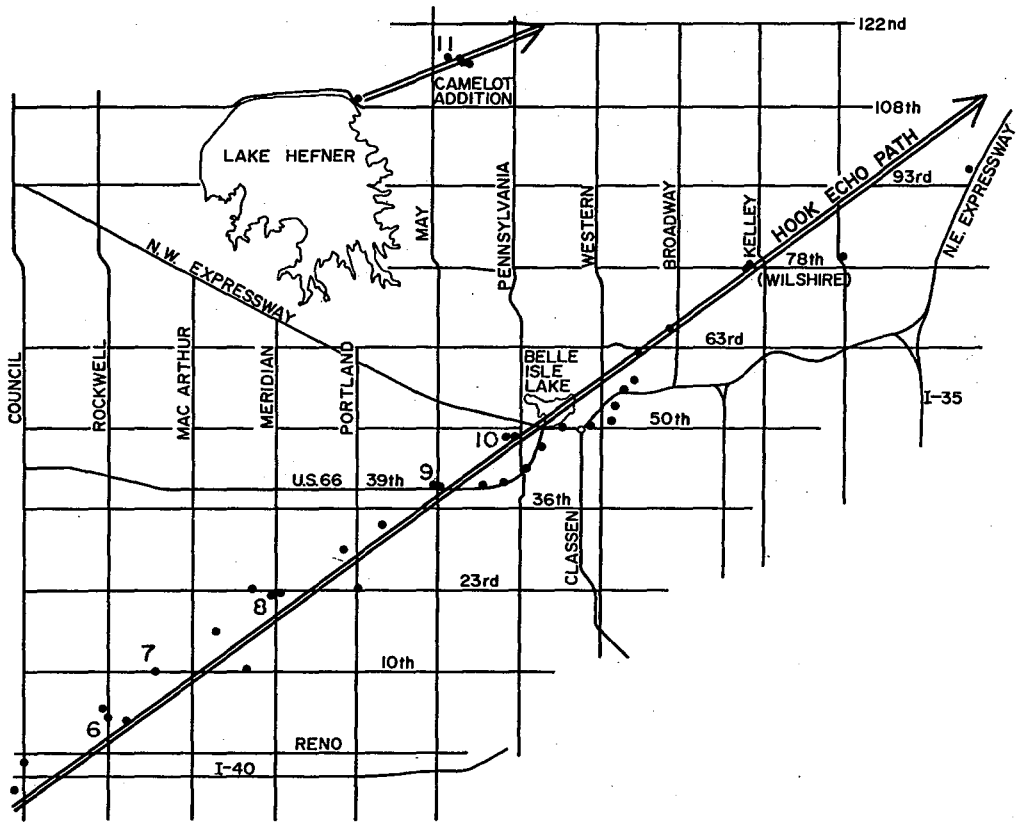

Figure 12. Locations of most intensive damage from Storm G's twin tornadoes. Double arrow indicates radar hook echo paths; solid dots refer to damaged structures described in text. Numbered dots refer to figures 6 - 11.

across the city, suggesting a tornado funnel formed on the back side of the cyclone, moved around the cyclone center to its forward side, then lifted or dissipated [4,5].

If this were the case, the tornado funnel's trajectory indicates the cyclone had higher tangential speed than forward speed. The tornado's distance from the cyclone center is given by the point of maximum departure of the arc from the straight line path, about one-half mile (fig. 13). Assuming the tornado stayed at this relative distance from the center, one can estimate the distance the center travelled while the tornado moved through its semi-circular arc. This distance measures one mile which the center covered (at 55 kt) in about one minute. The tornado's arc length, about two n miles, is traversed in the same time interval yielding 120 kt funnel translation speed (or 65 kt relative to the cyclone center). Superimposed upon this is tangential motion about the tornado funnel's own axis, probably less than 120 kt in view of the evidence that debris was generally distributed in the direction the small vortex was travelling, i.e., at an angle across the larger tornado cyclone's path. Even if maximum winds around the vortex had been 100 kt, the total wind relative to the ground would still have had a

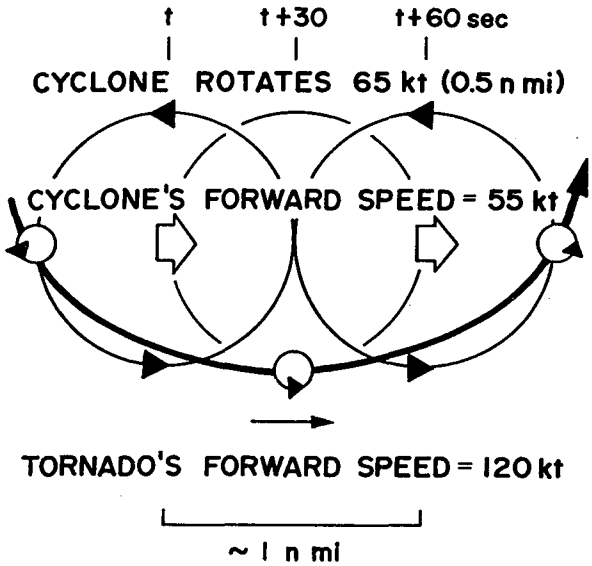

Figure 13. Schematic tornado path around larger cyclone that spins faster than rate of forward movement. Time and distances estimates are from actual damage path near Belle Isle Lake.

component in the direction of travel; that is, the debris would appear to have been laid out along a straight or gently curving arc giving the appearance that the damage had been caused by "straight line winds." This reasoning leads to estimated maximum tornadic wind (over the ground) less than 240 kt.

Several other locations experienced similar damage patterns. A line connecting points of most severe damage within a square mile or two area fell to the right of the path taken by the tornado cyclone. This was the case at Mustang, N. W. 10th and MacArthur, along N. W. 23d, along US 66 (N. W. 39th), around Belle Isle Lake, and finally just north of N. E. 78th (Wilshire Blvd.). Further, it is interesting to note that the maximum wind speed measured at NSSL station (4C) one-half mile west of the Mustang Shopping Center was 95 kt. This station appears to be left of the damage path (fig. 2) viewed in the direction of travel. If so, the measured wind is the sum of the tornado cyclone's wind minus the funnel's rotational component.

The typical noise signature of a tornado (roar of several freight trains) was not apparent in the Mustang storm. Instead, it was described as a single loud bang, as though an explosion had occurred. Yet, there was not much evidence of buildings exploding. Mostly roofs were torn off, and the large debris landed nearby or at most a block away. The rapidity with which this happened (again the high forward speed) may have changed the roar to something more like a report.

Except for a brilliant green light reported with the Camelot tornado, there is little evidence of unusual electrical phenomena with these storms.

5. ACKNOWLEDGMENTS

We acknowledge the contributions of several NSSL staff members who helpfully reviewed the paper and offered constructive criticisms.

6. REFERENCES

1. U. S. Department of Commerce, Environmental Data Service, 1970: Storm Data, Vol. 12, No. 4, April.

2. Oklahoma Publishing Company, 1970: Oklahoma City Times, Vol. LXXXI, No. 60, April 30 (Copyright 1970; published with permission).

3. Oklahoma Journal Publishing Company, 1970: Oklahoma Journal, Vol. 6, No. 260, May 1 (Copyright 1970).

4. Ward, N. B., 1972: The exploration of certain features of tornado dynamics using a laboratory model. J. Atmos. Sci., 29, 1194-1204.

5. Fujita, T. T., 1971: Proposed mechanism of suction spots accompanied by tornadoes. Preprints of Papers, Seventh Conference on Severe Local Storms, Amer. Meteor. Soc., Boston, Mass., pp 208-213.

PRELIMINARY RESULTS OF A STUDY OF THE VERTICAL PROFILE OF MEAN DIVERGENCE IN A REGION OF CONVECTIVE UPDRAFTS AND DOWNDRAFTS

R. J. Reed, R. C. Easter and T. J. Matejka

University of Washington
Department of Atmospheric Sciences
Seattle, Washington 98195

Mean mass and moisture convergence profiles are measured from five soundings taken around the periphery of a mesoscale area containing a convective cell marked by strong updraft and downdraft circulations. An elevated convergence maximum is found with small convergence (or divergence) near the ground. The moisture budget, based on the horizontal vapor convergence and precipitation measured at the ground, indicates the plausibility of the derived profile. The elevated convergence maximum is shown to be a consequence of the combined updraft-downdraft circulation. It is surmised that the same feature will be found in similar convective situations when measurements are made over synoptic scale grid elements.

1. INTRODUCTION

The release of latent heat by organized cumulus convection is the major source of energy for many tropical weather disturbances. It is thus of considerable importance in developing numerical prediction and general circulation models of the tropics to find ways of expressing the effects of small scale convection in terms of large scale parameters of the models. The cumulus parameterization problem is currently receiving much attention by numerical modellers and is the focal point of the forthcoming GARP Atlantic Tropical Experiment (GATE).

A simple parameterization scheme, first proposed by Ooyama (1964), has received extensive use in tropical modelling (Yamasaki, 1969, Hayashi, 1970; Chang, 1971, and others). In this scheme the convective heating is made proportional to the vertical motion at the top of the boundary layer. Thus the convergence of moisture within this shallow layer determines the heat release through the entire depth of the atmosphere. Although the assumption that the convergence takes place mainly in the planetary boundary layer may be valid for the hurricane, observational studies of weaker tropical disturbances (Williams, 1970; Reed and Recker, 1971; Yanai et al., 1973) reveal that the convergence, as measured by the large scale wind field, typically extends to a height of nearly 300 mb in the active part of a wave disturbance.

At first sight this finding seems to conflict with the idea, implicit in Ooyama's formulation, that the boundary layer is the main source of the mass transported aloft by the convection. But as pointed out by several authors (Williams, 1970; Reed and Recker, 1971; Wallace, 1972), the divergence measured from the large scale wind field reflects the combined effects of updrafts, the between cloud vertical motions, including downdrafts, if present, and associated entrainment and detrainment. If account is taken of all these factors, it is not difficult to imagine mean divergence profiles which differ markedly from the profile in a single convective cell.

Because of the possible wide range of large scale divergence profiles that can accompany convective activity, it is desirable to document the profiles that exist in different types of situations. Hopefully, such documentation will prove helpful in developing and testing parameterization schemes. The present study concerns the divergence profile that existed over the NSSL meso-network in the half-hour period centered on 2300 CST, April 29, 1970. During this period two convective cells moved across the network from southwest to northeast. Regions where air converged into these cells were readily apparent from surface wind observations. The observations also revealed the presence of strong outflow regions containing air whose origin must have been near 600 mb or 700 mb from consideration of its wet-bulb potential temperature. Thus this case provides a good opportunity to determine the profile that exists in situations where both active updrafts and downdrafts are present in the volume sampled. The environmental features believed to be responsible for the strong downdrafts occurring in this case, and in other similar cases, are the dry air prevailing at intermediate levels and the pronounced vertical wind shear.

In addition to determining the mean divergence profile and the associated vertical motion, we have measured the moisture convergence in the lower part of the air column. This will be compared with the rainfall in order to obtain a crude measure of the reliability of our results.

2. DIVERGENCE AND VERTICAL MOTION

The divergence measurements are based on five soundings, taken between 2241 CST and 2311 CST, which enclosed the updraft-downdraft system of the second cell. The soundings were corrected to a common time by positioning them relative to the radar echo at 2300 CST. Relative positions were determined by displacing the balloons from their actual positions by an amount equal to the vector displacement (positive or negative, as appropriate) of the radar echo in the time interval between 2300 CST and the sounding time. Actual balloon positions were determined from the known points of release and the data provided on balloon displacement.

The corrected balloon locations at 900 mb are shown in figure 1. The points are labeled according to the stations of origin of the balloons. The mean divergence was obtained by measuring the outflow from the approximately triangular area described by the balloon locations and dividing by the area (1,925 km^2). The outflow was assumed to vary linearly between locations. Radar echo contours for two levels of intensity are also shown in the figure. It is seen that all soundings were taken in the inactive region outside the

cells. Unfortunately, the two cells were joined, and it was not possible to obtain a representative sounding along the leg NOB-ELR.

The divergence profile measured by the above procedure is given in figure 2. Because of the premature termination of one of the soundings, it extends only to a height of 650 mb. Also shown is the vertical motion determined from mass continuity with the assumption of zero vertical motion at the surface. From the figure it is apparent that the mean divergence is close to zero at the surface and that the maximum convergence takes place between 700 and 800 mb. Values are intermediate in magnitude between those found within convective cells and within synoptic systems. The maximum vertical velocity of 83 cm sec^{-1} is also intermediate in size.

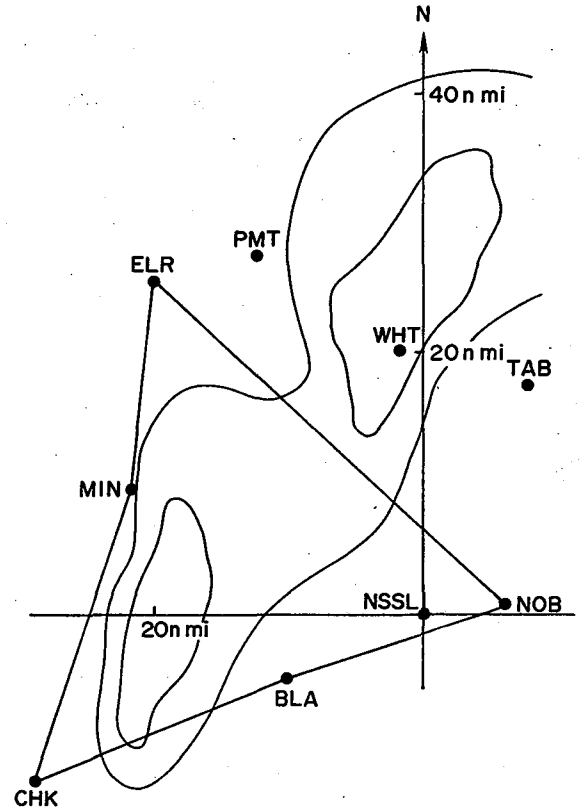

Figure 1. Corrected positions of soundings at 900 mb, 2300 CST, labeled according to station of origin of the balloons. The line segments enclose the area for which mass and moisture budgets were computed. Isocontours of radar echo intensity are also shown for log Z_e = 1.9 (outer area) and log Z_e = 3.5 (inner area).

As a check on the finding of reduced convergence near the ground, the divergence was also measured from the surface wind observations recorded at the more than 40 stations in the mesonetwork. Measurements were made for all quadrilaterals within the network and averaged to give the total divergence. With use of observations for 2245 CST, 2300 CST and 2315 CST an average total divergence of +10 x 10^{-5} sec^{-1} was found for the period centered about 2300 CST. Thus not only do the surface observations confirm the reduced convergence near the ground but indicate that net divergence actually existed. The difference between the value measured from the many stations in the surface mesonetwork and that obtained from the five sounding stations reflects, of course, the sampling error that can result when only a few observations are available in a region where the variables are rapidly fluctuating. However, the discrepancy does not invalidate the foregoing conclusion concerning the shape of the divergence profile. The elevated convergence shown in figure 2 must be a real feature. Otherwise it would be impossible to account for the heavy precipitation that occurred (see next section).

The shape of the divergence profile is explained schematically in figure 3. We envision an updraft-downdraft couplet in which the updraft draws air from the boundary layer and expels it at high levels and the downdraft incorporates air from intermediate levels and deposits it at the

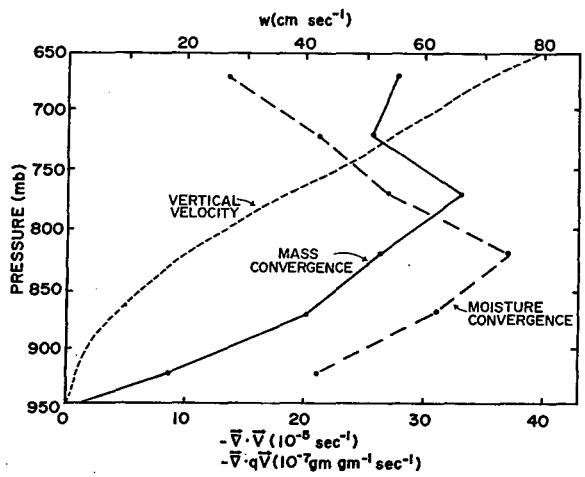

Figure 2. Velocity convergence ($-\nabla\cdot\vec{V}$), moisture convergence ($-\nabla\cdot q\vec{V}$) and vertical velocity profiles for the area shown in figure 1. Convergences are average values for depths of 50 mb. Surface values of the velocity convergence, based on data from five stations, is also shown.

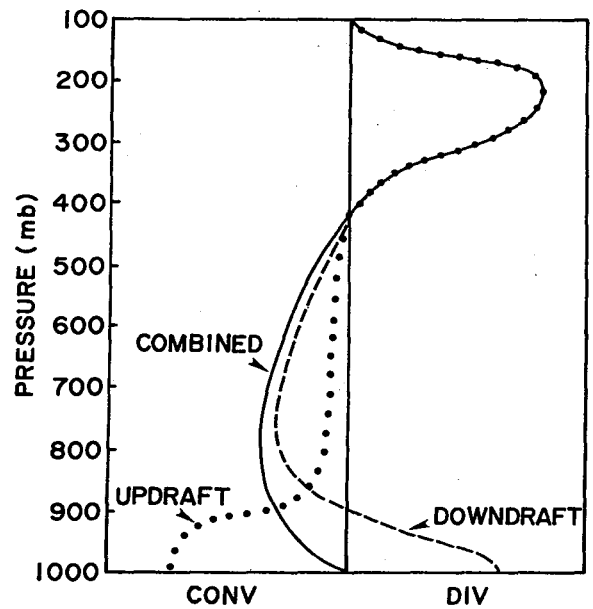

Figure 3. Schematic diagram of hypothesized divergence profiles in updraft and downdraft regions and the resulting average profile for the area.

ground. Some entrainment of air into the updraft and downdraft is allowed. However, the WHT sounding balloon, which was captured by the first cell, indicated near constancy of wet-bulb potential temperature and momentum with height in the updraft, and the surface observations in the core of the outflow region suggested near conservation of wet-bulb potential temperature in the downdraft. Consequently, we have treated entrainment as only a secondary effect.

In the scheme represented in figure 3 the factors determining the elevated convergence maximum are (1) the compensating convergence and divergence at low levels and (2) the inflow which feeds the downdraft at middle levels. This inflow is presumably compensated by the outflow from the cumulonimbus anvils. Soundings extending at least to 200 mb would be required to substantiate this feature.

3. MOISTURE BUDGET

Since computations were carried only to 650 mb, it is not possible to obtain a complete moisture budget. However, for the purpose of judging the reliability of the data, it is of interest to compare the horizontal vapor influx into the area in the layer between the surface and 650 mb with the

precipitation measured at the ground. The profile of the vapor flux is shown in figure 2. It was determined from integration of the moisture inflow along the boundary with use of the specific humidities given by the soundings and winds relative to the moving cell. The use of relative winds tends to reduce the storage term in the moisture budget, since it minimizes changes caused by movement of the convective systems into or out of the area. Local changes, or storage, in the moving coordinate system reflect true changes in the vapor content of the air.

If the equation for conservation of water vapor is integrated through the entire depth of the atmosphere, the precipitation, P, is given by

$$P = I + E - S$$
$$1.6 = > 2.8 + 0 - > 1.2 \qquad (1)$$

where I is the integrated horizontal inflow, E is the surface evaporation, and S is the storage. Horizontal inflow and storage of water in solid or liquid form is neglected in this equation.

The numbers below the symbols give the estimated values of the various terms expressed in gm cm^{-2} $hour^{-1}$. Thus the precipitation rate, based on the raingage measurements, was 1.6 cm per hour for the entire area. This rate was measured for the 30-minute period centered on 2300 CST. The vapor flow into the region below 650 mb was at the rate of 2.8 cm (gm) $hour^{-1}$. Since moisture convergence was still occurring at 650 mb and since the mass divergence presumably occurred at high levels where the specific humidity was small, it seems safe to assume that the total vapor influx exceeded this amount, as indicated by the prefixed sign. In view of the hour of day and the prevailing weather conditions the surface evaporation (or condensation) can be safely neglected. The storage is obtained as a residual quantity and must be equal to or greater than the value given.

About all that can be said of the foregoing numbers is that they do not violate common sense. Clearly there is sufficient moisture convergence into the column, despite the fact that the large scale mass convergence takes place aloft where the moisture values are smaller than in the boundary layer, to account for the observed precipitation. The storage of greater than 1.2 gm $hour^{-1}$ is large but perhaps not excessive if it is realized that the figure is based on a 30-minute precipitation rate and that the total precipitable water in the column is of the order of 3-5 cm. Certainly the net effect of the convective overturning should be to increase the moisture content of the air.

4. CONCLUDING REMARKS

The foregoing measurements have shown that the mean divergence profile in a region where strong updrafts and downdrafts exist simultaneously is characterized by an elevated convergence maximum and near zero convergence (or divergence) at the surface. The measurements are representative of

conditions on a space scale of tens of kilometers. There is therefore some question concerning the implication of these results for the synoptic scale, that is a scale of the order of a few hundreds of kilometers. On the large scale, several convective cells in various stages of development will occupy an elementary area in a situation such as that studied here. Some of these will be in the middle stage of development and will contribute to the type of profile described above. Others will be in the earlier and later stages and will likely exhibit profiles typical of the updraft and downdraft, respectively. However, together they should produce a profile similar to the one found here. Thus we may speculate that suitable measurements over synoptic scale areas will reveal the same elevated convergence maximum.

It is well known that synoptic scale convergences and vertical velocities are an order of magnitude smaller than the mesoscale values measured in this study. From this fact we conclude that the average spacing between intense cells must be a least three times the lateral dimension of the area employed in the measurements, that is, 3 x 50 km = 150 km.

Admittedly the data employed in this study were marginal for the purpose at hand. The soundings encompassed an area considerably less than a synoptic scale grid element and the calculations had to be terminated at 650 mb. The spacing of observations was not ideal for obtaining accurate line integrals. It is quite possible, however, that definitive results could be achieved by statistical treatment of multiple soundings taken in similar situations. The NSSL data archive may well be large enough to provide samples of sufficient size for carrying out the desired studies.

5. ACKNOWLEDGMENTS

This research was supported by the Atmospheric Sciences Section, National Science Foundation, under Grant GA-32439.

6. REFERENCES

Chang, C. P., 1971: On the stability of low-latitude quasi-geostrophic flow in a conditionally unstable atmosphere. J. Atmos. Sci., 28, 270-274.

Hayashi, Y., 1970: A theory of large scale equatorial waves generated by condensation heating and accelerating the zonal wind. J. Meteor. Soc. Japan, 48, 140-160.

Ooyama, K., 1964: A dynamical model for the study of tropical storm development. Geofisica Internacional (Mexico), 4, 187-198.

Reed, R. J., and E. E. Recker, 1971: Structure and properties of synoptic scale wave disturbances in the equatorial western Pacific. J. Atmos. Sci., 28, 1117-1133.

Wallace, J. M., 1971: Spectral studies of tropospheric wave disturbances in the tropical western Pacific. Rev. of Geophys., 9, 557-612.

Williams, K., 1970: Characteristics of the wind, thermal, and moisture fields surrounding satellite-observed mesoscale trade wind cloud clusters in the western North Pacific. Proceedings of the Symposium on Tropical Meteorology, Honolulu, June, 1970, published by Amer. Meteor. Soc.

Yamasaki, M., 1969: Large scale disturbances in a conditionally unstable atmosphere at low latitudes. Papers in Meteor. and Geophys., 20, 289-336.

Yanai, M., S. Esbensen, and J. H. Chu, 1973: Determination of bulk properties of tropical cloud clusters from large-scale heat and moisture budgets. J. Atmos. Sci., 30, 611-627.

DEVELOPMENT IN SEVERE STORMS AS REVEALED BY VIL ANALYSIS OF THE APRIL 29-30, 1970, STORM SYSTEM

Douglas R. Greene and Robert A. Clark

National Weather Service
Silver Spring, MD 20910

From digital radar data at several elevations, calculation of vertically-integrated liquid-water content (VIL) provides a means of detecting "explosive development" in severe storms. VIL analyses of two tornadic thunderstorms characterizes them by high and increasing VIL values just prior to tornado development. Another thunderstorm appeared tornadic and exhibited similar VIL characteristics, but tornado development was not confirmed.

1. INTRODUCTION

Through the use of digital radar data measured at successive elevation angles in a storm system, an analysis technique is developed which gives a new means of detecting areas of "explosive development" in severe storms. This indicator, mapped vertically-integrated liquid-water content (VIL), presents the three-dimensional characteristics of a storm system in a two-dimensional display. Constant altitude reflectivity maps or CAPPI's, which are useful in mesoanalysis and/or the study of thunderstorm dynamics, also may be generated from digital radar data. Although a CAPPI illustrates the most intense echoes it is necessary to look at the CAPPI for each level and integrate mentally the intensities through the depth of the storm. This procedure fails to reveal clearly the "explosive development" in storms as VIL does.

2. VERTICALLY-INTEGRATED LIQUID-WATER CONTENT

The concentration of liquid water in a cloud is of considerable meteorological importance. Its magnitude and spatial distribution are important factors in the study of cloud dynamics, since they indicate the degree of condensation and cloud development which have taken place (Mason, 1957). Unfortunately, there is, at this time, no method of rapidly and accurately measuring the magnitude of liquid-water content; however, the relative magnitude and distribution of liquid water may be determined by radar measurements if certain assumptions are made regarding the in-cloud drop-size distribution. An exponential drop-size distribution proposed by Marshall and Palmer (1948) seems to fit the distributions observed by several investigators. This distribution is given by

$$n(a) = N_o \exp(-ba), \tag{1}$$

where a is the drop diameter, n(a) is the number of drops with diameters between and and a + da and N_o and b are parameters in the distribution.

To use radar as an indicator of liquid-water content M, a relationship was obtained between M and radar reflectivity Z. Mathematically M and Z may be defined by

$$M = \frac{\rho_w \pi}{6} \int_o^x n(a)\ a^3\ da \tag{2}$$

and

$$Z = \int_o^x n(a)\ a^6\ da, \tag{3}$$

where x is the diameter of the maximum drop and ρ_w is the density of water (assumed to be unity in the cgs system). When the Marshall-Palmer drop-size distribution is used in (2) and (3), the error is very small if the upper limit of integration x is replaced by ∞. Integration yields

$$M = \frac{N_o \rho_w \pi}{6} \int_o^\infty \exp(-ba) a^3\ da \tag{4}$$

$$= \frac{N_o \rho_w \pi 3!}{6b^4} = \frac{N_o \rho_w \pi}{b^4}$$

and

$$Z = N_o \int_o^\infty \exp(-ba)\ a^6\ da = \frac{N_o 6!}{b^7} \tag{5}$$

$$= \frac{720\ N_o}{b^7}\ .$$

Eliminating the parameter b between (4) and (5) yields

$$M = \frac{N_o \rho_w \pi}{[720 \times 10^{18}\ N_o]^{4/7}}\ Z^{4/7}. \tag{6}$$

For $N_o = 8 \times 10^6 m^{-4}$ and $\rho_w = 1\ gm/cm^3 = 10^6\ gm/m^3$,

$$M = 3.44 \times 10^{-3}\ Z^{4/7}, \tag{7}$$

where the units of M are gm/m^3 and Z are mm^6/m^3. The factor 10^{18} in the denominator of (6) is required to convert the units of Z from m^6/m^3, as given in (5), to mm^6/m^3.

To present the three-dimensional echo characteristic as a two-dimensional quantity, (7) is integrated over the vertical extent of the storm. This quantity, which is defined as the vertically-integrated liquid-water content, symbolized by VIL, has dimensions of mass per unit area. VIL is given by

$$VIL = \int_{h_{base}}^{h_{top}} M \, dh' \tag{8}$$

$$= 3.44 \times 10^{-6} \int_{h_{base}}^{h_{top}} Z^{4/7} \, dh',$$

where h' is the height expressed in meters and VIL has units of kg/m^2. It should be noted that M and VIL represent the mass of raindrops in a unit volume and over a unit area, respectively. If $\rho_w = 1$ gm/cm^3, VIL also indicates the depth of water per unit area in mm. Since VIL is based on the relationship between M and Z, it would be incorrect to assume that VIL denotes all the in-cloud liquid water. Clouds containing a large number of small drops produce very small values of Z which may be below the detectable signal of the WSR-57 radar; thus, some liquid-water content M will not be detected. Hail also may produce fictitious values of liquid water due to enhanced radar return. This may be beneficial as an indicator of the severity of a storm, but it may be deceptive if the presence of the solid water is not recognized. Maps of VIL may be computed readily from tilt digital radar data by use of (8).

3. CASE STUDY

The VIL analysis technique was used to investigate the tornado producing meso-system occurring in central Oklahoma, April 29-30, 1970. Use was made of digital weather radar data collected by the National Severe Storms Laboratory (NSSL), NOAA, Norman, Oklahoma. Digital radar data for these systems were analyzed on a 2 n mile x 2 n mile grid over the region in central Oklahoma shown in figure 1. This storm system occurred under a synoptic situation typical of the Miller (1967) Type-B severe-weather pattern. This pattern is characterized by a south-westerly jet aloft, a marked intrusion of dry air at the 700 mb level, a southerly current of warm moist air from the surface to near 850 mb extending from the Gulf of Mexico into the analysis region, and a surface low and associated frontal system moving into the area from the west. This storm system was particularly significant in that the squall line associated with it spawned two destructive tornadoes that struck in the Oklahoma City[1] area in the middle of the night. One of these tornadoes had a path length of 140 mi (Environmental Data Service, 1970).

[1]All cities and towns referred to in this paper are located in Oklahoma, unless otherwise specified.

VIP maps were computed on a five-minute interval for this storm system from Arpil 29 at 2300 CST to April 30 at 0100 CST. Three severe storm cells were analyzed by use of these VIL maps. Each of these represents an example of "explosive development." Only the VIL maps needed to illustrate these developments are presented in this study.

3.1 Cell C

At 2300 CST this cell was located approximately 75 n miles WSW of NSSL. This cell contained already a tornado that had formed southwest of Altus, 35 minutes earlier. After it had developed a tornado, this cell maintained high values of VIL, about 40 kg/m^2, until 2315 CST[2], figure 2, when it underwent rapid development. In the 10-min interval from 2315 to 2325, figure 2 through 4, the maximum value of VIL increased to over 70 kg/m^2. By 2340 CST (fig. 5) the central value of VIL increased to 90 kg/m^2 and the echo formed a "dry" vault which is associated typically with tornadic storms. The following question remains unanswered: Did "explosive development" and the formation of the dry vault in an echo already containing a tornado indicate that the tornado has increased in size and become more violent or is this some function of resolution due to variations in the beam width and power density as the storm approaches the radar? If this were a function of resolution, one would expect to detect the vault in more detail as the range decreased, which actually occurred in this case. Errors due to side-lobe effects could cause a false return which would lead to overestimated echo tops at long ranges. This might yield a VIL value that is too large, due to the integration process. However, the value of VIL should decrease rather than increase as the storm approaches the radar. This effect should not, however, be very pronounced. Another question posed by this storm is, why, after displaying intense values of VIL, did the storm decrease in the central value of VIL after 2355 CST leveling off at a value of 45 to 50 kg/m^2 at 0015 CST? A possible explanation may be that the storm ejected some large hail, thus reducing the enhanced reflectivity. These questions can be answered only by a more complete study of this storm, as is being conducted at NSSL, and a ground survey of the damage along the path of the tornado.

3.2 Cell D

This cell formed and moved northwest of NSSL at a range too close[3] to collect data for the VIL map. By 2345 CST the range of this cell became distant enough to appear on the VIL map. From 2345 to 0005 CST this cell maintained a relatively constant value of VIL, about 30 kg/m^2. However, between 0005 and 0010 CST, figure 6 and 7, VIL increased to 48 kg/m^2 and the cell moved out of the analysis area maintaining these high values. This

---

[2]Although the VIL maps are referred to at a single time, this time is the beginning of the time interval required to collect the tilt digital data used in their computation. For the 1970 NSSL data, this collection time is of the order of three minutes.

[3]For elevation angle scans to a maximum of 20 deg, the lower range limit of the VIL map is 17 n miles from the radar.

case of explosive development is not supported by a confirmed tornado, but the near proximity of the tornado in Cell C, which followed approximately the same path as Cell D, may have confused any report of tornado damage due to Cell D. At 0010 CST Cell C was 50 n miles SW of the center of Cell D.

3.3 Cell E and F

Cell F presents another example of a confirmed tornado associated with "explosive development," as detected by a rapid increase in VIL. As in many tornadoes, no hook echo or echo-free vault was detected on radar and the "explosive development" occurred in the southernmost cell of a double cell system. Cell E is first detected on a VIL map as it moved into the analysis area 75 miles west of NSSL at 0005 CST. This cell followed a northeasterly path very similar to Cell C, while maintaining maximums in VIL of about 30 kg/m^2. At 0040 CST, figure 8, this cell split into a northern cell, retaining the label E, having a maximum VIL of 28 kg/m^2, and a southern cell, labeled F, with a maximum VIL of 20 kg/m^2. In the ensuing five minutes, figure 9, the value of VIL in Cell F increased to 39 kg/m^2, whereas Cell E decreased to 27 kg/m^2. This cell maintained these high values of VIL and moved NE to a location between Carnegie and El Reno by 0100 CST, as shown in figure 10. Although the "explosive development" took place at 0045 CST, the first tornado damage was reported to have occurred at 0100 CST, 25 miles southwest of Oklahoma City at the approximate location of the star in figure 10. The funnel could have formed at 0045 CST and not touched ground or touched ground in an isolated area, hence no reported damage until 0100 CST. This seems consistent with the nature of this particular storm, since observation of damage indicates that the funnel skipped and was on the ground only intermittently over its path (Environmental Data Service, 1970).

4. CONCLUSIONS

Two severe meso-scale storm systems have been analyzed by use of the VIL analysis technique (only one in this report) and additional storms should be investigated before any hypothesis is firmly espoused. Nevertheless, the results of this study appear to hold real promise for the detection and identification of potentially severe storms. The following conclusions may be inferred:

a. Tilt digital radar data collected over short-time intervals are beneficial in severe storm analyses. It is apparent that data collected at constant elevation angles will not reveal the complete character of a storm.

b. Vertically-integrated liquid-water charts preserve and present the three-dimensional characteristics of a storm system in a two-dimensional display and yield an integrated morphology of severe storm systems. If tilt digital radar data are available, these can be prepared in "real time" with a computer of reasonable size.

c. The change in trend of VIL provides a means of positively identifying severe storms capable of spawning tornadoes. Normal radar displays can indicate these storms only in favorable cases when a hooked echo, echo-free vault, or vortex pattern can be detected.

d. Vertically-integrated liquid-water content provides the basis for a model for forecasting the development of potentially severe storms. The results of this study indicate that tornado-producing meso-systems are characterized by (1) high values of VIL for approximately 1 hour prior to the reported tornado and then (2) a rapid increase in VIL to even greater values appears to accompany the development of a confirmed tornado. This marked increase in VIL appears to be an indicator of the "explosive development" of severe storms. This suggests that a high threshold value and a change in trend of VIL may be used as a tool in forecasting severe storms.

e. VIL can be computed from tilt digital data from a network of radar stations and a composite VIL formed. This composite would have many advantages over the present National Radar Summary Chart in that it would present an integrated three-dimensional display depicting the character and intensity of all storms in the network. The temporal nature of storm systems can be indicated by successive VIL's or by maps of the change in VIL per time interval. This application would approach the ultimate goal of the National Radar Network.

5. ACKNOWLEDGMENTS

The authors are grateful to the staff members of NSSL, in particular Dr. Edwin Kessler, Mr. Kenneth E. Wilk, and Mrs. Kathryn Gray, for their helpful comments on digital data processing and for providing the data used in this study. Acknowledgment is extended to the United States Army Electronics Command under Contract DAAB07-68-C-0073 (Project Themis), which provided the funds for computer rental and data reduction. Portions of this work by the senior author are in partial fulfillment for graduate degree requirements for the doctoral degree in meteorology at Texas A&M University.

6. REFERENCES

Environmental Data Service, 1970: Storm Data, 12, Asheville, North Carolina, 46 pp.

Marshall, J. S., and W. M. Palmer, 1948: The distribution of raindrops with size. J. Meteor., 5, 165-166.

Mason, B. J., 1957: The Physics of Clouds. London, Oxford Clarendon Press, 481 pp.

Miller, R. C., 1967: Notes on analysis and severe-storm forecasting procedures of the military weather warning center. Tech. Rept., 200, Air Weather Service, USAF, 170 pp.

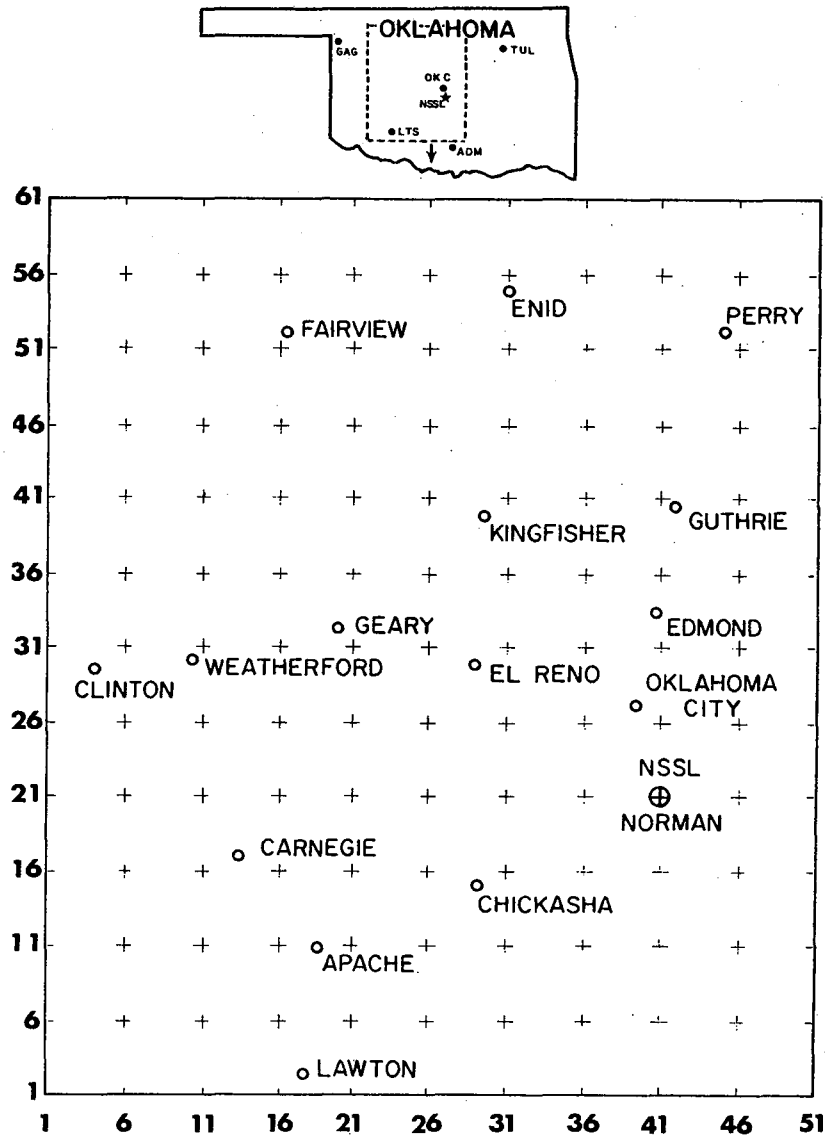

Figure 1. Illustration of grid and analysis area used in this study. Although a 2 n mile x 2 n mile grid was used, only each fifth grid point is shown on this diagram.

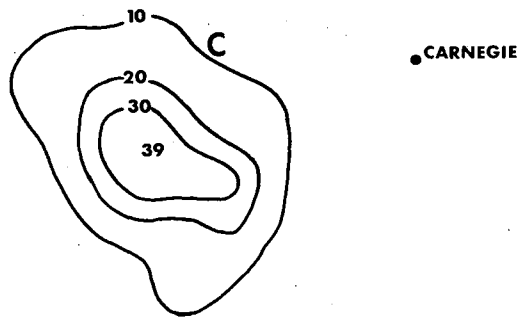

Figure 2. VIL map for 2315 CST, April 29, 1970. Isopleths are VIL in kg/m^2.

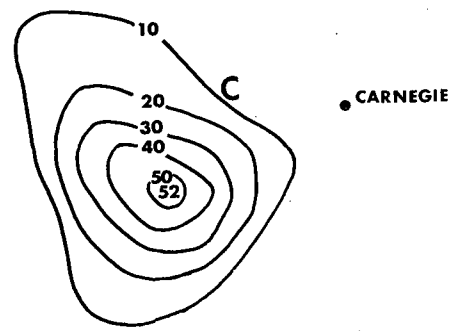

Figure 3. VIL map for 2320 CST, April 29, 1970. Isopleths are VIL in kg/m^2.

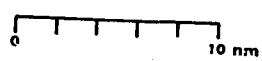

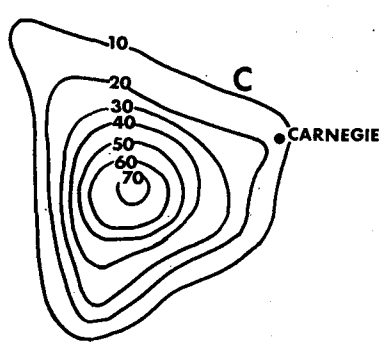

Figure 4. VIL map for 2325 CST, April 29, 1970. Isopleths are VIL in kg/m^2.

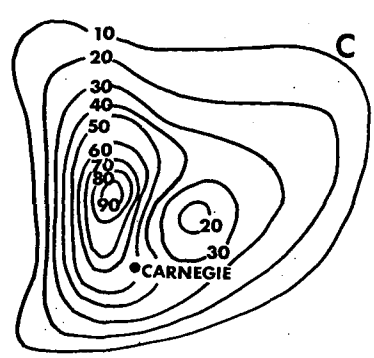

Figure 5. VIL map for 2340 CST, April 29, 1970. Isopleths are VIL in kg/m^2.

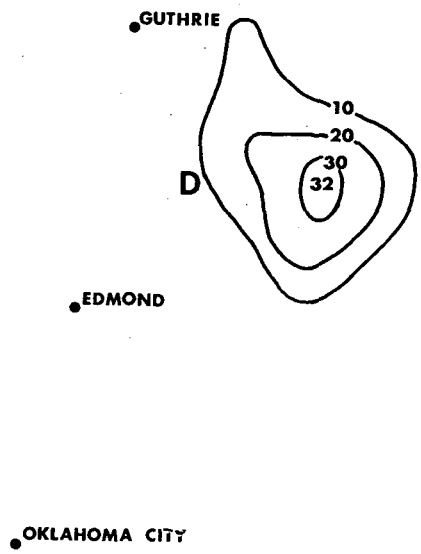

Figure 6. VIL map for 0005 CST, April 30, 1970. Isopleths are VIL in kg/m^2.

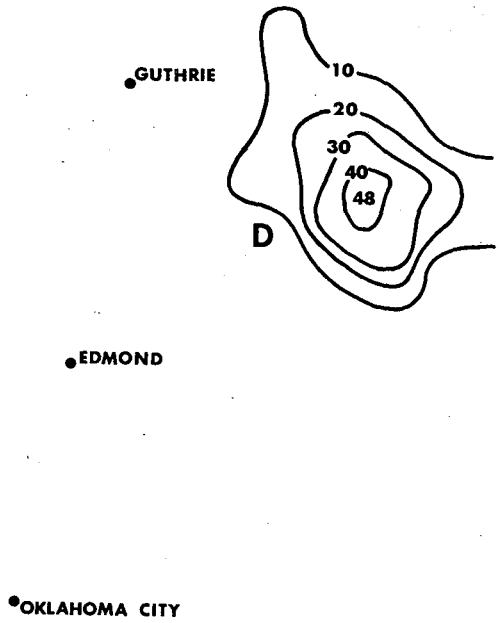

Figure 7. VIL map for 0010 CST, April 30, 1970. Isopleths are VIL in kg/m^2.

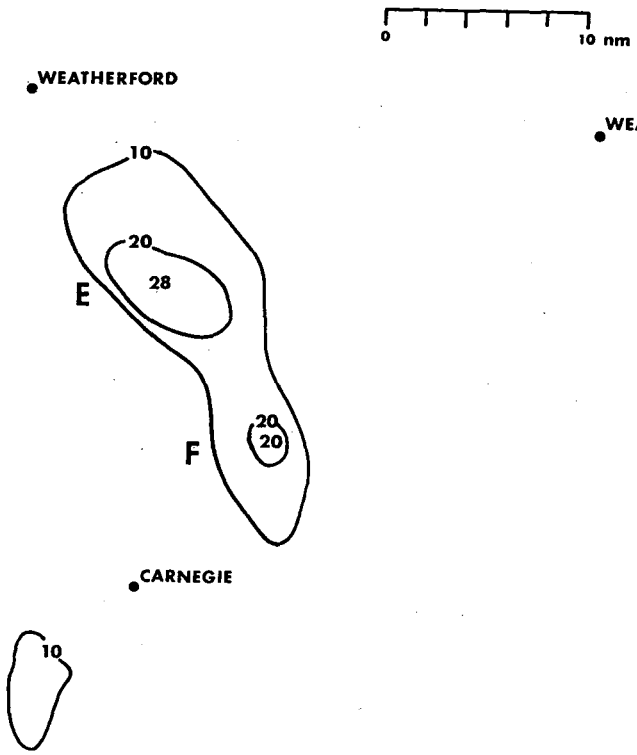

Figure 8. VIL map for 0040 CST, April 30, 1970. Isopleths are VIL in kg/m^2.

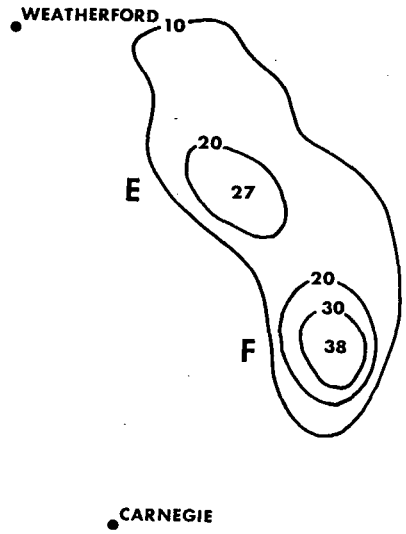

Figure 9. VIL map for 0045 CST, April 30, 1970. Isopleths are VIL in kg/m^2.

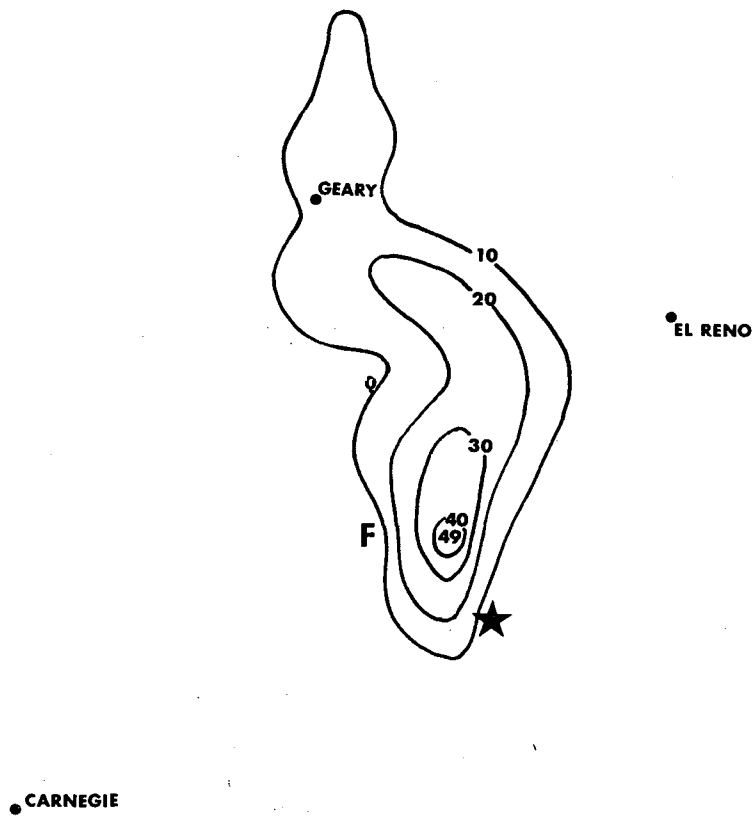

Figure 10. VIL map for 0100 CST, April 30, 1970. Isopleths are VIL in kg/m^2. The star indicates the approximate location of a confirmed tornado.

INFRASOUND FROM THE 29-30 APRIL 1970 STORMS

T. M. Georges and Gary E. Greene

Wave Propagation Laboratory
Boulder, Colorado 80302

We report the observable features of infrasound recorded at Boulder, Colorado, and San Diego, California, during the subject storm. Triangulation indicates that the emissions originated in north-central Texas, not in the Oklahoma City area.

1. BACKGROUND

Infrasound is the name given to a class of acoustic waves whose frequencies are subaudible but which travel through the atmosphere at essentially the local speed of sound. A long-period limit for acoustic waves exists at the atmosphere's acoustic-cutoff period, about four minutes in the troposphere.

Many kinds of natural infrasound have now been classified, but adequate models of natural source mechanisms exist for only a few. Georges and Young (1972) review techniques for observing infrasound with arrays of microbarographs and current knowledge about many different kinds of natural infrasound.

It has been known for over a decade that certain convective storms emit infrasound powerful enough to be detected over 1500 km away, but the precise emission mechanism remains unknown. These waves typically have amplitudes of about one microbar, periods between about 10 and 60 sec, and persist for one or two hours. More recently, a connection has been found between certain severe storms and a particular class of wavelike oscillations in the ionospheric F region, 200 to 300 km above the ground. These waves were observed with ground-based radio-echo sounders and have periods between two and five minutes. Georges (1973) has recently reviewed the history and phenomenology of both of these manifestations of severe-weather infrasound.

The purpose of this paper is to report the characteristics of infrasound recorded at four microbarograph arrays during the particular storm system that is the subject of the other papers in this report. Only by comparing the details of the emissions with the spatial and temporal characteristics of storm observables, such as those presented by the companion papers in this report, is much progress toward discovery of the emission mechanism likely. Conversely, it does not seem unreasonable to hope that discovery of the mechanism might in turn shed some light on severe-storm dynamics.

2. PROCEDURE

Data recorded at four microbarograph observatories during the interval 0000 to 1500 UT (1800-0900 CST) on 29-30 April were examined for evidence of

acoustic arrivals from the Texas-Oklahoma vicinity. The four observatories are at Boulder, Colorado (NOAA), Washington, D. C. (NOAA), Pullman, Washington, (Washington State University) and San Diego, California (Naval Electronics Laboratory Center). These are the only locations in the continental U. S. where suitable recordings were being made at the time and from which records are still available.

We analyzed analog tape recordings of pressure fluctuations from four microbarographs at each observatory by means of the NOAA Analog Correlator (Brown, 1963; Georges and Young, 1972), which automatically performs cross-correlation analysis to yield the speed and direction of coherent wave arrivals. In cases where acoustic wave arrivals were detected from roughly the correct direction and lasted for more than a few minutes, we measured arrival azimuth in each five-minute interval in which wave coherence (in the sense defined by Georges and Young) exceeded a certain threshold. That threshold is determined from experience in making realiable wave measurements with the analog correlator and is essentially equivalent to a broadband wave coherence of about 0.2 over the microbarograph array. Wave coherence is affected not only by propagation effects that cause "corrugations" on the wave fronts but also by non-acoustic "noise" at the sensors due to wind-advected turbulence and atmospheric gravity waves. During the intervals studied here, background noise level remained sufficiently low that we can assume that the variations in wave coherence during high S/N intervals are due primarily to variations in wave strength. (The variations during low S/N intervals may be caused by noise-level fluctuations, however.) The only exception is that high ambient noise began at Pullman at 0800 UT, precluding signal detection thereafter.

Frequency content of the waves is estimated by passing the signal through a narrow-band filter with adjustable center frequency and recording the frequencies of the two or three dominant frequency peaks that the signals usually exhibit. The portion of the wave frequency spectrum searched corresponds roughly to the 20 dB points on the overall frequency response of the recording and processing system, namely between wave periods of about 2 and 100 sec.

3. RESULTS

Strong, persistent infrasonic waves were detected at only two of the four observatories, namely Boulder, Colorado and San Diego, California. Weak waves of short or intermittent duration appeared in data recorded at Washington, D. C. and Pullman, Washington, so that it was possible to make only spot estimates of wave parameters.

Because some storm systems have been known to produce strong waves detectable several thousand kilometers away, the emissions from this system must be regarded as considerably less intense than the strongest waves observed from other storms. Maximum wave amplitude at Boulder was about 0.7 microbars and at San Diego was about 0.6 microbars.

Figure 1 summarizes the history of the important wave observables at Boulder during the period of interest, and figure 2 presents similar information for the San Diego data. The lower part of each figure is a time history of

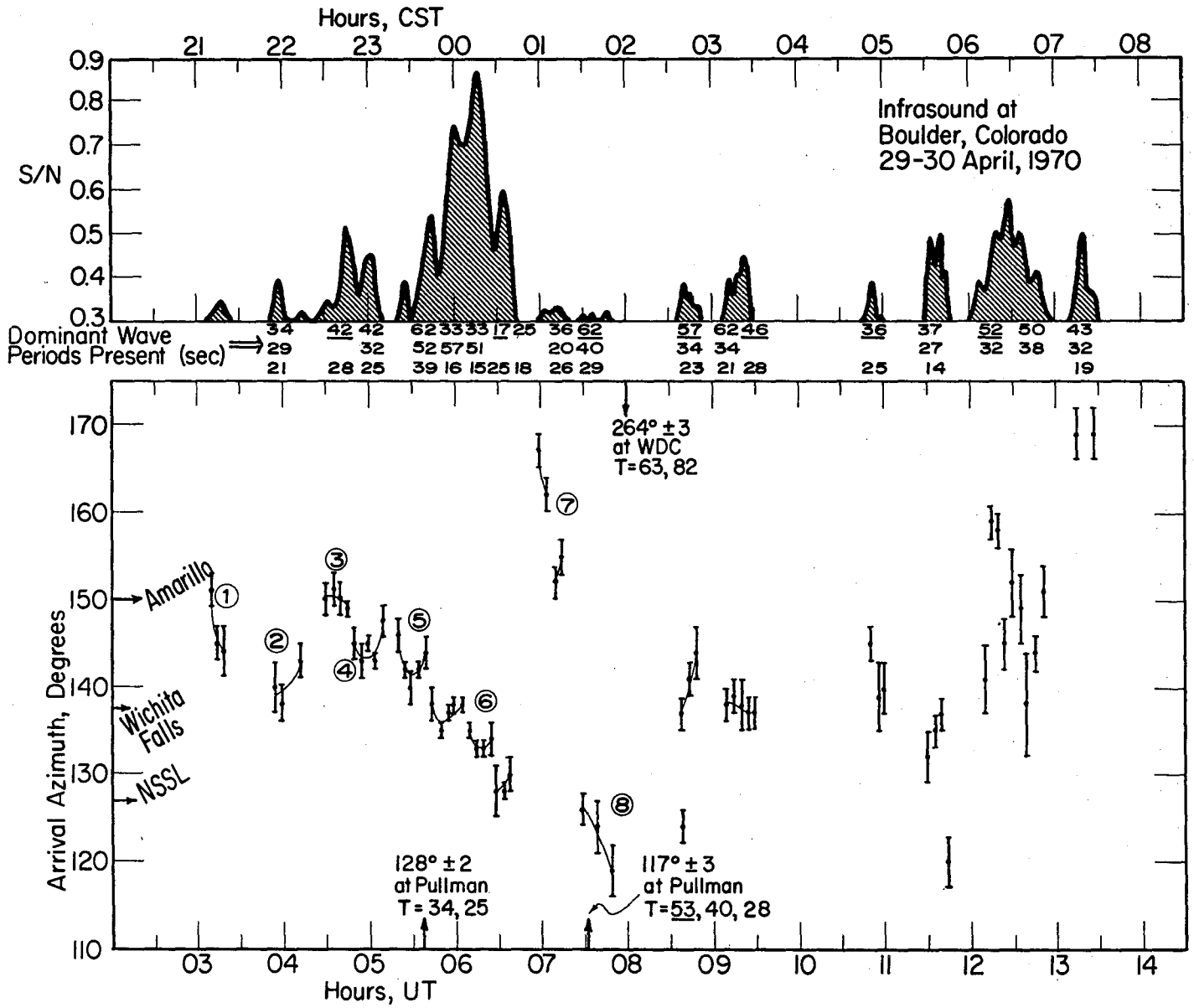

Figure 1. Time history of infrasonic wave strength (top), azimuth of arrival (bottom) and spectral content (middle) at Boulder, Colorado during the storm period.

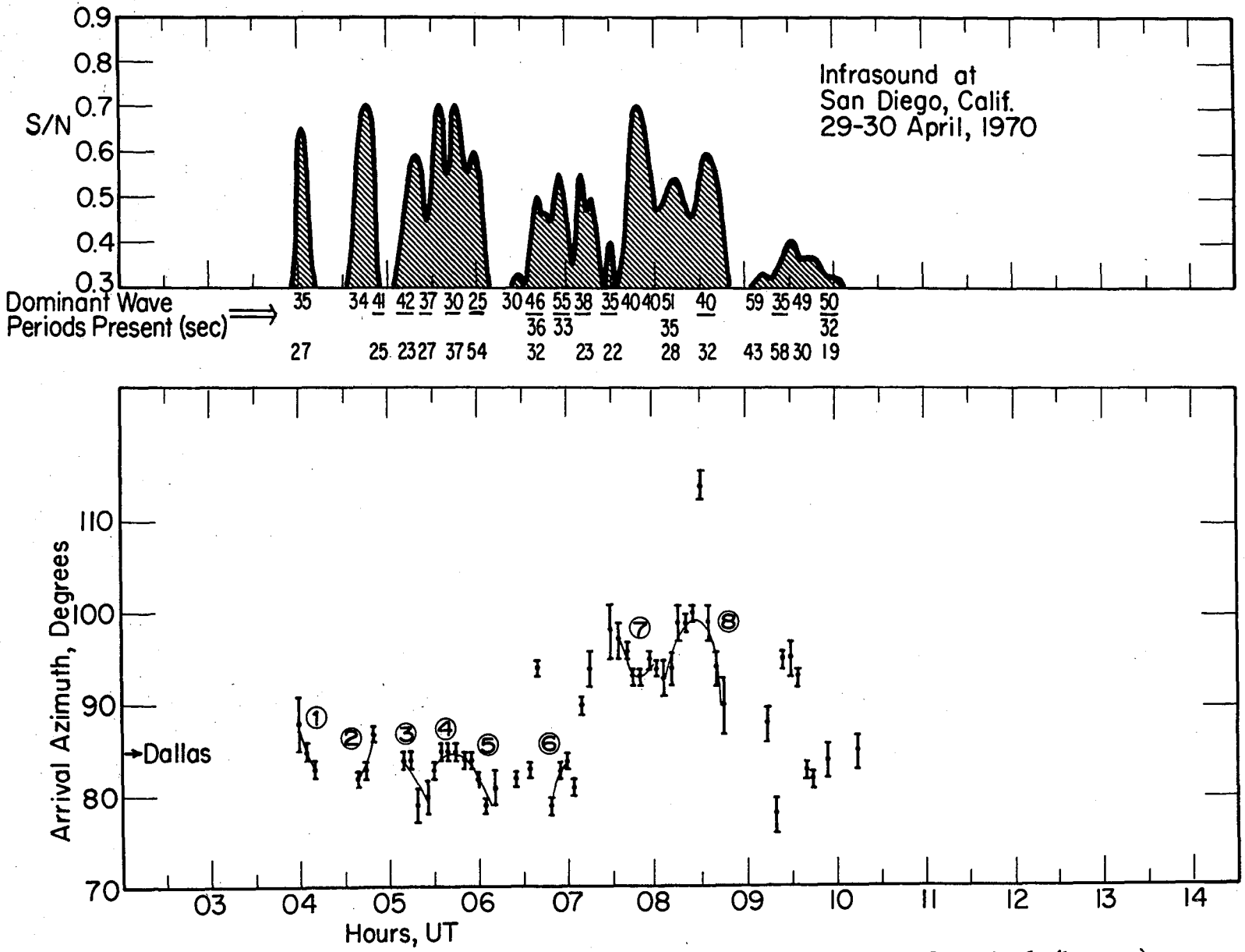

Figure 2. Time history of infrasonic wave strength (top), azimuth of arrival (bottom) and spectral content (middle) at San Diego, California during the storm period.

the azimuth of wave arrival. Reference locations are noted on the azimuth scale. Error bars indicate the probable error associated with azimuth determinations in the presence of noise and a finite sensor-array beamwidth, but are not intended to indicate errors associated with refractive effects of the propagation medium. Experience with many signals from known sources suggests that bearing errors due to propagation effects seldom exceeds 3°. Note that the indicated times are all times of wave arrival at the various observatories and have not been corrected for acoustic travel time. Such corrections usually amount to about 1100 km/hr, or in the case of propagation to Boulder, about 30 to 40 minutes and about 80 to 100 minutes to San Diego, depending on the exact source location assumed.

Brief arrivals at the other observatories are noted along the upper and lower time scales of figure 1. These estimates serve mainly to confirm the general source location in the Texas-Oklahoma area.

The top parts of figures 1 and 2 plot the "signal-to-noise ratio" at Boulder and San Diego defined by $S/N = R/(1-R)$, where R is the broadband wave coherence over each sensor array. The cause of the rather regular fluctuations in S/N is unknown; they may represent pulsations of source strength, regular fluctuations in noise level at the sensors, or propagation effects that cause amplitude scintillations at the sensors. Measurements of strong waves from nearby storms reveal similar fluctuations in source strength and direction, suggesting that the "pulsations" are a source property. Therefore, the times when S/N is largest are interpreted here as the times (when corrected for propagation time) of most intense emission.

In between the two plots of figures 1 and 2 are some numbers that give the results of wave spectrum analysis. The numbers indicate the dominant wave periods (in seconds) present at the indicated times; those underlined indicate that the spectrum is dominated by that particular wave period. In general, the spectral content varies rapidly with time, and there appears to be little relation between wave periods seen at different observatories at the same time (corrected for travel time).

Figures 1 and 2 contain enough information to permit us to calculate a time history of apparent source locations by triangulation between Boulder and San Diego. However, there is sufficient difference between the strength and azimuth histories at the two stations that there is some difficulty matching "event for event," which is necessary for meaningful triangulation. The best match seems to result from a relative time shift of about 50 minutes, (Boulder leading), which turns out to be a theoretically reasonable travel-time difference for a source in north-central Texas. Although major differences in strength exist between the two stations, it is possible to obtain a rough event-for-event match between the S/N records at Boulder and San Diego during the interval 0300-1000 UT. Between 1000 and 1400 weaker waves exhibiting greater azimuth scatter were present on Boulder records, whereas no significant waves arrived at San Diego from the direction of interest.

Using a 50-minute shift, we next calculated apparent intersections from corresponding bearings in eight 15-20 min time "blocks" suggested by azimuth groupings and S/N "pulsations." Blocks 7 and 8 yielded intersections well outside the geographical region of interest, whereas blocks 1 through 6

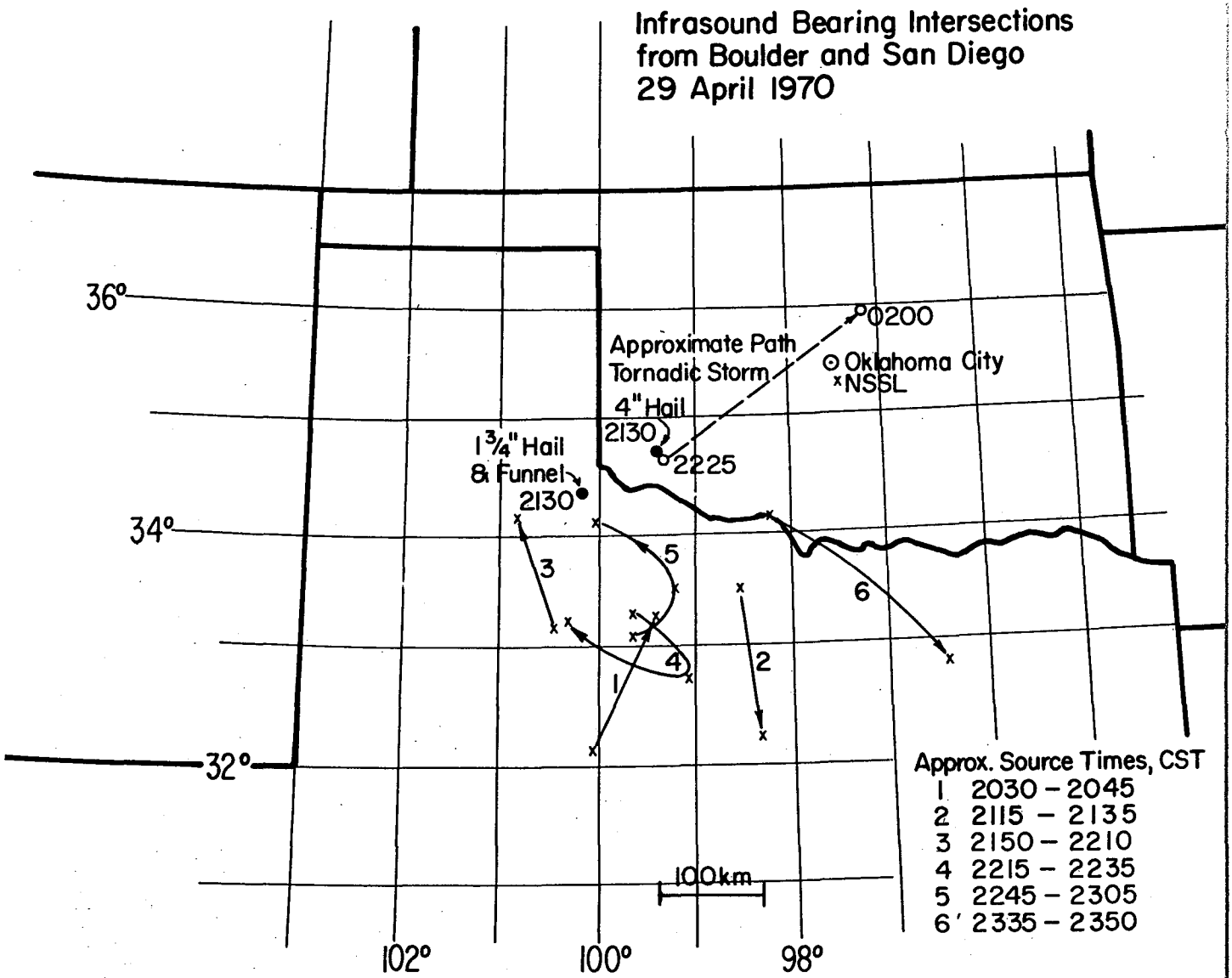

Figure 3. Tracks of infrasound bearing intersections constructed from the azimuth-time data in figures 1 and 2. Track numbers correspond to the numbered "events" in the previous figures.

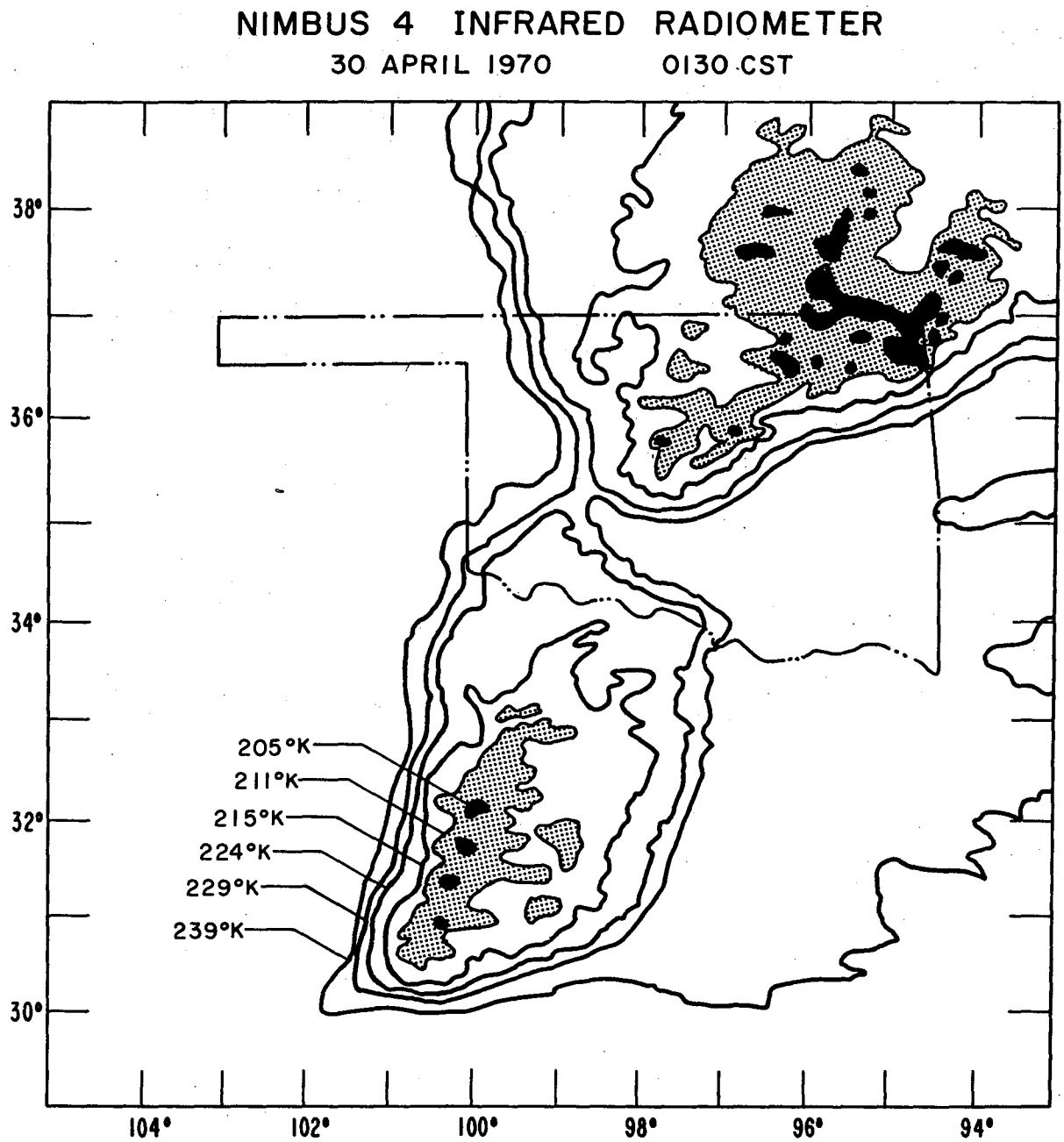

Figure 4. A partial tracing of the Nimbus 4 infrared radiometer temperature contours obtained during the passage of the frontal system across Texas and Oklahoma (outline shown).

yielded the intersection "tracks," or time histories illustrated in figure 3.

In view of the various azimuth errors inherent in both the wave propagation and in the data processing, the significance of the details of the tracks may certainly be questioned. The actual source locations should be well within 100 km of those indicated, however. For reasons arising from details of the propagation mechanism, there may be some justification for associating more accuracy with the locations at the beginning of each time block, than with those near their ends.

4. COMPARISON WITH OTHER OBSERVATIONS

Storm Data (NOAA, 1970) reports that a tornado formed in southwest Oklahoma at 2245 CST, traveled northeast and did not dissipate until reaching Stillwater at 0200 CST. Extensive damage was reported near Oklahoma City. The track connecting these beginning and end points is sketched on figure 3, although it is uncertain that the tornado followed such a track or even that only a single tornado was involved. (Such observations and reports are especially questionable when events occur at night.) This is presumably the same event studied intensively by other contributors to this volume. It seems virtually certain that the infrasonic waves recorded at Boulder and San Diego did not come from this Oklahoma storm, but rather from another storm system in northern Texas that was evidently part of the same widespread squall line.

Davies and Jones (1972) have reported observing the previously mentioned ionospheric waves during the passage of this storm system. The characteristic three-minute waves are visible between about 0400 and 1200 UT on records of his ionospheric soundings made near Oklahoma City. Davies and Jones show that at 1045 UT the waves come from the southwest of Oklahoma City, indicating possibly the same source we find.

The NOAA Radar Summary Charts show a line of storms passing across north-central Texas during the interval of infrasound generation. Several storm echoes in the line had indicated tops over 40,000 feet, with highest tops at 55,000 feet, but it has not been possible to identify specific storm echoes with the infrasound-source locations.

The Nimbus 4 infrared radiometer measurements during this storm period provide an excellent perspective of storm activity over the Texas-Oklahoma area at 0730-0737 UT (Wexler and Allison, 1972). The photograph on the cover of the Preprint Volume for the 15th A.M.S. Radar Meteorology Conference displays a color analysis of an IR photograph, reproduced in figure 4, in which the coldest temperatures indicate the locations of highest storm-cloud towers. The lower storm complex is closer to the area of infrasound emissions depicted in figure 3, but the time difference (an hour after block 6 arrived at Boulder) makes a direct association questionable.

5. REFERENCES

Brown, R. F., Jr., (1963): An automatic multichannel correlator. J. Res. NBS, 67c, 1, 33-38.

Davies, K. and J. E. Jones, (1972): Ionospheric disturbances produced by severe

thunderstorms, NOAA Professional Paper No. 6, U. S. Gov't. Print. Off., Washington, D. C.

Georges, T. M., (1973): Infrasound from convective storms: examining the evidence, Rev. of Geophys. Space Phys. 11, 571-594.

Georges, T. M. and J. M. Young, (1972): Passive sensing of natural acoustic-gravity waves at the earth's surface, Ch. 21 of Remote Sensing of the Troposphere, V. E. Derr, Ed., U. S. Gov't. Print. Off., Washington, D. C.

NOAA, (1970): Storm Data, 12, 4, Environmental Data Services, Asheville, N. C.

Wexler, R. and L. J. Allison, (1972): Radar and Nimbus 4 infrared measurements of the Oklahoma City tornadoes 30 April 1970, Preprints of the 15th AMS Radar Meteor. Conf., Amer. Meteor. Soc., Boston, Mass., 77-82.

RADIO-FREQUENCY ELECTRICAL ACTIVITY ASSOCIATED WITH SEVERE STORMS IN OKLAHOMA DURING APRIL 29-30, 1970

William L. Taylor

National Oceanic and Atmospheric Administration
Environmental Research Laboratories
Wave Propagation Laboratory
Boulder, Colorado 80302

The results of observing the radiation from lightning discharge processes indicated that major radio-frequency electrical activity was associated with the tornadoes that struck Oklahoma City during this period. Rates of occurrence of atmospherics at frequencies from 10 kHz to above 3 MHz were observed using short time constant circuits to preserve the burst nature of the received impulse signals. It is suggested that the parameter most indicative of tornadic activity is the number of bursts of high counting rates at frequencies above 1 MHz.

1. BACKGROUND

A scientific project to search for possible electromagnetic (e.m.) signatures suitable for tornado detection was initiated in 1969 by ESSA/Institute for Telecommunication Sciences. This project was subsequently assigned to NOAA/Wave Propagation Laboratory. This report summarizes the e.m. observations conducted during April 29 and 30, 1970 and includes the preliminary interpretation of the recorded data.

The concentration of energy within the relatively small volume of a tornado has been the subject of much investigation by prominent scientists for more than a century, but this concentration has not been explained in terms of the energy budget. The power required to drive a tornado vortex has been estimated to exceed 10^8 kW (Vonnegut, 1960), yet this is small compared to the energy available in a single thunderstorm cell which may exceed 10^9 kW (Braham, 1952). Various theories have been proposed over the years suggesting that a tornado may be produced by the concentration of kinetic energy resulting from the conservation of angular momentum through some not yet understood mechanism associated with the intense electrical activity associated with severe storms.

Many eyewitness accounts of unusual electrical activity in and around tornadoes have been reported during the last 20 or 30 years. Jones (1950) gives accounts of lightning and thunder being decidedly different during a

tornado than during ordinary thunderstorms; for example, the presence of St. Elmo's fire in the vicinity of a tornado funnel, and the rapid rate of "one stroke right after another" at the base of a cloud just ahead of the funnel. Jones (1965) also reported nighttime observations of approximately circular patches of flashing pale blue illumination originating from within severe storms. Vonnegut (1960) references some observations which are indicative of intense electrical discharges near and within the funnel.

Jones (1959) reported that the occurrence rate of atmospherics in the 10 kHz region of the spectrum increased as the intensity of a thunderstorm increased, but decreased to a relatively small value prior to a tornado formation. However, the occurrence rate at 150 kHz greatly increased during the formation of a tornado. More recently, the effects observed on television sets tuned to channel 2 (54 MHz) have been reported by Waite and Weller (1969) and by Biggs and Waite (1970).

The electrical charges within a thunderstorm cloud are usually dispersed throughout the cloud or discharged to the earth by the discrete current surges of lightning strokes. Electromagnetic fields radiated during a lightning stroke, called atmospherics or simply sferics, contain frequency components extending from a few Hertz to many megahertz. Recent works related to the lightning discharge include, for example, that of Bradley (1965), Dennis and Pierce (1964), Iwata and Kanada (1967), Mackerras (1968), Muller-Hillebrand (1961), Ogawa and Brook (1964), Taylor (1963) and Uman and McLain (1969).

If appreciable electric currents do flow either within or closely associated with the tornado funnel, as indicated by Brook (1967), and dispersed into the severe storm cloud, the process might well tend to be almost continuous in the form of corona sparks or a gaseous glow. This would tend to reduce the energy radiated at lower frequencies from return-strokes and increase the energy partitioned into higher frequencies from short-distance, rapid-occurrence dispersive processes within the cloud.

The initial work, using a mobile van operating in central Oklahoma during May 1969, consisted of intermittent observations of the resonant circuit responses at six frequencies in the 10 kHz to 500 kHz region using single stage filters with 1 kHz bandwidths. The analysis of these initial data showed that new equipment with greater dynamic range, wider bandwidth filters, and extending to much higher frequencies would be required to properly define the characteristics of radio-frequency electromagnetic radiation from severe storms.

2. INSTRUMENTATION

The design of equipment for the observation of e.m. signals from lightning discharge processes was dictated in part by the results from the 1969 observations, the cost of the instrumentation and the need to record some parameter closely associated with thunderstorm activity. To record and analyze the amplitude responses of several resonant circuits for individual impulses would require elaborate and expensive equipment. It was decided to observe the rate of occurrence of atmospherics, which would be represented by the average number of resonant circuit responses exceeding certain amplitude levels per unit of time.

Circuit responses for the atmospheric rate equipment are shown in figure 1. A transient signal radiated from a lightning discharge process arrived at the antenna which was a one meter long vertical whip. The transient passed through a high input impedance antenna coupler which in turn drove the transient through several hundred feet of coaxial cable to the main equipment van. It was then distributed to several single stage tuned circuits which were resonant at the desired frequencies. The bandwidth of each tuned circuit was 10 percent of the center frequency. The response signal was presented to a logarithmic amplifier and then rectified and smoothed. Five trigger circuits were individually adjusted to activate a one shot multivibrator each time the signal exceeded a predetermined level. The output of each one shot was integrated with a suitable time constant imposed and was presented to a data recorder through a logarithmic output driver.

The 25 μs time base for the circuit responses in figure 1 would be appropriate for a 1 MHz channel. A single transient is hardly recognizable in the rate data sample shown, which was for a 0.01 second integration time constant. Overall measured response time to 90 percent of the actual rate was about twice the time constant. The recorded rate for a very short duration burst of impulses would be less than the actual rate. Very few bursts are less than 20 ms and, therefore, the indicated rates should be reasonably accurate. The rate data can be interpreted as the average rate of atmospherics producing tuned circuit responses exceeding a selected amplitude threshold.

Two vertical monopole antennas with associated gain controls and amplifiers were used to cover the whole frequency band of interest. Each antenna was a 0.63 cm rod, one meter in length, with a 15 cm hemispherical corona cap at the top and an antenna coupler at the base. The antenna coupler was secured to a four-foot square aluminum base and the whole unit enclosed in a plexiglass dome. The low frequency system bandpass (3 dB reduction in response) from antenna input to the amplifier output extended from 2 kHz to 600 kHz. Bandpass of the high frequency system was from 300 kHz to 5 MHz and was 7 dB down at 10 MHz.

Calibrations were performed by inserting rectangular pulses into the antenna coupler through a dummy antenna. The amplitude of the pulses was adjusted to be equivalent to that of the desired free space field. The length of the pulses was adjusted to produce the same Fourier spectrum amplitude at a particular frequency, and thus the same tuned circuit response, as would be obtained from a single voltage step function of the desired amplitude. The amplitude responses of all the tuned circuits were the same since the decrease in spectral amplitude of the pulse was just compensated by the increase in bandwidth as the channel frequency increased. The actual pulse used had a rise time of about 0.05 μs which caused the pulse spectrum to change from 6 dB per octave to 12 dB per octave at a frequency of about 5 MHz.

After the threshold levels were adjusted, each recorded response was calibrated for occurrence rates. This was done by using rectangular pulses of the proper amplitude and pulse length for each channel. Rates were calibrated each decade starting with five pulses per second for 10 kHz, 100 kHz, and 1 MHz and starting with 1.6 pulses per second for all other frequencies. The maximum rate to which a set of channels could respond was limited by the bandwidth.

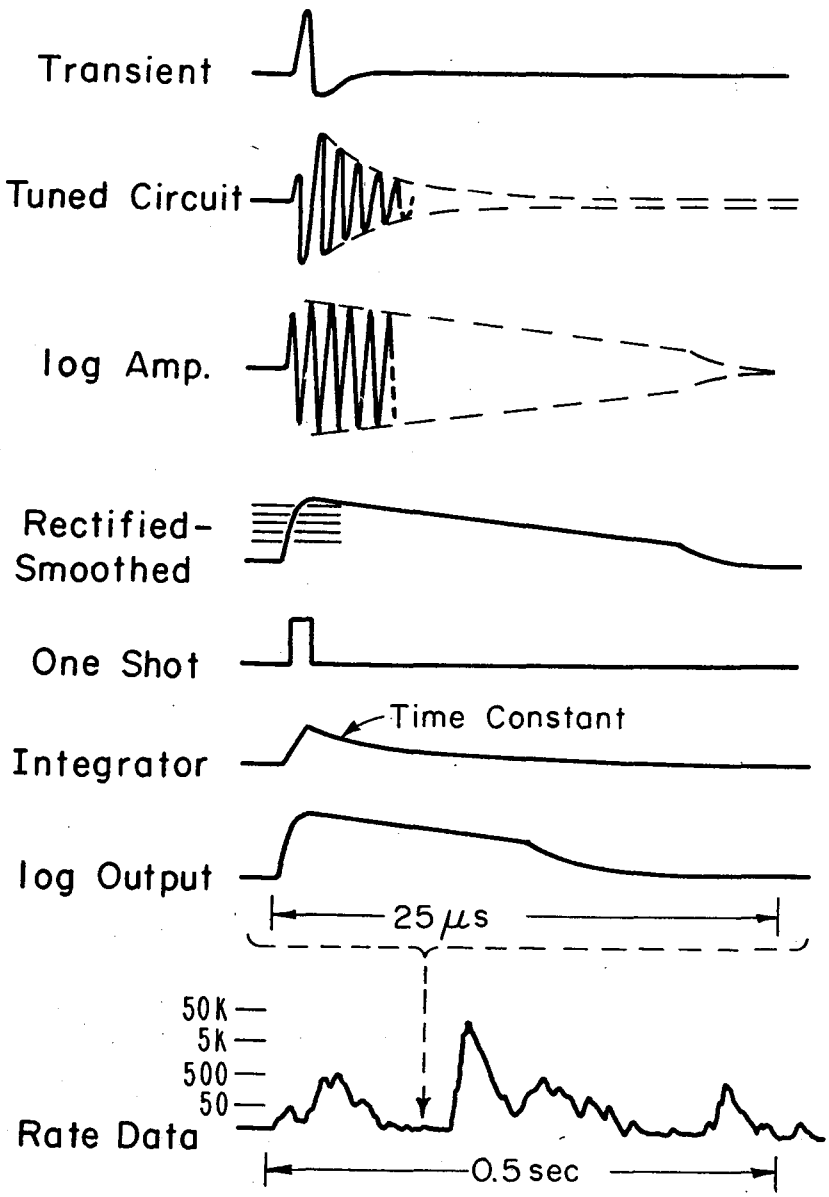

Atmospheric Rate Equipment Circuit Responses
Figure 1.

The directions of arrival of e.m. signals were obtained from two orthogonally positioned loop antennas in the vertical plane combined with the vertical electric antenna for sense. Each loop consisted of 16 turns on a 0.7 meter square frame covered by an electrostatic shield. The frequency response extended from 2 kHz to 600 kHz. A cathode ray tube of an oscilloscope was used to indicate the directions, and a 35 mm camera was used to record the CRT display. The camera was operated intermittently in an open shutter strip-film mode, at a rate of one time exposure frame each second, or operated such that time exposures of several minutes were obtained.

Time from a secondary time standard synchronized with NBS radio transmissions on WWV were mixed with the 31.6 V/m threshold rate data channels. Time codes took the form of a two-second pulse each minute, a four-second pulse each 10 minutes, and a 10-second pulse each hour. Small indicator lamps were used to time the direction of arrival film records.

All of the atmospheric rate data were recorded on FM magnetic tapes. These tapes were played back and the data transcribed onto paper charts. Reproductions from the paper charts were cut into narrow strips, aligned in time and presented in a single figure for a particular selection of data to assist the eye in following related events. Thirty channels of rate data were available for presentation. Observation frequencies were 10 kHz, 31.6 kHz, 100 kHz, 316 kHz, 1 MHz, and 3.16 MHz with five amplitude threshold levels for each frequency. These levels correspond to the electromagnetic fields at the antenna of 0.316, 1.0, 3.16, 10.0, and 31.6 V/m. Integration time constants were inversely proportional to frequency, varying from 1.0 seconds at 10 kHz to a minimum of 0.01 seconds at 1.0 and 3.16 MHz. There were other frequencies observed and other channels of data, but these will not be presented here.

3. OBSERVATIONS

The recording equipment was activated when there was a change of thunderstorms within 200 km of Norman, Oklahoma. Thunderstorm areas were tracked by associating the observations of atmospheric activity from the wideband direction of arrival display with precipitation echoes from WSR-57 weather radar operated by the National Severe Storms Laboratory (NSSL) at Norman. Actual data recording was started when thunderstorm activity began to either grow within or move into the general Oklahoma area and the recording ended when the activity began to dissipate or move outside a range of about 100 km.

During the 1970 spring tornado season in Oklahoma, 93 hours of observations were recorded during 13 periods of thunderstorm activity in April and May. The data presented in this report include only that obtained during an observation period totaling 13 1/2 hours on April 29 and 30, 1970.

Thunderstorms began to build by 1500 GMT on April 29 and were numerous in central Oklahoma by 1800 GMT (noon). Observations began at 1900 GMT although atmospherics activity was very low at that time. General movement of the thunderstorm areas during this whole period of activity was toward the northeast at about 75 km/hr (40 knots).

An example of weather radar precipitation areas and of the corresponding atmospherics direction of arrival display is shown in figure 2. Range from the center of the radar frame is given in nautical miles. The darkest portions represent locations of heaviest precipitation. The approximately circular radar echo area in the center of the frame resulted from ground clutter.

In figure 3, the directions of arrival of atmospherics are shown. The length of each trace from the center of the direction of arrival display is proportional to the atmospherics pulse amplitude. The darkest parts of the display indicate directions to the most active thunderstorms. In both figure 2 and figure 3, north is up and east is toward the right. Letter designations correspond to the storms identified by NSSL in the Preliminary Review of Storm Data for April 29-30, 1970. Other thunderstorm areas are indicated by numbers. These designations assist in identifying storm areas in these and subsequent figures.

Thunderstorm areas 2, 3, 6, and C are distinctive on the direction of arrival display in figure 3 and readily located on the radar frame in figure 2. Some of the other indicated precipitation areas and directional displays are not as easily related. The large precipitation area between storms 2 and 3 produced few large atmospherics as was likewise the situation between storms 3 and 4. Storm A produced no large atmospherics. Widespread atmospheric activity from 7, B, 8, and 9 was indicated. Area number 1 produced a recognizable number of atmospherics.

The atmospherics activity at approximately 2220-2240 GMT (figures 2 and 3) was relatively low with only a few lightning discharges per minute occurring from any of the storms. The amplitudes of atmospherics increased as storms 5 and 6 tended to merge into a single system and moved past NSSL.

The precipitation areas at about 0200 GMT are shown in figure 4. Atmospheric activity (data not shown) was very low with most discharges coming from areas 5 and 6. Storms C and D were just beginning to move out of the radar ground clutter but the electrical activity of these storms was extremely low. Storm E was about 100 n miles to the southwest and was increasing in electrical activity.

A marked increase in activity began about 0300 GMT. Signal amplitudes and atmospheric rates increased as Storm E moved closer to NSSL. By 0450 GMT the storm was just west of NSSL as shown in figure 5. About an hour earlier, however, the northern part of E was just west of NSSL and the southern part, which was the most electrically active was 40 to 50 n miles to the southwest of NSSL. The higher frequency channels of the atmospheric rate equipment were just beginning to indicate activity at this time.

A two-minute sample of rate data is shown in figure 6 centered on 0355 GMT. Each channel is aligned in time and arranged with the five channels of 10 kHz rates at the top, channels 6-10 for 31.6 kHz next, etc. Some channels of data were omitted from this and subsequent figures when there was either interference equipment malfunction, or no observed response. The frequency for each group of channels is indicated in a column on the far left of the figure. The threshold in volts per meter, which is the amplitude level the impulses must exceed before activating the counting circuits in each channel, is presented

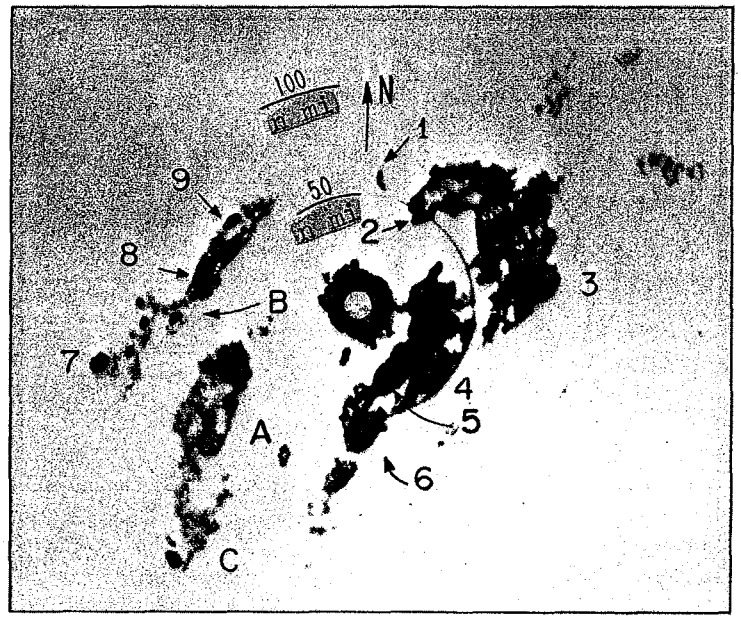

Radar Frame N° 5596
April 29, 1970 2220 GMT
Figure 2.

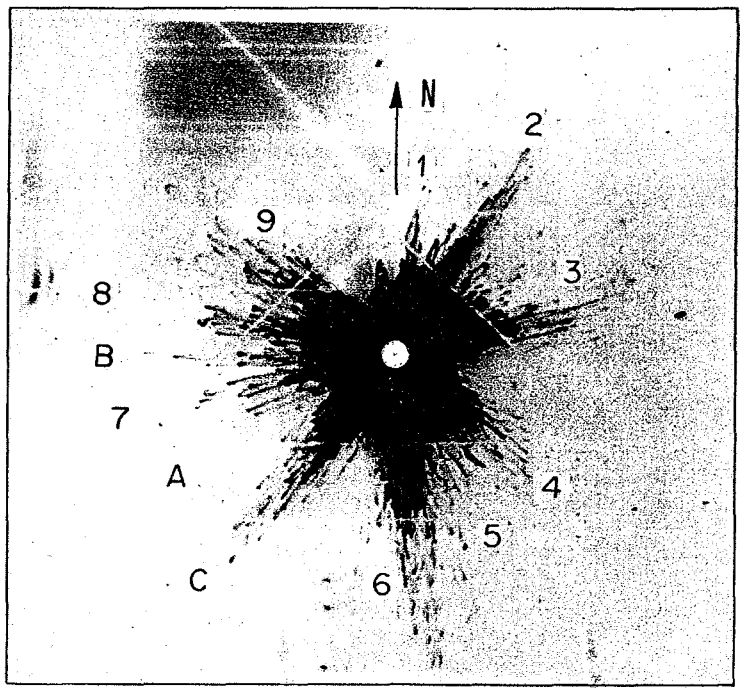

Atmospherics Direction of Arrival
April 29, 1970 2223-2240 GMT
Figure 3.

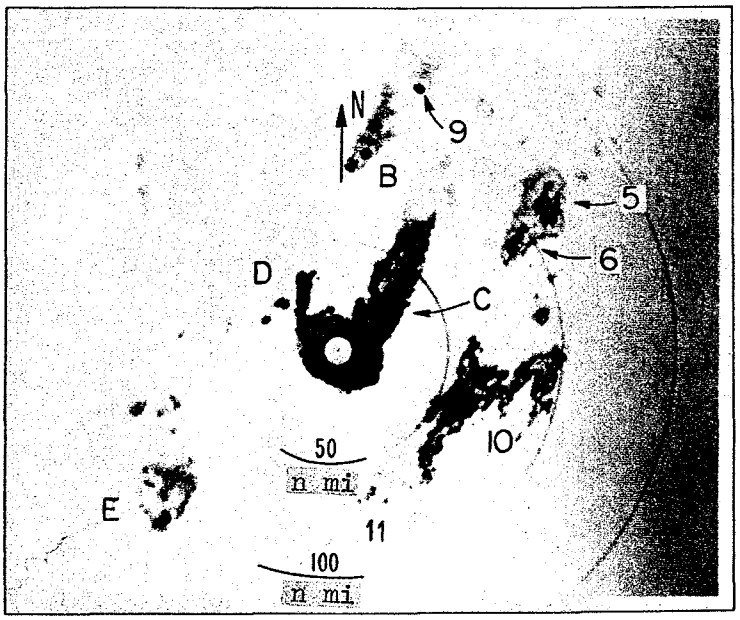

Radar Frame N° 6262
April 30, 1970 0202 GMT
Figure 4.

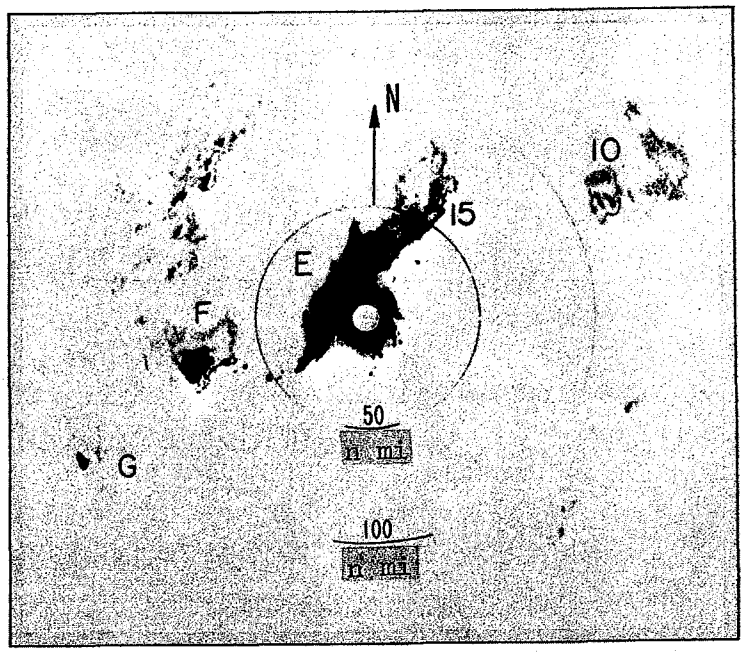

Radar Frame N° 6775
April 30, 1970 0450 GMT
Figure 5.

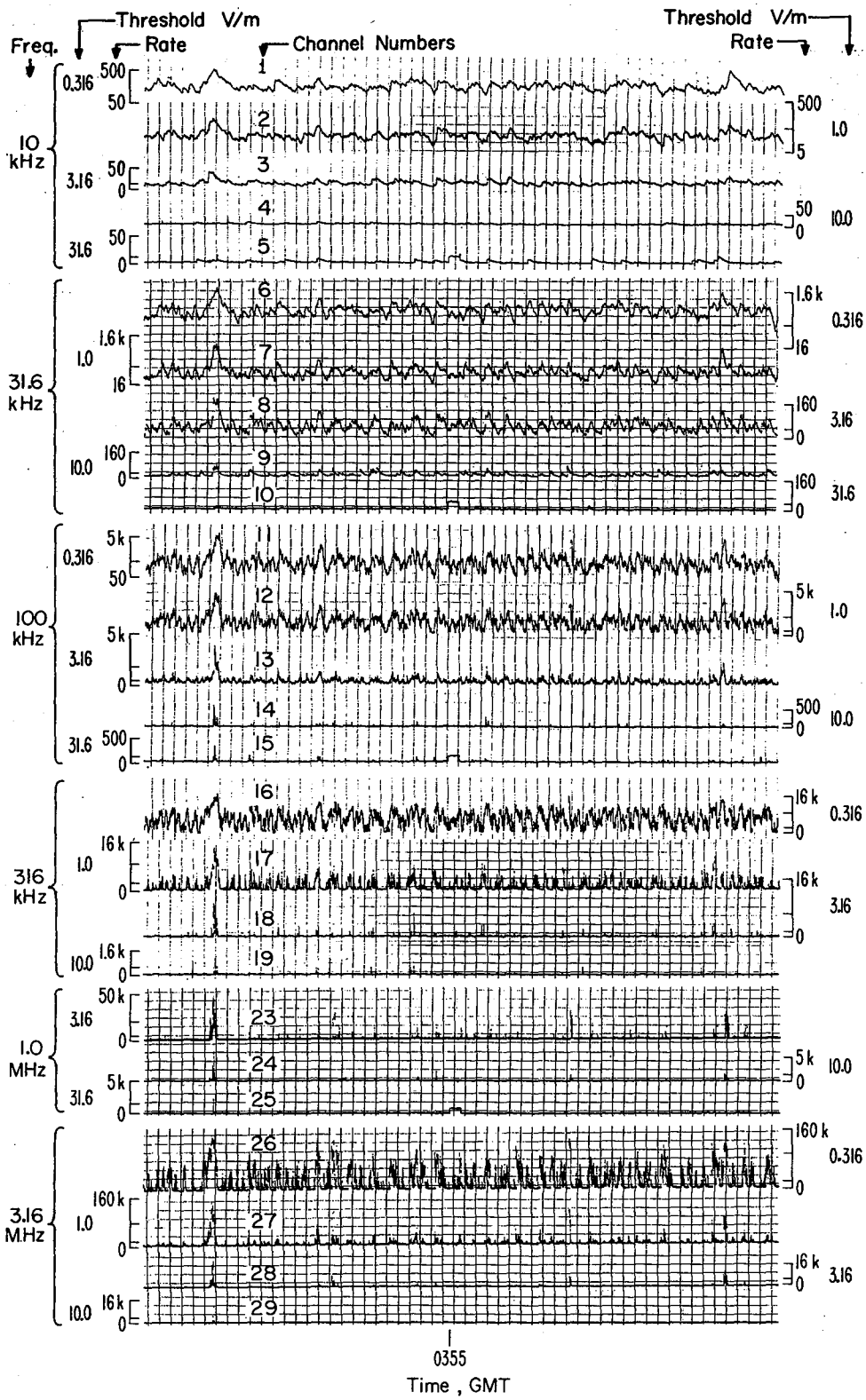

APRIL 30, 1970

Atmospherics Rate Data,
Figure 6.

in the second column on the left for the odd numbered channels and in the far right column on the even numbered channels. Thus we have the lower frequencies nearer the top with the threshold level increasing from top to bottom within each frequency. The data format is rate versus time with the impulse rates on an approximate logarithmic scale presented just to the left of the data for odd numbered channels and just to the right of the data for even numbered channels. Rates were calibrated each decade beginning at either 1.6 or 5.0 impulses per second. For example, channel 17 is the second channel of the 316 kHz group. It is an odd numbered channel, and therefore to the left of it is found that the threshold level is 1.0 V/m and the rate scale extends from zero to 16 k per second (k indicates thousands). The two other marks on the rate scale are for 160 and 1.6 k impulses per second. The responses to 1.6 and 16 impulse rates are too small to be shown. The rate varies approximately linearly between zero or the bottom rate mark and the first rate mark, and logarithmically thereafter. Greenwich mean time is shown along the bottom as indicated. The vertical grid lines are separated by two seconds. One-minute time marks are shown on the 31.6 V/m channels as square pulses two seconds in length.

Figure 6 shows the general appearance of the atmospheric rate bursts structure at approximately 0355 GMT during an increase in activity, but prior to the development of severe storms within 50 n miles of NSSL. The level of activity is low with equipment responses confined mostly to the smaller amplitude channels for each frequency. A lightning discharge associated with the northern part of Storm E and close to NSSL produced the high rate burst shown on most channels just left of the channel numbers. Note that the maximum rates indicated for this discharge are approximately proportional to frequency for corresponding amplitudes in each frequency group.

At 0450 GMT the southern part of Storm E was just west of NSSL as indicated in figure 5; the rate data showed a high level of atmospheric activity The maximum activity occurred at about 0505 GMT and a sample of the rate data is shown in figure 7. Almost no individual burst can be discerned but rather an almost continuous display of many small overlapping bursts. The large increase in activity on every channel is obvious when this data is compared with that obtained about an hour earlier as shown in figure 6.

Storm F was well organized and centered about 80 n miles SSW of NSSL at 0450 as shown in figure 5. Storm G had just come into the radar picture and was located about 130 n miles SW of NSSL. Atmospherics originating from neither Storm F nor Storm G could be identified through the high level of activity originating from the southern portion of Storm E at this time.

By about 0600 GMT, Storm E was beginning to break away from the NSSL area and move toward the northeast. Storm F was centered about 50 n miles west of NSSL and the leading portion of Storm G was located about 90 n miles from NSSL and moving along the same path that Storm F had followed. Electrical activity that had been decreasing from the maximum attained near 0500 GMT reache a minimum level indicated by atmospheric rate data which was below the activity level shown in figure 6.

Atmospheric rate data indicated activity began to increase again at about 0630 GMT. A steady increase continued until a maximum was attained at about

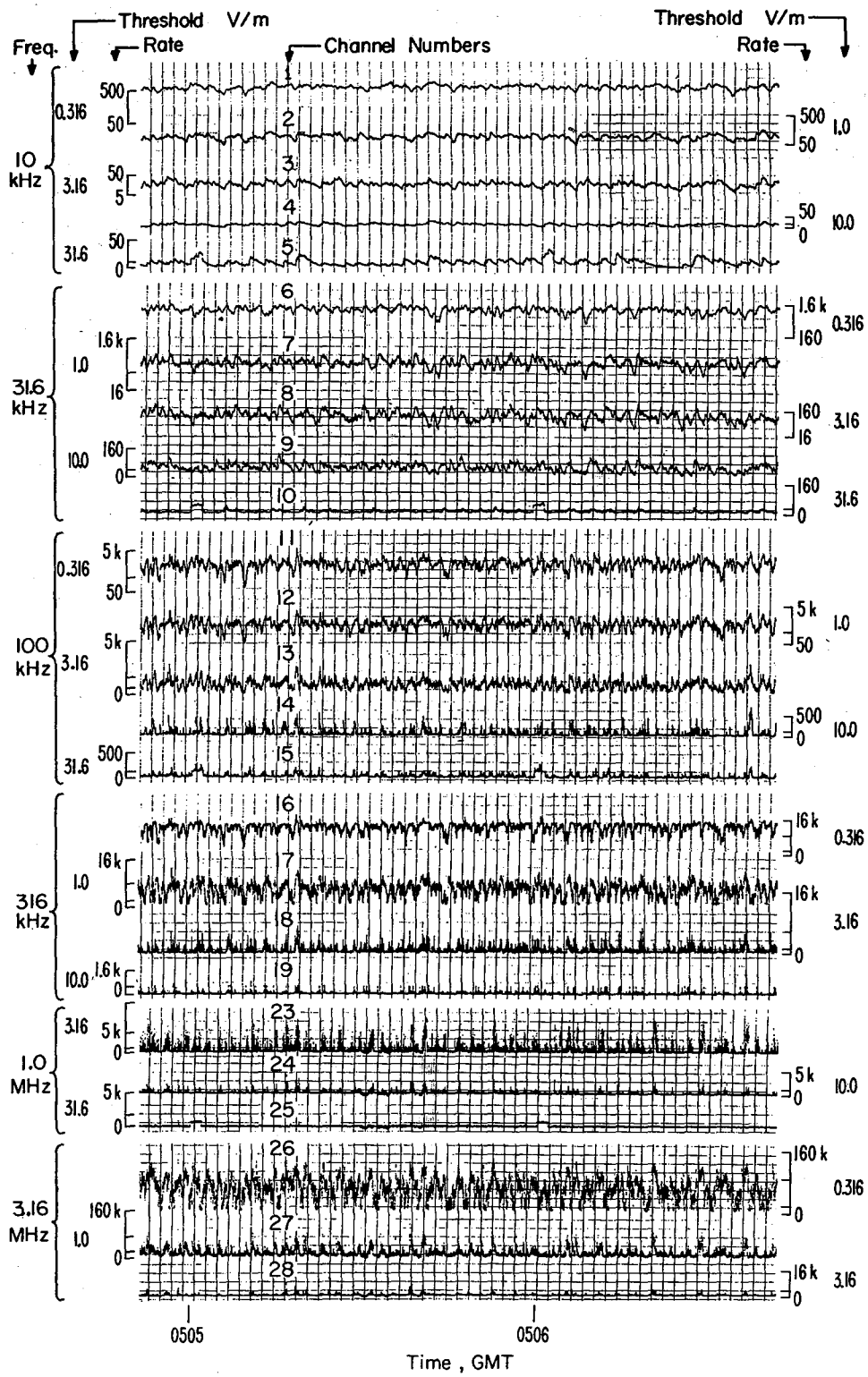

APRIL 30, 1970

Atmospherics Rate Data,

Figure 7.

0710 GMT. The radar record taken at 0703 GMT is shown in figure 8. This was approximately the time when the first Oklahoma City tornado was reported to have been in the northwestern section of the city, associated with the southern appendage of Storm F. This would place the tornado in the direction of about 335° at 23 n miles.

Direction of arrival data obtained during this period are shown in figure 9. This group of six exposures was similar to directional data previously shown but was for a time period of one second each compared to several minutes for the other data. The camera shutter was open continuously and the film was advanced between frames at a transport speed of 25 cm/s which required only a small fraction of a second. Film movement was actually vertical and the time between exposures moved up such that the top of the first frame is approximately the same time as the bottom of the second frame, and so on. Individual atmospherics that arrived during each film advance was recorded above and below the center of each time exposed frame.

The first one-second direction of arrival display on the left side of figure 9 was taken at one second after 0704 GMT, and the last display on the right was taken at six seconds after 0704. Atmospheric activity as indicated by the frames, tended to be more persistent from the directions of about 305° and 350° which are along lines from the center of NSSL radar ground clutter to the actual placement of letters G and F, respectively, in the figure. There were a few atmospherics from 40° associated with Storm E. If this first tornado was located in a direction of about 335° from NSSL at this time, that would place it between the areas of the greatest electrical activity.

The second tornado through the Oklahoma City area between 0720 and 0740 GMT was probably spawning almost due west of NSSL at the time of the radar frame in figure 8. The central part of the Storm G complex tended to bow out or rotate about the leading part of the storm as shown in figure 10. The first tornado had evidently dissipated by 0730 GMT and the second tornado was probably located about 17 n miles in a direction of about 340° from NSSL. The one-second directional displays starting at two seconds after 0733 GMT and ending at seven seconds after 0733 are shown in figure 11. The most persistent direction of arrival was about 335°. Although this was approximately the direction of the tornado at about this time, it was also the direction toward the main central part of Storm G which had been consistently active.

Electrical activity indicated by the rate data continued to increase after 0700 GMT and reached a broad maximum at about 0720 GMT. A two-minute sample of atmospheric rate data starting at about 0722 GMT is shown in figure 12. Unfortunately, a tape recorded malfunction prevented observations on data channels 11 through 16. Although the discharge burst rates are very high, the data represented here is not as impressive as that shown in figure 7. One reason for this is that no correction has been made for range, and the Storm E complex was closer to NSSL than Storm G was at the time of the data samples.

The lower portion of Storm G reached NSSL at 0745 GMT but by that time the burst character of the rate data indicated the storm was beginning to dissipate. The characteristic of the rate data indicative of the decaying

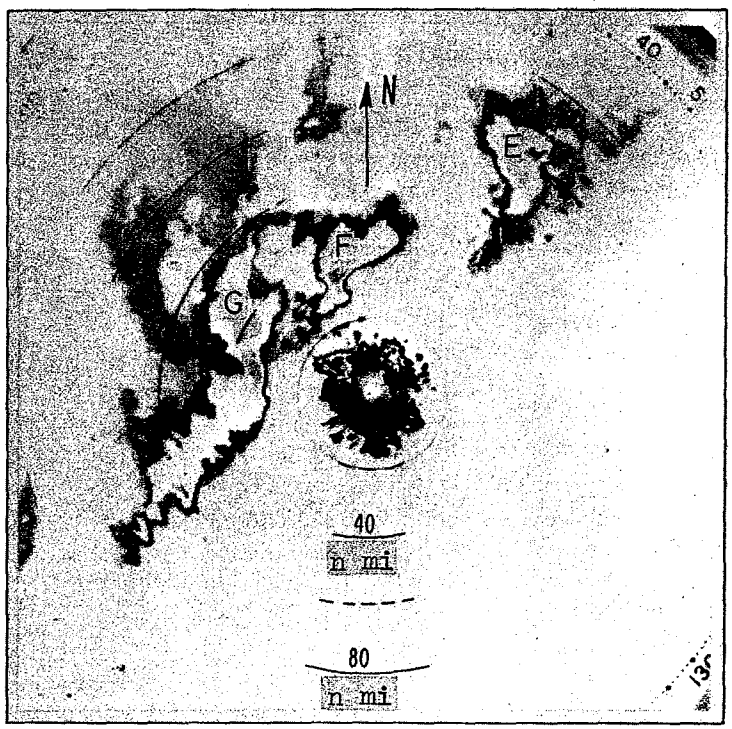

Radar Frame N° 0930
April 30, 1970 0703 GMT
Figure 8.

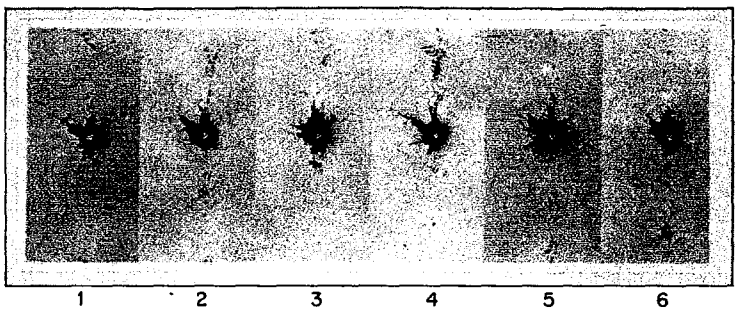

Atmospherics Direction of Arrival
April 30, 1970 0704 GMT
Figure 9.

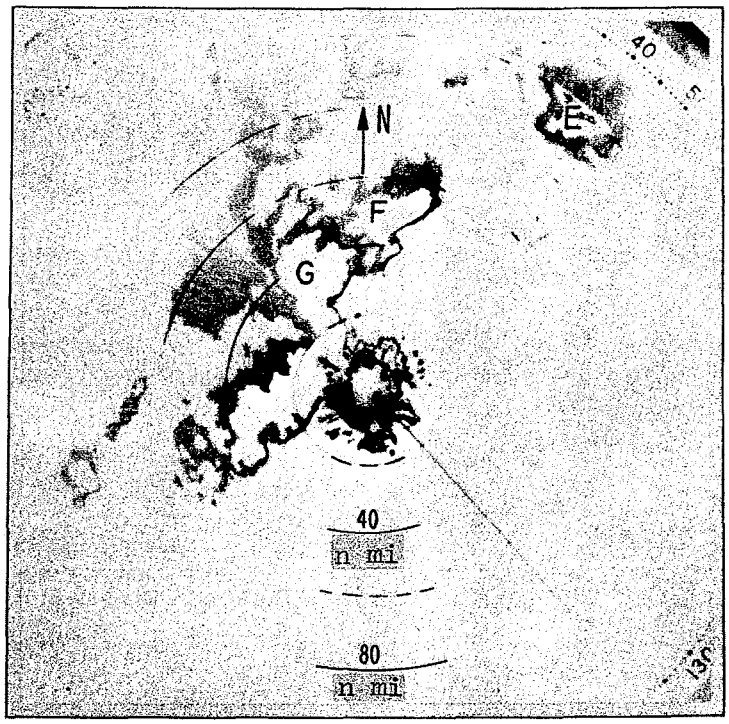

Radar Frame N° 1012
April 30, 1970 0730 GMT
Figure 10.

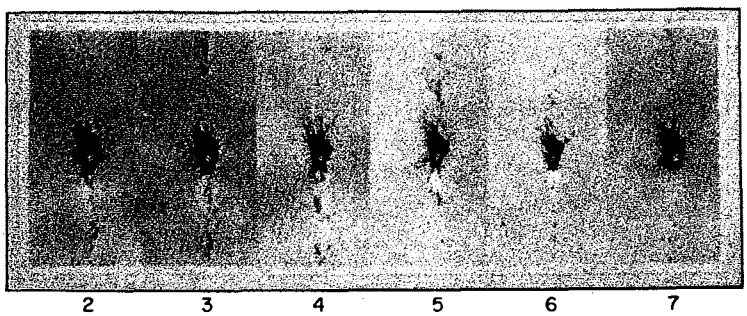

Atmospherics Direction of Arrival
April 30, 1970 0733 GMT
Figure 11.

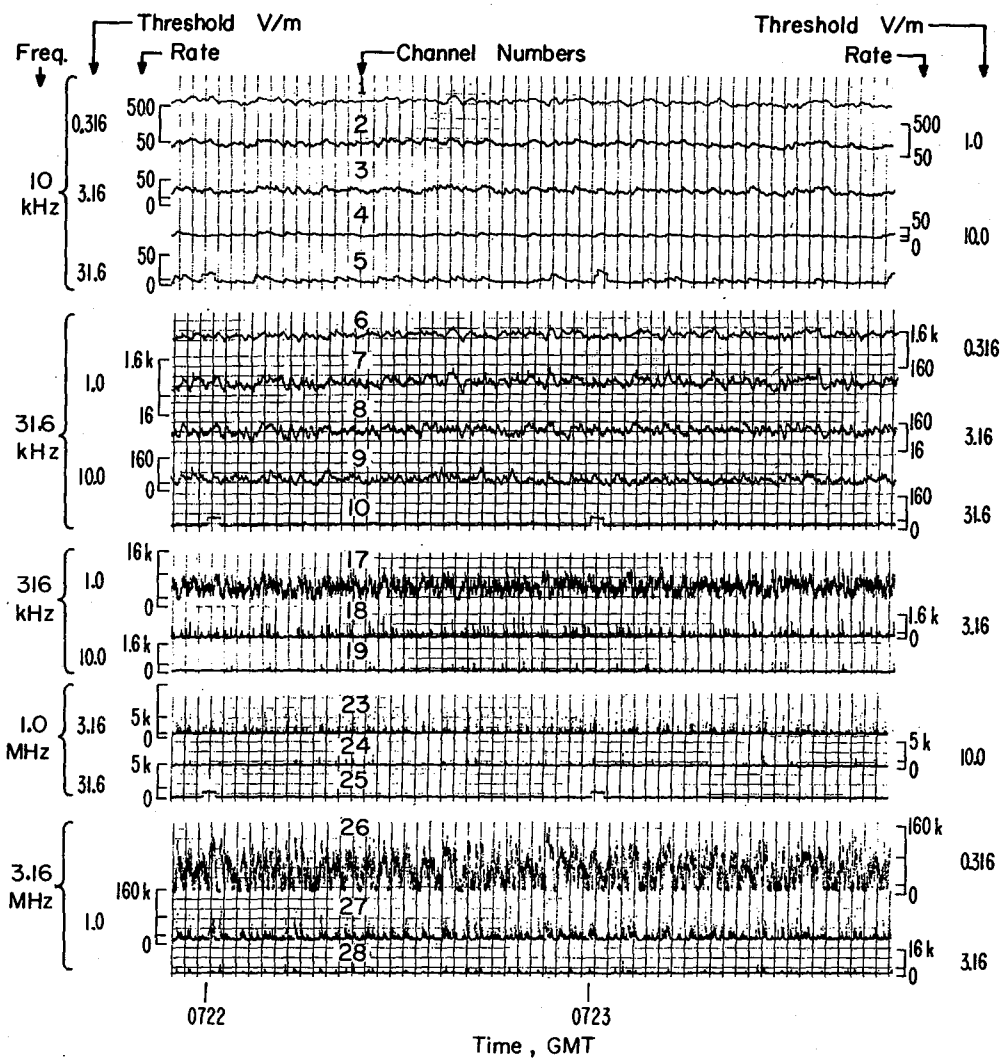

APRIL 30, 1970

Atmospherics Rate Data,
Figure 12.

state of a storm is shown in figure 13. This shows about four large individual bursts of atmospherics per minute at rates elevated far above the many small background of bursts. The tendency for the small bursts activity to decrease and the large bursts to become more infrequent continued until discrete bursts of atmospherics were occurring about once each minute by 0830 GMT at which time observations were terminated.

4. DISCUSSION

Selected portions of data collected during the April 29-30, 1970 period were presented here as representative samples of electrical activity in the form of atmospheric rates for periods of severe weather as well as for normal thunderstorm conditions. The general characteristic of the rate data during non-severe or normal thunderstorm conditions was that of a general low background rate of atmospherics with occasional short duration bursts of high rates produced by discrete discharges as shown in figure 6. Atmospheric activity greatly increased during severe storm conditions that produced many more bursts per unit of time and resulted in an enhanced background of almost continuous high rate with little or no individual bursts as shown in figures 7 and 12. The effect was not generally apparent at lower frequencies, below 100 kHz, but was easily recognized in the HF region.

The average burst rates - a measure of the frequency of occurrence of bursts of impulse counting rates exceeding 500 per second - for channels 27 and 28 of the 3.16 MHz group were used to indicate atmospheric activity levels for the April 29-30 period. Low burst rates of less than 10 per minute were presumed indicative of normal non-severe thunderstorm conditions. Medium burst rates between 10 and 25 per minute were presumed indicative of a very active thunderstorm with possible severe storm conditions. High burst rates in excess of 25 per minute were presumed indicative of severe storm activity with possible tornadoes.

Only low burst rates were observed until about 0340 GMT, and after about 0804 GMT. This includes the selected samples of data shown in figures 2, 3, 4 and 13. Medium burst rates represented by the atmospheric data shown in figure 6, were observed about 0340-0440 GMT, again about 0530-0700 GMT, and also about 0745-0805 GMT. High burst rates were observed during the passage of Storm E between 0440 and 0530 GMT as indicated in figures 5 and 7, and during the period of the two Oklahoma City tornadoes between 0700 and 0745 GMT as Storms F and G moved through the area as shown in figures 8 through 12.

These observations indicate that wide-band, high-dynamic range equipment operating in the correct frequency range is required for identification of electromagnetic characteristics peculiar to tornadoes. The parameter most suitable for use as a radio-frequency signature of tornadic activity is the number of bursts, per unit time, of high impulse counting rates, as measured at frequencies in the range 1 MHz to 100 MHz.

It is believed that the tornadoes occurring during this period which produced high burst rates are similar in electrical characteristics to most other tornadoes. However, in keeping with the whole history of radio and visual observations of tornadoes, it must be realized that perhaps most tornadoes, but not all, have major radio-frequency electrical activity

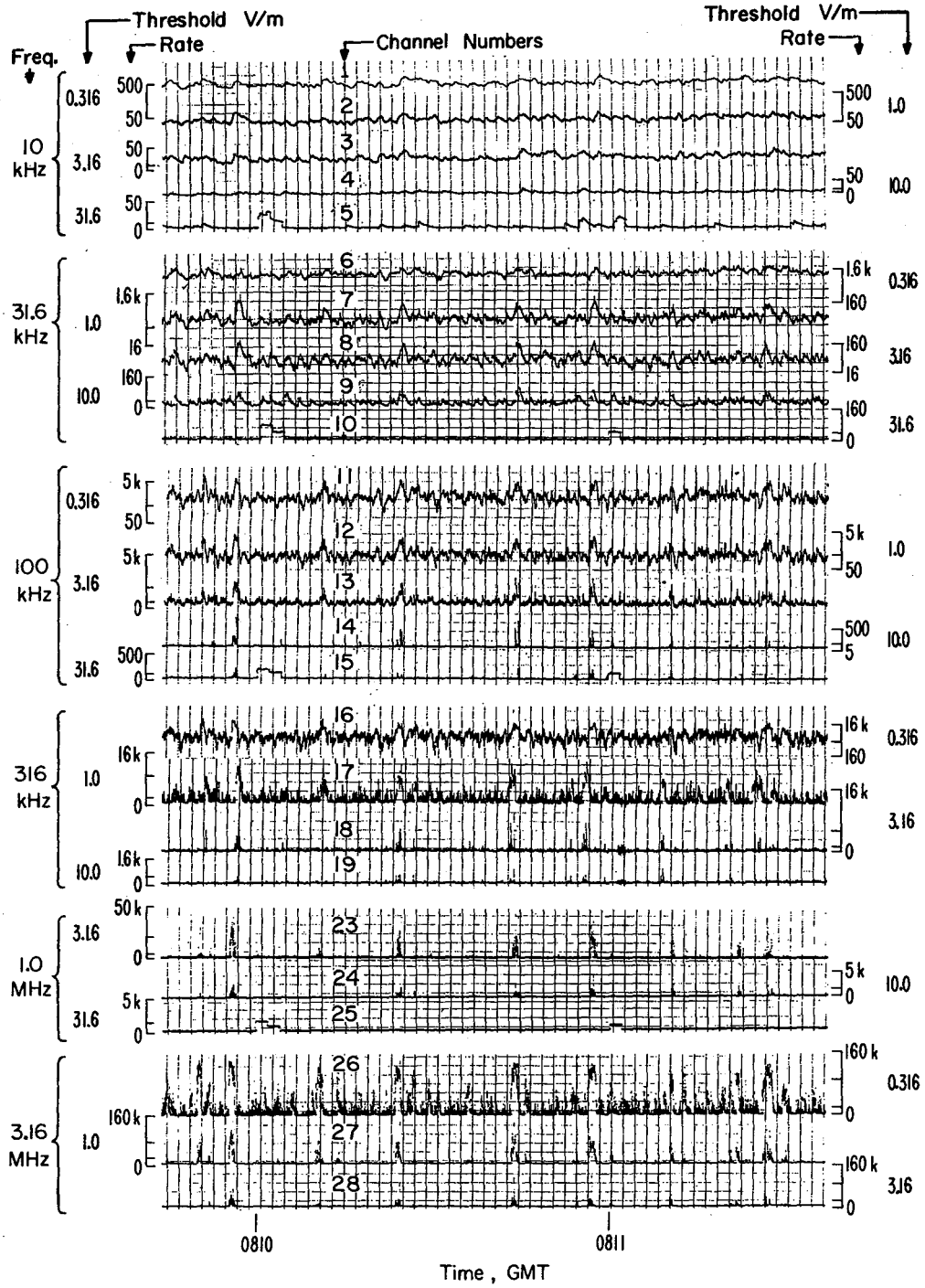

APRIL 30, 1970

Atmospherics Rate Data, Expanded

Figure 13.

associated with them. Conversely, a few severe storms, and a few non-severe storms as well, may have burst rates comparable to those associated with tornadic storms. It is not yet known whether it will be possible to provide a more unique distinction between tornadic storms and other high-burst-rate non-tornadic storms.

5. ACKNOWLEDGMENTS

I wish to thank H. Burdick for much of the equipment design and construction and for assisting with the observations, and also thank the many individuals in the NSSL who helped in support of this work. The observations for this work could not have been successfully completed without the extra financial support received from NSSL.

6. REFERENCES

Biggs, W. Gale, and Paul J. Waite (1970): Can TV really detect tornadoes? Weatherwise 23, No. 3, 120-124.

Bradley, P. A. (1965): The VLF energy spectra of first and subsequent return strokes of multiple lightning discharges to ground, J. Atmos. Terr. Phys. 27, 1045-1053.

Braham, R. R., Jr. (1952): The water and energy budgets of the thunderstorm and their relation to thunderstorm development, J. Meteor. 9, 227-242.

Brook, M., (1967): Electric currents accompanying tornado activity, Science 157, No. 3795, 1434-1436.

Dennis, A. S., and E. T. Pierce (1964): The return stroke of the lightning flash to earth as source of VLF atmospherics, J. Res. NBS/USNC-URSI, Radio Sci. 68D, No. 7, 777-794.

Iwata, A., and M. Kanada (1967): On the nature of frequency spectra of atmospheric source signals, Proc. Res. Institute of Atmospherics, Nagoya Univ. 14, 1-6.

Jones, H. L. (1950): The identification and tracking of tornadoes, URSI Comm. 4 Meeting, April 18.

Jones, H. L. (1959): The identification of lightning discharges by sferic characteristics, Recent Advances in Atmospheric Electricity, 543-556 Pergamon Press).

Jones, H. L. (1965): The tornado pulse generator, Weatherwise 18, No. 2, 78-80.

Mackerras, D. (1968): A comparison of discharge processes in cloud and ground lightning flashes, J. Geophys. Res. 73, No. 4, 1175-1183.

Muller-Hillebrand, D. (1961): The physics of the lightning discharge, Elektrotechnische Zeitschrift ETZ Issue A, 82, No. A8, 232-249.

Ogawa, T., and M. Brook (1964): The mechanism of the lightning discharge, J. Geophys. Res. 69, No. 24, 5145-5150.

Taylor, W. L. (1963): Radiation field characteristics of lightning discharges in the band 1 kc/s to 100 kc/s, J. Res. NBS, Radio Propagation 67D, No. 5, 539-550.

Uman, M. A., and D. K. McLain (1969): Magnetic field of lightning return stroke, J. Geophys. Res. 74, No. 28, 6899-6910.

Vonnegut, B. (1960): Electrical theory of tornadoes J. Geophys. Res. 65, No. 1, 203-212.

Waite, P. J., and N. Weller (1969): The Weller method: Tornado detection by television, Proc. of Sixth Conf. on Severe Local Storms, Amer. Meteor. Soc., Chicago, 169-171.

IONOSPHERIC DISTURBANCES DURING THE STORMS OF APRIL 29 AND 30, 1970, AT OKLAHOMA CITY

Kenneth Davies

Space Environment Laboratory
Boulder, Colorado 80302

Ionospheric wave-like disturbances with periods of 7 to 10 min (speed $\sim$ 180 m sec^{-1}) and 3 to 4 min (speed $\sim$ 1000 m sec^{-1}) were traced back to their sources at an altitude of 15 km. The calculated source positions were close to thunderstorm cells with cloud top heights greater than 50,000 ft (15.2 km). The horizontal speeds indicate that the 7 to 10 min waves are gravity waves, whereas the 3 to 4 min waves are acoustic. The source powers are of the order of 1 megawatt.

1. INTRODUCTION

Ionospheric data on traveling disturbances were acquired near Oklahoma City during the severe storms of April 29-30, 1970. The data discussed here are part of a more extensive study of ionospheric (acoustic) wave disturbances generated by severe thunderstorms discussed elsewhere by Davies and Jones (1972b).

For the benefit of readers not familiar with the inosphere, the following brief description is provided (see Davies 1965, 1969). The ionosphere is often defined as that part of the earth's atmosphere which contains sufficient ionization to affect the propagation of radio waves. Under this definition the ionosphere extends from about 50 km to about 1000 km and is divided into three regions within which layers of free electrons can exist with maxima of electron densities. The relevant regions and layers are given in table 1. Roughly speaking, the D region is responsible for the reflection of very low frequency (< 30 kHz) waves and for absorption of high frequency (3-30 MHz) waves. The E region causes refraction, reflection, and scatter of medium- and high-frequency waves. The upper F region, which is the more important in the present context, extends from about 180 km to the uppermost levels in the topside (above the peak of electron density).

Radio waves are reflected from an ionospheric layer on frequencies up to a maximum value. With vertical propagation, the maximum value is called the critical frequency. The critical frequency of a layer is a complicated function of time, season, solar activity, geographical and geomagnetic location, etc. The range of F2 layer critical frequencies varies from around 1.0 MHz to around 20 MHz.

Below the peak of the F2 layer, the ionized component of the ionosphere is embedded in the much denser neutral atmosphere. For example, at 300 km the atmosphere is rarely ionized more than 0.5 percent. Disturbances in the neutral atmosphere are communicated to the electrons via the ions, provided

TABLE 1 Ionospheric Regions and Layers

Region	Height (km)	Layer	Approximate Height, (km)	Approximate Daytime Electron Density (m^{-3})
D	50 to 90	C D	65 75 to 80	10^8 10^9
E	90 to 120-140	E1 E2 E_s	110 100	10^{11} ?
F	120-140 and up	F1,F1½ F2	200 >250	2×10^{11} 11^{12}

that the time scale is longer than the interval between successive ion-neutral collision which is of the order of 1 sec at 300 km. Such disturbances include neutral winds (see Kohl and King, 1967), gravity waves, and acoustic waves (see Hines, 1960). In this paper we are concerned with these types of disturbances.

2. ACOUSTIC WAVES FROM THUNDERSTORMS

Observations of man-made explosions (see Barry et al., 1966; Baker and Davies, 1968) and earthquakes (Davies and Baker, 1965; Yuen et al., 1969) have confirmed that disturbances with acoustic periods in the lower atmosphere can couple into the ionosphere. In November 1965, ionospheric wave-like disturbances with periods near 3 min were observed for several days over Boulder, Colorado, and were thought to be associated with tropospheric phenomena (see Davies, 1966). Georges (1967) suggested that the relatively narrow spectrum of these disturbances was the result of atmospheric filtering of acoustic-gravity waves. Georges (1969) observed these 3-min disturbances in the F region over the south-central United States and made a major contribution by showing that they were associated with severe weather fronts passing through the observing area. Further studies of this phenomenon have been reported by Georges (1968) and by Baker and Davies (1969), who found the following necessary conditions for the production of detectable disturbances:

(1) Cloud tops must be higher than 40,000 ft (12 km).

(2) Thunderstorm cells must lie within about 200-250 km from the point on the ground directly below the ionospheric reflection point.

Using the radar summary charts of the U. S. Weather Bureau (now the National Weather Service), Baker and Davies (1968) devised a severe weather index that ranged from 0 (no severe weather) to 5. They found that this index was always high (3 to 5) on days when disturbances were observed in the F2 region. However, on days of high severe weather index, ionospheric disturbances were not always observed. Similar observations of ionospheric disturbances associated with thunderstorms have been made in Alabama by Detert (1969). On the other hand, storms in Florida, which satisfy the conditions mentioned in the previous paragraph, do not appear to produce acoustic disturbances of comparable magnitude (see Davies and Jones (1972b).

3. THE RADIO TECHNIQUE

A radio wave of constant frequency is transmitted from one ground location to another via F layer reflection. Variations in the ionosphere are detected by the induced changes in the phase reflection heights of high frequency radio waves. The time rate of change of reflection height produces a frequency (Doppler) shift in the echo signal.

The continuous measurement of the Doppler shift is carried out by mixing the ionospheric echo with a local offset reference signal and recording the beat frequency on magnetic tape moving 1 inch min^{-1}. The frequency analysis is accomplished by fast playback (30 inches sec^{-1}) of the tape, resulting in a frequency multiplication of about 1800. The audio signal produced is spectrum analyzed by conventional means (Davies, 1969, section 9.3) and displayed on a facsimile chart). The smallest frequency shift in the original beat signal that can be measured with this technique is about 0.1 Hz.

The determination of the velocity vector of a disturbance is made by using spaced radio transmitters on several frequencies. The horizontal spacings together with measured time displacements give the horizontal trace velocity (magnitude and direction) while the spaced frequencies (reflected from different heights) together with the appropriate time displacements give the vertical trace speed (see Davies and Jones 1971, 1972b).

With the arrangement of spaced transmitters on 3.3, 4.0, and 5.1 MHz, shown in figure 1, observations were made from April to July 1970. Nine simultaneous Doppler records were obtained. To distinguish the three traces the three carriers were set 1 Hz apart.

4. ACOUSTIC-GRAVITY WAVES

In this paper we deal with waves having periods in the range from around 2 min to around 10 min. Acoustic-gravity waves are propagating oscillatory motions in a stratified atmosphere in which the restoring forces of buoyancy and elasticity are comparable (Hines, 1960). Acoustic waves have frequencies higher than the acoustic cut-off frequency ω_a, while gravity waves have frequencies lower than the buoyancy (or Brunt-Väisälä) frequency ω_g, as illustrated in figure 2. The frequency range between ω_g and ω_a is a forbidden region for propagating internal waves (i.e., surface waves may exist).

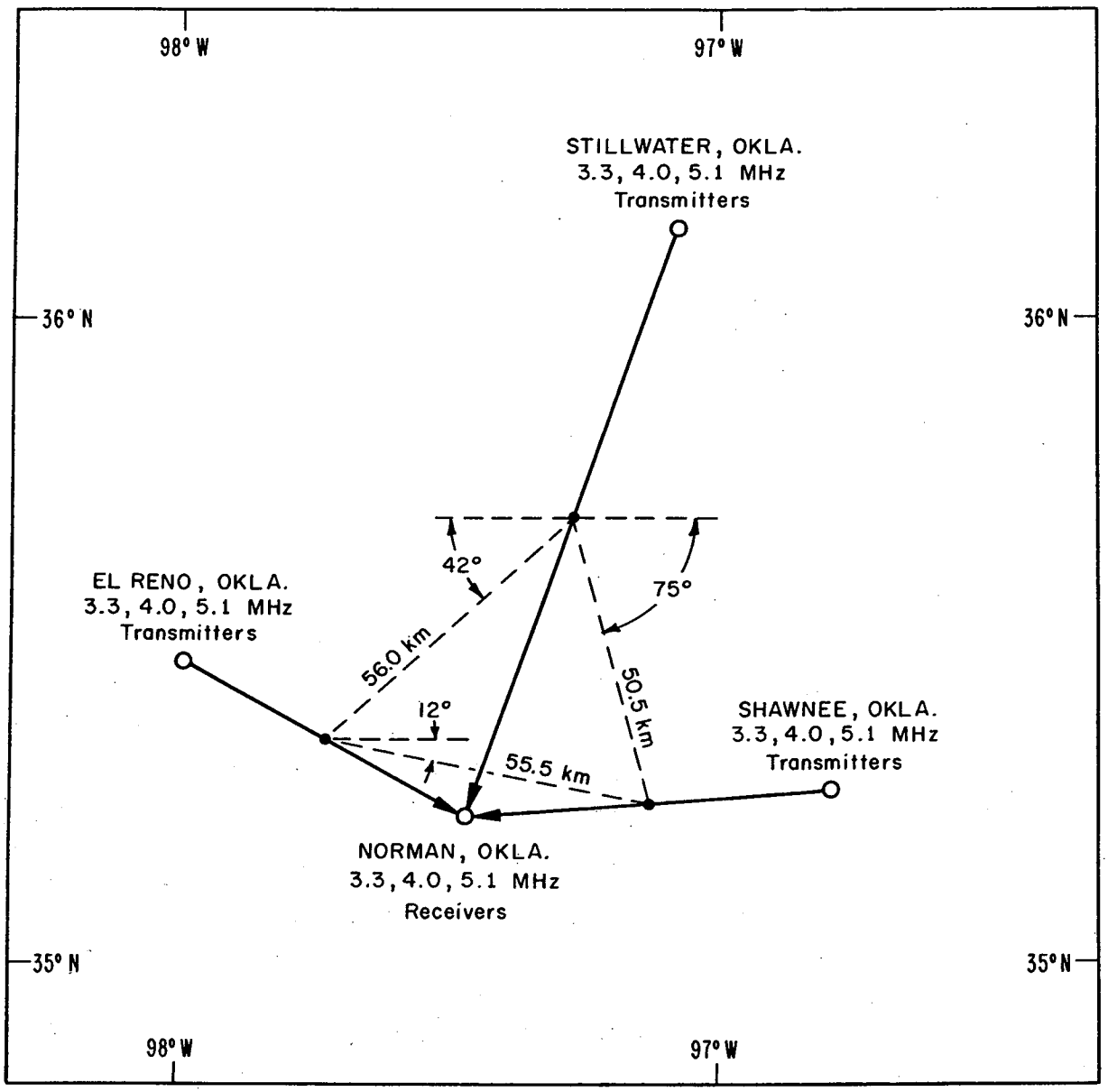

Figure 1. Spaced transmitters and receiving site in Oklahoma and radio frequencies.

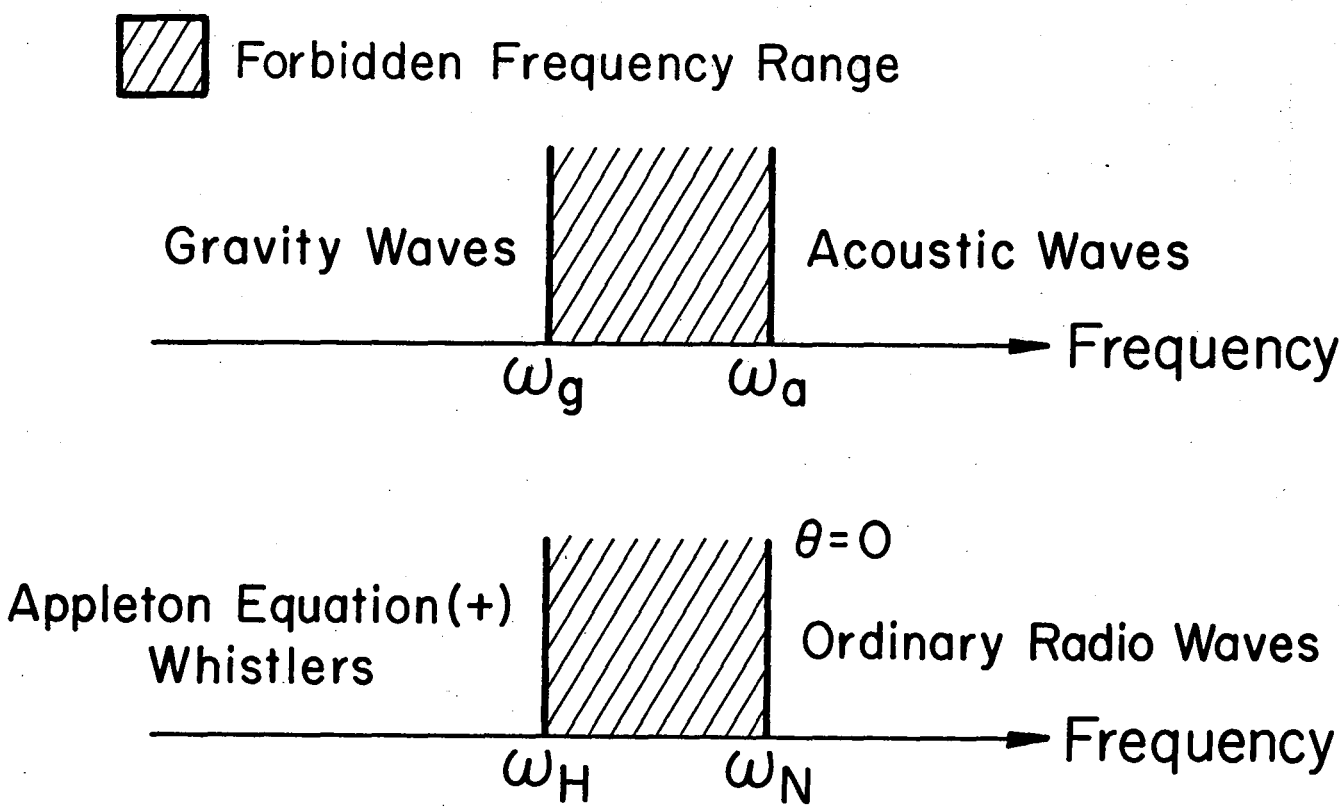

Figure 2. Frequency ranges of acoustic-gravity waves.

The propagation of acoustic-gravity waves is both dispersive (i.e., frequency dependent) and anisotropic (i.e., direction dependent). Because of these characteristics, the ray direction (direction of energy flow) differs from the phase direction, and the speed of energy propagation (group speed) differs from the phase speed. Hence, ray paths and transit times of these waves have to be calculated by elaborate ray tracing programs. Some sample ray paths for acoustic waves are shown in figure 3, for propagation through the 1962 U. S. Standard Atmosphere with a source at a height of 15 km. We see that for waves of a given frequency, there exists an iris near 150 km through which energy can penetrate to the F region where defocusing takes place. Alternatively, given the speed and direction of a wave at a point in the ionosphere, it is possible to trace the rays back to a given height and thus determine the distance or ground range of the source. Sample curves of ground range versus horizontal trace speed are given in figure 4.

Various sources of errors in the radio technique and the ray tracing are discussed by Davies and Jones (1971; 1972b).

5. THE IONOSPHERIC DISTURBANCE OF APRIL 29-30, 1970

The Doppler record for the night of April 29-30 is shown in figure 5. Recalling that local time is approximately UT - 6 1/2 hours, we see that during the afternoon of April 29, S-shaped disturbances occur with an average period of 9.0 min. These lasted until about 0130 UT, at which time a shorter period (3 to 5 min) disturbance appears. This persists throughout the night and into the following morning. It is this 3 to 5 min oscillation which appears to be a characteristic of ionospheric disturbances associated with severe thunderstorms over the central parts of the USA.

During the night, the ionospheric radio signals are spread in frequency. This spreading is thought to be caused by the presence of small-scale irregularities near the reflection level and is often associated with enhanced geomagnetic activity. The planetary magnetic A_p index for April 30 was 18, which indicates slightly disturbed conditions. In spite of the spread echoes, the presence of the 3-5 min period disturbances can be seen. Unfortunately, the record is unsuitable for detailed analysis until shortly before 1000 UT on April 30. Velocities calculated from the time differences near 1012 UT and near 1028 UT are superimposed on the radar films in figure 6.

We see from figure 6 that the horizontal trace speeds during the two periods 1005-1017 and 1021-1036 UT on April 30 are 850 m sec^{-1} and 2700 m sec^{-1}. These speeds are of the order of, but greater than, the sound speed in the F region and indicate that the waves are acoustic waves. The large horizontal speed during the second period shows that the wave is propagating nearly vertically. That is, the source is close to the point on the ground below the ionospheric reflection point.

The data indicate that the azimuth of the horizontal velocity changed abruptly from 206° east of north to 54°. This sudden change in direction suggests that the source of the disturbance changes suddenly from one part of the storm to another, as shown in the radar weather summaries of figure 7.

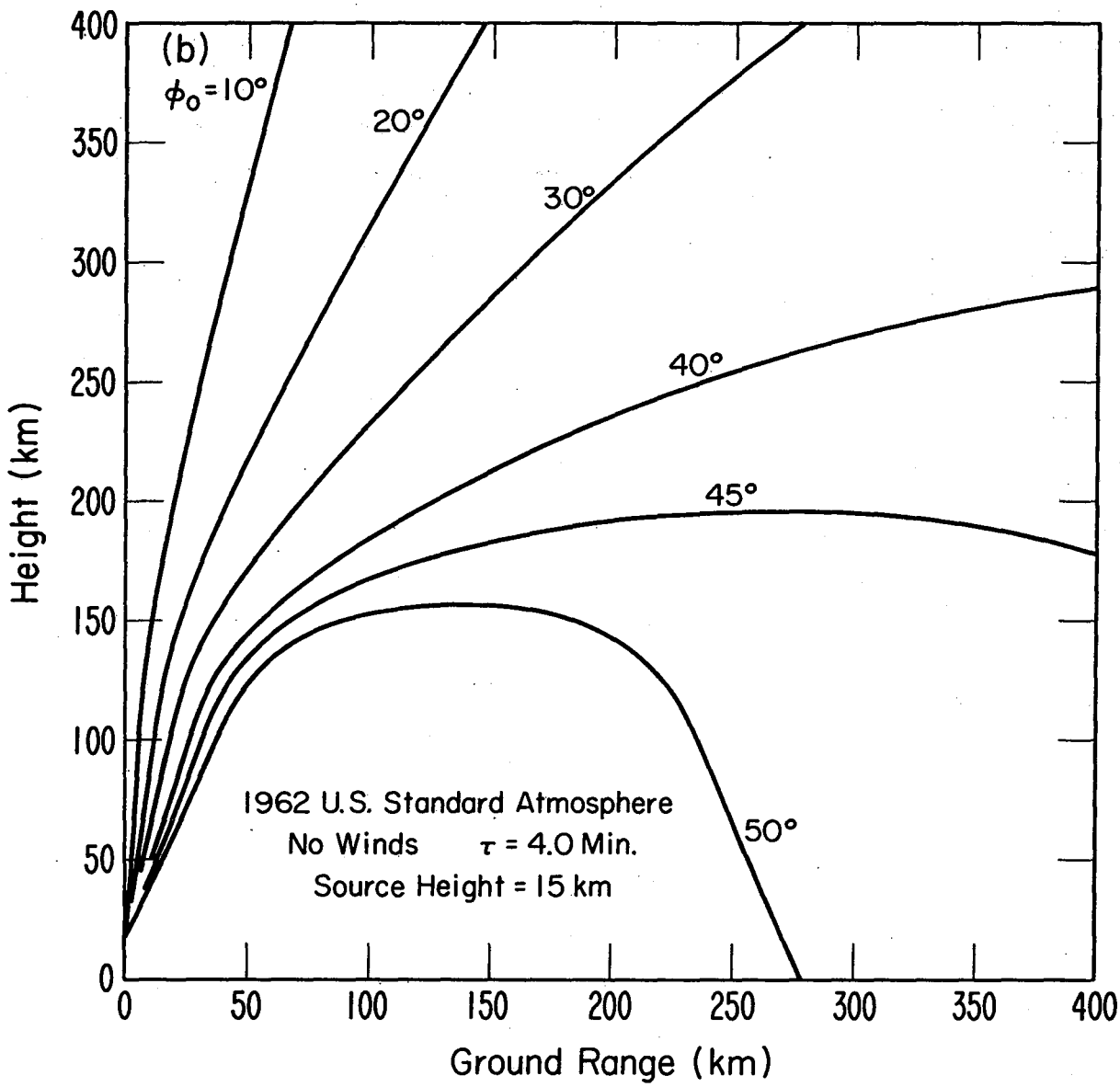

Figure 3. Ray paths of 4.0 min acoustic waves in the 1962 U. S. Standard Atmosphere.

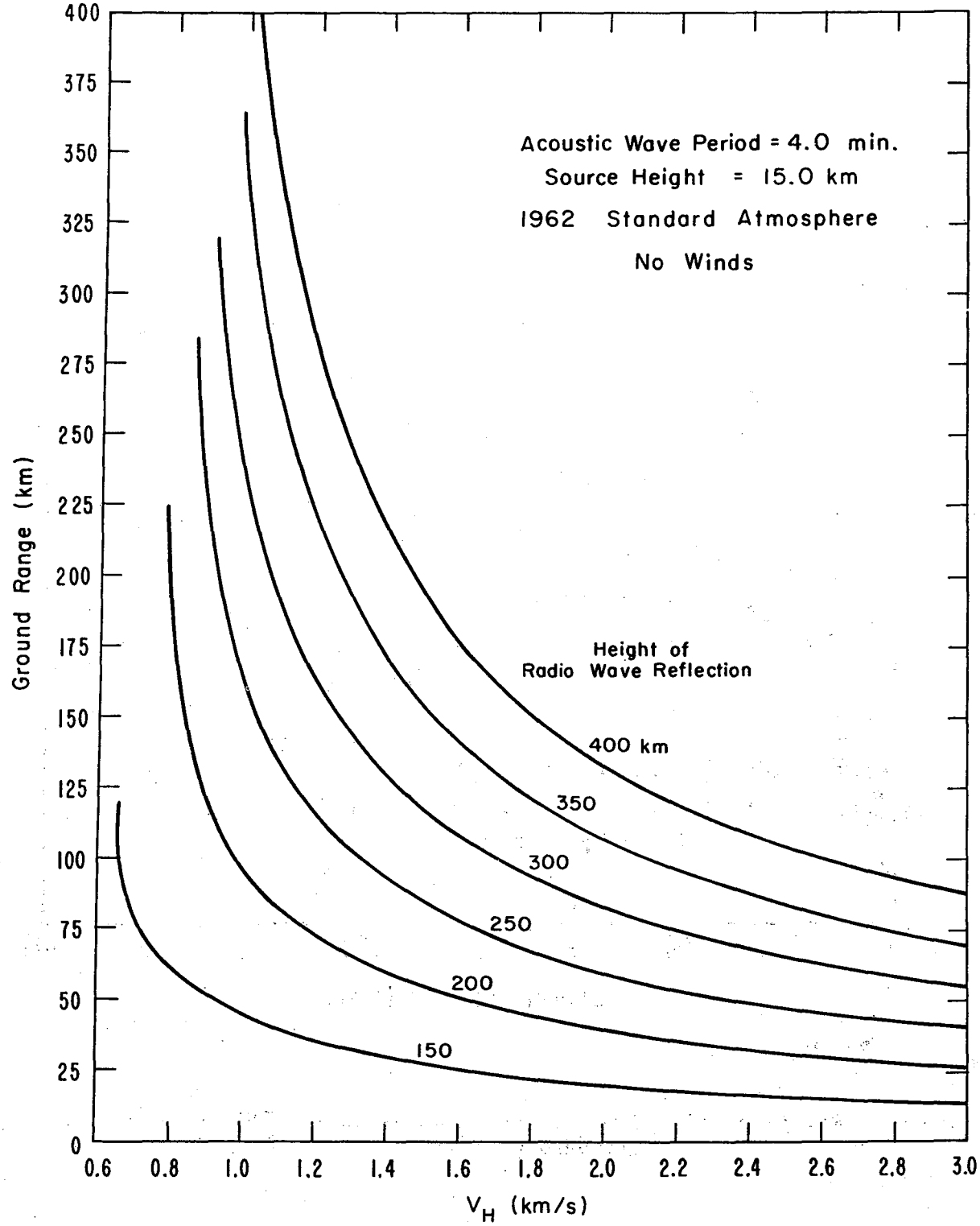

Figure 4. Ground range versus horizontal trace speed for 4.0 min acoustic waves in the 1962 U. S. Standard Atmosphere.

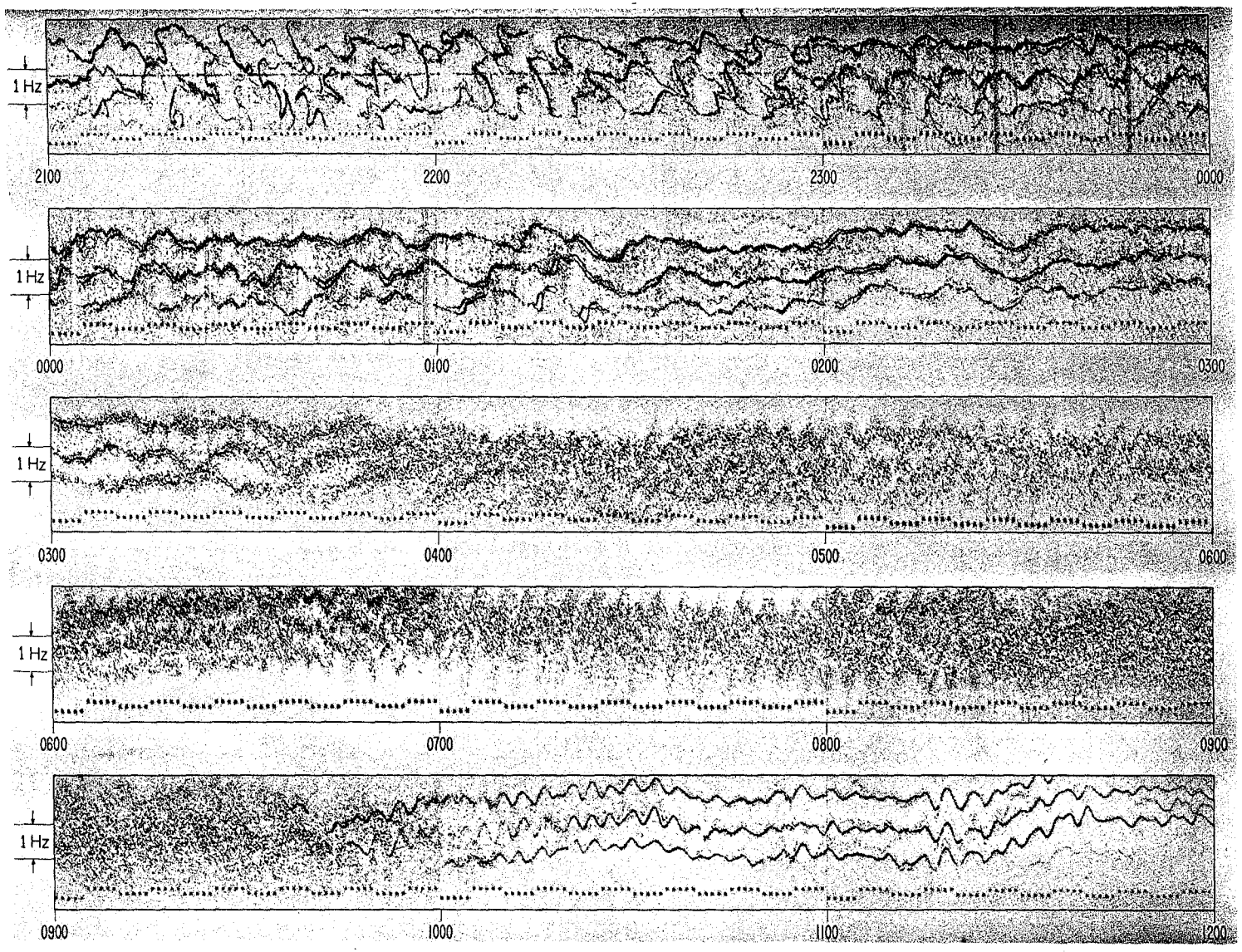

SHAWNEE, OKLA. (UPPER TRACE)
EL RENO, OKLA. (MIDDLE TRACE
STILLWATER, OKLA. (LOWER TRACE) } TO NORMAN, OKLA. 5.1 MHZ

APRIL 29, 1970, 2100 UT – APRIL 30, 1970, 1200

Figure 5. Doppler records on 5.1 MHz for the three Oklahoma paths, April 29-30, 1970.

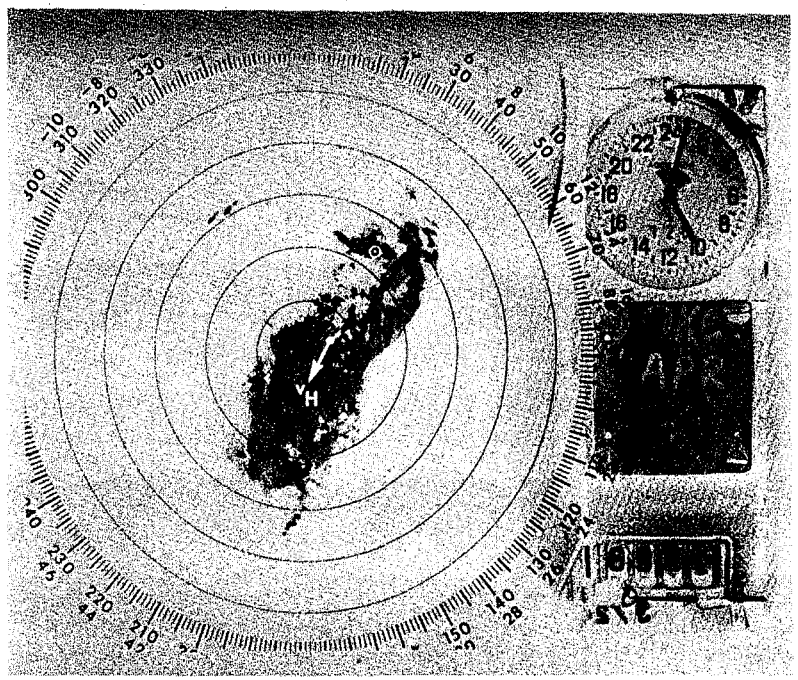

April 30, 1970 1002 UT
v_H = 850 m/sec
G. R. = 190 km

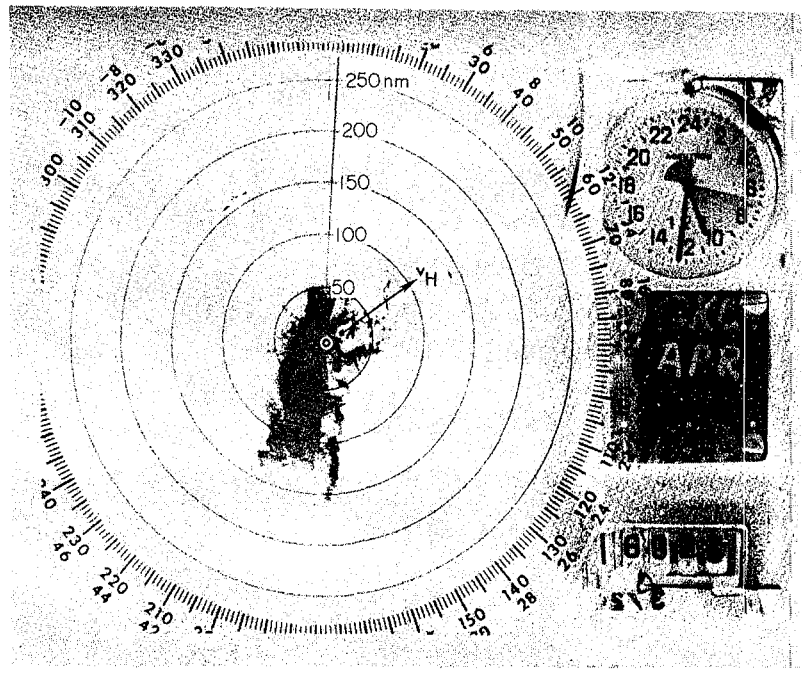

April 30, 1970 1031 UT
v_H = 2700 m/sec
G. R. = 40 km

OKLAHOMA CITY WEATHER RADAR
250 Nautical Mile Range
v_H = Horizontal Trace Velocity
G. R. = Ground Range
⊙ Denotes Point of Origin

Figure 6. Oklahoma City weather radar photographs (250 n miles range) and horizontal trace velocities for April 30, 1970.

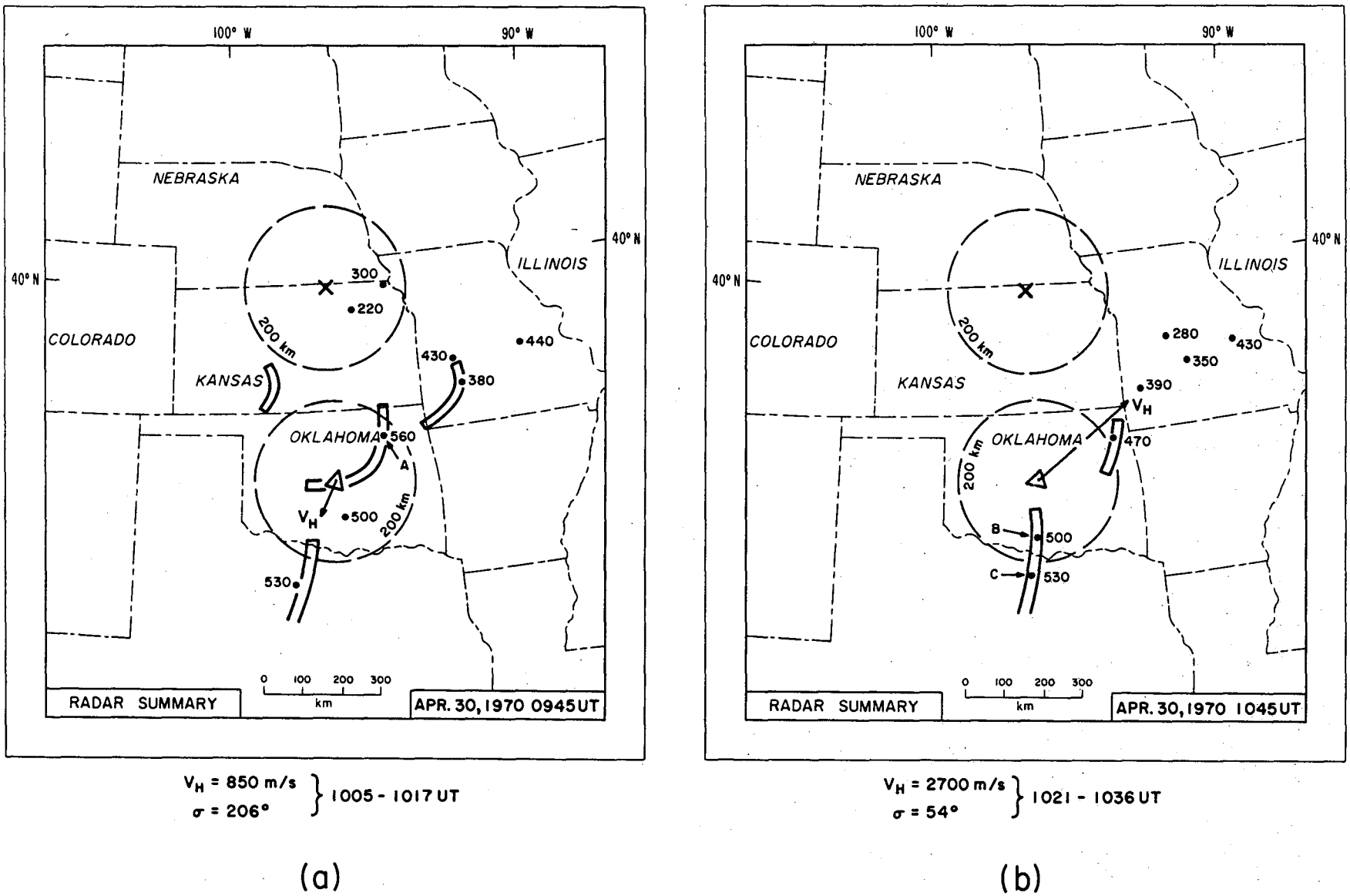

V_H = 850 m/s, σ = 206° } 1005 - 1017 UT

(a)

V_H = 2700 m/s, σ = 54° } 1021 - 1036 UT

(b)

Figure 7. Radar summaries with horizontal trace velocity vectors for two intervals on April 30, 1970.

Our data suggest that the sources of ionospheric disturbances are the individual storm cells. It appears that waves from one cell die away while those from another cell build up and eventually dominate. Near 0945 UT the primary source is probably that marked A, whereas at 1045 UT the primary sources were either or both of those marked B and C. All these cells meet the criteria listed in section 2 for producing observable ionospheric disturbances.

We shall return briefly to the S-shaped disturbance which occurred on the afternoon of April 29. This type of disturbance precedes several of the shorter period (nighttime) disturbances discussed above. They all occur during the daytime when the heights of reflection are low (e.g., 207 km on April 29) compared with the nighttime (e.g., about 350 km on April 30). Some simple theory which accounts for these S-shaped signatures has been given by Davies and Jones (1972). They proposed that reflection is from a sinusoidally corrugated surface for which the ratio of amplitude to wavelength exceeds a certain critical value. Measurements show that the speeds of these disturbances are of the order of 180 m sec^{-1}, which is appropriate to gravity waves. Thus it appears that we have a gravity wave with a period of 9 min. This period is less than the buoyancy period in the F region (around 12 min), which is contrary to what was said in section 4. This apparent inconsistency can be reconciled by posulating a horizontal wind component U parallel to the plane of propagation of the gravity wave. Now Hines and Reddy (1967) have shown that the intrinsic period t_i of an atmospheric wave as seen by an observer moving with a horizontal wind component U parallel to the horizontal trace velocity V_H is related to the period t observed on the ground by

$$t_i = t \frac{V_H}{V_H - U} , \qquad (1)$$

where V_H is measured from the ground. Thus a wave which appears to have an acoustic-wave period on the ground may have a gravity-wave period in the ionosphere. To estimate the required magnitude of U, we use the following numbers for the various parameters: V_H = 180 m/s, t = 9 min, t_B = 12 min. Putting $t_i = t_B$ in equation (1), we obtain U = 45 m sec^{-1}. This value of daytime neutral wind is in reasonable agreement with calculations based on temperature models (e.g., see Rishbeth 1972).

6. THE ACOUSTIC WAVE SPECTRUM

The spectrum of the ionospheric disturbance is important in that it is related, via atmospheric properties, to the spectrum of the source. The ionospheric record for the interval 1000-1200 UT on April 30 has been carefully scaled and the power spectrum determined by a technique described in greater detail in Davies and Jones (1972b). The spectrum given in figure 8 shows two characteristic peaks, one near 4.5 min and the other near 3.5 min. There is little power on frequencies less than 3.5 MHz, in accordance with the forbidden region of figure 2. On this occasion the gravity-wave spectrum appears to be frequencies below 1 MHz, the lower limit of our analysis.

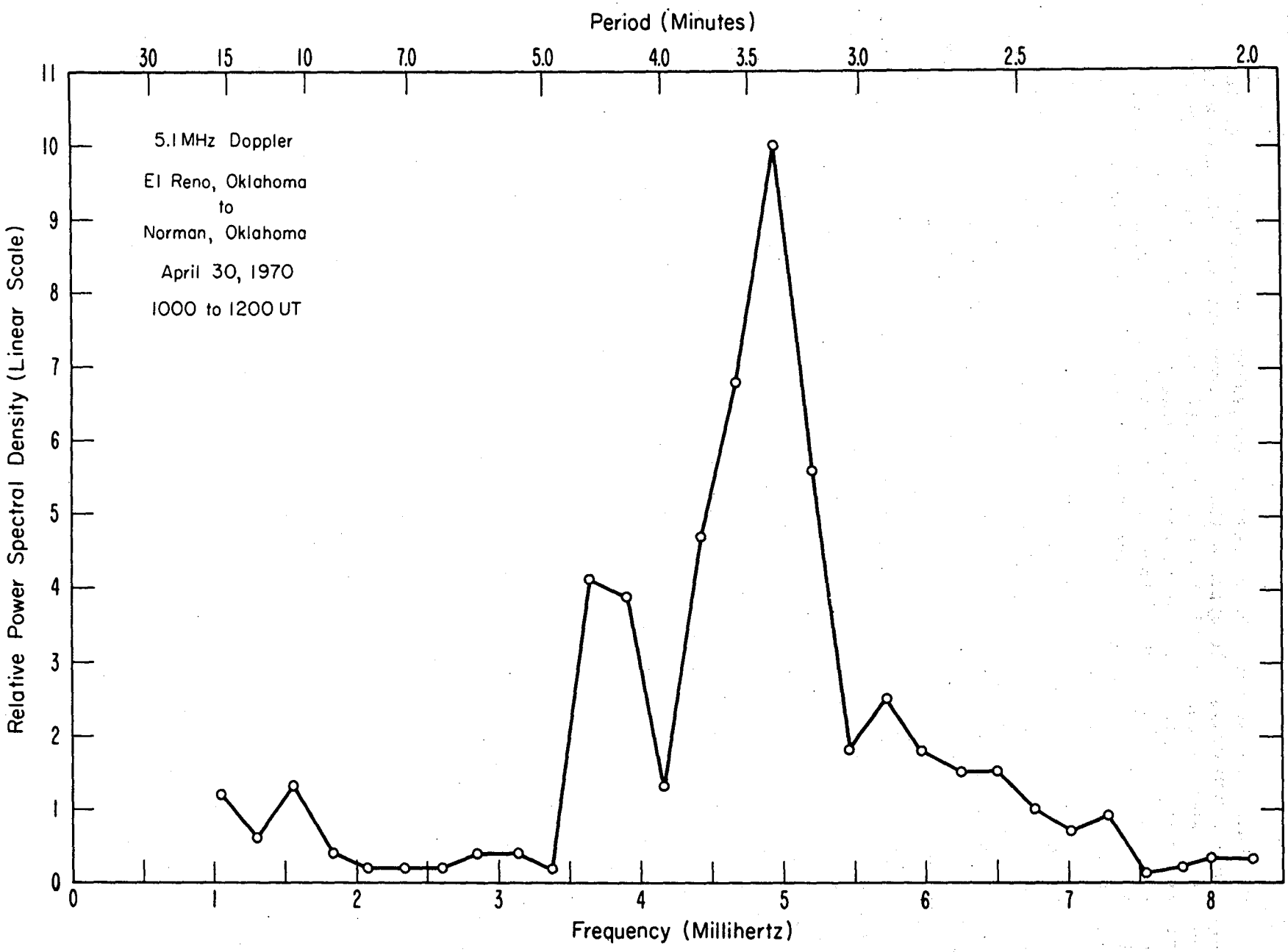

Figure 8. Power spectrum of the ionospheric disturbance of April 30, 1970, over the interval 1000-1200 UT.

It should be noted here that no attempt has been made to analyze the spectrum of the S-shaped disturbance. The S-shaped signatures are almost entirely the result of ray path distortion rather than of the shape of the ionospheric wave therefore the spectrum could be misleading.

7. DISCUSSION

The ionospheric records obtained near Oklahoma City on April 29-30, 1970 confirm other observations in this area during severe storms; namely that there are two types of disturbances:

(a) A quasi-sinusoidal wave with two spectral peaks, one near 4.5 min and the other near 3.5 min. The two waves travel with essentially the same horizontal trace speeds which are greater than the sound speed.

(b) An S-shaped type with periods between about 7 min and 10 min, which propagates with speeds appropriate to gravity waves.

A rough idea of the powers in the atmospheric waves is given in table 2 along with estimated source power, assuming no losses and inverse square spreading. The power in the S wave is considerably larger than that in the short-period disturbance. The values of S and P are probably lower bounds, because we have neglected the effects of the geomagnetic field on electron motion (see equation 53 of Davies and Jones, 1972b) and we have assumed that the reflection point is vertically above the source. Defocusing, atmospheric absorption, etc., will all act to make P larger than the values shown in table 2. In any case, the fraction of a thunderstorm's power which goes into these waves is extremely small.

A question which arises in these studies is "Why do the spectra of the short-period waves have two peaks." It is of interest to note that the average temperature at the tropopause over Oklahoma is approximately -55C. This temperature corresponds to an acoustic cutoff period of 4.52 min, which is very close to one of the observed periods. Chimonas and Peltier (1973 private communication) have recently pointed out that the observed periods of 4.5 and 3.5 are essentially the limits of the first and second acoustic modes of the atmosphere as calculated by Francis (1973) for the case of imperfectly ducted (leaky) modès.

8. ACKNOWLEDGMENTS

This work was partially supported by the Advanced Research Projects Agency, Nuclear Monitoring Research Office, under ARPA Order No. 1361.

We thank Dr. Edwin Kessler and his staff for facilities at the National Severe Storms Laboratory, NOAA, and Prof. W. Hughes of the Electircal Engineering Department, Oklahoma State University, for facilities at Stillwater.

Table 2. Power flux in the ionosphere and source power of acoustic-gravity waves (a) 3-5 min period, (b) S-shaped disturbance on April 30, 1970.

Wave	$\Delta f (sec^{-1})$	h(km)	$\rho (kg\ m^{-3})$	$C (m\ sec^{-1})$	$S (\mu W\ m^{-2})$	P(MW)
(a)	0.25	350	2×10^{-11}	850	0.5	0.36
(b)	0.5	207	3×10^{-10}	800	27	7.3

Power flux: $S = \frac{1}{2} P\ C \left(\frac{c\ \Delta f}{2f}\right)^2$

Source power: $P = 2\ \pi\ h^2\ S$

ρ = atmospheric density ($k\ m^{-3}$)

C = sound speed ($m\ sec^{-1}$)

h = reflection height (m)

f = radio frequency ($5 \times 10^6\ sec^{-1}$)

Δf = amplitude of frequency fluctuation (sec^{-1})

9. REFERENCES

Barry, G. H., L. J. Griffiths and J. C. Taenzer (1966): HF radio measurements of high-altitude acoustic waves from a ground-level explosion, J. Geophys. Res. 71, (17), 4173-4182.

Baker, D. M. and K. Davies (1968): Waves in the ionosphere produced by nuclear explosions, J. Geophys. Res. 73, (1), 448-451.

Baker, D. M. and K. Davies (1969): F2 region acoustic waves from severe weather, J. Atmos. Terr. Phys. 31, 11, 1345-1352.

Davies, K. (1965): Ionospheric Radio Propagation, U. S. Government Printing Office, Washington, D. C.

Davies K. (1966): Ionospheric effects of an earthquake and other geophysical disturbances, ESSA Symposium on Earthquake Prediction, U. S. Department of Commerce, Washington, D. C. 146-152.

Davies, K. (1969): Ionospheric Radio Waves, Ginn-Blaisdell, Waltham, 460 pp.

Davies, K. and D. M. Baker (1965): Ionospheric effects observed around the time of the Alaskan earthquake of March 28, 1964, J. Geophys. Res. 70, (9), 2251-2253.

Davies, K. and J. E. Jones (1971): Three-dimensional observations of traveling ionospheric disturbances, J. Atmos. Terr. Phys., 33, 39-46.

Davies, K. and J. E. Jones (1972a): Evidence for waves and winds in the ionospheric F region, Space Research XII, Akademie-Verlag, Berlin, 1149-1156.

Davies, K. and J. E. Jones (1972b): Ionospheric disturbances produced by severe thunderstorms, NOAA Professional Paper 6, U. S. Government Printing Office, No. 0317-00096.

Detert, D. G. (1969): A study of the coupling of acoustic energy from the troposphere to the ionosphere, Tech. Rept., Contract No. NAS 8-21079, AVCO Corp. Lowell, Mass., 197 pp.

Francis, S. H. (1973): Acoustic-gravity modes and large-scale traveling ionospheric disturbances of a realistic, dissipative atmosphere, J. Geophys. Res. 78, (13), 2278-2301.

Georges, T. M. (1967): Ionospheric effects of atmospheric waves, ESSA Tech. Rept. IER 57-ITSA 54, 341 pp.

Georges, T. M. (1968): HF Doppler studies of traveling ionospheric disturbances, J. Atmos. Terr. Phys. 30, 735-746.

Georges, T. M. (1969): Short-period ionospheric oscillations associated with severe weather, Proceedings of the Symposium on Acoustic-Gravity Waves in the Atmosphere, Boulder, Colo., July 15-17, 1968, ESSA, 171-178.

Hines, C. O. (1960): Internal atmospheric gravity waves at ionospheric heights, Can. Jour. Phys. 38, 1441-1481.

Hines, C. O. and C. A. Reddy (1967): On the propagation of atmospheric gravity waves through regions of wind shear, J. Geophy. Res. 72, 1015-1034.

Kohl, H. and J. W. King (1967): Atmospheric winds between 100 and 700 km and their effects on the ionosphere, J. Atmos. Terr. Phys. 29, 1045-1062.

Rishbeth, H. (1972): Thermospheric winds and the F region: A review, J. Atmos. Terr. Phys. 34, (1), 1-47.

Yuen, P. C., P. F. Weaver, R. K. Suzuki and A. S. Furumoto (1969): Continuous traveling coupling between seismic waves and the ionosphere evident in the May 1968 Japan earthquake data, J. Geophys. Res., Space Phys., 74, (9), 2256-2264.

PARTIAL LIST OF OTHER PAPERS

Allison, L. J., Joseph Steranka, G. Thomas Cherrix and Ernest Hilsenrath, 1972: Meteorological applications of the Nimbus 4 temperature-humidity infrared radiometer, 6.7 micron channel data. Bull. Amer. Meteor. Soc., Vol. 53, No. 6, 526-535.

Canipe, Yates Julio, 1973: On the structure and development of severe local storms as revealed by digital radar observations. Ph.D. Dissertation, Texas A&M University, College Station, Texas, 142 pp.

Canipe, Yates Julio and J. E. Vogel, 1973: Detailed analyses of tornado-producing thunderstorms using digital radar. Preprints of Papers, Eighth Conference on Severe Local Storms, Amer. Meteor. Soc., Boston, 57-60.

Davis, Kenneth and John E. Jones, 1972: Ionospheric disturbances produced by severe thunderstorms. NOAA Professional Paper 6, United States Department of Commerce, 47 pp.

Davies-Jones, R. P. and J. H. Henderson, 1973: Characteristics of thunderstorm updraft soundings. Preprints of Papers, Eighth Conference on Severe Local Storms, Amer. Meteor. Soc., Boston, 1-5.

Ellrod, G. P., 1973: Time variation of latent heat release during severe storms estimated from radar. Preprints of Papers, Eighth Conference on Severe Local Storms, Amer. Meteor. Soc., Boston, 69-72.

Ellrod, G. P., 1973: Time variation of latent heat release during the evolution of Oklahoma thunderstorms as estimated from radar observations. University of Wisconsin, Department of Meteorology, Report 73-1, Prepared for National Science Foundation Grant No. G1-31278X, 52 pp.

Freeman, John C., Sam B. Ross, Joseph L. Goldman and Sheran McCants, 1973: A mesoscale computing scheme applied to the severe storms case of April 29-30, 1970. Preprints of Papers, Eighth Conference on Severe Local Storms, Amer. Meteor. Soc., Boston, 328-330A.

Greene, D. R. and R. A. Clark, 1971: An indicator of explosive development in severe storms. Preprints of Papers, Seventh Conference on Severe Local Storms, Kansas City, 97-104.

Lee, J. T., 1971: Aerial survey of tornado-producing thunderstorms. Preprints of Papers, Seventh Conference on Severe Local Storms, Kansas City, 49-53.

Operations Staff, 1971: The NSSL surface network and observations of hazardous wind gusts. NOAA Technical Memorandum ERL-NSSL-55, Norman, Oklahoma, 81 pp.

Taylor, W. L., 1973: Electromagnetic radiation from severe storms in Oklahoma during April 29-30, 1970. Jour. Geo. Research, Vol. 78, No. 36, 8761-8777.

NATIONAL SEVERE STORMS LABORATORY

The NSSL Technical Memoranda, beginning with No. 28, continue the sequence established by the U. S. Weather Bureau National Severe Storms Project, Kansas City, Missouri. Numbers 1-22 were designated NSSP Reports. Numbers 23-27 were NSSL Reports, and 24-27 appeared as subseries of Weather Bureau Technical Notes. These reports are available from the National Technical Information Service, Operations Division, Springfield, Virginia 22151, for $3.00, and a microfiche version for $0.95. NTIS numbers are given below in parentheses.

No. 1 National Severe Storms Project Objectives and Basic Design. Staff, NSSP. March 1961. (PB-168207)

No. 2 The Development of Aircraft Investigations of Squall Lines from 1956-1960. B. B. Goddard. (PB-168208)

No. 3 Instability Lines and Their Environments as Shown by Aircraft Soundings and Quasi-Horizontal Traverses. D. T. Williams. February 1962. (PB-168209)

No. 4 On the Mechanics of the Tornado. J. R. Fulks. February 1962. (PB-168210)

No. 5 A Summary of Field Operations and Data Collection by the National Severe Storms Project in Spring 1961. J. T. Lee. March 1962. (PB-165095)

No. 6 Index to the NSSP Surface Network. T. Fujita. April 1962. (PB-168212)

No. 7 The Vertical Structure of Three Dry Lines as Revealed by Aircraft Traverses. E. L. McGuire. April 1962. (PB-168213)

No. 8 Radar Observations of a Tornado Thunderstorm in Vertical Section. Ralph J. Donaldson, Jr. April 1962. (PB-174859)

No. 9 Dynamics of Severe Convective Storms. Chester W. Newton. July 1962. (PB-163319)

No. 10 Some Measured Characteristics of Severe Storms Turbulence. Roy Steiner and Richard H. Rhyne. July 1962. (N62-16401)

No. 11 A Study of the Kinematic Properties of Certain Small-Scale Systems. D. T. Williams. October 1962. (PB-168216)

No. 12 Analysis of the Severe Weather Factor in Automatic Control of Air Route Traffic. W. Boynton Beckwith. December 1962. (PB-168217)

No. 13 500-Kc./Sec. Sferics Studies in Severe Storms. Douglas A. Kohl and John E. Miller. April 1963. (PB-168218)

No. 14 Field Operations of the National Severe Storms Project in Spring 1962. L. D. Sanders. May 1963. (PB-168219)

No. 15 Penetrations of Thunderstorms by an Aircraft Flying at Supersonic Speeds. G. P. Roys. Radar Photographs and Gust Loads in Three Storms of 1961 Rough Rider. Paul W. J. Schumacher. May 1963. (PB-168220)

No. 16 Analysis of Selected Aircraft Data from NSSP Operations, 1962. T. Fujita. May 1963. (PB-168221)

No. 17 Analysis of Methods for Small-Scale Surface Network Data. D. T. Williams. August 1963. (PB-168222)

No. 18 The Thunderstorm Wake of May 4, 1961. D. T. Williams. August 1963. (PB-168223)

No. 19 Measurements by Aircraft of Condensed Water in Great Plains Thunderstorms. George P. Roys and Edwin Kessler. July 1966. (PB-173048)

No. 20 Field Operations of the National Severe Storms Project in Spring 1963. J. T. Lee, L. D. Sanders and D. T. Williams. January 1964. (PB-168224)

No. 21 On the Motion and Predictability of Convective Systems as Related to the Upper Winds in a Case of Small Turning of Wind with Height. James C. Fankhauser. January 1964. (PB168225)

No. 22 Movement and Development Patterns of Convective Storms and Forecasting the Probability of Storm Passage at a Given Location. Chester W. Newton and James C. Fankhauser. January 1964. (PB-168226)

No. 23 Purposes and Programs of the National Severe Storms Laboratory, Norman, Oklahoma. Edwin Kessler. December 1964. (PB-166675)

No. 24 Papers on Weather Radar, Atmospheric Turbulence, Sferics, and Data Processing. August 1965. (AD-621586)

No. 25 A Comparison of Kinematically Computed Precipitation with Observed Convective Rainfall. James C. Fankhauser. September 1965. (PB-168445).

No. 26 Probing Air Motion by Doppler Analysis of Radar Clear Air Returns. Roger M. Lhermitte. May 1966. (PB-170636)

No. 27 Statistical Properties of Radar Echo Patterns and the Radar Echo Process. Larry Armijo. May 1966. The Role of the Kutta-Joukowski Force in Cloud Systems with Circulation. J. L. Goldman. May 1966. (PB-170756)

No. 28 Movement and Predictablity of Radar Echoes. James Warren Wilson. November 1966. (PB-173972)

No. 29 Notes on Thunderstorm Motions, Heights, and Circulations. T. W. Harrold, W. T. Roach, and Kenneth E. Wilk. November 1966. (AD-644899)

No. 30 Turbulence in Clear Air Near Thunderstorms. Anne Burns, Terence W. Harrold, Jack Burnham, and Clifford S. Spavins. December 1966. (PB-173992)

No. 31 Study of a Left-Moving Thundersrorm of 23 April 1964. George R. Hammond. April 1967. (PB-174681)

No. 32 Thunderstorm Circulations and Turbulence from Aircraft and Radar Data. James C. Fankhauser and J. T. Lee. April 1967. (PB-174860)

No. 33 On the Continuity of Water Substance. Edwin Kessler. April 1967. (PB-175840)

No. 34 Note on the Probing Balloon Motion by Doppler Radar. Roger M. Lhermitte. July 1967. (PB-175930)

No. 35 A Theory for the Determination of Wind and Precipitation Velocities with Doppler Radars. Larry Armijo. August 1967. (PB-176376)

No. 36 A Preliminary Evaluation of the F-100 Rough Rider Turbulence Measurement System. U. O. Lappe. October 1967. (PB-177037)

No. 37 Preliminary Quantitative Analysis of Airborne Weather Radar. Lester P. Merritt. December 1967. (PB-177188)

No. 38 On the Source of Thunderstorm Rotation. Stanley L. Barnes. March 1968. (PB-178990)

No. 39 Thunderstorm - Environment Interactions Revealed by Chaff Trajectories in the Mid-Troposphere. James C. Fankhauser. June 1968. (PB-179659)

No. 40 Objective Detection and Correction of Errors in Radiosonde Data. Rex L. Inman. June 1968. (PB-180284)

No. 41 Structure and Movement of the Severe Thunderstorms of 3 April 1964 as Revealed from Radar and Surface Mesonetwork Data Analysis. Jess Charba and Yoshikazu Sasaki. October 1968. (PB-183310)

No. 42 A Rainfall Rate Sensor. Brian E. Morgan. November 1968. (PB-183979)

No. 43 Detection and Presentation of Severe Thunderstorms by Airborne and Ground-Based Radars: A Comparative Study. Kenneth E. Wilk, John K. Carter, and J. T. Dooley. February 1969. (PB-183572)

No. 44 A Study of a Severe Local Storm of 16 April 1967. George Thomas Haglund. May 1969. (PB-184-970)

No.45 On the Relationship Between Horizontal Moisture Convergence and Convective Cloud Formation. Horace R. Hudson. March 1970. (PB-191720)

No. 46 Severe Thunderstorm Radar Echo Motion and Related Weather Events Hazardous to Aviation Operations. Peter A. Barclay and Kenneth E. Wilk. June 1970. (PB-192498)

No. 47 Evaluation of Roughness Lengths at the NSSL-WKY Meteorological Tower. Leslie D. Sanders and Allen H. Weber. August 1970. (PB-194587)

No. 48 Behavior of Winds in the Lowest 1500 ft in Central Oklahoma: June 1966 - May 1967. Kenneth C. Crawford and Horace R. Hudson. August 1970.

No. 49 Tornado Incidence Maps. Arnold Court. August 1970. (COM-71-00019)

No. 50 The Meteorologically Instrumented WKY-TV Tower Facility. John K. Carter. September 1970. (COM-71-00108)

No. 51 Papers on Operational Objective Analysis Schemes at the National Severe Storms Forecast Center. Rex L. Inman. November 1970. (COM-71-00136)

No.52 The Exploration of Certain Features of Tornado Dynamics Using a Laboratory Model. Neil B. Ward. November 1970. (COM-71-00139)

No.53 Rawinsonde Observation and Processing Techniques at the National Severe Storms Laboratory. Stanley L. Barnes, James H. Henderson and Robert J. Ketchum. April 1971. (COM-71-00707)

No. 54 Model of Precipitation and Vertical Air Currents. Edwin Kessler and William C. Bumgarner. June 1971. (COM-71-00911)

No. 55 The NSSL Surface Network and Observations of Hazardous Wind Gusts. Operations Staff. June 1971. (COM-71-00910)

No. 56 Pilot Chaff Project at the National Severe Storms Laboratory. Edward A. Jessup. November 1971. (COM-72-10106)

No. 57 Numerical Simulation of Convective Vortices. Robert P. Davies-Jones and Glenn T. Vickers. November 1971. (COM-72-10269)

No. 58 The Thermal Structure of the Lowest Half Kilometer in Central Oklahoma: December 9, 1966 - May 31, 1967. R. Craig Goff and Horace R. Hudson. July 1972. (COM-72-11281)

No. 59 Cloud-to-Ground Lightning Versus Radar Reflectivity in Oklahoma Thunderstorms. Gilbert D. Kinzer. September 1972. (COM-73-10050)

No. 60 Simulated Real Time Displays of Velocity Fields by Doppler Radar. L. D. Hennington and G. B. Walker. November 1972. (COM-73-10515)

No. 61 Gravity Current Model Applied to Analysis of Squall-Line Gust Front. Jess Charba. November 1972. (COM-73-10410)

No. 62 Mesoscale Objective Map Analysis Using Weighted Time-Series Observations. Stanley L. Barnes. March 1973. (COM-73-10781)

No. 63 Observations of Severe Storms on 26 and 28 April 1971. Charles L. Vlcek. April 1973. (COM-73-11200)

No. 64 Meteorological Radar Signal Intensity Estimation. Dale Sirmans and R. J. Doviak. September 1973. (COM-73-11923/2AS)

No. 65 Radiosonde Altitude Measurement Using Double Radiotheodolite Techniques. Stephan P. Nelson. September 1973. (COM-73-11934/9AS)

No. 66 The Motion and Morphology of the Dryline. Joseph T. Schaefer. September 1973. (COM-74-10043)

No. 67 Radar Rainfall Pattern Optimizing Technique. Edward A. Brandes. March 1974.

No. 68 The NSSL/WKY-TV Tower Data Collection Program: April - July 1972. R. Craig Goff and W. David Zittel. May 1974.

☆ U.S. GOVERNMENT PRINTING OFFICE — 784-577/1275 REGION NO. 8